

Optical Studies of Nanostructured ZnO

Gerard Tobin (B.Sc.)
School of Physical Sciences
Dublin City University

A thesis submitted to



for the degree of
Doctor of Philosophy

Research Supervisor
Dr. Enda McGlynn

May 2005

Declaration

I hereby certify that this material, which I now submit for assessment on the programme of study leading to the award of Doctor of Philosophy is entirely my own work and has not been taken from the work of others save and to the extent that such work has been cited and acknowledged within the text of my own work.

Signed: 

ID Number: 50161253

Date: 13 may 2005

Contents

Title page		i
Declaration		ii
Contents		iii
Abstract		viii
Chapter One	Introduction	1
1.1	<i>Introduction</i>	2
1.2	<i>Band theory of solids</i>	4
1.2.1	Metals, insulators and semiconductors	4
1.2.2	The Kronig-Penney model	6
1.2.3	Effective mass	8
1.2.4	Fermi level	9
1.2.5	Band structure	10
1.3	<i>Physical properties of Zinc Oxide</i>	12
1.4	<i>Pulsed Laser Deposition</i>	14
1.5	<i>Material characteristics</i>	17
1.5.1	Optical characterisation	18
1.6	<i>Outline of remainder of thesis</i>	20
	<i>Chapter One References</i>	21
Chapter Two	Experimental Arrangement	23
2.1	<i>Photoluminescence measurements</i>	24
2.1.1	Experimental arrangement	24
2.1.2	Excitation source	25
2.1.3	Spectrometer	27
2.1.4	Detector	29
2.1.5	Closed cycle cryostat	31
2.2	<i>Time resolved PL measurements</i>	32
2.2.1	General principles of TCSPC	32
2.2.2	Signal Processing	34
2.2.3	Time resolved PL experimental details	35
2.2.4	Data from time-resolved PL measurements	37

4.2.1	Background characteristics	77
4.2.2	Hall measurements on PLD-grown samples	80
4.3	<i>Photoluminescence of PLD samples</i>	81
4.3.1	Low temperature PL spectra	85
4.3.2	Temperature Dependence of PL emission from PLD samples	87
4.4	<i>Green Band</i>	92
4.5	<i>Reflectance</i>	94
4.6	<i>Summary</i>	100
	<i>Chapter Four References</i>	101
Chapter Five	High Excitation Effects and Random Lasing	103
5.1	<i>Introduction</i>	104
5.2	<i>Theory of lasing</i>	105
5.2.1	Interaction of light with matter	105
5.3	<i>Non linear effects</i>	109
5.3.1	Intermediate excitation regime	109
5.3.2	High excitation regime	111
5.4	<i>Lasing conditions and cavity effects</i>	113
5.4.1	Conditions for lasing	113
5.4.2	Stimulated emission	114
5.5	<i>Random lasing effects with no defined cavity structure</i>	114
5.5.1	Theory of random lasing	115
5.6	<i>Identification of effects due to high excitation intensities</i>	117
5.6.1	Non-linear optical processes and their spectral identification	118
5.6.2	Stimulated emission and lasing effects	119
	<i>Chapter Five References</i>	121
Chapter Six	High excitation and Random Lasing Results I	122
6.1	<i>Introduction</i>	123
6.2	<i>Discussion of spectral features</i>	125
6.3	<i>Investigation of high excitation effects using a spherical lens</i>	129
6.3.1	Eagle Picher bulk material	129

6.3.2	PLD ZnO sample (i)	133
6.3.3	PLD ZnO sample (ii)	135
6.3.4	PLD ZnO sample (iii)	136
6.3.5	Discussion of spherical lens setup	139
6.4	<i>Investigation of high excitation processes using a cylindrical lens</i>	141
6.4.1	Eagle Picher ZnO bulk material	141
6.4.2	PLD ZnO sample (i)	143
6.4.3	PLD ZnO sample (ii)	144
6.4.4	PLD ZnO sample (iii)	147
6.5	<i>Discussion of cylindrical lens setup and comparison with data obtained using spherical lens experimental arrangement.</i>	147
6.5.1	Effects of exciton diffusion on non-linear processes	149
6.5.2	Effect of differences in excitation geometry	155
	<i>Chapter Six References</i>	157
Chapter Seven	High excitation and Random Lasing Results II	159
7.1	<i>Variable stripe length results at room temperature</i>	160
7.1.1	Eagle Picher bulk ZnO	160
7.1.2	PLD ZnO sample (i)	163
7.1.3	PLD ZnO sample (ii)	164
7.1.4	PLD ZnO sample (iii)	166
7.1.5	Discussion of the VSL technique at room temperature	170
7.2	<i>Low temperature VSL studies</i>	170
7.2.1	Eagle Picher bulk ZnO material	171
7.2.2	PLD ZnO sample (i)	174
7.2.3	PLD ZnO sample (ii)	176
7.2.4	PLD ZnO sample (iii)	179
7.2.5	Discussion of the low temperature VSL	181
7.3	<i>Gain measurements from RT and low temperature VSL data.</i>	182
7.4	<i>PDA experiment at room temperature</i>	186
7.4.1	Eagle Picher Bulk ZnO Material	187
7.4.2	PLD ZnO Sample (i)	188
7.4.3	PLD ZnO Sample (ii)	189
7.4.4	PLD ZnO Sample (iii)	191

7.4.5	Low Temperature PDA Measurements	195
7.4.6	PLD ZnO Sample (iii)	195
7.5	<i>Summary of results</i>	197
	<i>Chapter Seven references</i>	198
Chapter Eight	Conclusions and Futher work	199
8.1	<i>Conclusions</i>	200
8.2	<i>Future work</i>	202
	<i>Chapter Eight references</i>	204
Appendix A	Photomultiplier Tube Specifications	A1
Appendix B	Equipment Specifications	B1
Appendix C	Time Resolved Analysis	C1
Appendix D	Spectrograph and PDA Specifications	D1
Appendix E	Hall measurements of PLD-grown samples	E1
Appendix F	Sample images	F1

Abstract

Optical studies of nanostructured ZnO

Photoluminescence (PL) spectroscopy and associated techniques are used to investigate the optical properties of zinc oxide (ZnO) samples. For samples grown by the pulsed laser deposition (PLD) technique we see evidence from PL measurements that they are of reasonably good quality, showing strong band-edge emission at both room and low temperatures. The low temperature PL is mainly due to near bandedge emission which increases in intensity with the annealing temperature of the PLD samples, which is interpreted as due to the increase in crystallite size and quality with annealing. We comment on the effects of strain and electric fields on the PL spectra as a function of annealing. Some evidence is also seen to favour the oxygen vacancy model of the green band. The PLD-grown material was referenced against a commercially grown bulk ZnO material of high quality.

An investigation into the processes involved in ZnO when it is optically pumped with high excitation values is undertaken. Identifications of the various non-linear features seen are presented. Measurements of optically pumped stimulated emission from the bulk material and PLD-grown samples have been made using an Nd: YAG laser. We discuss the results of high intensity optical excitation of both the bulk crystal and nanocrystalline samples. The effect of the various grain sizes in the PLD material on the emission processes is discussed. Lasing effects in these samples are identified and the nature of the processes examined, the origin of the laser cavity in the ZnO samples is discussed in relation to models of random lasing from the literature. We also comment in particular on the possible reasons why we fail to see any lasing effects in the bulk sample and present a simple model, which may partly answer this question.

Chapter One

Introduction to Semiconductor Properties

While most people are quite familiar with highly conductive and highly insulating materials in their everyday life, with examples such as copper wire and plastic insulation commonplace, the properties of semiconductors, although equally, if not more, important are less widely appreciated. Despite this lack of explicit public awareness, the semiconductor industry, in its various forms, is one of the cornerstones of our economic and technological advancement over the past 60 years, and the search for new materials and devices continues to drive this advance. In section 1.1 we briefly review the broad aspects of the semiconductor industry and the technological drivers in wide band gap materials research in particular. In section 1.2, the electronic properties of semiconductors generally are discussed. The properties of zinc oxide (ZnO), the semiconductor material investigated in this work, are outlined in more detail in section 1.3. In section 1.4 the pulsed laser deposition growth method used for the majority of ZnO samples studied in this work is described and finally an overview of optical characteristics is reviewed in section 1.5.

1.1:Introduction

Semiconductors have been at the heart of the advancement of technology for many decades and continue to be so. The industry advances both through new developments in the application of existing materials, such as silicon (Si) technology, and the search for and exploitation of emerging “new” materials. One of the strongest technological drivers in the compound semiconductor industry, and particularly dealing with optoelectronic devices, is the development of efficient short wavelength optoelectronic devices, specifically light emitters such as LED’s and laser diodes (LDs).

The development of efficient short wavelength photonic and other devices constitutes a multi-billion dollar industry at present, with the market up 221% since 1999 to 1.35 billion US\$ and is projected to grow at a steady rate as demands continue to rise up to 4.5 billion US \$ by 2007 [1] (also indicated by the market research from Strategies Unlimited [2]). While GaN has emerged as the dominant material in use at the moment, the future progress across platforms such as nanotechnology, smart materials, sensors and also compatibility with existing (predominantly Si) processing technology will place ever greater demands on the materials systems suitable for such developments.

In terms of this future vision ZnO presents many major advantages compared to GaN. Among these we may count the availability of large area single crystals for

homoepitaxy of device structures, the large excitonic binding energy of 60meV which enables excitonic emission at room temperature and above, the relative ease with which ZnO may be grown, excellent control of morphology and other properties, and the ability to grow such structures on Si. These properties constitute major advantages over existing and projected GaN technology and offers the very real prospect of satisfying many of the demands which the future of photonics and optoelectronics will impose. A recent review by *Pearton et al.* [3] includes a summary of the main aspects of ZnO materials and devices. It is an ideal candidate for optical devices for use in optical data storage (DVD), laser printing and integrated photonic circuits, in addition to broader applications in sensor and other technologies. In addition, ZnO is a chemical compound that is environmentally friendly and bio-compatible, which can ease environmental concerns centring on mass production issues [4].

One of the main challenges in the achievement of the technological goals for ZnO and its alloys is to fully understand the materials science involved in the growth of high quality thin films. Given that a large amount of literature on the optical and electronic properties of bulk ZnO exists since the 1950's and before [5], the utilization and transfer of such knowledge and data to thin film growth and characterisation is a key area of research. ZnO thin films have been successfully grown by a variety of techniques such as pulsed laser deposition (PLD), metal-organic vapour phase epitaxy (MOVPE), molecular beam epitaxy (MBE), magnetron sputtering and others. Among these techniques, PLD has been consistently shown to grow films of the highest quality and is excellently suited to this material system [6-9].

The present study investigates the possibilities of ZnO as an emitter of light in the blue and UV regions and specifically concentrates on the nanocrystallinity of the material grown by PLD and its effects on the optical properties, including stimulated emission behaviour. Samples are characterized mainly using the photoluminescence technique and derivations of this, which gives an insight into the processes important for light emitting devices and provides useful feedback information for growers.

1.2: Band theory of solids

The optical and electronic behaviour of different types of materials can be largely explained by the band theory of solids. The electrons surrounding the nuclei have well defined energy levels in the isolated atom and when two atoms are distant from each other, there is no interaction between their electron wave functions. When two atoms are brought together the electron wave functions begin to overlap and consequently interact. This interaction will cause the initially degenerate levels of the separate atoms to split slightly. In a crystalline solid material many, many atoms are brought together, and when the distance between atoms approaches the equilibrium interatomic spacing the split energy levels form essentially continuous bands of energies separated by energy gaps, where there are no propagating electron states. This model of band formation is known as the tight-binding method, and is outlined in detail in the book by *Harrison* [10]. The highest occupied band is called the valence band, and the lowest unoccupied band is termed the conduction band. The energy gap between the highest state in the valence band and the lowest in the conduction band is termed the band gap, denoted by E_g . Depending on how the valence/conduction bands are filled the material can be classified as a metal, semiconductor or insulator.

1.2.1: Metals, insulators and semiconductors

Every crystalline solid has its own characteristic energy band structure, which can be categorised into the three different classes, metals, insulators and semiconductors.

A band that is completely empty of electrons cannot take part in electrical conduction, as there are no electrons to conduct. A band that is completely full of electrons cannot take part in electrical conduction either because when an electric field is applied to an electron it cannot move to a higher state in the band because all the higher states are full or if it is at the highest state the forbidden gap lies immediately above the top of the allowed band. Thus to have electrical conduction, one must have electrons in bands which are only partially filled. Thus if either the conduction or valence bands are partially filled with electrons they can contribute to current conduction in the material.

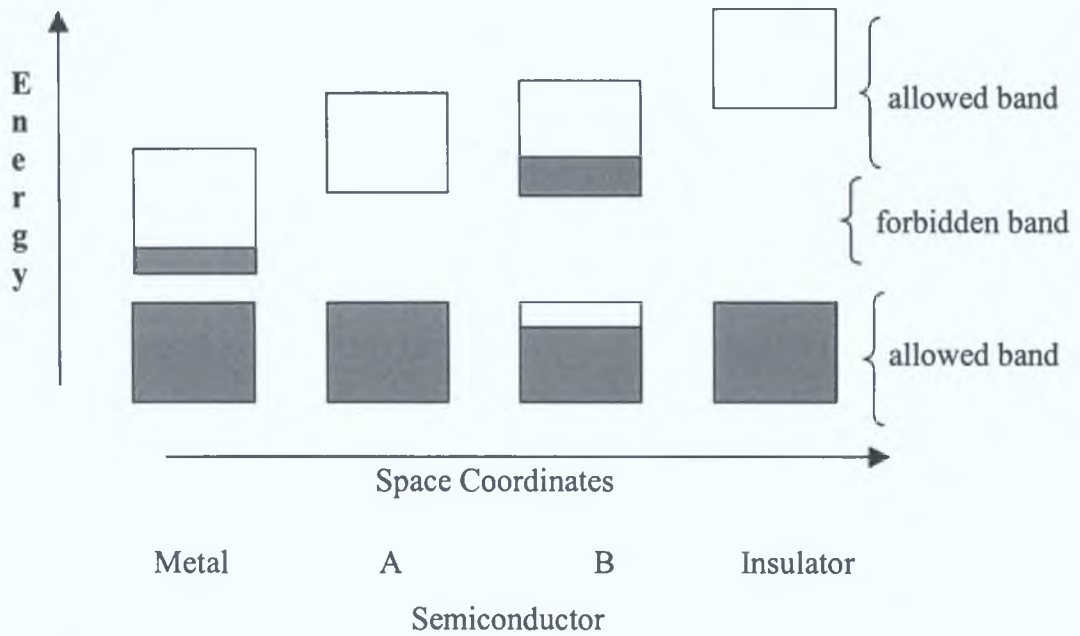


Figure 1.1: Drawing of the energy bands for metals, insulators and semiconductors [11].

In figure 1.1 the typical band structures of metals, insulators and semiconductors are drawn. In the case of the energy-band diagram for a metal, we see that the valence band is partially filled with electrons and hence can contribute strongly to electrical conduction in the material. For the case of the insulator, the valence band is completely full and the conduction band is empty and the forbidden energy gap is large (compared to the thermal energies at room temperature, hence reducing the probability of thermal excitation of carriers from one band to another), and consequently the material cannot effectively conduct electricity.

Semiconductors, as the name implies, lie somewhere in the middle of these classes. Semiconductors typically have the electronic distribution of insulators at low temperatures, i.e. the valence band is completely full and the conduction band is empty, but the energy gap is smaller (and comparable to or less than, the thermal energy at room temperature). We show this situation for semiconductors in figure 1.1 above, where there are two cases, (A) at very low temperatures (0K) where the valence band is full and the conduction band is empty, i.e. an insulator. However since the size of the band gap is much smaller than that of an insulator, at room temperatures (B) thermal excitation of electrons from the valence band to the conduction band may occur, resulting in partially filled bands, and hence enabling electrical conduction. The vacant state left in the valence band is called a hole and a more detailed analysis shows that a nearly full band with a single empty level behaves like a charge carrier with the same

magnitude of charge as the electron but of an opposite sign. Thus thermal excitations can create such electron-hole pairs and thus enable conduction in the material at elevated temperatures. These materials are known as intrinsic semiconductors.

Another way to increase conduction in semiconductors is to introduce an impurity atom into the lattice in a method called doping and the materials produced in this way are known as extrinsic semiconductors. When an impurity atom is introduced additional levels are created in the energy band structure usually within the band gap. Depending on the atomic species, such impurities may either donate their electrons to the conduction band or accept electrons from the valence band, thus either partially filling or emptying the conduction and valence bands, respectively, and enabling electrical conduction.

1.2.2: The Kronig-Penney model

The formation of energy bands can be predicted from a solution of the Schrödinger equation for the periodic potential provided by a crystal lattice. This periodic potential may be considered a perturbation on the free electron energy levels. This approach to the band structure problem is known as the nearly-free electron model. The electron energy versus wavevector curve for a free particle is shown in *figure 1.2*.

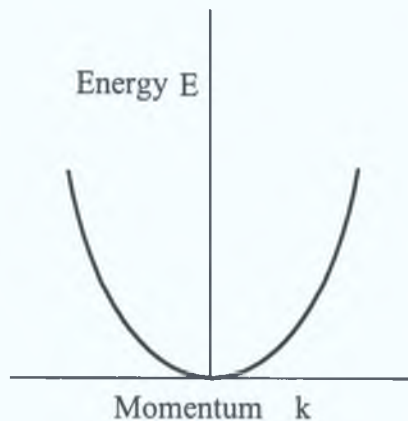


Figure 1.2: Energy versus momentum curve for a free electron.

A complete solution of the Schrödinger equation for a realistic potential involves extremely detailed mathematical models and rather sophisticated approximations, but a relatively simple model using a periodic square well potential was used by Kronig and Penney [12], which captures the essential details, and which we will outline below. The model predicts that the motion of an electron in a periodic lattice is again characterised by “bands” of allowed energies separated by forbidden regions. The Kronig-Penney

model predicts that discontinuities will occur on the otherwise parabolic free electron E - k curve when

$$k = \frac{n\pi}{a} \quad \text{where } n = 1, 2, 3 \dots \quad (1.1)$$

where a is the lattice constant, as shown in *figure 1.3* due to the perturbation by the periodic crystal potential. These k values define the boundaries of the Brillouin zones, shown in *figure 1.3*.

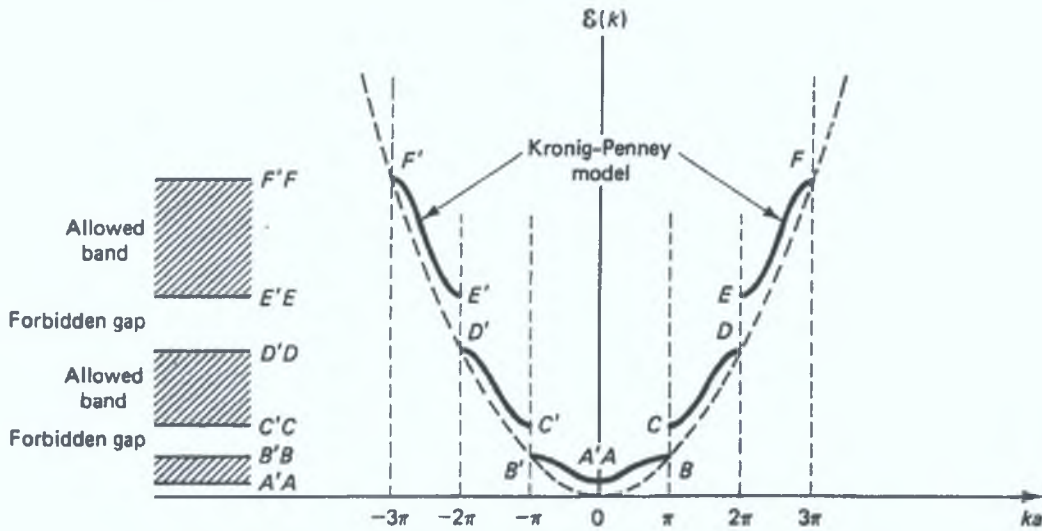


Figure 1.3: Plot of E - k for the Kronig-Penney model [12]. The solid curves represent the allowed energy bands AB, CD and EF. The energy intervals BC and DE are the forbidden zones. The E - K curve for a free electron is shown as the dashed curve.

The energy bands on the E vs. k curve may be folded back into the first Brillouin zone ($-\pi/a < k < \pi/a$) and the electron energy states in the crystal are then characterised by the so-called “crystal momentum”, denoted by k , which may be translated so that it always lies in the first Brillouin zone. For crystalline solids the crystal momentum in some sense takes on the role of the free electron wavevector, and is the quantum number associated with lattice translations in the crystal [13]. For optical absorption, emission and other processes such as scattering, conservation of the crystal momentum becomes the key principle in determining the allowed transitions. *Figure 1.4* shows the energy bands of the material plotted in the first Brillouin zone (the reduced zone scheme).

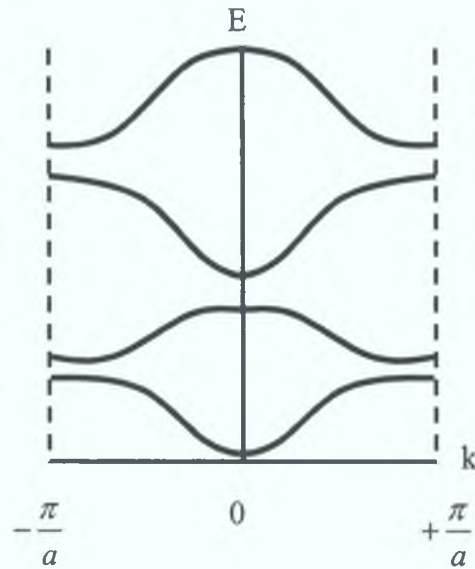


Figure 1.4: Reduced zone representation of the E-k curve

1.2.3: Effective mass

An electron moving in a crystal does not behave in the same way as an electron moving in a vacuum. This is not surprising as an electron travelling through a crystal lattice is interacting with all the different potentials that it sees depending on its direction through the lattice. This can be taken into account using a free electron-type relationship and changing the mass of the electron from its actual vacuum mass to its “effective” mass in the crystal.

For a completely free electron, the energy is related to the momentum (p) by

$$E = \frac{p^2}{2m} \quad (1.2)$$

where m is mass. Momentum is related to the wavelength according to

$$p = \frac{h}{\lambda} \quad (1.3)$$

where h = Planck’s constant

The propagation constant of a wave is denoted by k , where

$$k = \frac{2\pi}{\lambda} \quad (1.4)$$

Equation 1.2 can be rewritten to express the energy momentum in terms of k instead of p according to

$$E = \frac{\hbar^2 k^2}{2m} \quad (1.5)$$

where $\hbar = \frac{h}{2\pi}$.

Equation 1.5 relates the energy of particle E with the propagation constant k . Figure 1.2 is a plot of equation 1.5, which shows the energy relationship for a completely free electron. The E - k curve is parabolic and all values of energy are allowed. If one differentiates equation 1.5 twice with respect to k and rearranges to find an expression for m :

$$m = \frac{\hbar^2}{d^2E/dk^2} \quad (1.6)$$

Semiconductors, for the most part, have carriers (either electrons or holes) generally localised close to the band edges, where the E vs. k curves are parabolic to a good approximation, because the band edge is an energy extremum. Hence one may treat the behaviour of the carriers as being rather similar to that of free electrons, but with the effect of the lattice incorporated in a renormalisation of the mass, determined by the curvature of the E vs. k curve. It is possible to calculate the mass of a particle given its E - k diagram since the mass is inversely proportional to the curvature of the E - k curve. Although equation 1.6 was derived to describe the free electron, it still holds true for electrons and holes in crystals, so in general

$$m^* = \frac{\hbar^2}{d^2E/dk^2} \quad (1.7)$$

where m^* is the effective mass of the particle (which will have a tensor form for low symmetry crystals).

1.2.4: Fermi level

A population of electrons in a solid obey Fermi-Dirac statistics describing their distribution among the energy levels in the valence and conduction bands. The distribution of electrons over a range of allowed energy levels at thermal equilibrium is described by:

$$f(E) = \frac{1}{1 + \exp\left(\frac{E - E_F}{kT}\right)} \quad (1.8)$$

The function $f(E)$, the Fermi-Dirac distribution function, gives the probability that an electron will be able to occupy an available energy state E at absolute temperature T and the quantity E_F the Fermi level. If the energy level E is at the Fermi level then

$$f(E) = \frac{1}{1 + \exp(0)} = \frac{1}{2} \quad (1.9)$$

Therefore the Fermi level is simply a reference energy level at which the probability of finding an electron is one half.

The rectangular distribution in *figure 1.5* implies that at 0K every available energy state up to E_F is filled with electrons, and all states above E_F are empty. The symmetry of the distribution of empty and filled states above E_F makes the Fermi level a natural reference point in calculations of electron and hole concentrations in semiconductors. Raising the temperature causes some levels above E_F to become filled and therefore, since the function is symmetric some levels below E_F become empty. The nature of this distribution ensures that the holes in the valence band and the electrons in the conduction band remain close to the valence and conduction band edges, respectively.

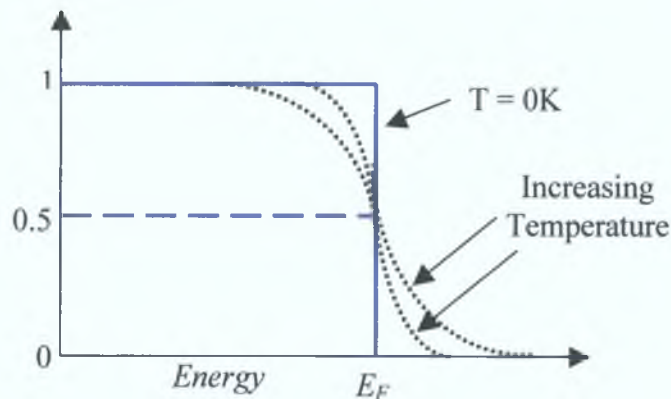


Figure 1.5: The Fermi-Dirac probability function at $T = 0\text{ K}$ and at $T > 0\text{ K}$.

1.2.5: Band structure

In *equation 1.1* the parameter “ a ” is the internuclear distance of the atoms within the crystal lattice, and we have considered only the one dimensional crystal situation, i.e. a line of atoms. In a real, three dimensional crystal, the internuclear distance varies with crystal direction, and hence so will also the band structure. Plotting energy values as a function of k in each of the three principal crystal directions ($\langle 001 \rangle$, $\langle 110 \rangle$, $\langle 111 \rangle$ for cubic crystals) shows the major features of the band structure of most cubic semiconductors. In *figure 1.6* the E versus k diagrams for both GaAs and silicon are shown. Both illustrate the directional character of electronic band structure, due to changes in lattice properties along different crystalline axes. The diagram shows the differing band structure along the (100) and (111) directions. We also note that the smallest energy gap between the valence band and conduction band may not occur at

the centre of the Brillouin zone ($k = 0$). *Figure 1.6(a)* demonstrates that GaAs is a direct band gap semiconductor, with its conduction band minimum directly above the valence band maximum at the zone centre. *Figure 1.6(b)* indicates that silicon has an indirect gap, with the lowest minimum in the conduction band displaced from the zone centre. In this case an electron transition from the top of the valence to the bottom of the conduction band must undergo a significant change in the wavevector. This distinction is important when discussing the light emission and absorption mechanisms in the material.

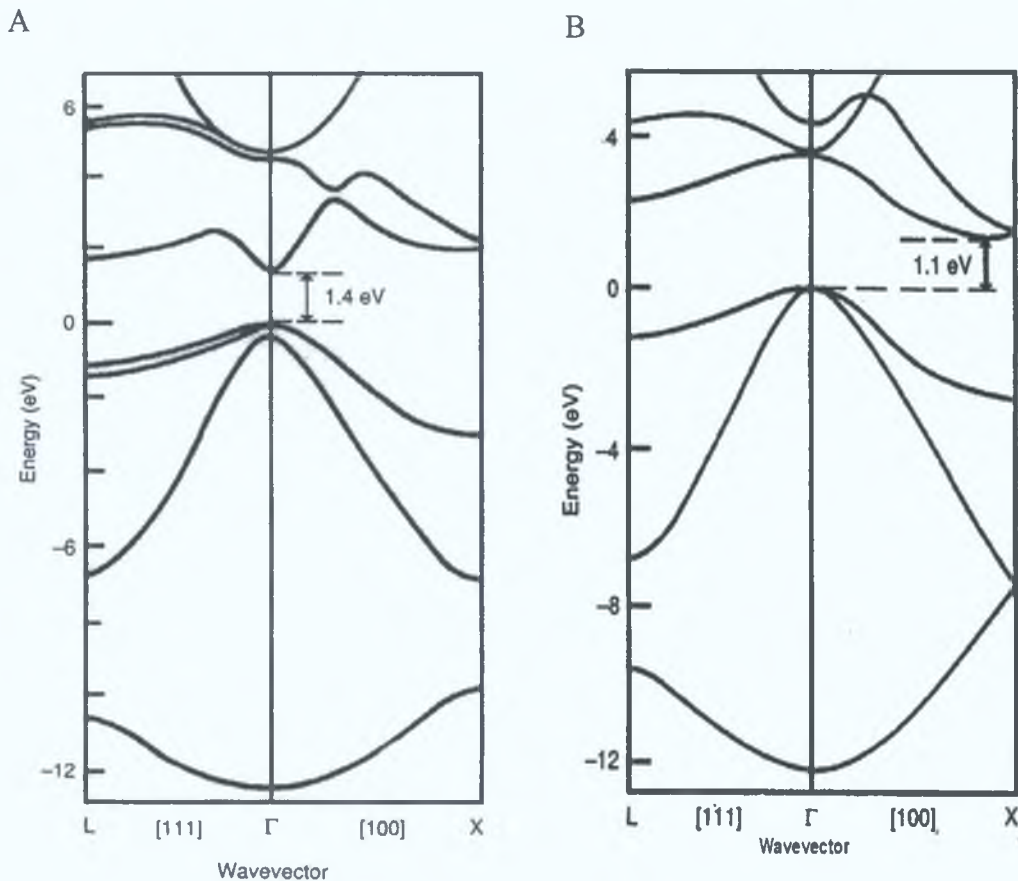


Figure 1.6: (A) Energy versus wavevector diagram for GaAs, (B) Energy versus wavevector diagram for silicon [14].

The band structure for ZnO, which is examined in this work, is shown in *figure 1.7*. ZnO has a hexagonal crystal structure, thus the crystal directions are different to those used for cubic crystals (the direction M corresponds to the $(10\bar{1}0)$ crystal direction in hexagonal coordinates [15]). However the same broad principles apply, and the figure below shows that ZnO is a direct band gap material, with its conduction minimum directly above the valence band maximum.

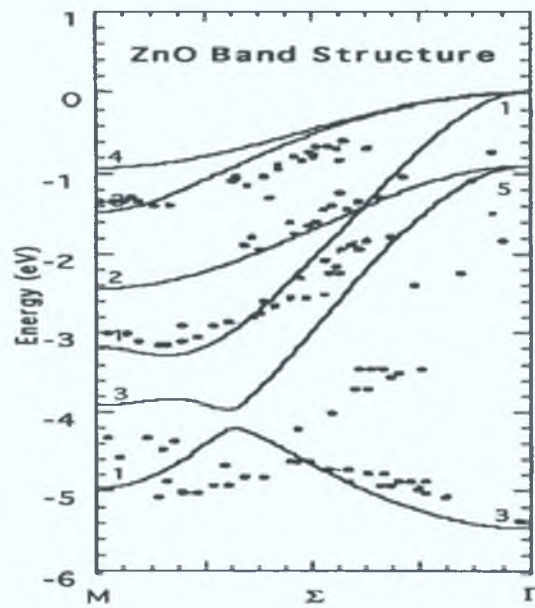


Figure 1.7: Energy band diagram of ZnO [16].

This general introduction will be expanded upon in subsequent chapters, which discuss optical processes in ZnO more thoroughly.

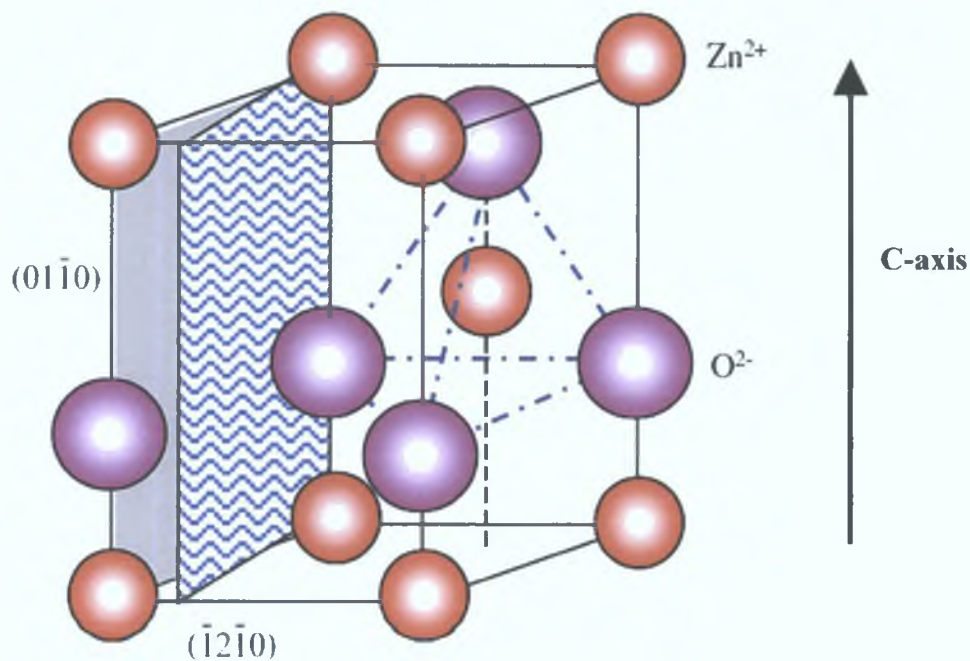
1.3: Physical properties of Zinc Oxide

ZnO is a wide band gap II-VI material with a direct band gap (3.37eV at room temperature (RT)) in the UV range and a large exciton binding energy (~60 meV), which makes it particularly suitable for short wavelength photonic applications, as mentioned before. An overview of ZnO and its general physical properties can be seen in *table 1.1* along with a comparison with other semiconductor materials.

Material		ZnO	ZnS	ZnSe	GaN	6H-SiC
Crystal Structure		Wurtzite	Wurtzite	Zinc-blende	Wurtzite	Wurtzite
Lattice Constant	a(Å)	3.249	3.823	5.668	3.189	3.081
	c(Å)	5.207	6.261	...	5.185	15.117
Band Gap Energy at RT	E_g (eV)	3.37	3.8	2.70	3.39	2.86
Cohesive Energy	E_{coh} (eV)	1.89	1.59	1.29	2.24	3.17
Melting point	T_m (k)	2248	2103	1793	1973	> 2100
Exciton Binding Energy	E_h (meV)	60	39	20	21	...
Dielectric constant	$\epsilon(0)$ (E C)	8.75	9.6	9.1	8.9	9.66
	$\epsilon(\infty)$ (E C)	3.75	5.7	6.3	5.35	6.52

Table 1.1: Comparison of ZnO properties with other wide band gap semiconductors.

The large bond strength is reflected by the high melting point and the relatively high cohesive energy, which promises a large damage threshold for various types of radiation. The bonding in ZnO is covalent, however it is highly polar because of the electronegativity of the oxygen species. Due to the large exciton binding energy ZnO offers the possibility of light emitting devices utilising the efficient exciton emission mechanism up to and above room temperature. ZnO is one of the hardest materials in the II-VI group and for this reason the degradation of the material due to the generation of dislocations during device operation should not be a problem, unlike the case for other II-VI materials, which have been notoriously plagued by dark line and other types of defects [17]. ZnO has a very high melting point and therefore it can withstand high temperature annealing and other treatment processes associated with doping, contact formation etc. However, annealing tends to disrupt the material stoichiometry, with preferential dissociation of the O species, leading to defect formation. Thus, annealing treatments tend to be carried out in an O atmosphere [18]. ZnO has a wurtzite structure where every atom has four nearest neighbours and 12 next neighbours as seen in *figure 1.8*. There are four atoms per unit cell and every atom of one type (group II) is tetrahedrally coordinated with four atoms of other type (group VI). Due to the tetrahedral coordination of wurtzite structures ZnO can often be modeled as a perturbed tetrahedral structure.



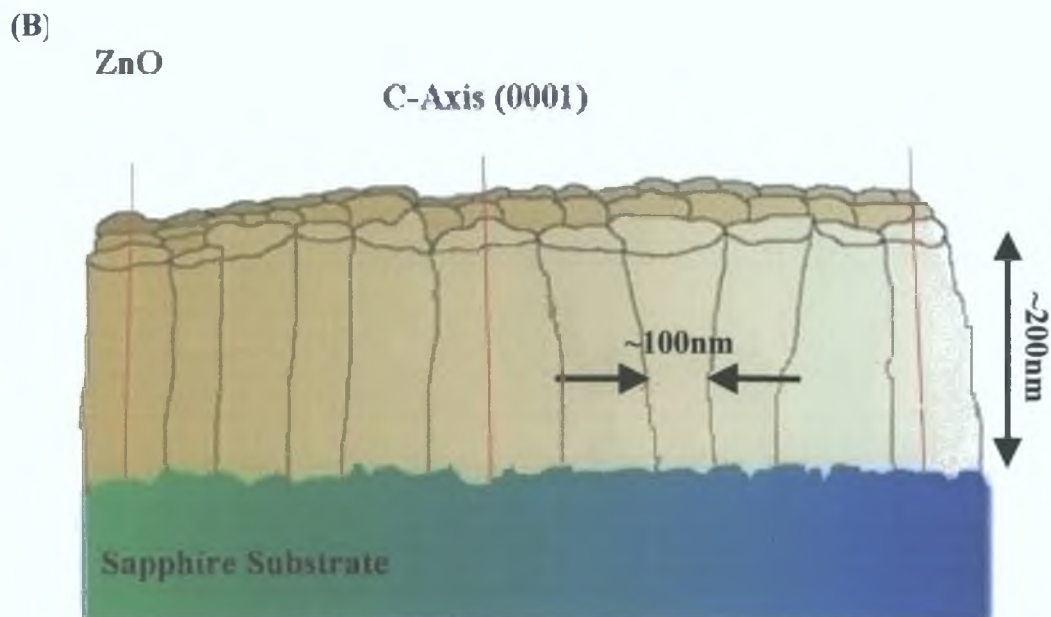


Figure 1.8: (A) The wurtzite structure model of ZnO [19]. (B) Schematic diagram of PLD-grown ZnO films showing C-axis oriented grains. The c-axis is perpendicular to the sapphire substrate [20].

The majority of ZnO samples used in this work (grown by PLD) are thin films with a granular structure, with an average grain size of the order of ~ 100 nanometers. The grains are oriented with the c-axis perpendicular to the growth substrate and maintain a constant in-plane epitaxial relationship to the substrate. We describe the structure as “epitaxially ordered nanocrystalline” from here on. A detailed description of the sample morphology studied in this work will be given in chapter four. The surfaces of the nanocrystalline films may be either Zn- or O-terminated.

1.4: Pulsed Laser Deposition

There are a multitude of different thin film growth techniques used to grow semiconductor materials. This section will only concentrate on one technique as the thin films investigated in this thesis were grown by Pulsed Laser Deposition (PLD) technique. The principle of PLD growth is shown in *figure 1.9*, where a high-powered pulsed laser is focused through an optical window onto a target in a vacuum chamber. The target is fabricated from the growth material, zinc oxide in our case (or possibly zinc metal). Above a certain laser power density, target ablation occurs, forming a plasma plume (containing a range of highly energetic ionised species, clusters etc.). Material from the plume is then allowed to recondense on a substrate where film growth

occurs. The substrate in our case is *c*-plane sapphire, which is commonly used as a substrate for ZnO thin film growth. It has a lattice mismatch of less than 15% with ZnO. This mismatch value has a considerable effect on the film growth, and in particular on the dislocation density and granular structure.

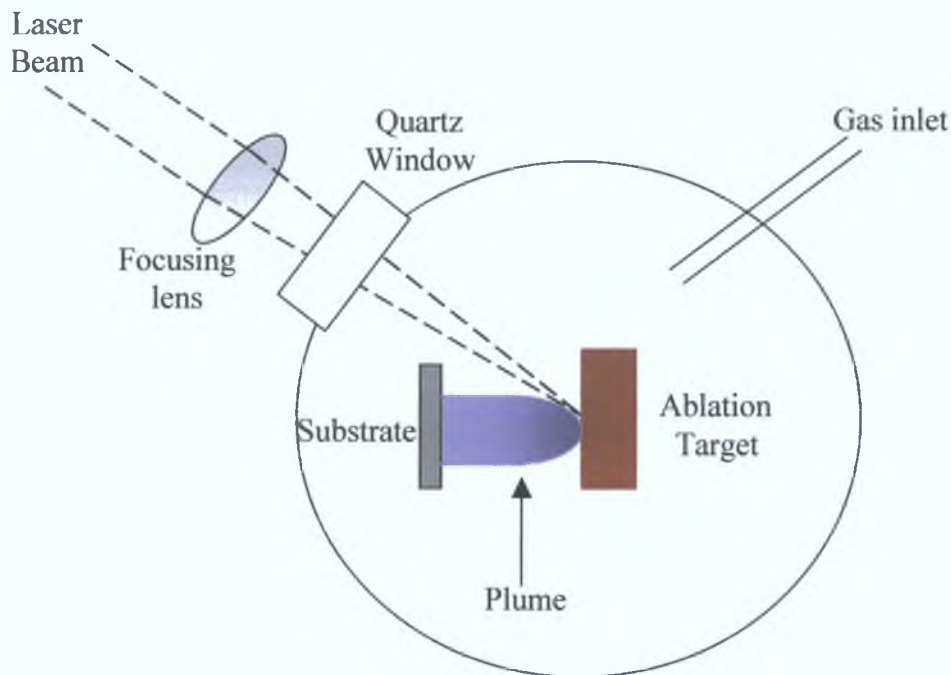


Figure 1.9: Schematic of the pulsed laser deposition technique.

The growth chamber may also be pressurised with a background gaseous atmosphere, which may be a mixture of inert and reactive species which can alter the chemical reactions and plasma plume dynamics and significantly influence the growth. In the growth of our samples the chamber was pressurised with O_2 , which is often used in PLD growth of ZnO to compensate for the commonly observed oxygen deficiency in films grown in vacuum [18]. Table 1.2 gives a comparison of the major advantages and disadvantages associated with the PLD growth technique. A review of this technique is given in reference 21.

<i>Advantages [21]</i>	<i>Disadvantages</i>
<ul style="list-style-type: none"> • Almost any type of material may be ablated, and hence quite refractory species may be grown with PLD • There is an excellent degree of control over the growth dynamics, with good thickness and interface abruptness [22] • Stoichiometric materials ablation / transport means that the target composition is quite faithfully mirrored in the film • Substrate temperatures determined by adatom mobility requirements rather than necessity to maintain a chemical reaction • Gas environment / pressure / ionization state are variable parameters allowing relatively easy exploration of growth parameter space • The small target size needed enables mutli-target samples holders even in UHV environment and hence enables complex heterostructure growth 	<ul style="list-style-type: none"> • The main disadvantage is associated with the purity of the starting, particularly the target, materials. This has traditionally been viewed as the major weakness of PLD for semiconductor growth as targets were usually manufactured by sintering, which can introduce a high level of contamination • Structural damage in the film caused by the bombardment by high kinetic energy ablation particles from the plasma plume • Limited / no control of spatial distribution of material within the ablation plume makes it difficult to grow uniform larger area films

Table 1.2: Advantages and disadvantages of pulsed laser deposition technique.

It has been repeatedly shown that ZnO films of the highest quality can be grown by the PLD technique [23, 24], both in terms of the electronic and optical properties of the film. Recent publications have shown strong evidence that ZnO structures grown by PLD have excellent device potential [23,25].

There are still some challenges to be resolved to enable ZnO to progress to the next stage of development where it can be used for device production and provide a credible alternative to GaN for wide band gap applications. The main problem with ZnO is that

usable and reproducible p-type doped ZnO has not yet been reported and independently verified [26]. The difficulties in producing p-type doped material arise from a variety of causes. ZnO naturally occurs with a substantial n-type background concentration ($\sim 10^{15} \text{ cm}^{-3}$ in bulk material), whose origin may lie in native defects such as oxygen vacancies or highly soluble extrinsic impurities such as hydrogen [27]. This n-type contribution must be compensated by suitable acceptors in order to form a p-type region. However, acceptor dopants introduced into the crystal may be autocompensated by the formation of native defects [28]. Low solubility of the acceptor dopants in the host material is another potential problem [29]. In addition, many of the acceptor levels associated with the common candidate impurities are deep levels and hence will not be completely ionized at room temperature. Further problems may occur in the case of impurities with an amphoteric character such as Li, which tend to make the material semi-insulating [30]. The realization of reliable and reproducible p-type material is a key aim because most efficient solid-state emitters involve a p-n junction structure of some type. The future of ZnO as a commercial light-emitting device thus depends on creating a reliable p-type doping method.

1.5: Material characteristics

Growth techniques such as PLD can introduce a variety of defects in the material grown, which can completely change the optical and electronic properties of thin films compared to the bulk material. For this reason it is important to have techniques that can investigate, characterise and monitor the creation of new materials [31]. These techniques become particularly important in the study of relatively new materials like ZnO, where many of the bulk properties are as yet not fully determined [32].

There are three main aspects of interest in the characterisation of thin films:

- Electrical characterisation
- Physical/chemical characterisation
- Optical characterisation

Electrical characterisation generally provides information on electrical properties such as resistivity and carrier concentrations, but it generally does not uniquely identify the impurities involved. A major disadvantage with this form of characterisation is that it generally requires contacts to be formed to the sample, which may render the sample useless for further processing, and it has little or no spatial discrimination [31]. The

formation of contacts may also lead to the introduction of defects, which would not otherwise have been present in the film.

Physical/chemical characterisation generally yields information on the gross structural, compositional and defect parameters, and may also yield impurity identifications. The methods used are generally not very sensitive at the lower level of impurity densities found in semiconductors and they often require rather elaborate equipment. Techniques such as x-ray diffraction (XRD), scanning electron microscopy (SEM), atomic force microscopy (AFM) and secondary ion mass spectroscopy (SIMS) all provide information on aspects of the structural, compositional and defect characteristics [31]. The principal characterisation technique reported in this thesis will be optical characterisation, as discussed in the next section.

1.5.1: Optical characterisation

Optical characterisation of materials is useful in determining such parameters as physical device dimensions, layer thicknesses, impurity and defect identification and concentrations. The maturity of the laser industry has led to optical diagnostic tools becoming ever more accessible. Optical characterisation techniques have the following advantages over the other two characterisation categories:

- They are generally non-contact techniques
- They are non-destructive
- They require little or no sample preparation

The most widely used optical techniques include:

- Reflectivity and transmission, including ellipsometry, modulation spectroscopy, etc.
- Raman spectroscopy and other scattering techniques
- Photoluminescence (PL)
- Infrared (IR) spectroscopy

With these techniques it is possible to measure various important parameters of a semiconductor material. A list of semiconductor properties that can be characterised by Raman, PL and IR spectroscopy is given in *table 1.3* [31].

Semiconductor Properties	Optical methods		
	<i>PL</i>	<i>Raman</i>	<i>IR</i>
Band			
Gap	✓		✓
Effective mass			✓
Band offset	✓		
Free earrer			
Concentration		✓	✓
Mobility		✓	✓
Scattering time		✓	✓
Resitivity		✓	✓
Lattice			
Alloy composition	✓	✓	✓
Orientation		✓	
Crystallinity	✓	✓	
Stress	✓	✓	
Impurity and defect			
Presence and type	✓	✓	✓
Concentration	✓	✓	✓
Microstructure			
Layer thickness			
Surface behaviour	✓	✓	
Interface behaviour	✓	✓	✓
Layer-by-layer behaviour			✓

Table 1 3 Synopsis of Optical Characteristic Techniques [31]

1.6 Outline of remainder of thesis

Chapter two describes the important aspects of the experimental arrangement and procedures and a detailed description of the equipment used. Chapter three discusses the photoluminescence characterisation technique and presents results at both room and low temperatures from bulk ZnO material that is subsequently used as a reference in the analysis of the PLD-grown ZnO material. In chapter four the PLD-grown ZnO samples are discussed and their photoluminescence results analysed with particular attention to the material quality and defects associated with the film morphology. Chapter five introduces the various concepts associated with high level optical excitation in ZnO, such as non-linear optical bands associated with biexcitons and the electron-hole plasma state, in addition to a discussion of random lasing processes in granular material in comparison with the conventional laser structure in semiconductors. Chapters six and seven present the results of high level optical excitation studies on both bulk and PLD-grown ZnO material. The identification of features associated with non-linear optical processes, and the observation of stimulated emission and lasing at both room and low temperatures is discussed. The final chapter presents a summary of the experimental results and the possibilities for future research.

Chapter One References

- [1] <http://www.cermetinc.com/markets.htm>
- [2] <http://su.pennnet.com/>
- [3] S.J.Pearton, D.P.Norton, K.Ip, Y.W.Heo, T.Steiner, *J.Vac.Sci.Tech B* v22, (2004), 932.
- [4] T.Minami, *Semicond. Sci. Technol.* 20, 2005,S35.
- [5] G.Heiland, E.Mollwo, F.Stockmann, *Solid State Phys.*, 8, (1959), 191.
- [6] J.F.Muth, R.M.Kolbas, A.K.Sharma, S.Oktyabrsky, J.J.Narayan, *JAppl. Phys.* 85, (1999), 7884.
- [7] T.Makino, T.Yasuda, Y.Segawa, A.Ohtomo, K.Tamura, M.Kawasaki, H.Koinuma, *Appl. Phys. Lett.* 79, (2001), 1282.
- [8] S.Krishnamoorthy, A.A.Iliadis, A.Inumpudi, S.Choopun, R.D.Vispute, T.Venkatesan, *Solid State Elect.* 46, (2002), 1633.
- [9] M.Lorenz, H.Hochmuth, R.Schmidt-Grund, E.M.Kaidashev, M.Grundmann, *Ann. Phys. (Leipzig)* 13, (2004), 59.
- [10] W.A.Harrison, *Electronic structure and the properties of solids : The physics of the chemi.,San Francisco, Freeman, (1930).*
- [11] M.N.Rudden, J.Wilson, *Elements of Solid State Physics, 2nd Edition, Wiley, (1993).*
- [12] R. de L. Kronig, W.G. Penney, *Proc. Roy. Soc. (London)*, A130, (1930), 499.
- [13] C.Kittel, *Introduction to Solid State Physics, 8th Edition, Wiley, (2005).*
- [14] J. R. Chelikowsky and M. L. Cohen, *Phys. Rev. B* 13, (1976), 826.
- [15] G. F. Koster, *Solid State Physics 5*, edited by F. Seitz and D. Turnbull ,Academic Press Inc., New York, (1957).
- [16] J.E.Jaffe, A.C.Hess, *Physical Rev B*,Vol.48, No.11 (1993), 7903.
- [17] K. Prior, *Contemp. Phys.* 37 (1996) 345.
- [18] Z.Z.Zhi, Y.C.Liu, B.S.Li, X.T.Thang, Y.M.Lu, D.Z.Shen, X.W.Fan, *J.Phys.D*, 36, (2003), 719.
- [19] Z.L.Wang, *J.Phys:Condens.Matter*, 16, (2004), R829.
- [20] G.Tobin, J.Fryar, E.McGlynn, J-P.Mosnier, M.O.Henry, *Proc. ICPS 2002; Edinburgh,Scotland,UK; 2002; Poster*
- [21] P.R.Willmott, J.R.Huber, *Rev. Mod. Phys.*, Vol.72, No.1, (2000).
- [22] D.B.Chrisey, G.K.Hubler, *Pulsed Laser Deposition of Thin Films, Wiley, (1988).*
- [23] A.Ohtomo, K.Tamura, K.Saikusa, K.Takahashi, T.Makino, Y.Segawa, H.koinuma, M.Kawaski, *Appl.Phys.Lett.* 75 (1999) 2635.

- [24] T.Makino, G.Isoya, Y.Segawa, C.H.Chia, T.Yasuda, M.Kawaski, A.Ohtomo, K.Tamura, H.Koinuma, *J.Cryst.Growth* 214/215 (2000) 289.
- [25] A.Tsukazaki, A. Ohtomo, T.Onuma, M.Ohtani, T. Makino, M. Sumiya, K. Ohtani, S.F. Chichibu, S.Fuke, Y.Segawa, H.Ohno, H.Koinuma, M.Kawasaki, *Nature Materials* Vol 4 No 1,(2005), 42.
- [26] D.C.Look, B.Claflin, *Phys.Stat.Sol.(b)*, No.3, (2004), 624.
- [27] W. Walukiewicz, *Phys. Rev. B.* 50, (1994), 5221.
- [28] D. C. Look, R. L. Jones, J. R. Sizelove, N. Y. Garces, N. C. Giles, and L. E.Halliburton, *Phys. Stat. Solidi (a)* 195, (2004),171.
- [29] C. G. Van de Walle, D. B. Laks, G. F. Neumark, and S. T. Pantelides, *Phys. Rev. B*47, (1993), 9425.
- [30] D. Zwingel, *J. Lumin.* 5, (1972), 385.
- [31] Sidney Perkowitz, *Optical Characterisation of Semiconductors: Infrared, Raman and photoluminescence spectroscopy*, Academic Press Ltd., London UK, 1993 and references therein
- [32] Landolt-Bornstein, U.Rossler(Ed.), *Numerical Data and function Relationships in Science and Technology-New Series III, Vol. 41B.* Springer, Berlin, 1999 and references therein.

Chapter Two

Experimental Arrangement

The following chapter will describe the important aspects of the experimental arrangement and procedures. The experiments were centred on a 1-metre spectrometer in the Czerny-Turner configuration. There are three main optical experiments carried out in this study. Firstly there was a photoluminescence (PL) experiment, which was based on an established system, described in section 2.1. Secondly a time resolved PL measurement system was developed and tested, outlined in section 2.2, which involved incorporating it into the existing photoluminescence experiment. Thirdly the PL apparatus was modified to enable the exploration of high level excitation, stimulated emission and lasing effects, discussed in section 2.3. For all the experiments, alterations of the data acquisitions systems had to be implemented. A schematic diagram of each experiment is presented, as well as a description of the equipment used. A more detailed discussion of some equipment is given, as an understanding of the limits of the equipment is required to appreciate the acquired results discussed later in the thesis.

2.1: Photoluminescence measurements

Photoluminescence is the optical radiation emitted by a material resulting from its decay from a nonequilibrium excited state which was generated by an external optical excitation. Three distinct processes take place resulting in light emission from the system, (1) absorption of light (2) radiative recombination and (3) escape of the radiation. Most of the processes mentioned occur in the region within the absorption length of the illuminated surface, and the emitted light escapes mostly through the surface.

2.1.1: Experimental arrangement

Figure 2.1 illustrates the photoluminescence system, containing the main elements, which are the excitation source, the sample mounting and cooling, the spectrometer and the data acquisition system.

An optical excitation source (typically a laser) is directed onto a sample e.g. ZnO crystal, which has been placed inside a cryostat. Collection optics at the output window of the cryostat captures the luminescence and directs it on to the entrance slit of the spectrometer. The grating spectrometer disperses the incoming light and by scanning the grating, directs various wavelengths onto the exit slit of the spectrometer. These photons are counted by the photomultiplier tube (PMT). The acquisition system (Spectramax™, Jobin-Yvon Corporation) correlates the results acquired from the

photomultiplier and the wavelength position of the spectrometer, generating an output spectrum in the conventional form. The useful spectral range of the instrument is between 350nm and 600nm, and this is determined by the combined responses of the grating and the PMT (*appendix A and B*).

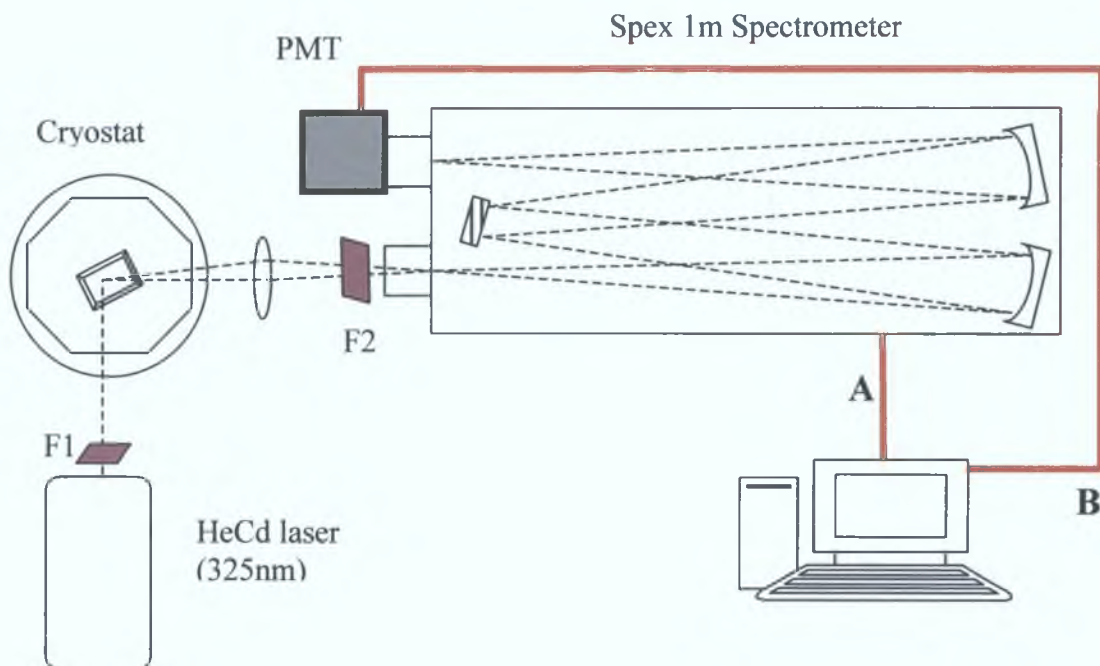


Figure 2.1: Schematic of the PL arrangement. A: Controls and receives information from the spectrometer by the computer. B: Outputs of the PMT via data scan into a controlling computer.

2.1.2: Excitation source

For normal PL measurements a HeCd laser (IK series IK5652R-G Kimmon Corporation, see *appendix B*) operating at 325nm (3.81eV) was used to excite the ZnO samples with an output power of ~40mW unfocused on the sample. *Figure 2.1* shows that a filter labelled F1, (bandpass filter between 300nm and 400nm, Schott glass model UG11) is used to block the laser plasma emission and ensure that predominantly the UV line (325nm) is transmitted to excite the sample. Filter F2 (long pass filter, Schott glass model UG14) prevents the 325nm laser line from reaching the spectrometer while allowing the longer wavelength luminescence light to pass.

The luminescence observed will typically be emitted from a region corresponding closely to the volume excited by the laser (determined by the penetration depth of the 325nm radiation). Depending on the sample thickness the luminescence may be

distributed over the entire sample volume or only the surface region. The thickness of the ZnO samples examined in this work that were grown by the PLD technique were on average between 150-200nm. To calculate the penetration depth for a 325nm laser incident on ZnO material, we need to know the absorption coefficient (α) at 325nm. We have used the graph shown in *figure 2.2* obtained from *Sans et al* [1]. The relationship between the absorption coefficient and the penetration is obtained by noting that at the penetration depth the intensity is $1/e$ of the incident intensity and hence:

$$d = \left(\frac{1}{\alpha} \right) \quad (2.1)$$

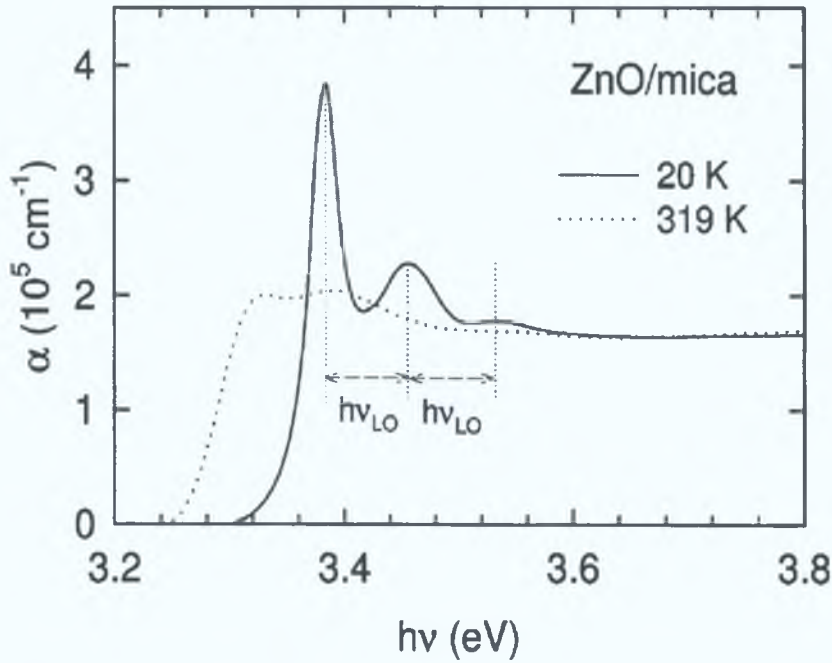


Figure 2.2: Absorption spectra of a ZnO film deposited on mica, measured at two different temperatures (20K and 319K). $h\nu_{LO}$ is the principal LO phonon energy in ZnO ($\sim 73\text{meV}$) [1].

As shown in *figure 2.2* at 3.81eV (energy of HeCd laser photons) the absorption coefficient of the crystal is $\sim 1.6 \times 10^5 \text{ cm}^{-1}$ which corresponds to a penetration depth of $\sim 63 \text{ nm}$. The data shown in the work of *Sans et al* [1] is for ZnO thin films grown by the PLD technique and therefore this value should be broadly comparable to the samples investigated in this study. The penetration depth for a bulk crystal maybe some what different but a lack of absorption measurements in the literature in the region of 3.8 eV complicates the matter. However, for energies of $\sim 3.8 \text{ eV}$ which are far above the exciton resonance energies, the value should be less affected by details of the crystal structure and perfection and thus the PLD material value ought be a reasonable estimate even for the bulk material. Thus we see that the penetration depth of the excitation laser

is certainly less than 100nm. For the Nd:YAG laser used in high excitation level studies, with a photon energy of ~ 3.5 eV (355 nm), the penetration depth will be of the same order of magnitude.

2.1.3: Spectrometer

The results that are presented for this work are obtained almost exclusively using a grating based monochromator (model SPEX 1704, Jobin-Yvon) and drawn in *figure 2.3*. This is a 1-metre focal length spectrometer employing two concave mirrors of 100mm diameter and a ruled diffraction grating in a Czerny-Turner configuration [2].

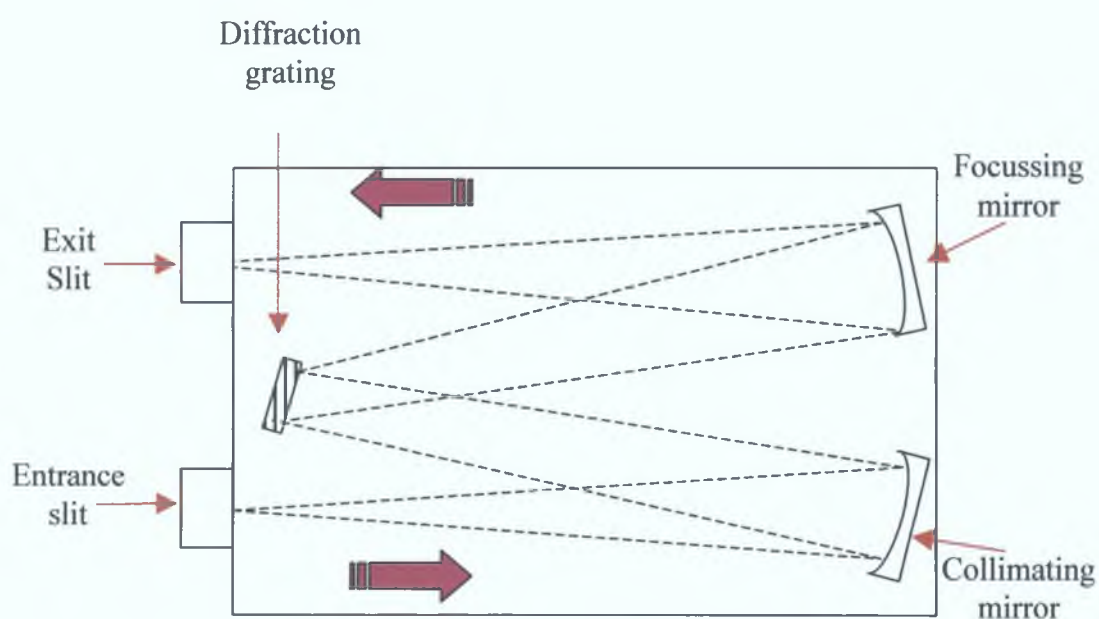


Figure 2.3: Schematic diagram of the Czerny-Turner configured spectrometer.

This design involves a classical plane grating illuminated by collimated light (ISA model 510-05, 1200 lines/mm, blazed at 330nm, see *appendix B*). The incident light diverges from the entrance slit and is collimated by a concave mirror (collimating mirror) and the diffracted light is focused onto the exit slit by a second concave mirror (focusing mirror). Ideally since the grating is planar and classical, and used with collimated incident light, no aberrations should be introduced into the diffracted wavefronts. [3]

Each wavelength is imaged individually by rotating the grating to scan through the spectrum. This moves the grating relative to the incident and diffracted beams, changing the wavelength diffracted toward the collimating/focusing mirror.

The most important features of the spectrometer from the point of view of this work are related to resolving power and spectral resolution and these are discussed further below.

Resolving power

The resolving power R , of a grating spectrometer is a fundamental measure of the capability of the grating to separate two closely spaced spectral lines, with infinitely narrow slits assumed. The Rayleigh criterion states that two wavelengths λ_1 and λ_2 , are resolved if the central maximum of one line falls on a diffraction minimum of the other and is expressed as

$$R = \frac{\lambda}{\Delta\lambda} \quad (2.2)$$

This is ultimately related to the illuminated grating area [4].

Spectral resolution

Resolving power is a property solely of the diffraction grating and the geometry under which it is employed, and assumes infinitely narrow slits, however, finite entrance and exit slits are required to give a finite energy throughput for the system. While the resolving power can be considered as a fundamental measure of the grating to resolve closely spaced wavelengths, in practice the ability of a spectrometer to resolve two wavelengths λ_1 and $\lambda_2 = \lambda_1 + \Delta\lambda$ depends not only on the grating but on the dimensions and location of the entrance and exit slits, the abnormality in the images and the magnification of the images. This measure of the ability of a grating system to resolve nearby wavelengths is more relevant to our investigation than its resolving power, since it takes into account the effect the slit images have on the system. While resolving power is dimensionless, the units of spectral resolution are in nanometres [4].

An investigation of spectrometer resolution has been undertaken using the HeCd laser line at 325nm. Since this laser line is relatively narrow (linewidth of < 0.001 nm, see *appendix B*), it may be treated as perfectly monochromatic source and one can examine the broadening effects of different slit widths. *Figure 2.4(a)* shows the Full Width Half Maximum (FWHM) measured for the 325 nm HeCd line for a variety of entrance/exit slit widths (entrance slit width = exit slit width in all cases). When the slits are set at their widest position of 3.00mm, one gets a (FWHM) for the laser line of 3.545nm and when the slits are set at 0.1mm, the FWHM is 1.0 nm. We show the corresponding lineshapes in *figure 2.4(b)*. The bands seen in the PLD-grown ZnO films can have

FWHM of the order of $\sim 50\text{nm}$ and thus far exceed the instrumental FWHM. For the majority of our samples, the linewidths we observe are sample-limited, and the spectrometer resolution has negligible effect on the spectra. However good resolution is required when investigating narrow bands, seen for example in bulk ZnO material at low temperature where the PL peaks have linewidths substantially less than one nm width and are quite closely spaced.

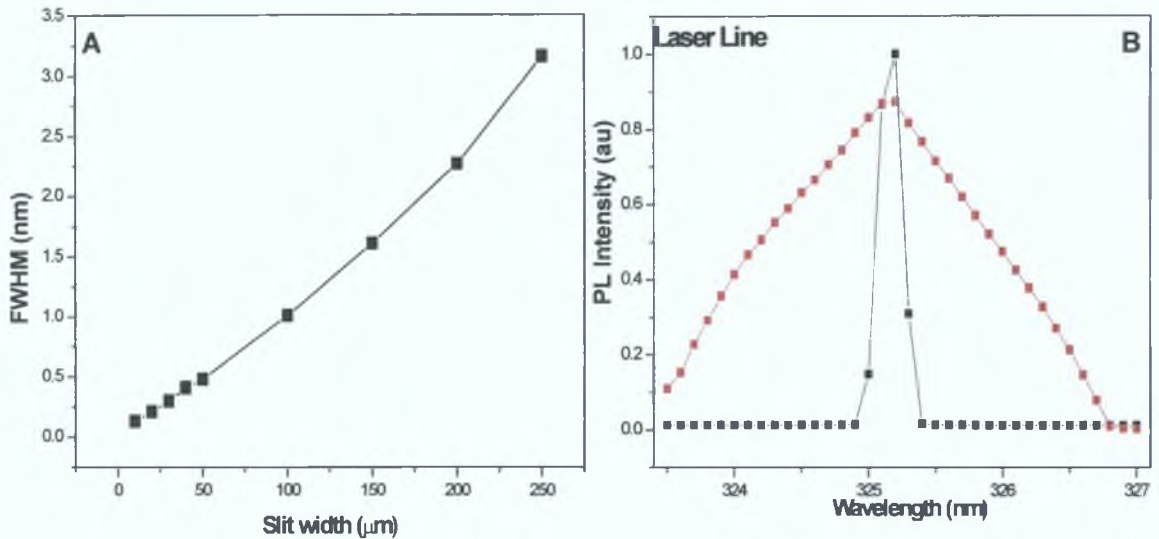


Figure 2.4: Examination at the 325nm laser line using the spectrometer, slit widths are the same at both entrance and exit. (A) Shows the development of the FWHM at different slit widths (B) is a spectrum of the extremes (i) Slit width $300\mu\text{m}$ (ii) Slit width $20\mu\text{m}$ (Increment 0.1nm).

2.1.4: Detector

The detector system used in this work is a photomultiplier tube (PMT), which is air-cooled to -25°C to reduce noise due to dark count fluctuations. The PMT (Hamamatsu model R3310-02) can be configured for photon-counting, voltage or current output and has a wide spectral range (300 to 1040nm) (Appendix A). A PMT works on the principal that when a photon is incident on the photo emissive cathode it causes an electrode to be emitted. The higher positive potential at the first dynode causes the free electron to impinge on that dynode causing several more electrons to be released. These electrons are then drawn towards the next dynode, causing more electrons to be released. These electrons continue multiplying until they reach the anode where an output current is measured. This process takes only nanoseconds. The PMT used incorporates an InGaAs (Cs) photocathode and linear focused CuBeO dynodes. The response time for the anode pulse rise time is 3.0ns and the electron transit time is 23ns [5]. The quantum efficiency

(QE) of the PMT is defined as the ratio between the numbers of electrons emitted by the photocathode to the number of incident photons. For the PMT used in this work the QE at -25°C is typically 15% [5]. QE is a strong function of the incident photon wavelength. The background noise, once the PMT was cooled to its operating temperature, was $\sim 2\text{-}3$ counts per second (cps) in a darkened room at a entrance/exit slit width of $400\mu\text{m}$, when the spectrometer was set to 500nm . For most of the PL measurements the data acquisition system was set in photon counting mode, where each photon generates a single pulse and the spectrometer integrates the number of pulses at a particular wavelength for a set time (e.g. 1s). A discriminator is used to set a voltage, which causes low amplitude noise (1 nA) pulses to be ignored whereas higher amplitude signal pulses (10 nA) are counted. As the dark count is $\sim 3\text{-}5\text{cps}$ and the system can count to 1×10^6 pulses, the dynamic range is $\sim 10^6$ and the S/N ratio potentially of the same order. In analog acquisition mode, used for high level excitation measurements, the signal can be either taken either as voltage or current pulses from the PMT. Using the data acquisition software (SpectrAcq2TM) this signal is sampled by the analog to digital converter (ADC). The ADC samples the signal every two milliseconds. The input amplifiers have a long time constant so that transient signals and noise spikes are averaged out during the 2-millisecond interval between samples.

Figure 2.5 shows the efficiency of both the photomultiplier and the spectrometer illustrating that they are both at their most efficient at $300\text{-}400\text{nm}$. This region is the most important when investigating ZnO through optical techniques. In this region i.e. $300\text{-}400\text{nm}$, there can be several close lying spectral lines in the case of ZnO so a highly efficient PMT and spectrometer operation is most important at this region.

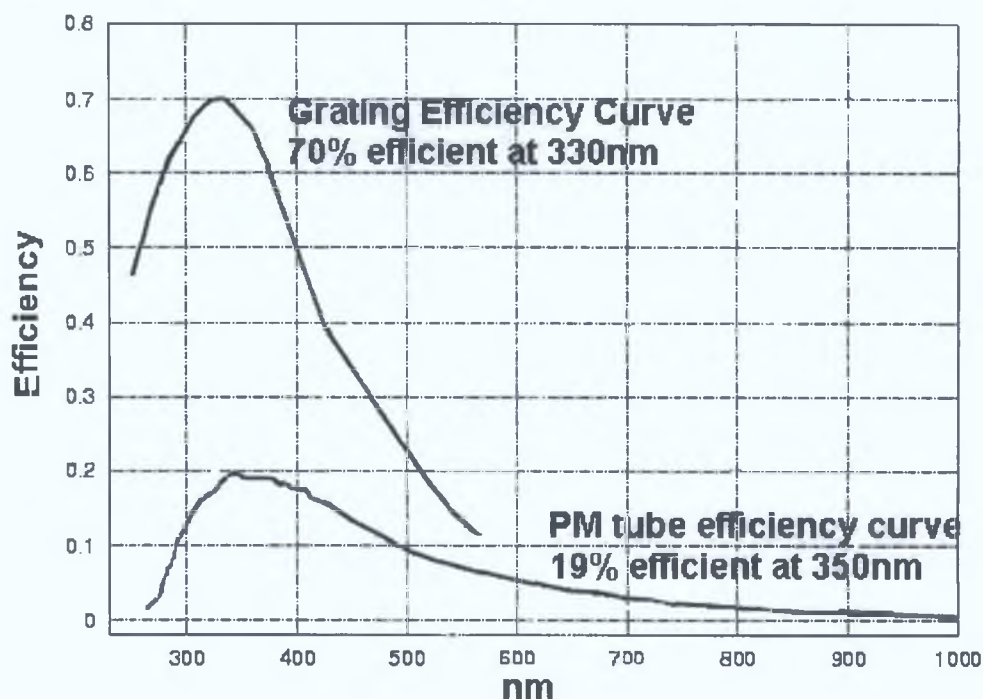


Figure 2.5: Efficiency curve for Hamamatsu photomultiplier tube and grating blazed for the visible region. Courtesy of Mr. Dermot Gorman [6].

2.1.5: Closed cycle cryostat

The sample is enclosed in a closed cycle cryostat to enable it to be held at controlled temperatures down to 4.2K (Janis Corporation, model SHI-950-5). The heat exchanger in the cryostat is cooled via a closed cycle Gifford-MacMahon process. The temperature was measured at the heat exchanger and a resistive heater connected to a temperature controller maintained the desired temperature. The sample tube is connected by a copper strap to the heat exchanger and the sample cooled via exchange gas in the sample tube. Temperature measurement and control are also possible via a sensor and heater on the sample stick. The cryostat is enclosed in a vacuum jacket to ensure thermal insulation from the environment. These low temperatures are necessary to reduce the thermal broadening and quenching of the luminescence transitions, as the broadening at an absolute temperature T is of the order kT [7]. This gives a significant broadening of 25meV at 300K and reduces to $< 1\text{meV}$ at 10K. Cooling produces sharper and more readily defined peaks in PL spectra and tends to reduce the role of thermal ionisation effects and competing nonradiative paths for recombination, giving a higher efficiency for the photoluminescence process which results in an improved signal to noise ratio.

The sample is placed on the sample stick and held using PTFE thread seal tape, which gives a stress free mounting and sufficient flexibility at low temperatures. The laser is typically incident at $\sim 45^\circ$. The windows used in the cryostat are made of quartz glass, which have very slight effect on the transmission of the laser or luminescence from the sample. The temperature sensors used in the cryostat were Silicon Diodes. The sensors and heaters were connected to a Lakeshore (model 330) microcontroller-based auto tuning temperature controller. The temperature may be accurately controlled to $\pm 0.2\text{K}$ over extended time periods [8].

2.2: Time resolved PL measurements

As part of this initial aspect of this work, a PL lifetime measurement system was commissioned, calibrated and tested. Time Correlated Single Photon Counting (TCSPC) is a common technique for fluorescence lifetime measurements. The principle of TCSPC is the detection of single photons and the measurement of their arrival times with respect to a reference signal, usually from the excitation light pulse. TCSPC is a statistical method and a highly repetitive light source is needed to accumulate a sufficient number of photon events for the required statistical data precision [9]. The TCSPC system we used is from Edinburgh Instruments Ltd, which incorporates its own flashlamp head as well as dedicated software and PC plug in card (T900) (*appendix B*).

2.2.1: General principles of TCSPC

As seen in *figure 2.6* the excitation light source excites a sample with a fast pulse, which supplies the start signal. The excited sample emits luminescence and the first detected photon provides the stop signal. TCSPC may be best explained by comparing it to a fast stopwatch with two inputs as displayed in *figure 2.6*. The clock is started by a START reference pulse and stopped by a STOP signal pulse. The time measured for one START-STOP sequence will be represented by the addition of one more count to a histogram in which the channels on the x-axis represent the time delay between start and stop.

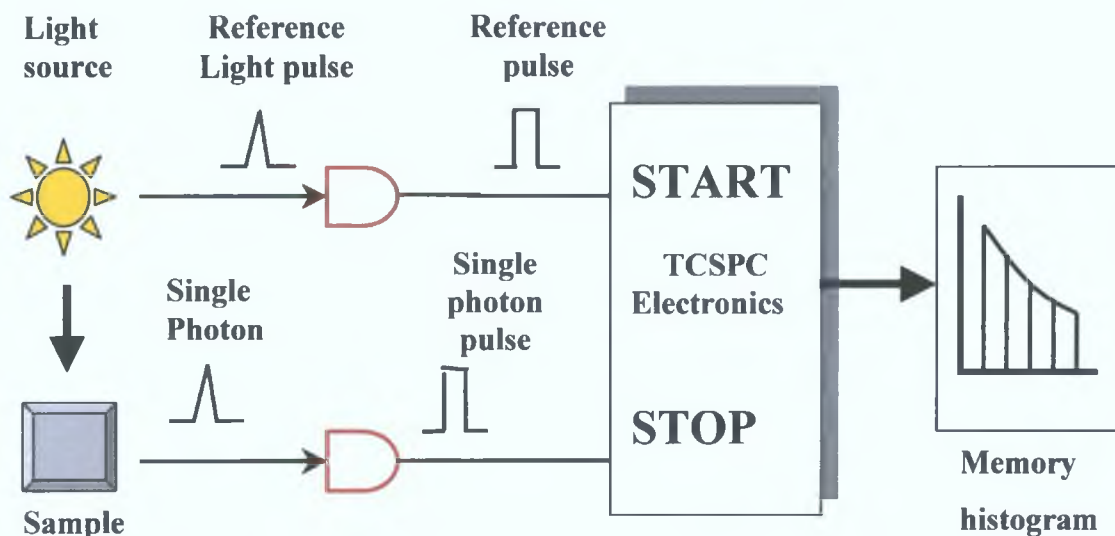


Figure 2.6: Experimental arrangement of Time Correlated Signal Photon Counting system.

With a highly repetitive light source millions of START-STOP sequences can be measured in a short time. The resulting probability histogram of photon counts versus channels represents the shape of the fluorescence decay as demonstrated in *figure 2.7*.

Generally the pulses to the TCSPC electronics are generated by a single photon emission. Single photons can be detected with photo detectors having an intrinsic high gain, for instance a PMT. For statistical reasons it is important to ensure that no more than one single photon event per light flash is detected. The start pulse is provided by a PMT located within the flashlamp setup, while the stop pulse (from the luminescence photons) comes from the PMT on the exit slit of the spectrometer.

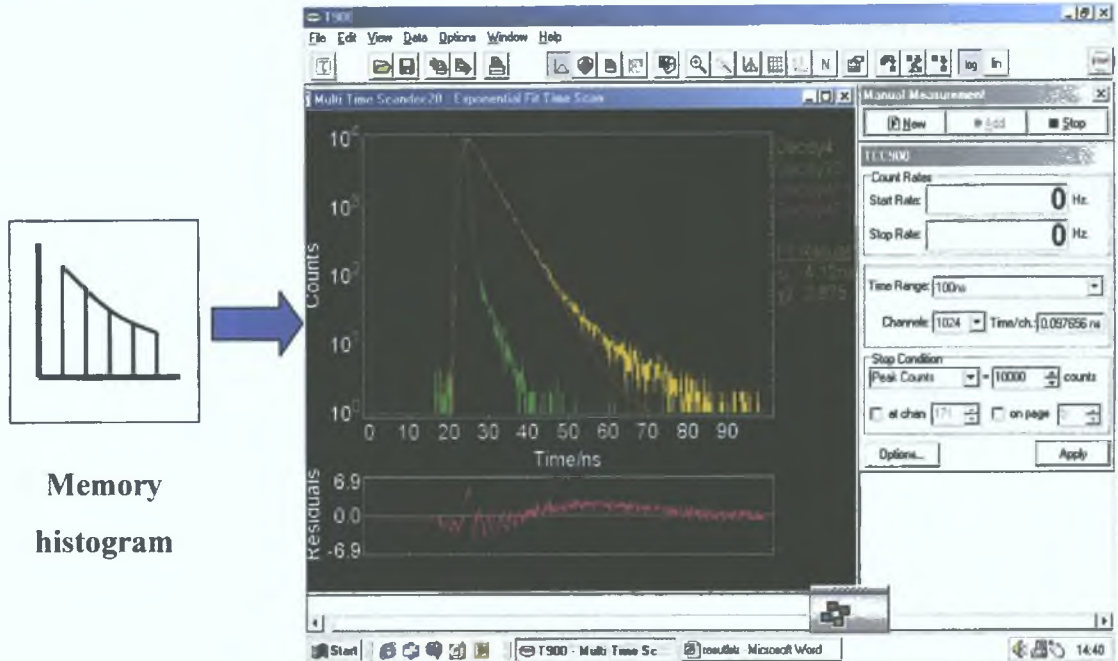


Figure 2.7: Histogram and Computer Interface for the time resolved PL experiment.

2.2.2: Signal processing

The main electronic components for signal processing in TCSPC are constant fraction discriminators (CFD), electrical delays (Del), the time-to-Amplitude converter (TAC), Amplifier (Amp), analogue to digital Converter (ADC) and digital memory (Mem). An overview of the signal processing components arrangement is shown in figure 2.8.

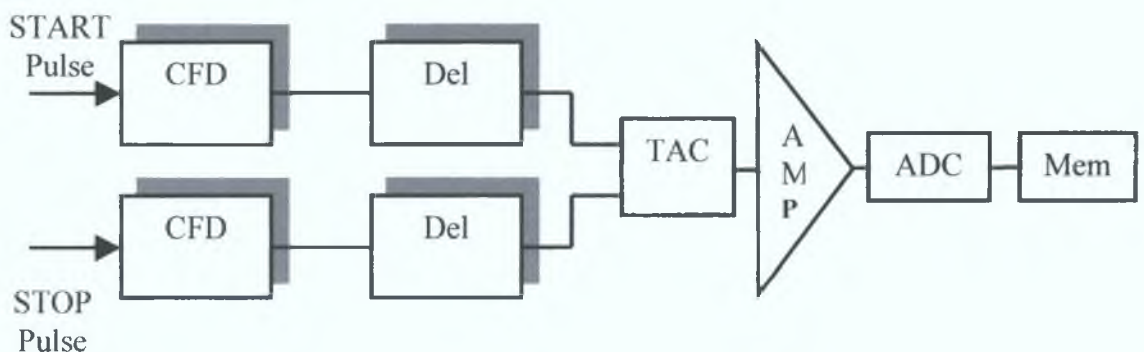


Figure 2.8: Signal Processing Components of Time Correlated Signal Photon Counting system.

At the input of the detectors, incoming pulses are discriminated with respect to the pulse height. Only pulses greater than a given threshold will be accepted for further signal processing. In this way small amplitude noise pulses are eliminated. The CFD's on both the start and the stop inputs analyse the pulse shape of the individual pulses. The portion of the steepest slopes of the leading edge on the incoming pulses is taken as selection

criteria for the temporal position. At the output of the CFD the pulses are re-shaped to a standard height and shape. The TAC is the fast clock, started by the START pulse and stopped by the STOP pulse. The START pulse initiates the growth of a ramp signal. Depending on the arrival time of the STOP pulse the ramp will have a lower or higher value. Once the growth of the ramp has been stopped, the level will remain constant for a defined period. The TAC output pulse can then be amplified, thus effectively stretching the time axis. The minimum and maximum available TAC amplitude determines the time range [9].

2.2.3: Time resolved PL experimental details

The optical system used for the time-resolved PL is similar to the PL system except that the excitation source is a flashlamp head as shown in *figure 2.6*. The flashlamp head is a discharge lamp (*Appendix B*), where an electrical breakdown between two electrodes due to a very high voltage generates a fast light pulse. There is a range of filler gases for the flashlamp head, which have different spectral characteristics allowing a variety of sample species to be excited. Hydrogen (see *table 2.1*) was chosen as the filler gas because it has narrow pulses without an after-pulse tail. Photons are emitted over the entire visible spectral range, with greatest intensity in the UV range, and hence this filler gas is suitable for studies of a wide range of materials including ZnO (*Appendix B*).

Filler Gas	Parameters	Standard Conditions	Settings
Hydrogen	Electrode gap width	1.0mm	1.1 - 0.7 mm
	Gas Pressure	0.4bar	0.7 - 0.2 bar
	High Voltage	6.8kV	7.2 - 6.2 kV
	Pulse Frequency	40khz	50 – 5 kHz

Table 2.1: Parameters of the flash lamp head with hydrogen filler gas.

Firstly, the time resolved PL system was tested using solutions of known standards with known luminescence lifetimes. The most popular standard is a dilute solution of anthracene in cyclohexane, the decay time for which, if at 25°C, is independent of excitation and emission wavelengths [10]. A second solution of 9-cyanonanthracene in cyclohexane was used because it provided luminescence at a different wavelength and has a known longer decay time compared to the first solution [11]. Both samples also have the advantage of not having to be degassed. Photoluminescence spectra were

recorded with the HeCd of the two solutions as shown in *figure 2.9*. Based on these spectra the spectrometer was set to the strongest peak in the region when the TCSPC measurements were being made.

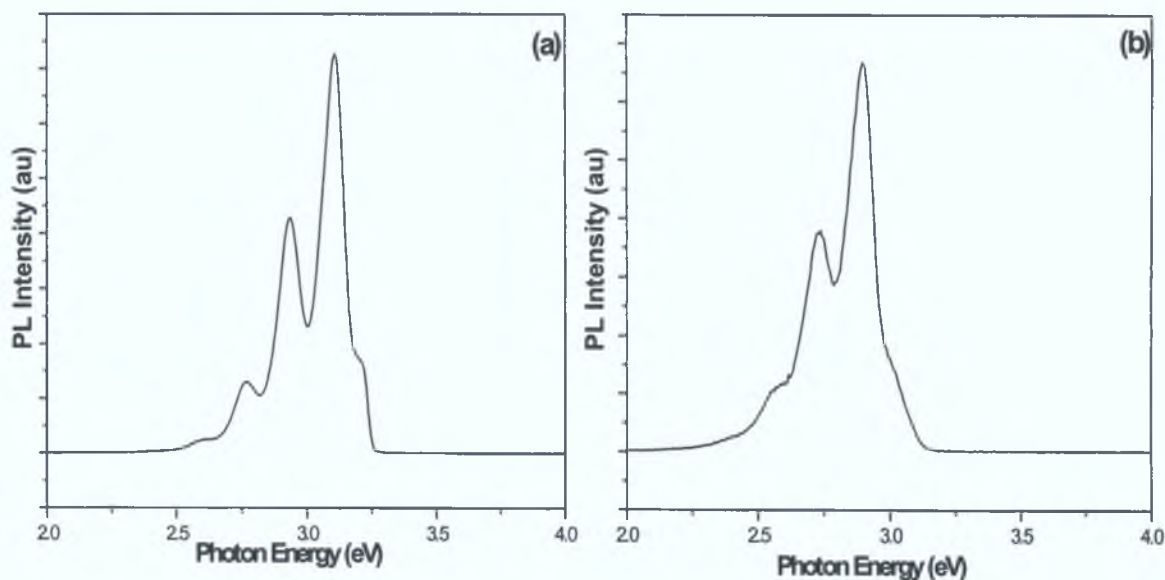


Figure 2.9: (a) PL spectra of anthracene in cyclohexane 3×10^{-5} molarity (peak at $\sim 399\text{nm}$) (b) 9-cyanonanthracene in cyclohexane 1×10^{-5} molarity (peak at $\sim 428\text{nm}$)

Spectra of calibration samples obtained using HeCd laser, range 300-700nm, Integration 1.0s, Increment 1.0 nm, Slits $100\mu\text{m}$.

The flashlamp head with filler gas as described above was used as an excitation source and the current output of the photomultiplier tube on the spectrometer exit slit was fed to the T900 card to provide the STOP pulse. The output from the PMT connected to the flash lamp head is fed into the T900 card to provide the START pulse. Time resolved measurements could then be recorded. Various parameters could be changed to optimise the collection of data. The background count must be quite low as the PL signal levels excited by the flashlamp are rather weak. Setting the discrimination levels for the PMT signals appropriately optimised the background count. Other parameters that could be modified were time range, stop conditions, TAC settings, and CFD settings.

An instrumental response was recorded by capturing the output of the flashlamp head using the TCSPC apparatus (*Appendix C*), in effect measuring the temporal profile of the source. It was captured at the same wavelengths as the time resolved measurements were to be taken at. This response is taken so that the time decay of the lamp is known and if needed, can be subtracted from the resulting time resolved spectra if required.

The instrument response can be used to track any drifts over time in the instrument performance.

The test solutions mentioned in *figure 2.9* were placed in fluorimeter cuvette (Type 23 Q.10, Chandos Intercontinental), which had four optically clear sides. The cuvettes were made of quartz and had no effect on the spectra. This cuvet was mounted on a stand and aligned with both the entrance slits of the spectrometer and the flashlamp head.

2.2.4: Data from time-resolved PL measurements

Figure 2.10 illustrates the photoluminescence spectra of the solution anthracene in cyclohexane excited using the flashlamp head, with a main peak at $\sim 399.0\text{nm}$. The molarity used was based on values recommended from the literature [10]. It is seen that the spectra in *figure 2.10* closely resembles that in *figure 2.9(a)*, which was obtained with HeCd excitation.

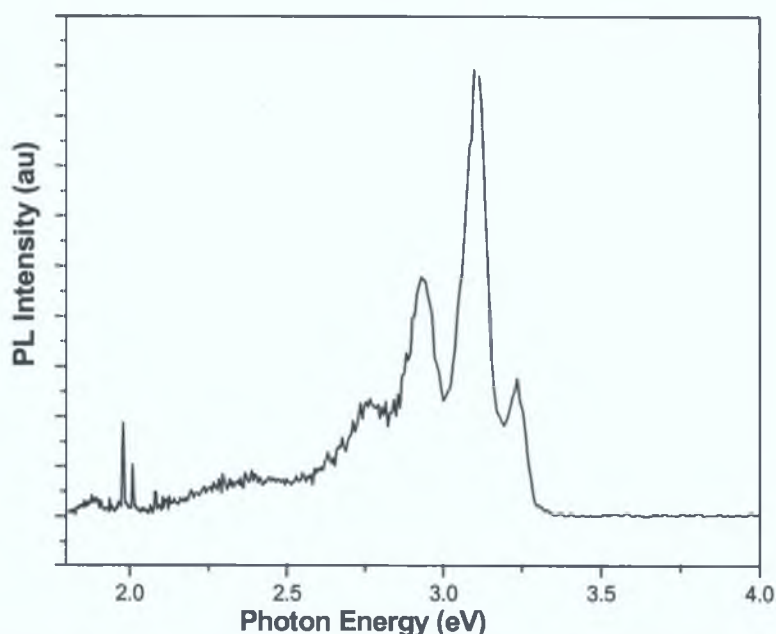


Figure 2.10: PL Spectra of anthracene in cyclohexane 3×10^{-5} molarity excited by the flashlamp head. Integration 1.0s, Increment 1.0 nm, Slits $800\mu\text{m}$.

The data in *figure 2.11* demonstrates the TCSPC histogram from the sample of anthracene in cyclohexane. Points to note about the TR graph are: (1) the characteristic lifetime τ_1 value is just below the “fit results” and should be compared to the reference value in the *table 2.2*; (2) the green decay graph is the instrument response function; (3) the yellow decay graph is the decay from the sample and (4) the red line through the decay graph is the reconvolution line (*Appendix C*), this line takes into account noise

that is produced by effects of sample excitation and signal generation. The highlighted areas of yellow in *table 2.2* are the values of interest given in literature [10,11].

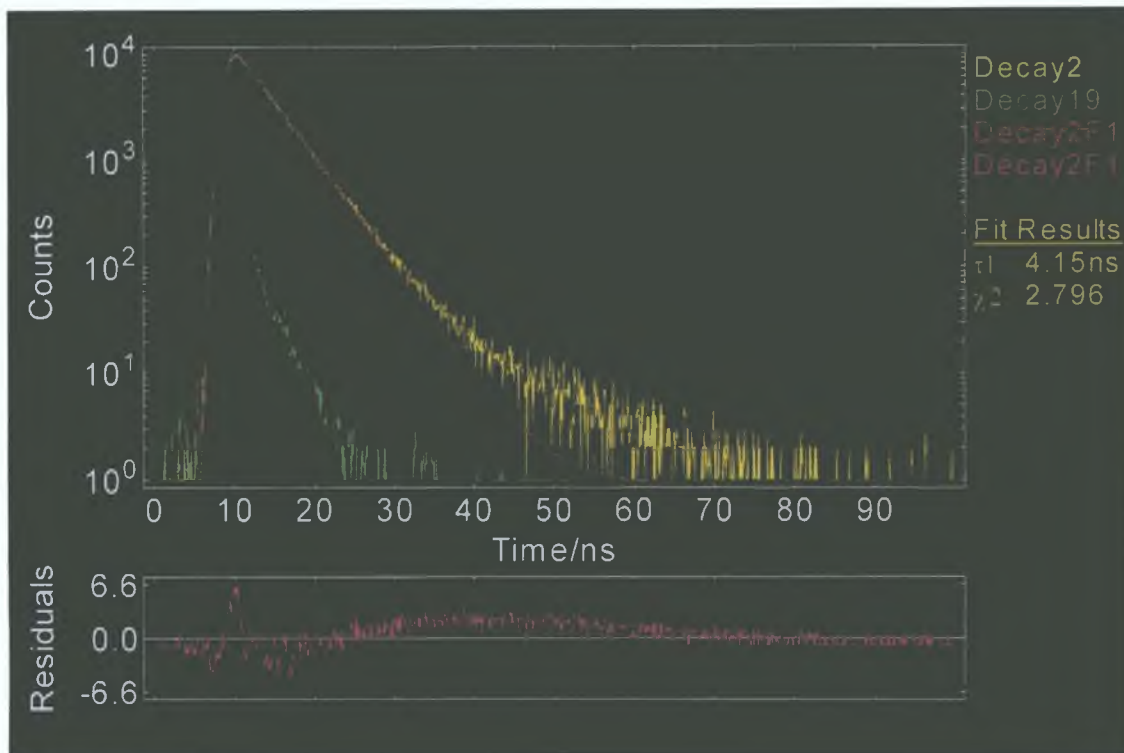


Figure 2.11: Time resolved spectra for anthracene in cyclohexane 3×10^{-5} molarity

Compound	Value τ_0 from [10]	Value τ_0 from [11]	Value from present work
Anthracene in cyclohexane	5.23ns @ 405nm	5.20 ± 0.08 ns @ 405nm	
Anthracene in cyclohexane (Undegassed)	4.10ns @ 405nm	4.17 ± 0.04 ns @405nm	4.15 ± 0.006 ns @ 399nm

Table 2.2: Table of lifetime results compared for anthracene in cyclohexane.

Figure 2.12 shows the photoluminescence spectrum of the solution 9-cyanonanthracene in cyclohexane, excited by the flash lamp. The main peak is at ~ 428.0 nm. The molarity used for the solution was based on that recommended by reference [11], and was 1×10^{-5}

mol Again one may observe that the spectra in *figure 2 12* closely resembles that in *figure 2 9(b)*, which was obtained with HeCd excitation

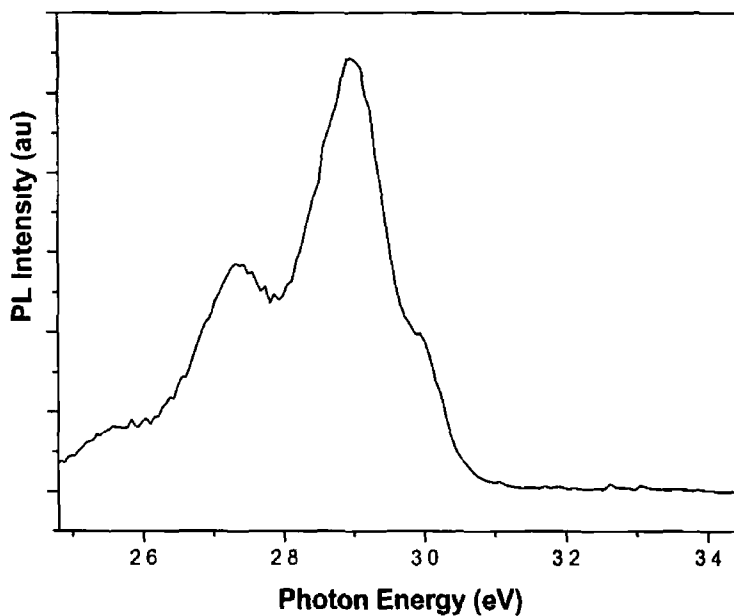


Figure 2 12 PL Spectra of 9-cyanonanthracene in cyclohexane, 1×10^5 molarity, excited by the flashlamp head Integration 1 0s, Increment 1 0 nm, Slits $800 \mu\text{m}$

The data in *figure 2 13* demonstrates the TCSPC histogram from this sample Similar comments pertain to this figure as to *figure 2 11* The highlighted areas of yellow in *table 2 3* are the values of interest [11, 12]

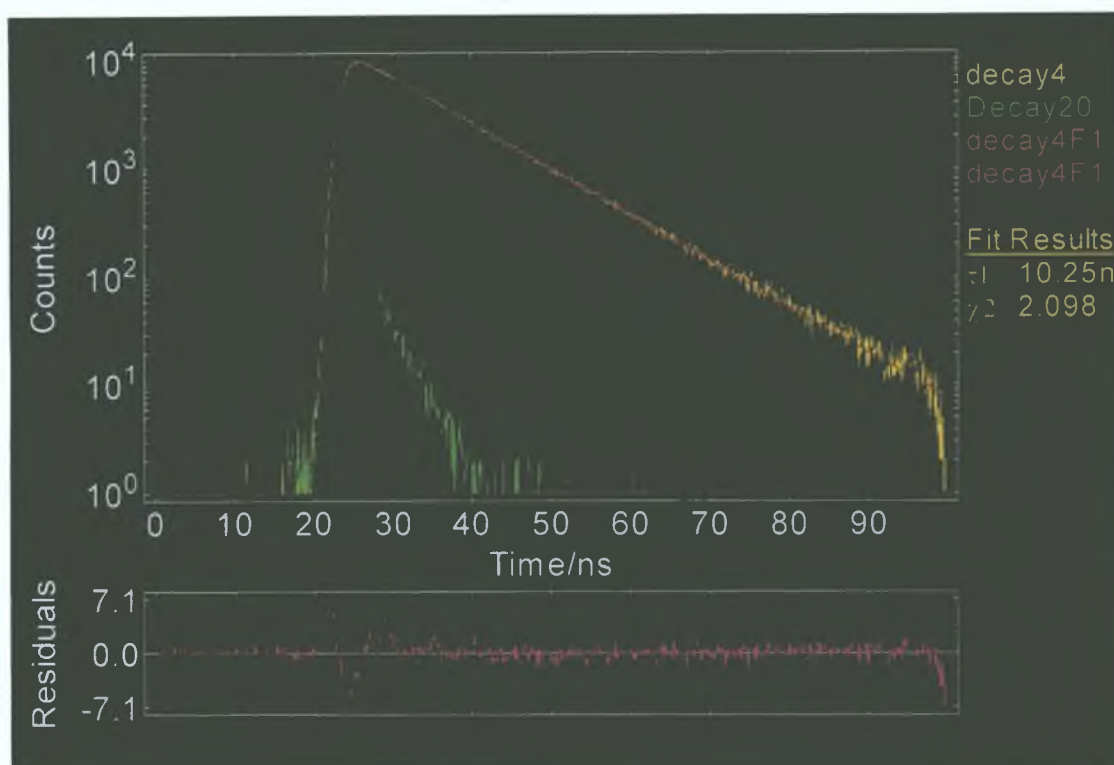


Figure 2.13: Time resolved spectra for 9-cyanonanthracene in cyclohexane 1×10^{-5} molarity.

Compound	Value τ_0 from [11]	Value τ_0 from [12]	Value from present work
9-cyanonanthracene in cyclohexane	$12.8 \pm 0.2\text{ns}$ @440nm	12.8ns @440nm	
9-cyanonanthracene in cyclohexane (Undegassed)	$10.5 \pm 0.3\text{ns}$		$10.25 \pm 0.03\text{ns}$ @ 428nm

Table 2.3: Table of lifetime results for 9-cyanonanthracene in cyclohexane.

The main point to note about the results is that characteristic lifetimes of both anthracene in cyclohexane and 9-cyanonanthracene in cyclohexane solutions compare well with what was found in the literature [10, 11, and 12] and demonstrate that the TCSPC system commissioned in this project functions well. The two samples that had been used in the experiments were chosen because they were easily prepared, characteristic lifetimes existed for non-degassed versions in the literature and they were

the least self-absorbing liquids tried. They also emit in the spectral region where the spectrometer performs well. Some samples that we used were too absorbing and so no luminescence could be observed, e.g. ruthenium based sol-gel compounds. The two samples have a sizeable difference in lifetimes, and one is substantially longer than the lamp flash duration allowing accurate deconvolution.

An investigation was then undertaken on the ZnO PLD-grown samples. However it became clear very quickly that the limits of the equipment would not allow results to be acquired. The lifetimes of the exciton emission in the UV is shorter than the time resolution of the flashlamp setup (in the sub-nanosecond regime). This is to be expected as sub-nanosecond lifetimes are typically observed for exciton emission in semiconductors [13]. The short lifetimes are due to the high oscillator strength of the transition [14]. Reviews of the existing literature show that time-resolved PL studies on ZnO have typically used a frequency tripled mode locked Ti:sapphire laser pulses with a wavelength around 275nm and a pulse width below 1ps as an excitation source [15] and use a streak camera for PL detection, which was capable of a resolution of 10ps. Neither of these key pieces of equipment was available for this project, but nevertheless, the development of the time resolved photoluminescence system was a valuable introduction to the principles of single photon data acquisition methods. The present TCSPC system could perhaps be used to study slower, deep-level, transitions in ZnO and other materials (such as the “green” band which is in the μs range [16]), but the majority of our work concentrates on the faster, band edge, transitions.

2.3: High excitation level PL measurements

The final experimental arrangement developed was used to investigate emission mechanisms in ZnO under high levels of optical excitation or pumping, and to study stimulated emission and lasing processes therein. In order for a semiconductor material to show such effects, large excitation intensities are required to excite the material, beyond those easily achievable with a CW laser such as the HeCd mentioned earlier. These high level excitation measurements were thus carried out using a pulsed laser, where the optical intensity during the pulse is sufficiently high. The laser used is a frequency-tripled Nd:YAG (*Appendix B*) laser in conjunction with a focussing lens, to define an excitation area on the sample and to control the power density. The emission intensity spectra from the sample was then analysed using a spectrometer and photomultiplier tube as discussed in section 2.2.4.

2.3.1: High excitation level measurements: Experimental arrangement

The high excitation experimental system is shown in *figure 2.14* and again is similar to the PL experimental arrangement. The main differences are firstly the excitation source, which is the frequency-tripled output of an Nd:YAG at $\sim 355\text{nm}$ and secondly the optics used to image the laser onto the sample. For high level excitation it is necessary to focus the laser spot onto the sample surface, and the degree of defocusing may be used to control the power density. In the close up image of the sample in *figure 2.14*, two different ways to excite the sample are shown. A spherical lens creates a circular profile or a cylindrical lens generates a stripe profile. The sample is placed at 90° to the incoming laser so that all parts of the spot or stripe profile are at the same focus condition. The luminescence is collected from the sample edge and directed towards the spectrometer; the data acquisition for these measurements is analog in nature, generally using a boxcar (described below), as photon counting is not possible due to pulse pileup as the excitation pulse width and luminescence decay time are both of the order of, or less, than the pulse width of the PMT. For the systematic investigation of high excitation effects, one needs to controllably vary the pumping intensity on the sample surface. While this may be done by defocusing the lens, this invariably leads to changes in the size of the excited region. Thus we chose to vary the excitation power density using a neutral density filter combination, without changing the focus condition of the lens.

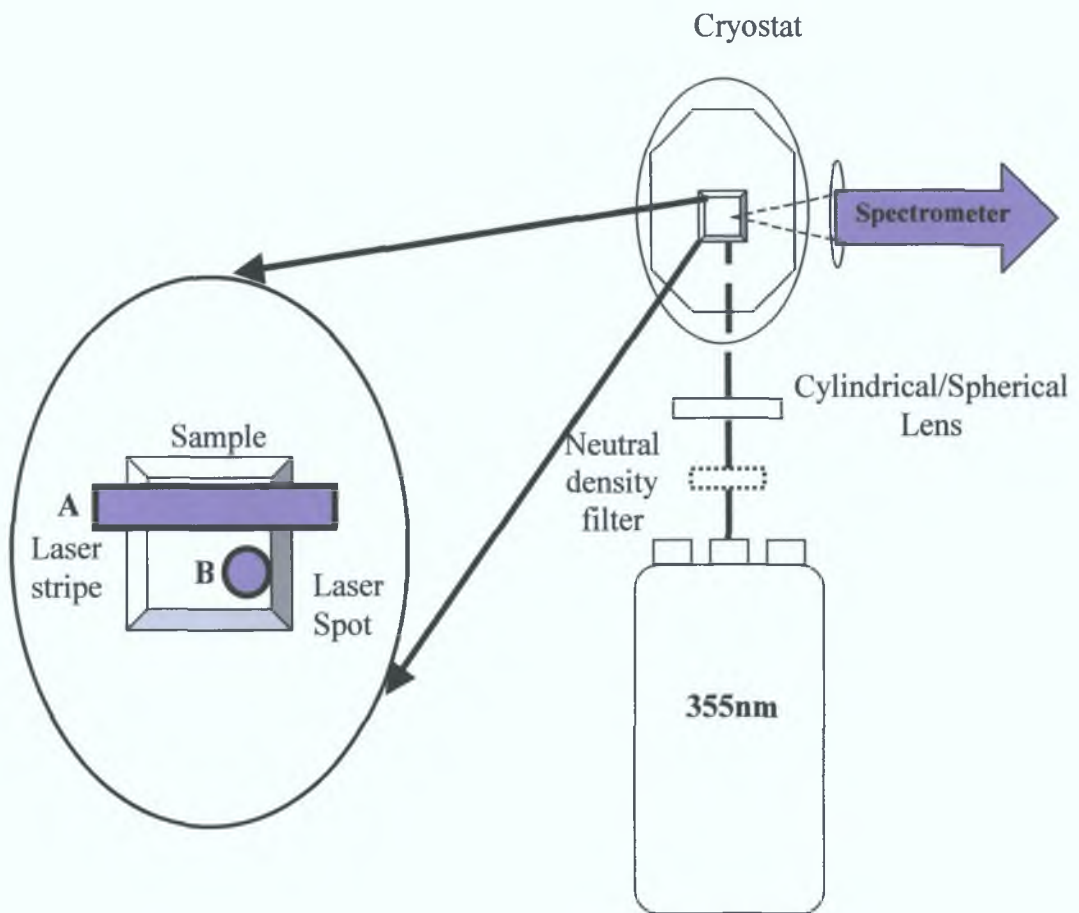


Figure 2.14: Experimental arrangement for the investigation of high excitation effects in ZnO material. Close up of sample shows different excitation areas (A) stripe (B) spot.

The pulsed laser source used was synchronised with the data collection using a boxcar integrator (Stanford Research systems Models SR250). This was necessary as the total time-averaged luminescence power excited by the Nd:YAG was very weak compared to the HeCd excited luminescence. The boxcar was incorporated into the system as it is designed to recover fast analog signals from a noisy background. The Nd:YAG gives a synchronisation signal which is a negative going signal of width $10\mu\text{s}$. This output as well as the analog PMT output due to the luminescence captured from the spectrometer was fed to the boxcar integrator. The output of the PMT could then be collected synchronously with the pump laser firing. The output from the boxcar integrator is then normalised to provide a voltage, which is proportional to the average of the input signal during the sampling gate. This output is then similar to the analog PL signal output and can be read by the same data acquisition software as used in this mode in the PL experimental arrangement.

2.3.2: Source for high level excitation

For high excitation studies the frequency-tripled Nd:YAG line at 355nm was used. The laser used was a Surelite II® supplied by Continuum Lasers operating with a ~5ns pulse width (FWHM) at a pulse repetition rate of 10Hz (at 532nm) with a pulse power of 160mJ (corresponding to 1.6 W averaged over a 1 second interval) [17].

2.3.3: Control of laser beam power

The power of the Nd: YAG is well above the damage threshold of the samples to be investigated (by a factor of $\sim 10^2$) and also the damage threshold for conventional neutral density filters; consequently an arrangement was needed to decrease the power output initially to an acceptable level. This arrangement is shown schematically in *figure 2.15*. The incoming beam from the Nd: YAG laser is incident on a glass slide, where ~4% is reflected downwards and the rest is transmitted and collected at a beam dump. The downward reflected beam then travels onto a silicon slide. The majority is reflected again (~90%). A beam dump is also situated under the silicon slide for safety reasons. The choice of components in this arrangement is important as the unattenuated laser will ablate many different materials and components, and thus one must choose relatively inexpensive consumable-type components such as glass slides and silicon wafers. This optical arrangement reduces the power sufficiently to allow us to make measurements on ZnO samples. Laser power meters are used to measure output beam power.

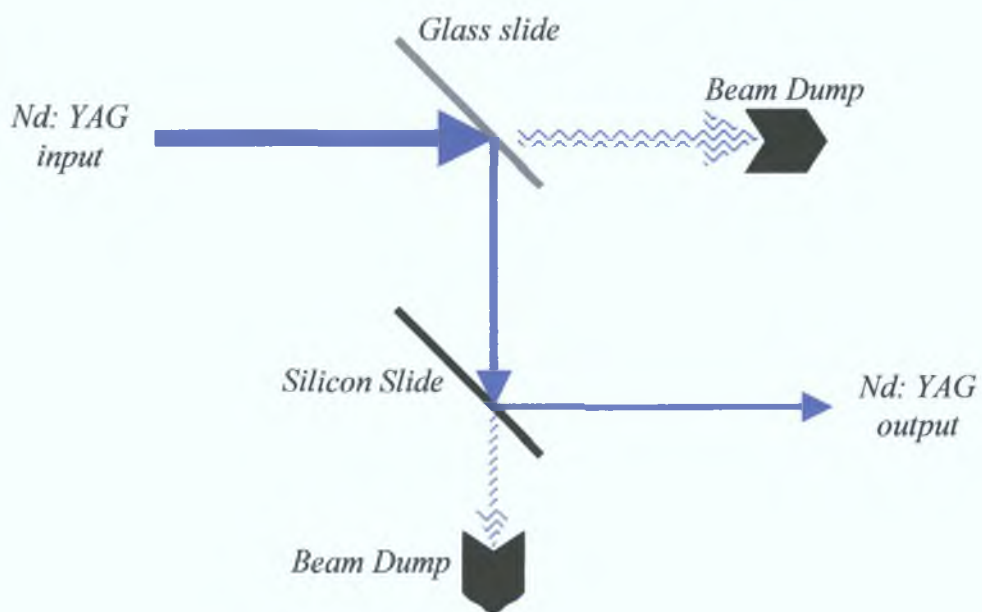


Figure 2.15: Attenuating the power output of the laser using glass and Silicon slide.

The laser power incident on the sample surface may then subsequently be controlled using a neutral density filter, without damaging the filter.

The question of the pulse to pulse stability of the incident laser power naturally arises as the investigation of high level excitation effects is critically dependent upon having a controllable and reasonably steady pumping intensity to explore different power regimes. Our data indicate that the pulse to pulse instability of the laser used in this work is of the order of $\pm 10\%$, which is slightly on the high side, but does allow reasonably confident discrimination of various regimes of power density. The spectra in these experiments were acquired with a step size of 0.1nm and slit widths of 500 μm . The large slit widths were necessitated by the rather low averaged luminescence intensities. The narrow step size was necessary to allow simultaneous acquisition of the laser pulse during the spectrum, which served as an internal intensity reference. The relatively large slit width also tends to compensate for slight “wandering” of the laser spot on the sample surface, which can affect the collection efficiency.

2.3.4: Variable stripe length method

In certain circumstances, when it is believed that stimulated emission and lasing effects are being observed, it is useful to measure the optical gain in the sample. A relatively simple method to study the gain in the sample is the Variable Stripe Length (VSL) method [18]. The gain is determined from the dependence of the amplified luminescence intensity on the variable length of an excited stripe on the surface of the samples. This technique has the advantage that the crystal need not be fabricated to form an optical cavity in order to determine its gain.

A cylindrical lens was used to form a rectangular excitation stripe, one end of which is located at the sample edge, while the other end of the excitation stripe is defined by the shadow cast by an adjustable jaw, which in practice is the jaw of a vernier callipers, allowing precise control of the stripe length. An excitation stripe of Nd:YAG laser light of controllable length is then imaged onto the sample as shown in *figure 2.16*. The data acquired with the VSL method had to be normalised because there was a slight increase in intensity of the laser line that appeared in the spectra with increasing stripe length. This increase was the result of the increased capture of luminescence associated with the physically larger excitation stripe length, as the excitation density of the laser was

kept constant. The graphs that appear in chapter seven were normalised to the highest laser line intensity (normally the longest stripe length).

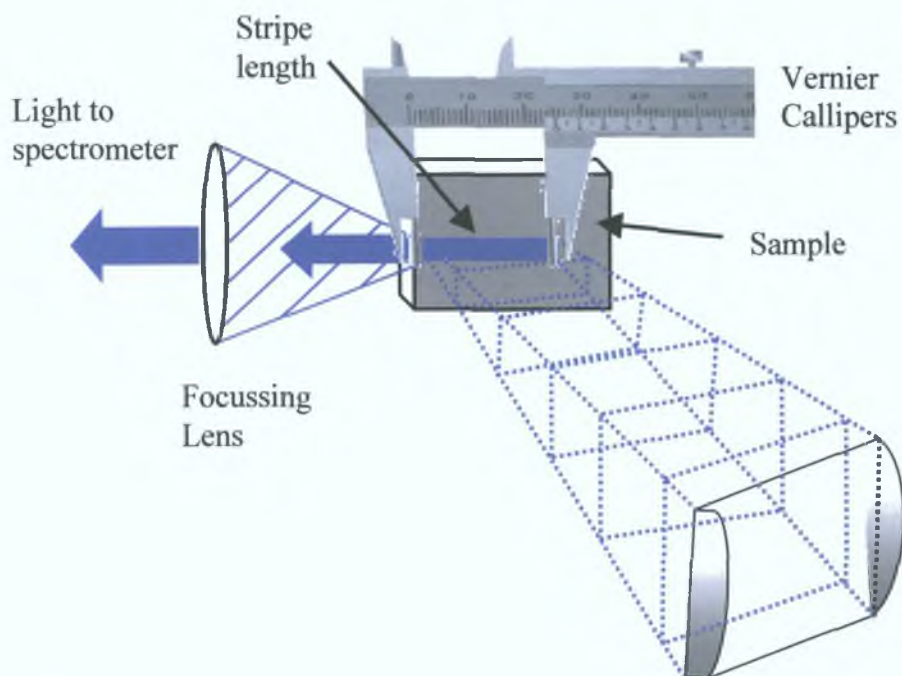


Figure 2.16: Experimental arrangement for the VSL method to measure sample gain.

2.3.5: PDA camera Arrangement

Some measurements of high excitation effects were performed using a photo diode array (PDA) based spectrometer system, allowing us to capture the complete emission spectrum corresponding to a single laser pulse, and to capture a series of these to study the variability in both the laser excitation energies and the emission intensity and spectral details, and to gauge the possible influence of one on the other.

The PDA camera used was an Andor Technology model DH520 (*Appendix D*), and was attached to a 1/8 m spectrograph (MS125 Spectra-Physics) (*Appendix D*) with a resolution of 0.22nm [19]. The other aspects of the experimental layout were identical to those used for other high excitation effects experiments except the resultant luminescence was sent onto the entrance slits of the integrated PDA-spectrometer system. The schematic layout of the spectrograph is illustrated in *figure 2.17*.

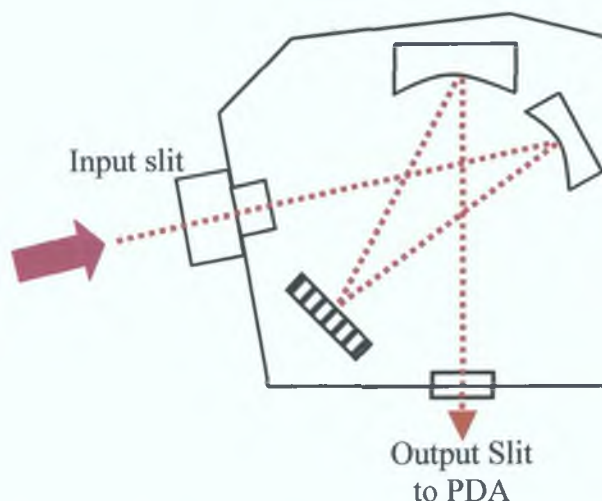


Figure 2.17: Optical Configuration of the spectrograph with the PDA at the exit slits.

2.3.6: Details of PDA operation and readout

The PDA camera is positioned at the output slits of the spectrograph. A PDA is a silicon-based semiconductor device with a 2-D matrix of MOS capacitors forming pixels [20]. This matrix is usually referred to as the image area, arranged in rows and columns. Luminescence emission from the experiment strikes these photodiodes. The reverse-biased photodiodes discharge a capacitor at a rate proportional to the photon flux. When the integration period of the detector is complete, a series of switches closes and transfers the charge to a shift register. After the transfer to the shift register is complete, the switches open and the capacitors attached to the photodiodes are recharged and a new integration period begins. At the same time as the luminescence energy is being integrated, the data is read out of the shift register by an A/D converter. The digitised data is then displayed on a computer. The PDA was air-cooled to temperatures of -10° to -30°C , which was necessary to eliminate a substantial fraction of the noise in the spectra. The PDA had a spectral range from 180 to 850nm with a quantum efficiency at room temperature of the order of 15%.

Binning is a process that allows charge from two or more pixels in a column to be combined on the PDA chip prior to readout. One may bin an entire column of the PDA in order to generate an effectively 1-D array, but with a substantially higher signal than in any single row, which results in a better signal to noise ratio for each element in the 1-D row. This is especially relevant for weak emission signals as each step of the readout process contributes to noise. In the spectra acquired in this work this full vertical binning procedure was used. The total pixel readout time was $16\mu\text{secs}$. For the majority of scans, where stripe length variations and their effects on the emission signal were

investigated, the acquisition mode was set in accumulation mode, i.e. 100 scans, each corresponding to a single laser pulse, were summed and the result plotted. Effectively averaging 100 different spectra, in a manner similar to that using the boxcar integrator method. The PDA set-up therefore provided an excellent independent check on the results from the boxcar set-up. For the investigation of laser modes the kinetic series mode was used. In this mode one has the option of acquiring and storing separately a sequence of single scans, each corresponding to a single laser shot. This allows us to explore the pulse to pulse variability of the excitation laser output and the spectral emission from the sample and to gauge the extent and importance of both. The exposure time throughout the experiment was set to 0.04s, which is the collection time of the PDA before readout. The background was recorded before each spectrum was taken. This was done to reduce any noise effects due to external stray light sources e.g. indicator LED's on various equipment.

The Nd YAG used as the pump laser intensity has an external triggering options. The Q-switch trigger was configured so that the firing of the pump laser triggered the PDA camera capture. This requires the input of 2 TTL negative going signals (5V \rightarrow 0V, 10 μ s wide). The first TTL signal called "Q-switch command" fires the Pockels cell and precedes lasing by \sim 170ns. The second TTL signal called the Fire Command causes the pump laser lamps to flash. This signal occurs after the pump laser pulse with a delay of \sim 180 μ s. A delay generator was incorporated into the experiment so that the pump laser firing was at a fixed time relative to the PDA camera. The window region for PDA acquisition was then optimised over the duration of a single emission pulse, to enable us to resolve lasing modes and their pulse to pulse variation.

Chapter Two References

- [1] J.A.Sans, A.Segura, M.Mollar, B.Mari, *Thin Solid Films*, 453-454, (2004), 251.
- [2] ISA Jobin-Vyon SPEX, *Guide for Spectroscopy*.
- [3] SPEX model 1704 manual.
- [4] *Diffraction Grating handbook*, Fourth Edition, Richardson Grating Laboratory.
- [5] Hamamatsu® R3310-02 Photomultiplier Tube Spec. Sheet.
- [6] Dermot Gorman, M.Sc Thesis “Photoluminescence and Excitation studies of semiconductors” (2001).
- [7] S. Perkowitz, *Optical Characterisation of Semiconductors: Infrared, Raman and Photoluminescence spectroscopy*, Academic Press Ltd., London UK, (1993).
- [8] Model 330 Autotuning Temperature Controller, user manual, Lakeshore®.
- [9] TCSPC system manual, Edinburgh Instruments® (2000).
- [10] D.O.O’Connor, D.Philips, *Time Correlated Single Photon Counting*, Academic Press, London, (1984).
- [11] D.M.Rayner, A.E.McKinnon, A.G.Szabo, *Can. J.Chem.*, 54, (1980), 446.
- [12] K.P.Ghiggino, A.J.Roberts, D.Philips, *J.Phys.E.Sci.Instrum.*, Vol 13, (1980) 446.
- [13] V.V.Tavnikov, A.Freiberg, S.F.Savikhin, *J.Lumin.*, 47, (1990), 107.
- [14] V.Srinivas, J.Hryniewicz, Y.J.Chen, C.E.C.Wood, *Phys.Rev.B*, Vol 46, No16, (1992), 10193.
- [15] R.E. Sherriff, D.C.Reynolds, D.C.Look, B.Jogai, J.E.Hoelscher, T.C.Collins, G.Cantwell, W.C.Harsch, *J.Appl. Phys.*, Vol 88, No 6, (2000).
- [16] M.Anpo, Y.Kubukawa, *J.Phys.Chem.*, 88, (1984), 5556.
- [17] Panther OPO operation and maintenance manual, Continuum® (2000).
- [18] K.L.Shaklee, R.F.Leneny, *Appl. Phys. Lett.*, Vol 18, No 11, (1971).
- [19] www.spectra-physics.com
- [20] Andor Technology manual for model DH520

Chapter Three

Photoluminescence

Photoluminescence (PL) is an optical characterisation technique for semiconductor materials. The advantages associated with this technique are that it is a non-contact, non-destructive technique and it requires little sample preparation. However the main disadvantage of PL is that the intensities measured are not quantitatively related to the concentration of the various impurity species. In section 3.1 the theory behind PL is outlined and PL results in section 3.2 are presented for the Eagle Picher bulk ZnO sample, which will be used as a reference for subsequent analysis of PLD-grown ZnO materials. In section 3.3 other PL bands associated with bulk ZnO material are discussed. The majority of the discussion is based on a comparison of our low temperature data with that in the literature, which shows the excitonic features of ZnO rather clearly. We finish by discussing briefly aspects of room temperature PL measurements.

3.1: Theory of photoluminescence

Photoluminescence (PL) is the term given to the luminescence produced when a material has been excited by photons. In PL, an optical transition occurs from an excited state to a lower electronic state, usually resulting from either intrinsic transitions (such as band to band or free excitons) or transitions at defects or impurities and complexes in the material. Thus PL is spectroscopic in nature, with the emission intensity monitored as a function of wavelength or energy. The spectra in this report may be explained by an understanding of the conduction and valence bands and the occurrence of energy levels within the energy band gap.

3.1.1: Bandstructure

The band structure of ZnO is shown in chapter one *figure 1.7*. The valence band has its maximum at the Γ point i.e. at $k = 0$, the conduction band minimum is also at the Γ point and is isotropic and parabolic; it is therefore a direct bandgap semiconductor. It has a hexagonal wurtzite structure, the valence bands (derived mostly from atomic P-orbitals) are split by the hexagonal crystal field and spin orbiting splitting into three sub-bands which are usually labelled from higher to lower energies as A, B and C bands with symmetries Γ_7 , Γ_9 and Γ_7 [1]. This can be seen in *figure 1.7* of chapter one. This symmetry assignment is still the origin of debate and controversy in the literature however, and we give the most commonly agreed assignment, while some other groups claim that an assignment of Γ_9 , Γ_7 and Γ_7 . to the A, B and C valence band symmetries best explains the experimental data [2,3].

As discussed below, optical emission in semiconductors is often described in terms of bound electron-hole pairs (or excitons). Due to the presence of three distinct valence bands closely spaced in energy, there are also three closely spaced exciton bands in ZnO, labelled A, B and C excitons (*figure 3.1*). Therefore in the case of ZnO, the B exciton is where the hole is created in the second valence band (B band), and consequently it's energy (B valence bandgap minus the binding energy of the exciton) is greater than the A exciton and less than the C exciton. Examples of spectra showing these A, B and C excitons will be seen in chapter four.

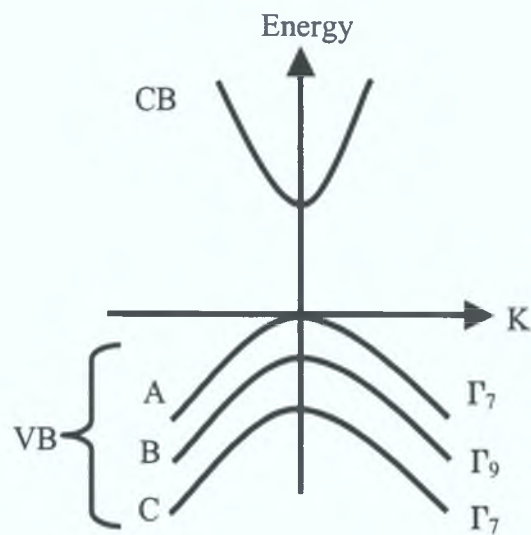


Figure 3.1: Schematic diagram of the band structure of hexagonal semiconductor around the Γ point, splitting into three valence bands.

3.1.2: Recombination

Excess carriers generated under optical illumination must eventually recombine. This may happen in several ways. In addition to intrinsic band to band and free exciton processes, defects may introduce additional recombination pathways for the electron and hole or exciton. When present in sufficiently high concentrations such defects can significantly lower the material quality and it's potential for use in devices such as light-emitting devices. Ranges of defect states are conventionally identified in the literature. A shallow donor state is a state with an energy level just below the conduction band edge. At room temperature these defects are thermally ionised, donating an electron to the conduction band, and increasing the free carrier density in this band. Donors are usually formed by substitutional atoms situated in the periodic table one column to the right of the ones they replaced. Donors can also be formed by interstitials, which have

weakly bound electrons such as Li, H, or Na in a II-VI compound [4]. These foreign atoms can appear in materials at the growth stage due to various sources of contamination, or may be introduced deliberately to tailor the electronic properties of the material. Shallow acceptor states conversely are levels just above the valence band edge, usually formed by substitution of atoms one column to the left in the periodic table of the atoms, which they replace. Acceptors may also be formed by interstitial species such as oxygen interstitials in the ZnO lattice etc [4,5]. Recombination mediated by such shallow levels is often radiative and clear donor- and acceptor-related features are seen in many semiconductors. Interactions between charge carriers on donors and acceptors may be seen in optical spectra in typical donor-acceptor (DA) pair emission.

Deep levels close to the centre of the forbidden gap may also occur, and are often associated with point defects with a substantially different ionic radius compared to the host atom, or with complexes of point defects [6]. These states can act as carrier recombination or trapping centers. These may decay radiatively, but in many cases act as non-radiative decay channels, with the excess energy of carriers recombining at these levels carried away by single or multiple phonons. They are therefore also known as “luminescence killers”.

PL is a rather sensitive technique and can detect emission from rather low defect concentration levels (of the order of 10^{14} cm^{-3} and often lower, well below the doping levels commonly used in devices) [7].

3.1.3: Intrinsic recombination – band to band recombination

The band gap of a semiconductor can be described as either a direct gap or indirect gap. In the case of the direct gap semiconductor, where the conduction and valence band edges occur at the same value of crystal momentum k (usually $k = 0$, shown in *figure 3.2(a)*), if the sample is excited by a photon with energy greater than the band gap, then an electron-hole pair is created, with an electron being excited to the conduction band, leaving a hole in the valence band. The electron then thermalises down to the valence band edge. The electron may then later radiatively recombine with the hole and emit a photon with an energy given by

$$\hbar\omega = E_g + E_e + E_h \quad (3.1)$$

where $\hbar\omega$ is the photon energy, E_g is the gap energy associated with a band to band transition and E_e and E_h are the electron and hole energies, respectively, measured with

respect to the corresponding band edge. At room temperature, the PL emission lies at approximately the band gap energy but extending to slightly higher energies due to the thermal energies of the recombining electron and hole.

In the case of indirect band gap semiconductors (where the conduction and valence band edges occur at different k values, as in *figure 3.2(b)*) the recombination involves the loss or gain of crystal momentum of the electron due to an interaction with a phonon and the energy of the emitted photon is given by

$$\hbar\omega = E_g + E_e + E_h \pm \hbar\Omega \quad (3.2)$$

where $\hbar\Omega$ is the energy of the momentum-conserving phonon and the \pm sign corresponds to phonon absorption and emission respectively [7]. Both direct and indirect band gap semiconductors are illustrated in *figure 3.2*.

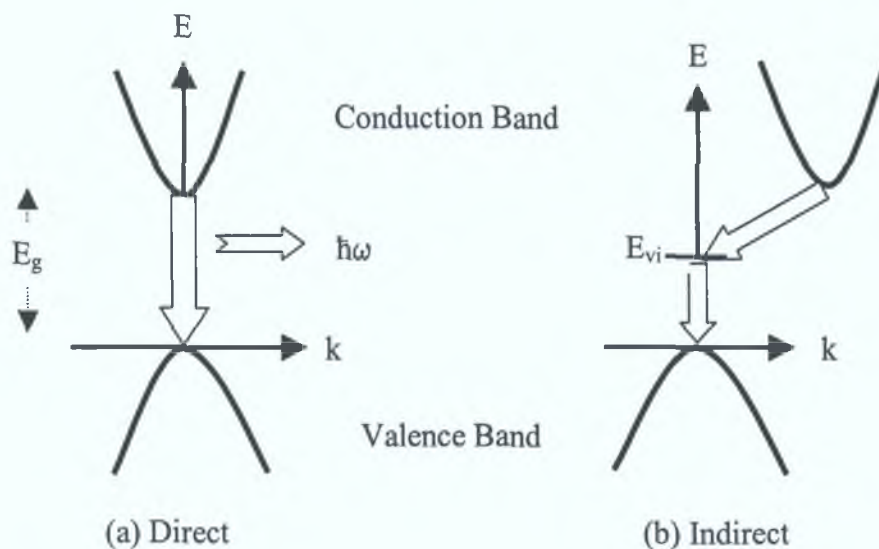


Figure 3.2: Direct and Indirect electron transitions in Band Gap semiconductors.

(a) Direct transition with accompanying photon emission, (b) indirect transition via a virtual level.

The distinction between direct and indirect band gap materials is important when selecting materials suitable for manufacturing photonic devices such as light emitting diodes (LEDs) or laser diodes (LDs). Direct band gap materials have a much greater radiative efficiency at the band edge, as no phonon is required for PL emission, so the process is described by first order perturbation theory, while the transition across an indirect gap material is described by second order perturbation theory, and hence is an intrinsically less probable process. A discussion about direct and indirect transitions has

taken place in chapter one. We will consider only direct gap materials from this point, as the ZnO material studied in this thesis is a direct gap material.

3.1.4: Intrinsic recombination – free excitons

At low temperature and with low excitation densities, the electron hole pair excited by the external pumping source forms a bound pair called a free exciton (FE) due to their mutual Coulomb interaction. In a high purity material where the number of defects and impurities that can trap excitons is low, free exciton luminescence can be observed and occurs at an energy in a direct gap

$$\hbar\omega = E_g - E_x \quad (3.3)$$

where E_x is the exciton binding energy, which can be simply modelled in many cases using the Bohr hydrogenic scheme [8].

3.1.5 Defect recombination

If the concentration of defect centres, such as donors, acceptors and other impurities, increases in the material then the probability that the free carriers / excitons, which diffuse through the material will be captured by such traps increases greatly. In fact most of the highest quality ZnO is dominated by bound exciton emission. Excitons trapped at shallow donors or acceptors sites are bound with a binding energy of the order of a few to 10's of meV, (typically roughly a 0.3 of the donor or acceptor ionisation energy in ZnO)[9]. These bound-excitons recombine leading to impurity specific bound-exciton luminescence at low temperatures. The energy of a photon associated with bound-exciton luminescence is given by

$$\hbar\omega = E_g - E_x - E_B (\pm \hbar\Omega) \quad (3.4)$$

where E_B is the binding energy of the exciton to the neutral donor or acceptor. The phonon energy term ($\hbar\Omega$) is included if the bound-exciton decay involves the emission of a momentum-conserving phonon, which is dependent on the details of the local exciton binding. Excitons and free carriers may also be trapped and recombine at deep defects resulting in PL emission in the mid band gap energy range, often with very large linewidths due to phonon coupling effects. There are also other radiative and non-radiative recombination's pathways available to the electron hole pairs. Thus analysis of PL spectra can be used to detect impurities and defects in materials and estimate the purity of the material, in addition to studying various aspects of the defects, e.g. symmetry, electrical activity, etc.

3.1.6: Spectral analysis of PL data

In order to explain how PL can be used to yield information about semiconductor materials, an example of a PL spectrum for a ZnO sample is shown in *figure 3.3*.

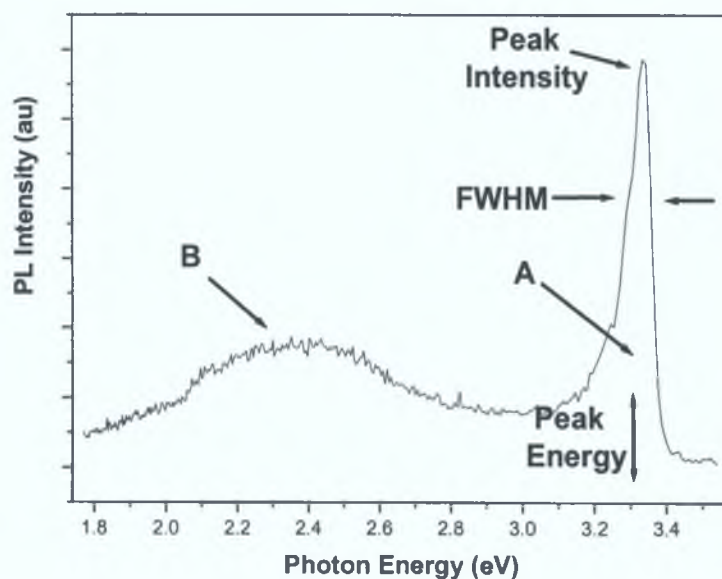


Figure 3.3: Spectra of ZnO sample grown by PLD measured at 200K where A indicates the peak associated with the band edge, B the deep level transition and FWHM indicates the full width at half maximum height of a particular band. Slits 100 μ m, Integration 1.0s, Increment 1.0nm.

The peak intensity positions may be influenced by various effects, such as variations in the composition of the alloy in ternary and quaternary epitaxial layers or due to variations in quantum well widths in quantum well samples. Strain, electric and magnetic fields and free carrier density also have an effect on the line positions observed in PL. For example changing the Zn: Cd ratio in a ternary $Zn_xCd_{1-x}O$ alloy will alter the peak position by changing the energy associated with the band gap transition. The wavelength range observed in electro-luminescent and lasing devices is generally close to the band-band emission seen in PL as similar processes are involved; hence PL is useful in determining the ultimate device potential for a material system. Variations in the full width half-maximum (FWHM) can be caused by a number of factors including doping, strain, electric fields etc. Additional factors such as peak asymmetry provide further information on the microscopic details of the system. Many different factors contribute to the appearance of PL spectra, as shown in *table 3.1*.

<i>Lineshapes</i>	<i>Peak Wavelength</i>	<i>Intensity</i>
Temperature	Temperature	Temperature
Impurity Concentration	Excitation Intensity	Excitation Intensity
Carrier/exciton density	Band gap energy	Spectrometer response
Strain inhomogeneities	Strain	Electric Field
Electric field	Electric field	Carrier density
	Magnetic Field	
	Carrier density	

Table 3.1: Influences on the features of photoluminescence spectra

The PL spectra presented in this work are plotted with intensity in arbitrary units on the Y-axis, because as already stated there is no direct quantitative relation between two samples with respect to intensity. The x-axis is shown in either wavelengths (nanometers (nm)) or photon energy (electron volts (eV)). These units will interchange as certain classifications are commonly made in nm and others in eV.

3.2: PL Eagle Picher bulk ZnO results

In our work, many measurements are made on PLD material, where substantial strains, defect concentrations and electric fields can affect the peak positions and lineshapes. In order to try to correctly assign the physical origin of the peaks we believe it is necessary to have a reference material so that the PLD-grown material can be compared to high quality single crystal material. Single crystal material was purchased from Eagle Picher Corporation and used as the reference material in this study. This material is of excellent quality and provides a suitable reference material. The Eagle Picher (EP) ZnO material [10] was grown by the seeded chemical vapour transport (SCVT) technique and typically has a donor concentration in the $1 \times 10^{17} \text{ cm}^{-3}$ range [11] with hydrogen (H) and some aluminium (Al) or gallium (Ga) contamination, in various combinations but in small quantities. The dislocation density is in the region of $10^4 - 10^5 \text{ cm}^{-2}$. It is crucial to characterise this material in detail before any experiments are conducted so that the

results may be used as a reference for subsequent interpretation of experimental data. In *figure 3.4* the low temperature spectra of the bulk ZnO material is shown.

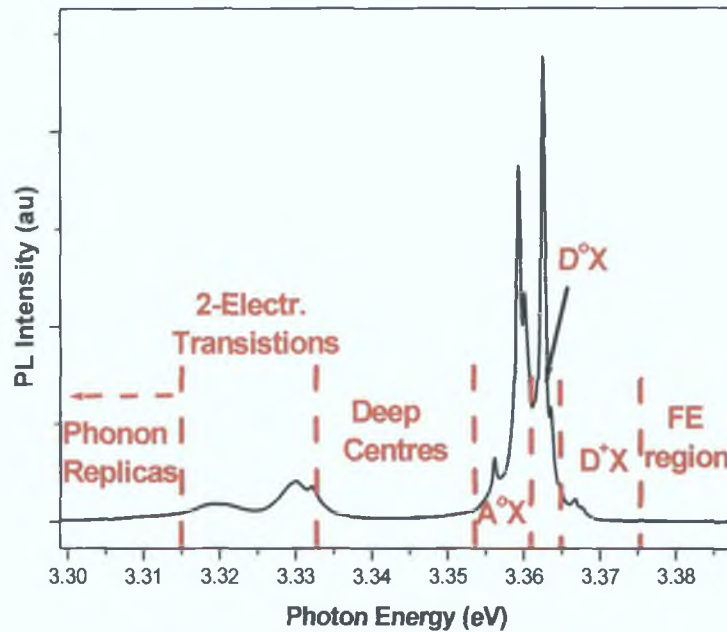


Figure 3.4: Low Temperature (25K) EP material with the regions assigned from Klingshirn et al. [12] with an increment of 0.01nm, integration 3.0s and slits of 10 μ m.

3.2.1: Assignment regions

Among the earliest classification of PL lines in ZnO was by Klingshirn et al [12] whereby the band edge PL in bulk ZnO is divided into seven regions, which are depicted in *figure 3.4*:

- free exciton ($3.3765\text{eV} < \text{FE} < 3.3925\text{eV}$);
- excitons bound to ionised donors ($3.3646\text{eV} < \text{D}^+\text{X} < 3.3765\text{eV}$);
- excitons bound to neutral donors ($3.3605\text{eV} < \text{D}^0\text{X} < 3.3646\text{eV}$);
- excitons bound to neutral acceptors ($3.3536\text{eV} < \text{A}^0 < 3.3605\text{eV}$);
- exciton bound to deeper centers ($3.3329\text{eV} < \text{E} < 3.3536\text{eV}$);
- two-electron transitions ($3.3151\text{eV} < \text{E} < 3.3329\text{eV}$);
- phonon replica region ($\text{E} < 3.3151\text{eV}$).

The regions D^+X , D^0X and A^0 are known collectively as the Bound Exciton Complex (BEC) region. These regions taken from the reference [12] are not exact, with differences in the excitation power, in the calibration of the spectrometer and its resolution in comparison to *figure 3.4*. However they are used as a starting reference point in the assignment of the bands. The categorisation of regions by *Klingshirn et al*

[12] was based upon Haynes rule, which relates the binding energy of the exciton to the neutral complex (lowest free exciton state at $k = 0$) to the binding of the additional carrier to the point defect. The rule is given by

$$E_B = K_D \times E_D, \quad (\text{for donors}) \quad (3.5)$$

$$E_B = K_A \times E_A, \quad (\text{for acceptors}) \quad (3.6)$$

where K_D and K_A are constants depending on the ratio of effective hole and effective electron mass [13]. E_B is the bound exciton energy; E_D and E_A are the energies of the donor and acceptor respectively. These constants are predicted theoretically for II-VI compounds [13], and in the case of ZnO these constants have been measured experimentally, initially giving a value of ~ 0.1 [14] (which was used by *Klingshirn* in his classification scheme) and more recently have been found to be ~ 0.37 for both donors and acceptors [15]. Therefore for the remaining discussion *Klingshirn et al* [12] classification will be disregarded and the convention used by *Schildknecht et al* [15] (based on *Schildknecht et al* [15] recent determination of the constants for Haynes rule) will be used.

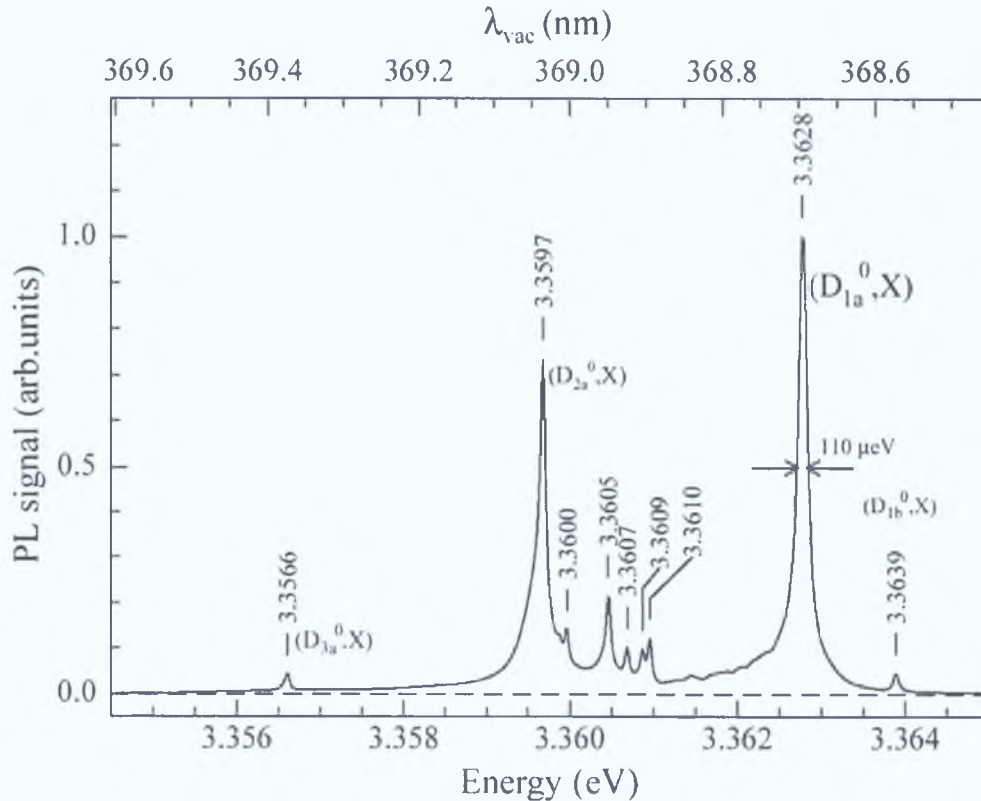


Figure 3.5: PL spectrum at 4.5K of an Eagle Picher ZnO material. *Schildknecht et al* [15].

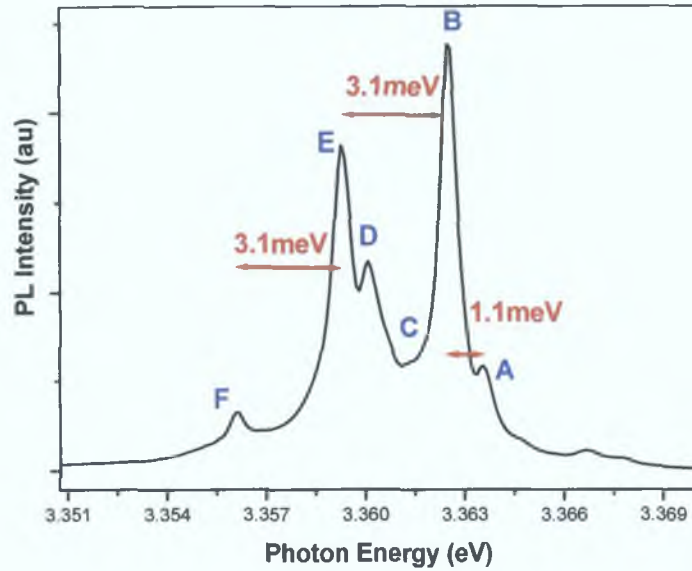


Figure 3.6: Close up of Bound Exciton region at 25K of the Eagle Picher material. Comparison should be drawn with figure 3.5, visually. The separation marked in red is similar to the results taken from literature [15]. The lines are labelled A to F, naming convention used for this work. Increment 0.01nm, Integration, 3.0s, Slits 10 μ m.

A comparison of PL spectra of the Eagle Picher material from our laboratory with published work is used to assign the lines in the BEC region. Data from *Schildknecht et al* [15] (figure 3.5) was used as a comparison because (1) Eagle Picher material was also used in their work, (2) both spectra were taken at low temperature and (3) the work is recent (2003). Figure 3.5 and 3.6 show that the spectra are visually comparable and broadly similar except that the spectra in the work of *Schildknecht* [15] is taken at 4.5K. Therefore they may only be compared quantitatively after appropriate temperature correction. These spectra values are compared in table 3.2.

<i>Schildknecht</i> [15] identified Peaks <i>Fig 3 5</i>	<i>Schildknecht</i> (eV Peak Position) <i>Fig 3 5</i>	<i>Schildknecht</i> peak – (0.4meV*)	Identified peaks in this work <i>Fig 3 6</i> (corrected for refractive index of air in conversion to eV)	eV (Peak Position) <i>Fig 3 6</i>
D _{1b} ^o ,X	3 3639	3 3635	A	3 3635
D _{1a} ^o ,X (FWHM= 11meV)	3 3628	3 3624	B (FWHM= 82meV)	3 3624
	3 3610	3 3606	C	3 3613
	3 3609	3 3605		
	3 3607	3 3603		
	3 3605	3 3601	D	3 3600
	3 3600	3 3596		
D _{2a} ^o ,X	3 3597	3 3593	E (FWHM=1.55meV)	3 3592
D _{3a} ^o ,X	3 3566	3 3562	F	3 3561

*shift correction to take account of the rise in temperature from 4.5K (*Schildknecht et al*) to 25K in this present study

Table 3 2 Assignment of peaks and values between Schildknecht reference [15] and the present work

The sample temperature was 25K for the spectra acquired in this work compared to the *Schildknecht* work [15], which was obtained at 4.5K. Consequently a correction of the peak energy position was required to compensate for the band gap shrinkage between 4.5K and 25K. The corrected spectra may then be used to correlate the lines. When the peak positions of the observed emission peaks are plotted against increasing temperature they follow closely the trend of the energy band gap, which is known to reduce. It is possible to estimate the emission peak position at certain temperatures rather accurately using a semi-empirical formula

$$E(T) = E(0) - \frac{\alpha T^2}{\beta + T} \quad (3.7)$$

This formula is known as the Varshni formula, [16] with α , β and $E(0)$ fitting parameters. Where $E(0)$ is the energy of the emission band to be fitted at 0K. Using the Varshni formula it is possible to calculate the difference between the emission bands at 4.5K and 25K and justify the correction that is shown in *table 3.2*. *Ko et al*, [17] have used this formula for ZnO with a $E(0)$ value for the donor bound exciton emission of 3.3651eV. The other fitting parameters used in this reference were $\alpha = -7.3 \times 10^{-4}$ eV/K and $\beta = -1077$ K. The shift for the bound exciton emission line was determined for temperatures between 4.5K and 25k to be 0.4meV. We have used this data to correct our results.

Table 3.2 indicates the lines observed in our and *Schildknecht* study are very close in energy. The difference in the *Schildknecht* value adjusted to 25K and the values acquired in this work were less than 0.01meV on average. This is within the experimental error of the spectrometer caused by slight slippages in the spectrometer drive etc. or slight errors in the fitting parameters used in the Varshni equation [18].

3.2.2: Nature of peaks

Returning to *figure 3.4*, examining the spectra from higher energy to lower energy, the first resolved peak is labelled as A in *figure 3.6*. *Schildknecht et al* [15] reports this line as D_{1b}°,X . It is further identified using thermalisation data as an excited state of the D_{1a}°,X feature (feature labelled B in our data).

The dominant peak in the bulk ZnO material is at a maximum at 3.3624eV and labelled as line B in *figure 3.6*. This line can also be referred to as D_{1a}°,X using *Schildknecht's* [15] convention. The microscopic origin of this line has for many years remained undecided. It was shown through theoretical studies that hydrogen (H) acts like a shallow donor in ZnO [19] and ought to be a common impurity in ZnO, especially in material grown by the seeded vapour phase method used by EP. Experimental studies by *Look et al* [6] investigated the PL lines associated with hydrogen and found that after annealing the EP ZnO material above 600°C the B line disappears [20]. This is the temperature at which hydrogen leaves the ZnO lattice. The B line was then reintroduced by exposure to a H plasma [20]. *Hofmann et al* have used electric paramagnetic resonance (EPR) and electron nuclear double resonance (ENDOR) spectroscopy, to study this feature and also attributes this line to a hydrogen donor [11]. This shows agreement that the B line emission is due to recombination of an exciton bound to a

hydrogen donor. *Meyer et al* [1] reaffirmed the identification of the B line as hydrogen, and this line was shown to disappear at temperatures of 600°C and above as explained previously [6].

The next peak is labelled as C (relatively weak compared to the B peak) in *figure 3.6* at the energy position of 3.3613eV. The corresponding region in *Schildknecht's* [15] work contains three lines, which lie very close together and appear at energy positions of 3.3610, 3.3609 and 3.3607 eV at 4.5K. The C line we observe is most probably due to the combined emission from these three features and overlaps from the B, D and E bands. Given the relative weakness of this feature and the closely lying overlapping bands the spectral alignment between our own data and *Schildknecht* is not as close as other lines. Thermalisation studies in reference [15] identify the peak at 3.3610 eV as an excited state of the D_{2a}^0, X feature (labelled as feature E in our data below). The feature we observe labelled as C is only seen at higher temperatures (> 20K), consistent with a thermalising transition.

We also observe two more peaks labelled as D and E. The D line is at 3.3600eV and corresponds to the line observed by *Schildknecht* at ~3.3605 eV at 4.5K. *Schilling et al* [21] investigated the effects of aluminium (Al) implanted into ZnO and was noted that after implantation of Al the corresponding line to the D line had a luminescence signal 16 times larger than the unimplanted ZnO. When argon (Ar) was implanted no such increase was seen. The D line was shown to be the only line that was affected by the implantation in the whole spectrum. From these results it may be concluded that the D line luminescence originates from the recombination of electron hole pairs bound to an impurity center related to Al. Further investigation of the D line with secondary ion mass spectroscopy (SIMS) confirmed *Schillings et al's* [21] assignment of this defect as Al-related [1].

Between the D and the E line positions, the data shown by *Schildknecht et al* has a very weak line with a temperature-corrected value at 3.3596eV. This does not appear in the 25K spectra in our work, almost certainly due to the relative weakness of this feature and the proximity and width of the E line.

The line labelled E is at 3.3592eV which *Schildknecht* refers to as D_{2a}^0, X . *Reuss et al* [22] investigates this E-line and its association with gallium (Ga). They implanted Ga

into ZnO and studied through PL the effects that annealing has on the samples. It was noted that in the implanted ZnO, the lines referred to as B and D in this work disappear after annealing, with the E line remaining. The emission feature E can thus be assigned to emission of excitons bound to Ga related neutral donors. Other reports in literature have shown that Ga is associated with the E emission line also [23,24]; in particular, radioactive isotope implantations undertaken by our own group confirm the involvement of Ga in this defect [25]. This has also been confirmed via SIMS data [1].

Finally identification of the line F at 3.3561eV in *figure 3.6*, which *Schildknecht* designates D_{3a}^0, X , has been associated with sodium (Na) in the literature [1]. *Tomzig et al [14]* investigated Na doped crystals and the emission line F has been described as due to an exciton bound to a neutral Na acceptor. [14]. However some difficulties are associated with this assignment; if the F line is a Na-related acceptor bound exciton transition it is expected that excitons will only bind on neutral shallow acceptors [1]. There is no evidence of donor-acceptor pair transitions involving the proposed Na acceptor [1]. Magnetic resonance studies by *Meyer et al* may resolve this discrepancy. These workers have proposed that the F line is associated with indium (In), i.e. a neutral donor bound exciton. They have used substrates which showed no indication of an F line and performed diffusion experiments with In, which reveals the appearance of a peak at the expected F-line position. The presence of In in the crystal was confirmed by SIMS [1].

As a final confirmation of our assignments we note that the separation between the peaks in *figure 3.6* for A / B is 1.1meV, B / E is 3.1meV and E / F is 3.1meV, which agrees very well with the spectra shown in *figure 3.5* [15].

3.2.3: Discussion of other designations of PL features in bulk ZnO

The other major designation of near band edge luminescence lines in ZnO is the so-called I-line series, which originated in the work of Reynolds in the 1960's [26]. There has been a long history of confusion over the assignment of these lines, with different authors disagreeing on the precise designation of particular members of the series to certain features, which has been fuelled by the fact that, up to recently, the chemical identifications of the features was unknown, and also because different members of the series were dominant in samples grown by different techniques, with varying conditions of strain etc. However, opinions have converged over the last ~ 2 years on the positions

of the various members of the I-line series and their chemical origins in many cases. The best currently available assignment is presented in tabular form by *Meyer et al* [1], and is reproduced below in *table 3.3*, where the various I-line series members are tabulated, along with *Schildknecht's* designation, and our A, B, C etc assignment. We also include the chemical identifications, where known.

<i>Schildknecht</i> Labelled Peaks [15]	eV (Peak Position) 4.5K	Identified in this work	eV (Peak Position of own work) 4.5K (corrected)	<i>Meyer et al</i> Labelled Positions [1]	eV (Peak Position) 4.5K	Chemical Identity
D _{1b} ⁰ ,X	3 3639	A	3 3639	I ₁	3 3718	
D _{1a} ⁰ ,X	3 3628	B	3 3628	I ₂	3 3674	
	3 3610	C	3 3617	I ₃	3 3665	
	3 3609			I ₄	3 3628	H
	3 3607			I ₅	3 3614	
	3 3605	D	3 3604	I ₆	3 3608	Al
	3 3600			I ₇	3 3600	
D _{2a} ⁰ ,X	3 3597	E	3 3596	I ₈	3 3598	Ga
D _{3a} ⁰ ,X	3 3566	F	3 3565	I ₉	3 3567	In
				I ₁₀	3 3531	
				I ₁₁	3 3484	

Table 3.3 Assignment of peak positions compared between *Schildknecht* [15] and the present work in comparison to *Meyers et al's* convention [1]

3.3 Other bands in bulk ZnO material

The bound exciton complex region has been analysed in reasonable detail and the peaks observed have been assigned to previously observed features in the literature. Inspecting *figure 3.4* at lower energies (< 3.35 eV) indicates that there are broader bands that exist in the EP bulk material. These bands will be discussed in the following sections.

PL spectra on a linear scale show no indication of the FE peak mentioned in 3.1.4. It is expected to be weak and become stronger with increasing temperature, as bound excitons become thermally dissociated from donor centres. However, the introduction of

a log scale makes it possible to observe these peaks and the FE may be assigned as shown in *figure 3.7*.

There is no real structure visible in the region 3.35 to 3.30eV as shown *figure 3.7*. The acceptor bound exciton features associated with the N acceptor in ZnO [27] are observed in this region (at ~ 3.315 eV). This spectral region appears to be the energy range where acceptor bound exciton feature may be expected, given the evidence for rather deeper acceptor levels in ZnO compared to donor levels [28]. The absence of any visible acceptor bound exciton luminescence in our samples indicates that there is little acceptor compensation of the dominant donor species.

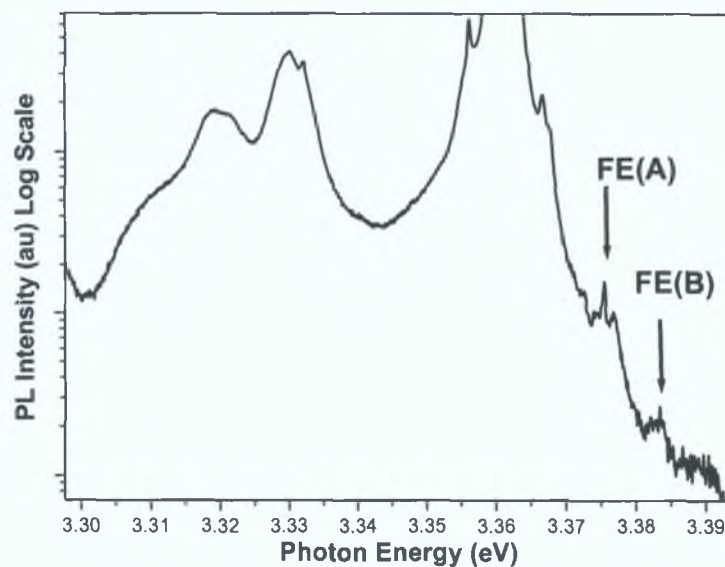


Figure 3.7: EP material, close up of figure 3.4, two electron transition and deep centre regions recorded at 25K with intensity shown as log scale. Increment .01nm, integration 3.0s, slits 10 μ m.

3.3.1: Two electron satellite

At lower energies (below 3.34eV) we observe the two-electron transition region, also known as the “two-electron satellite” (TES). These transitions are due to a process where the donor electron of a D^0X complex is transferred in the recombination process from its ground state into an excited state, i.e. during the recombination of an exciton bound to a neutral donor, the donor final state can be the 1s state (D^0X) or the 2s,2p state (TES line). The lines lying in the bound exciton region should replicate at a lower energy in the TES. As seen in *figure 3.8* there is an apparent replication between the two sets of lines regarding energy. The lines in question are the dominant B and E lines. The separation of the donor bound exciton (D_{1a}^0X) (B line) and the highest intensity peak of the TES1 area is 32.7meV. The second separation between the E line and TES2

is 40.7meV. Apart from the line broadening the TES section of the spectra does mirror the BEC region as shown in *figure 3.8*.

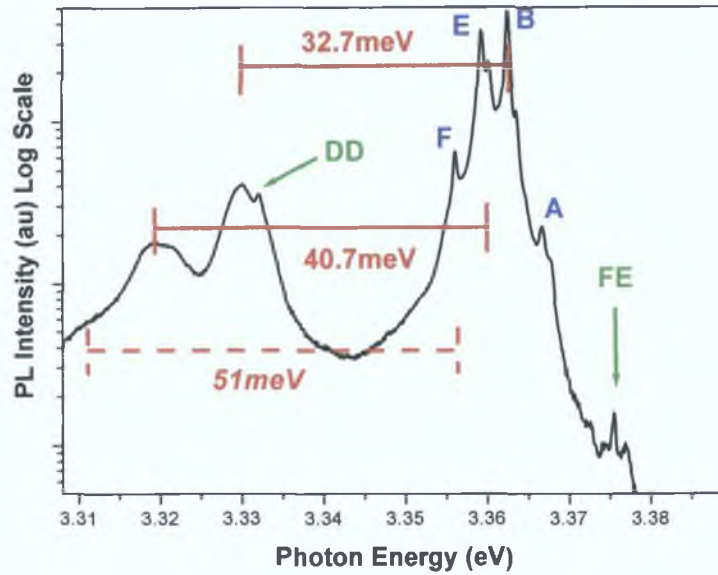


Figure 3.8:EP material (25K), notation for identification of the two electron satellite with intensity shown on a log scale. Increment 0.01nm, integration 3.0s, slits 10 μ m.

The effective mass theory (EMT) gives a good description of the excited p-like donor states. The ionisation energy of the donors can be calculated from the spacing $\Delta E(1s \leftrightarrow 2p)$, i.e. the energy of the separation between the TES and the bound excitons plus one quarter of the theoretical EMT donor Rydberg energy R^* .

$$E_D = \Delta E(1s \leftrightarrow 2p) + \frac{1}{4} R^* \quad (4.9)$$

Schildknecht et al [15] report a theoretical EMT donor binding energy of 56meV (i.e. the EMT Rydberg energy R^*) and we use this figure in our subsequent calculations. *Table 3.4* summarises our data for the exciton localisation energy, E_{LOC} , the $E_{1s \rightarrow 2p}$ energies from the TES separations and the calculated donor binding energies for the B, E and F features in our spectra. Our data are in good agreement with the literature values.

$E(D^0, X)$ (eV)(± 0.1 meV)	Labelling	$E_{LOC} = E(FE) - (D^0, X)$ (± 0.1 meV)	$E_{1s \rightarrow 2p}$ (meV) (± 0.1 meV)	E_D (meV) = $E_{1s \rightarrow 2p} +$ $1/4 E_{D, EMT}$
3.362	$D_{1a}^0, X(B) I_4$	13.4	32.7	46.7
3.359	$D_{2a}^0, X(E) I_8$	16.4	40.7	54.7
3.356	$D_{3a}^0, X(F) I_9$	19.4	$\sim 51 \pm 2$	65 ± 2

Table 3.4: Energy values of the main donor bound exciton lines and their relation to the TES transition.

In *figure 3.8* we observe a weak TES3 at a separation of 51 meV from the corresponding bound exciton features. This is also observed by *Schildknecht et al* and is marked by a question mark in *figure 3.9*, taken from their paper [15]. This feature is not as clearly identified in our data due to the lower resolution of the spectrometer used, however it does appear as a visible shoulder in *figure 3.8*. This rather tentative identification is reflected in the larger error on the value of E_D as seen in *table 3.4*. *Figure 3.8* also shows a peak labelled as DD (deep donor), a very weak feature also seen by *Schildknecht et al* [15], related to a transition at an unknown deep donor defect.

Figure 3.9 shows the data from reference [15], which we have used extensively as a comparison for our work. The energy positions and line separations for the donor bound excitons labelled in *figure 3.9* and the work presented here are broadly correct. The bound excitons labelled D to F are neutral donor bound excitons, demonstrated by the observation of the TES associated with each donor bound exciton. While some controversy still exists concerning the donor/acceptor nature of these defects (see e.g. Zeeman data presented by *Gutowski et al* [29]), the accumulation of data presented in references [1, 15] and elsewhere gives rather strong confirmation that the emission lines A to F are due to neutral donor bound excitons.

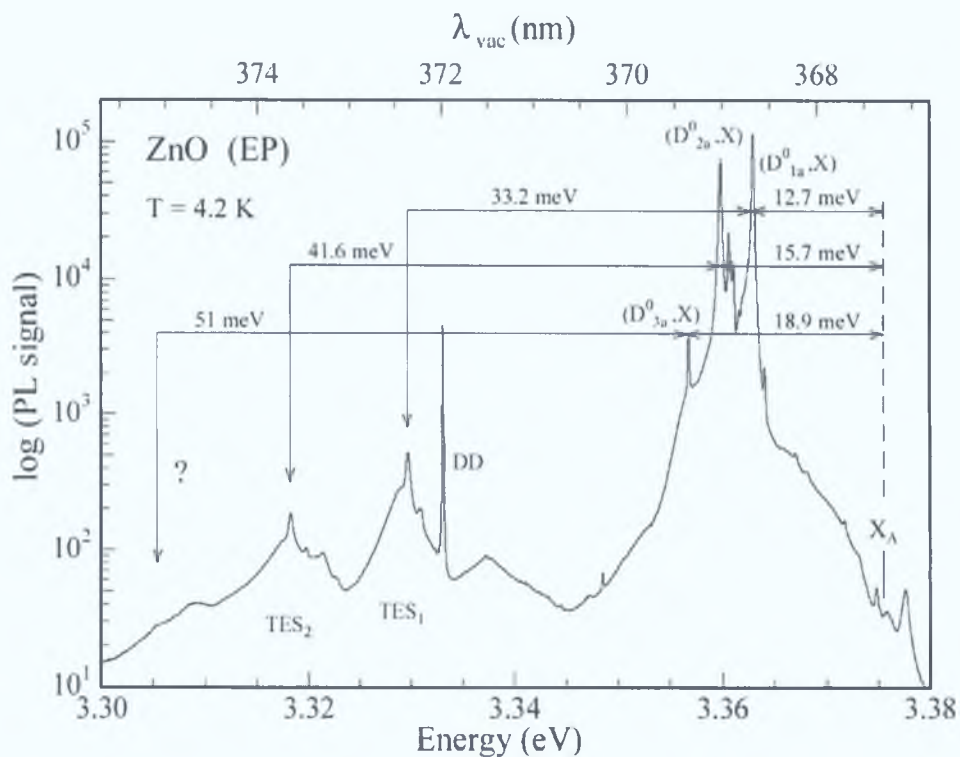


Figure 3.9: Schildknecht et al [15], PL spectra showing the TES relationship with the donor bound excitons.

3.3.2: Phonon replicas

Phonon assisted annihilation of bound excitons results in essentially a replica of the direct annihilation of the bound exciton broadened slightly by the dispersion of the phonons involved [30]. It has been shown that ZnO possesses a strong electron-phonon coupling leading to pronounced longitudinal optical (LO) phonon replicas observed in the PL spectra of bulk ZnO [31].

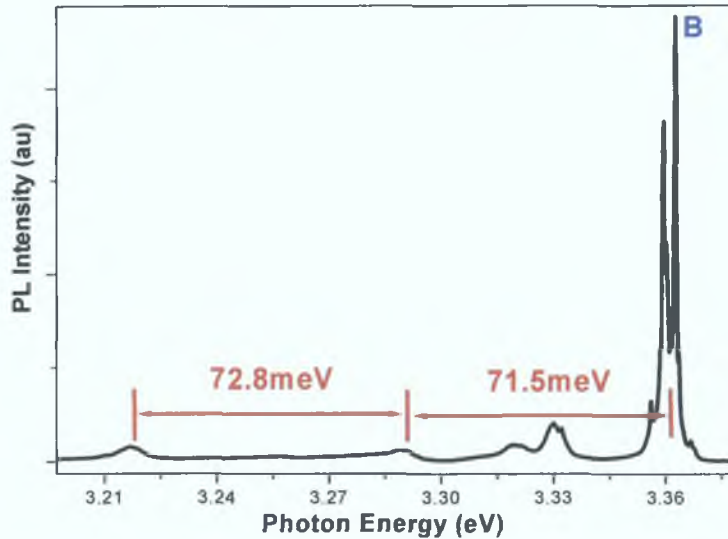


Figure 3.10: The Phonon Replica region separation with the B line highlighted in the PL spectra of bulk ZnO at 25K. Increment 0.01nm, Integration, 3.0s, Slits 10 μ m

In the phonon replica region there are two broad bands at 3.289eV and 3.216eV as seen in figure 3.10. We can assign the broad bands as phonon replicas of the D^0, X . The separation of the first broad band (1LO) with the B line (I_4) is 71.5meV and the separation of the two replicas (1LO-2LO) is 72.8meV. These separation energies are close to the energy of the longitudinal optical phonon reported in ZnO, $E_{LO} = 72$ meV, in fact there are two longitudinal optical modes propagating parallel and perpendicular to the c-axis with energies of 71.46 and 72.95meV respectively [32]. The LO phonon replicas are roughly two orders of magnitude less intense than the BEC lines, similar to the situation in most II-VI semiconductors.

3.3.3: Room temperature measurement

The PL data at low temperatures are undoubtedly the most informative data, in terms of providing details on excitonic structure and for analysis of the bulk material. Many of our subsequent measurements of PL, particularly at high excitation levels, are made at room temperature however. Consequently we discuss briefly the PL data from Eagle Picher bulk ZnO material investigated at room temperature, 300K. Perhaps the most

significant difference in this data is the shift to lower energies (due to band gap narrowing, as discussed earlier) and the expected thermal broadening of the band edge luminescence (which still shows a distinct structure) and the emergence of a strong broad-band emission in the green spectral region at ~ 500 nm (~ 2.53 eV), shown in *figure 3.11*. Study of the evolution of the bands between low temperature and 300K reveals a gradual thermal ionisation of the shallow donor bound exciton feature and the appearance of the free exciton band with a main peak at 3.28eV.

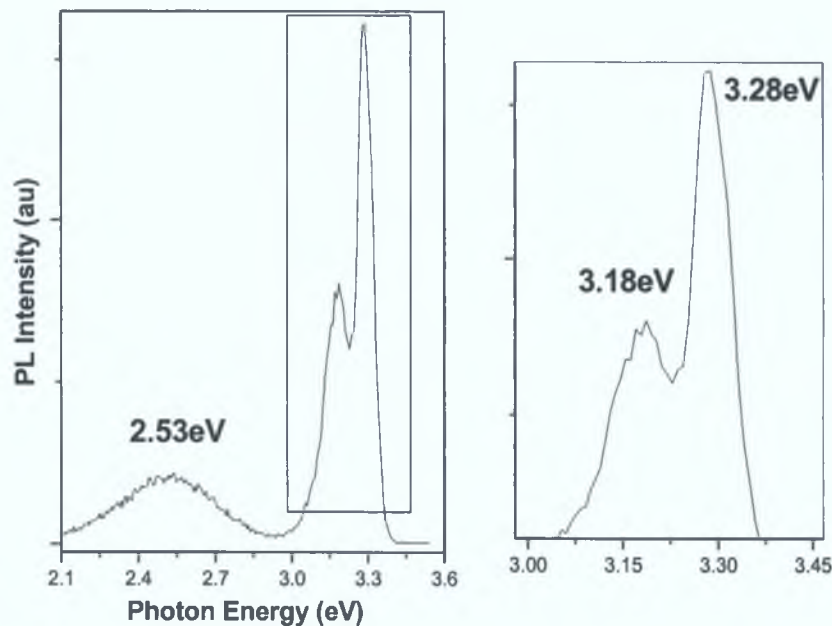


Figure 3.11: Room Temperature PL of the Eagle Picher ZnO material. Inset: Close up of FE area. Increment 1.0nm, integration 1.0s, slits 10 μ m.

The line at 3.18 eV may be due to a donor-acceptor pair transition but actually occurs close to the expected redshifted position (~ 3.2 eV) of the unidentified deep donor bound exciton line seen at low temperature [15], which may survive to room temperature given its large localisation energy. The discrepancy in energy position can be resolved by taking into account the broadness of the band due to the rise in temperature. There is very little reported work on Eagle Picher bulk material at room temperature, and consequently identification of such broad peaks is more difficult at higher temperatures.

3.3.4: Green band

In *figure 3.11* a broad band at ~ 2.53 eV (450-550nm) is seen and is widely known in ZnO and referred to as the “green band”. It generally grows with increasing temperature in most materials studied [33], and it is surrounded by ceaseless controversy over its

microscopic origin. The presence of this band is generally associated with poor quality material (based on the presence of deep levels in the band gap), though in fact it is seen in samples of varied origin, both bulk material and thin film samples, and hence this association with poor material quality is rather suspect. Some of these issues are discussed later in the thesis. Many groups have proposed different models to explain the green band luminescence of ZnO. Early work suggested that the green band was associated with oxygen vacancies in ZnO [34]. Others investigated the idea that the interstitial Zn and oxygen are the centers responsible for green luminescence [35] *Bylander et al*, [36] reported that the green luminescence arises from an electronic transition from an interstitial Zn to a Zn vacancy. Extrinsic defects such as copper (Cu) have also been linked to green luminescence in ZnO also [37]. However, it should also be noted that an additional confusion is introduced by the realisation that there are in fact at least two distinct “green bands”, one with a well defined phonon sideband structure at low temperatures (the band studied by *Dingle* [37]), and the other a broad, featureless band which is stronger at higher temperatures [34]. The structured green band has been identified with Cu, as mentioned above and rather strong evidence supports this assignment, but this assignment is often carried across without question to the unstructured green band. The green band we observe in our samples is the unstructured band and we will confine our attention to this band subsequently.

Certainly the pervasive nature of this unstructured green band in samples from such varied origins tends to indicate that its origin is associated with native defects rather than extrinsic species. Despite the conflicting experimental and (particularly) theoretical evidence, in my opinion the most satisfactory explanation for the origin of this green band is that the defect responsible for the emission is associated with the presence of oxygen vacancies in the material. Experimental work by *Vanheusden et al* [38] in which oxidation and reduction treatments were performed on commercial ZnO powders, allowed them to vary the intensity of the green emission. In this model, the green band is attributed to transitions at a singly charged oxygen vacancy (V_o^+). Using magnetic resonance experiments *Leiter et al* [39] have reported properties of the unstructured green band very similar to those displayed by anion vacancies in a variety of ionic crystals and hence concluded that this band originates from oxygen vacancies, confirming *Vanheusden et al's* [38] assignment. We discuss this issue in a later chapter, where our data on PLD-grown material points to the same conclusions as these workers,

and also demonstrates some of the dangers of using the green band intensity in isolation as a measure of crystal quality.

3.4 Discussion

The investigation of a high purity ZnO material grown by seeded chemical vapour transport has taken place. The low temperature PL spectra are dominated by very sharp bound exciton lines, which are followed by a two electron satellite transition and phonon replicas. The assignment of lines in these regions was undertaken through a comparison with the literature, and excellent agreement was obtained. The confusion in the literature over the naming conventions for band edge features was noted. This single crystal material is now used as a reference point for PLD-grown ZnO samples studied in the following chapters. Comparison of the PL spectra from PLD-grown material with bulk ZnO can indicate the relative quality of the PLD material and allow us to understand the various defects in the poorer quality samples.

References Chapter Three

- [1] B.K.Meyer, H.Alves, D.M.Hofmann, W.Kriegseis, D.Forster, F.Bertram, J.Christen, A.Hoffmann, M.Straburg, M.Dworzak, U.haboeck, A.V.Rodina, *Phys.Stat.Sol. (b)* No 2, (2004), 231.
- [2] D.C.Reynolds, D.C.Look, B.Jogai, C.W.Litton, G.Cantwell, W.C.Harsch, *Phys.Rev.B.60*, (1999), 2340
- [3] B.Gil, *Phys.Rev.B. 64*, (2001),201310-1.
- [4] C.G. Van de Walle, *Physica B*, 308-310, (2001), 899.
- [5] H.-J.Egelhaaf, D.Oelkrug, *J. Cryst. Growth*, 161, (1996), 190.
- [6] D.C Look,C.Coskun,B.Clafin,G.C.Farlow, *Physica B*, 340-342, (2003)
- [7] S. Perkowitz, *Optical Characterisation of Semiconductors: Infrared, Raman and Photoluminescence spectroscopy*, Academic Press Ltd., London UK, (1993).
- [8] R.J. Elliott, *Phys. Rev. Vol.108, No.6*, (1957), 1384.
- [9] R.A. Stradling and P.C. Klipstein, *Growth and characterization of semiconductors*, Adam Hilger, Bristol, UK, (1990).
- [10] Eagle-Picher Technologies,L.L.C.,200 B.J. Tunnell Blvd, Miami, OK 74354,USA, www.epcorp.com
- [11] D.M.Hofmann, A.Hofstaetter, F.Leiter, H.Zhou, F.Henecker, B.K.Meyer, *Phys. Rev. Lett.*, Vol. 88, No. 4, (2002).
- [12] C.F.Klingshirn, *Semiconductor Optics*, Springer, (1997).
- [13] R.E Halsted and M.Aven, *Phys. Rev. Lett.*, 14, (1965), 64.
- [14] E.Tomzig and R. Helbig, *J.Lumin.*, 14, (1976), 403.
- [15] A.Schildknecht, R.Sauer, K.Thonke, *Physica B* 340-342, (2003).
- [16] Y.P. Varshni, *Physica (Utrecht)* 34, (1967), 149.
- [17] H.J. Ko, Y.F.Chen, Z.Zhu, T.Yao, I.Kobayashi, H.Uchikil, *Appl. Phys. Lett.*, Vol76, No. 14, (2000).
- [18] C.Boemare, T.Monteriro, M.J.Soares, J.G.Guilherme, E.Alves, *Physica B* 308-309, (2001), 985.
- [19] C.Van Der Walle, *Phys. Rev. Lett.*, Vol 85, No 5, (2000).
- [20] K.Ip, M.E.Overberg, Y.W.Heo, D.P.Norton, S.J.Pearnton, C.E.Stutz, S.O.Kucheyev, C.Jagadish, J.S.Williams, B.Luo, F.Ren, D.C Look, J.M.Zavada, *Solid State Elect.*, 47, (2003), 2255.
- [21] M.Schilling, R.Helbig, G.Pensl, *J. Lumin.*, 33, (1985), 201.
- [22] F.Reuss, C.Kirchner, Th.Gruber, R.King, S.Maschek, W.Limmer, A.Waag, P.Ziermann, *J.Appl.Phys.*, Vol 97, No 7, (2004), 3385.

- [23] H.J.Ko, Y.F.Chen, S.K.Hong, H.Wenisch, T.Yao, D.C.Look, *Appl.Phys.Lett.*, Vol 77, No 23, (2000), 3761.
- [24] H.Kato, M.Sano, K.Miyamoto, T.Yao, *J.Cryst.Growth*, 237-239, (2002), 538.
- [25] K. Johnston, M. O. Henry, D. McCabe, E. McGlynn, M.Dietrich, ISOLDE collaboration, M.Xia, Submitted *Phys. Rev.B*, (2005).
- [26] D.C Reynolds, C.W. Litton, T.C. Collins, *Phys. Rev.*, Vol 140, No5A, (1965).
- [27] D.C.Look, B.Claflin, *Phys.Stat.Sol.*, (b) 241, No.3, (2004), 624.
- [28] D.C.look, D.C.Reynolds, C.W.Litton,R.L.Jones, D.B.Eason, G.Cantwell, *Appl. Phys. Lett.*, Vol.81,No.10 (2002), 1830.
- [29] J.Gutowski, N.Presser, I.Brosler, *Phys. Rev. B*, Vol.38, No. 14, (1998).
- [30] R.L Weiherr, W.C.Tait, *Phys.Rev.*, 166, (1968), 791.
- [31] D.C.Reynolds, D.C.Look, B.Jogai, H.Morkos, *Solid State Commun.*,101, (1997), 643.
- [32] D.C.Reynolds, T.C.Collins, *Excitons, their properties and uses*, Academic Press, (1981).
- [33] E.McGlynn, J.Fryar, G.Tobin, C.Roy, M.O.Henry, J-P.Mosnier, E.de Posada, J.G.Lunney, *Thin Sold Films*, 458, (2004), 330.
- [34] P.H.Kasai, *Phys.Rev.* 130, (1963), 989.
- [35] M.Liu, A.H.Kitai, P.Mascher, *J.Lumin.*, 54, (1992), 35.
- [36] E.G.Bylander, *J.Appl.Phys.*, 49, (1978), 1188.
- [37] R.Dingle, *Phys.Rev.Lett.*, 23, (1969), 579.
- [38] K.Vanheusden, W.L.Warren, C.H.Seager, D.R.Tallant, J.A.Voigt, B.E.Gnade, *J. Appl. Phys.*, 79, (1996), 7983.
- [39] F.Leiter, H.Zhou, F.Henecker, A.Hofstaetter, D.M.Hofmann, B.K.Meyer, *Physica B*, 308-120, (2001), 908.

Chapter Four

Photoluminescence of PLD material

The following chapter discusses the photoluminescence (PL) results obtained from the samples grown using the PLD growth technique. Section 4.1 outlines briefly some aspects of the nature of the defects observed in the PLD-grown materials studied in this work. In section 4.2 the physical characteristics of the PLD materials, determined by a variety of experimental techniques, are outlined. The PLD samples were investigated at both low and room temperatures by the PL technique to establish the quality of the samples grown and the data obtained is discussed in sections 4.3 and 4.4. In section 4.5 reflectance measurements are presented for the PLD ZnO samples, which allow more detailed interpretations of the optical properties of the material.

4.1: Defects

Chapter three has outlined the main aspects of the PL technique and the information it can give about e.g. bulk ZnO, in terms of the presence of various donor species, phonon replicas and other aspects of the PL spectrum. While bulk material provides an excellent testbed for the PL technique enabling a variety of materials parameters to be extracted, the study of nanocrystalline thin film materials (such as those grown by PLD) requires us to understand aspects of the film morphology in order to be able to interpret and utilise the PL and other optical spectroscopic data correctly. Perhaps one of the most pertinent type of defects in nanocrystalline material which is not seen in bulk single crystals are extended defects of the dislocation and grain boundary type between different grains. The presence of these extended defects is intimately related to the effects of the substantial lattice mismatch between the substrate and the ZnO thin films, which exists for most common substrates (e.g. sapphire, Si, glass etc.). As the films grow dislocations are formed which relieve the strain energy in the film. Grain boundaries are also formed by the coalescence of individual islands during growth. The substrate used for the samples studied here was *c*-plane sapphire, which has a lattice mismatch with ZnO of $\sim 14\%$, much greater than that used in epitaxy of typical III-V compounds and which does lead to a substantial concentration of extended defects in the thin film.

4.2: PLD material – sample preparation

The PL spectra discussed in this chapter are recorded from ZnO samples grown by the Department of Pure & Applied Physics, Trinity College Dublin [1]. The thin film samples were grown by the pulsed laser deposition (PLD) technique referred to in chapter one. A ceramic polycrystalline ZnO target (99.99%) and a KrF excimer laser

($\lambda=248\text{nm}$) with a laser energy density of $1.7\text{J}/\text{cm}^2$ at a pulsed repetition rate of 10Hz and pulse width of 26ns were used for the ablation process. The target to substrate distance was $\sim 4\text{cm}$. The ZnO films were deposited on (0001) sapphire substrate at an oxygen (99.99%) pressure of 0.3mbar and the substrate temperature was maintained at 400°C during growth. Typically the films were $150\text{-}200\text{ nm}$ thick, giving a deposition rate of $0.025\text{nm}/\text{pulse}$. Some of the samples were further annealed in O_2 (0.3mbar) at temperatures of 400°C and 500°C , in the growth chamber immediately after deposition. Annealing is a process where heating a crystal to a certain temperature takes place to rid the crystal of any lattice damage that originates from the growth process. The anneal times are not equal in duration, therefore the individual effect that the anneal temperature or time has on the samples, cannot be separated. However as shown in *table 4.1*, sample (iii) has a larger annealing effect i.e. longer time, higher temperature than sample (ii). The effect of the annealing on the average grain size (nm) of these samples was investigated using XRD [1].

The main part of the PL spectra discussion will be based upon three ZnO samples prepared as shown in *table 4.1*. We used a single ZnO crystal from the Eagle Picher Corporation [2] as a reference material as discussed in the previous chapter.

Sample	Annealing temp ($^\circ\text{C}$)	Annealing time (min)	Average Grain Size (nm)
(i)	No anneal	0	32
(ii)	400°C	10	67
(iii)	500°C	15	79

Table 4.1: Annealing conditions for three ZnO samples and the effect on the average grain size (nm) as measured by XRD.

4.2.1: Background characteristics

Colleagues in Trinity/DCU undertook some of the following work to characterise the samples and a number of the results are presented here to give background characteristics to the samples used in this project [1]. The crystal structure and quality of the samples were investigated by X-ray diffraction (XRD) in the θ - 2θ mode (Siemens D500 using Cu K_α radiation).

Figure 4.1 shows the θ - 2θ XRD measurements of the ZnO samples described in *table 4.1*. The spectra are dominated by the (0002) and a weak (0004) ZnO peaks along with the prominent (0006) sapphire peak. The sapphire peak is not seen for sample (i),

possibly due to increased surface scattering due to surface roughness (measured by atomic force microscope, see below) in this case. The dominance of the (0002) and (0004) peak indicate that ZnO thin films are highly textured along the (0001) growth direction. [3]. The lattice parameters of the ZnO thin films can be calculated from the diffraction angle corresponding to the $(10\bar{1}0)$ and (0002) planes. The intensity of the $(10\bar{1}0)$ peak is less intense than the (0002) peak intensity due to the high degree of c-axis orientation, the growth direction. The average values of c- and a-axis lattice constants of the PLD-grown ZnO samples are 0.518nm and 0.330nm, respectively, and the values of all the samples were the same within experimental error (± 0.001 nm). The average grain size (parallel to the (0002) direction) of the ZnO films can be estimated from the full width half maximum (FWHM) of the (0002) peak using Scherrer's relation [4].

$$t = \frac{\lambda}{B \cos \theta_B} \quad (4.1)$$

where λ is wavelength, B is the angular width .

The range of annealing temperatures used has been reported to lead to major grain growth. [5]. The higher annealed samples show a decrease of (0002) peak FWHM and consequent increase in grain size with increasing annealing temperature as shown in table 4.1.

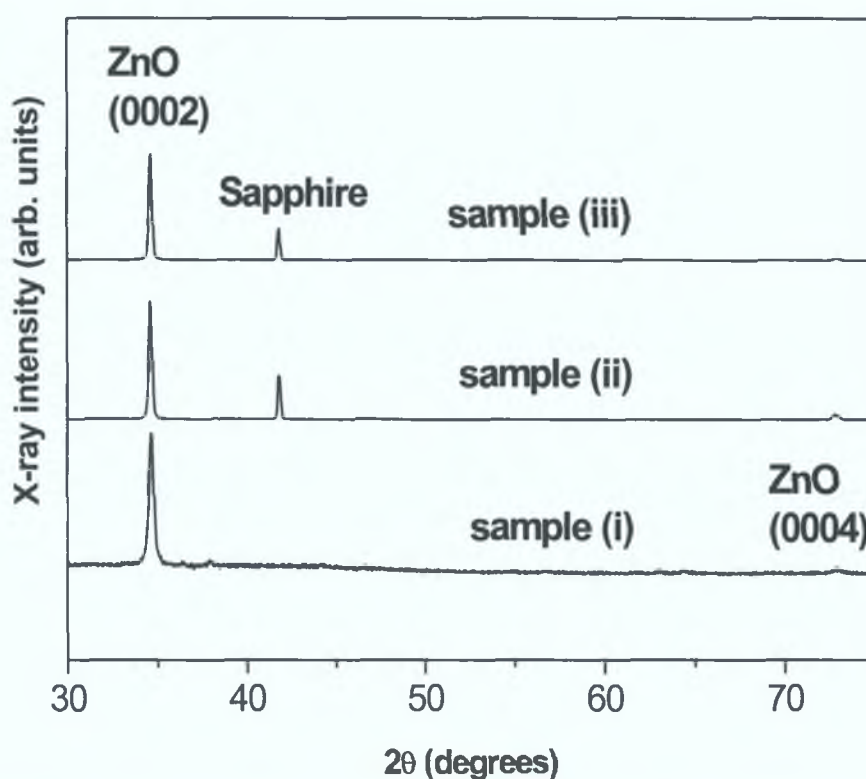


Figure 4.1: XRD of the three samples grown by PLD technique. The data are dominated by the (0002) ZnO peak. Sample (i) not annealed, sample (ii) annealed at 400°C for 10 mins and sample (iii) annealed at 500°C for 15 mins.

Figure 4.2 shows the phi scan of sample (iii) for the ZnO(10 $\bar{1}$ 1) plane and the sapphire (10 $\bar{1}$ 4) planes. The presence of peaks in the ZnO phi scans separated by 60° confirms the in-plane epitaxial ordering for all these samples and the angular displacement (30°) of the ZnO and the sapphire peaks confirms the epitaxial relationship between ZnO and sapphire as (0001)_{ZnO} // (0001)_{Sapphire} perpendicular to the substrate and [10 $\bar{1}$ 0]_{ZnO} // [11 $\bar{2}$ 0]_{Sapphire} in the plane of the substrate [6]. Similar phi scans were obtained for the other PLD samples, with the same epitaxial relationship in evidence (not shown). There was evidence of an additional epitaxial orientation in the sample annealed at 400°C, however the relative magnitude of this second orientation was rather small compared to the dominant orientation.

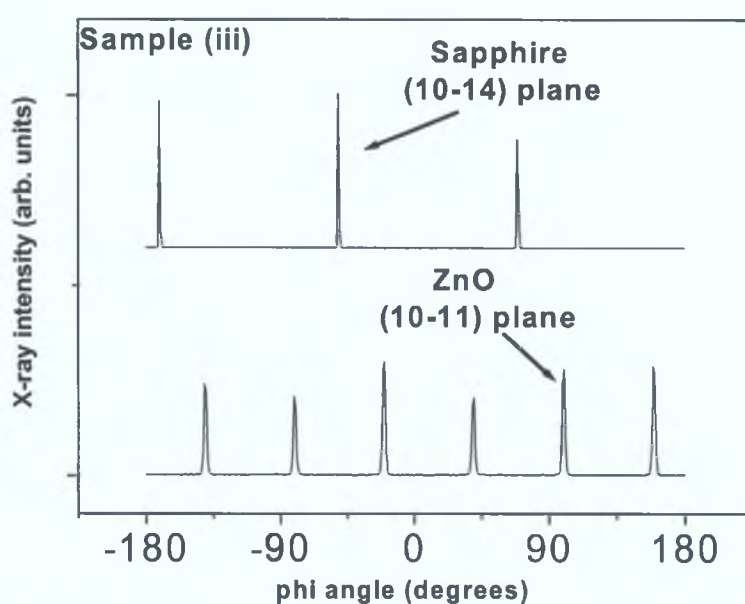


Figure 4.2: XRD phi scan of sample (iii) annealed at 500°C for 15 mins, for the ZnO(10 $\bar{1}$ 1) plane and the sapphire (10 $\bar{1}$ 4) plane.

Atomic Force Microscopy (AFM) (Nanoscope IIIA) [1], measurements of lateral grain size confirm the results obtained from the XRD. The lateral grain sizes are 135 ± 40 nm for the sample annealed at 400°C and 180 ± 50 nm for the sample annealed at 500°C. They also clearly show the increase in grain size with annealing conditions. The surface roughness, taken as a standard deviation of the AFM tip height across a $2\mu\text{m}$ profile was also seen to change with increasing grain size from a value of >10 nm sample (i) down to ~ 3 nm for the samples annealed at 500°C [7]. Thus the samples can be described as epitaxially ordered nanocrystalline material. Raman measurements also show that these samples are oriented with the c-axis perpendicular to the substrate and that there is a

continuous increase in the epitaxially ordered nanocrystallites grain size with increased annealing temperatures [1]. Raman data also show the presence of substantial electric field effects, which cause an enhancement of Raman scattering intensities [1,7]. These electric field effects are associated with charge trapping at grain boundaries, leading to the formation of strong electric fields in depletion regions. The annealing process clearly produces a recovery of the crystal structure and increase of the grain size, and corresponding diminution of these electric field effects. We note that in our experimental conditions, the increase in grain sizes is achieved after annealing for relatively short times; this effect was also observed in the case of magnetron sputtered ZnO [8].

4.2.2: Hall measurements on PLD-grown samples

Thonkes *et al* [9] investigated Eagle-Picher material with Hall measurements with typical carrier concentrations at room temperature of the order of $(1-2) \times 10^{17} \text{ cm}^{-3}$. Such carrier concentrations are typical of nominally undoped single crystal ZnO material. We have performed Hall effect measurements on the PLD-grown material using an Accent™ (HL5500PC) standard Hall measurement system. The contacts were scribed onto the sample surface using an Indium/Gallium paste mixture, which proves to be an effective Ohmic contact to bulk ZnO for periods of a few hours. From the results (*appendix E*) there is an average increase in the sheet resistivity with the annealed samples. For comparative purposes, Jin *et al* [10] took Hall measurements of PLD-grown ZnO samples. Their material was grown at progressively higher oxygen pressures and substrate temperatures. It was noted the resistivity of the films increases with the increasing substrate temperature and oxygen pressure [10], in broad agreement with our data, and with the plausible supposition that the defect density (and hence background concentration) reduce with increased annealing. The sheet concentration of the PLD samples presented in this work is in the $(1-2) \times 10^{14} \text{ cm}^{-3}$ regime (Jin *et al* sheet concentration was 10^{17} cm^{-3} , for a substrate temperature of 400°C and an oxygen pressure of 200mTorr, the values were tending towards the results in this work when the PLD parameters were nearly on a par to the work in this thesis). However, a number of glaring anomalies cast some doubt over our Hall data. The Hall voltage of sample (iii) gave a positive value; and the values saturated as the current input was changed. A positive value would indicate that the sample has P-type conductivity, which almost certainly is not the case. It was also noted in the experiment that the Hall voltage value flipped from positive to negative with no consistency for sample (iii). In the other

samples the Hall voltages were always of a negative value. The list of results for the Hall experiment on the PLD samples are seen in *appendix E*.

These Hall results give convincing proof of a fact that is becoming well known in the ZnO community, i.e. that Hall measurements of ZnO poly- or nanocrystalline material can be notoriously inconsistent. The main problem centres on creating a dependable contact on the poly/nanocrystalline ZnO material, compared to bulk contacts [11]. A number of physical effects come into play in the case of such thin film materials, which are largely absent for bulk material. These include the adsorption of oxygen at grain boundaries [12] and the persistent photoconductivity associated with this effect, which means that samples are highly sensitive to the ambient light levels in which they are prepared. Another important effect is electrical conduction along grain boundaries, which may dominate the Hall signals obtained, and may far outweigh the contribution of carriers in the body of the film. The conduction processes in the body of the film may also be dominated by the electrical barriers at the grain boundaries. The combination of all these effects renders Hall measurements of thin film material notoriously difficult. This is increasingly being realised within the community. A number of reports of unfeasibly large P-type concentrations are extant in the literature [13], in addition to very many examples of unrepeated or unrepeatable demonstrations of P-type conductivity and variations in results over a period of days or weeks; all such anomalies may be due to the highly sensitive nature of the contacting process to such films. The evidence from our data shows the difficulties in making reliable Hall measurements on such systems. We have not attempted to address the various causes of unreliability outlined above, and we concentrate henceforth on studying the optical properties of the thin film material.

4.3: Photoluminescence of PLD samples

Detailed, low temperature PL studies of the band edge emission from epitaxially-ordered nanocrystalline materials have not attracted as much scientific attention as those on bulk material because the band edge photoluminescence spectra lack structure compared to the bulk crystal, due to the effects of substantial line-broadening in the poorer quality material. Despite this, the PL spectrum merits attention because it can provide valuable information on the quality and purity of the materials grown. The other difficulties in analysis arises from the fact that luminescence from epitaxially ordered

nanocrystalline materials can be very weak compared to the bulk crystal, so equipment has to be more sensitive, with low noise levels.

In *figure 4.3*, the PL results from the three PLD-grown ZnO samples measured at both room temperature (300K) and low temperature (20K) are presented. The data shown in *figure 4.3** have been normalised for ease of comparison. These spectra show that all the samples have strong band edge, UV emission and varying amounts of green band emission. Similar results for ZnO grown by the PLD technique have been reported in the literature [10], for samples with varying grain sizes.

*

- Sample (i) at 300K \times 130 and at 20K \times 5
- Sample (ii) at 300K \times 58 and at 20K \times 0.4
- Sample (iii) at 300K \times 23 and at 20K \times 1

Multipliers allow comparison of the three sample intensities at the same temperature but can't be used to compare 300K data to 20K data for any sample(s).

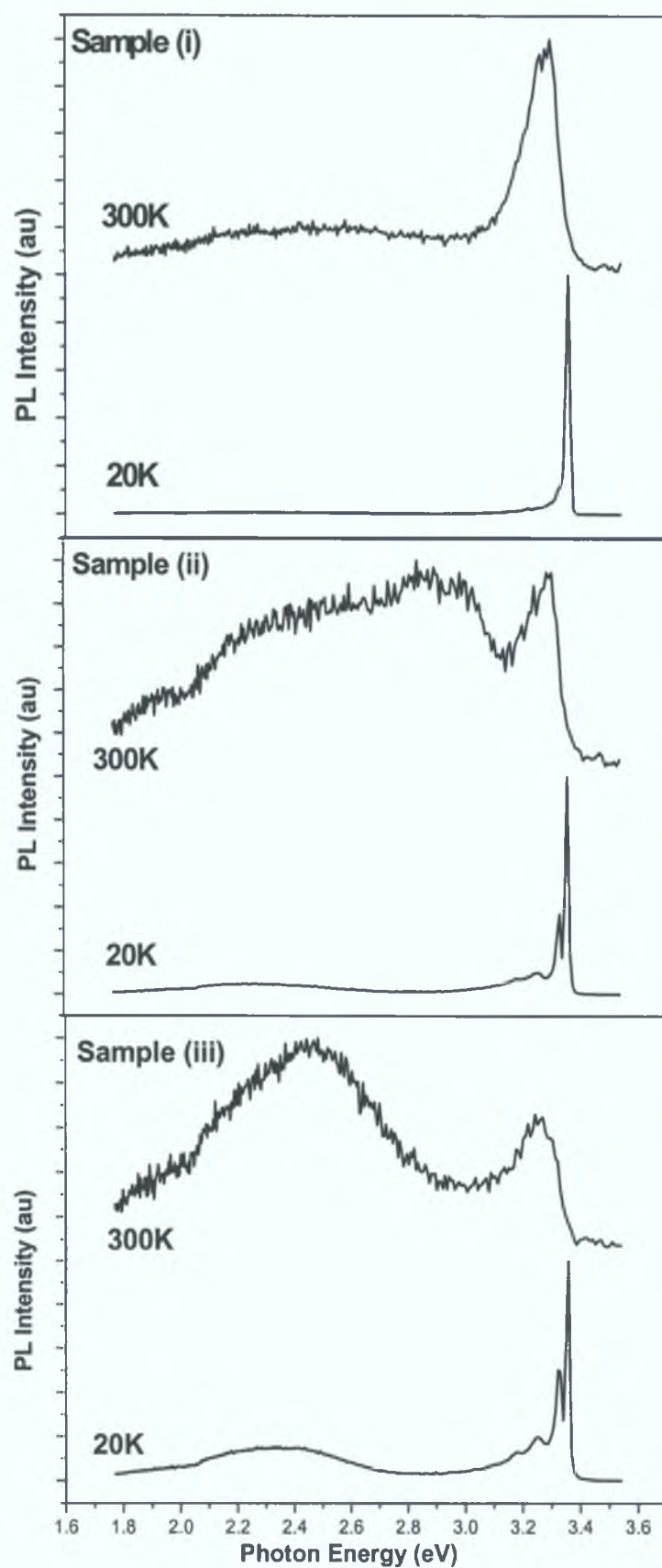


Figure 4.3: PL data for the three PLD-grown ZnO samples recorded at 20K and 300K where sample (i) is unannealed, sample (ii) annealed at 400°C for 10 mins and sample (iii) annealed at 500°C for 15 mins. Increment 1.0nm, Integration 1.0s, slits 100 μ m.

Perhaps the most significant difference in the data at 300K and 20K is the shift to lower energies (due to band gap narrowing, as discussed in chapter three) and the expected thermal broadening of the band edge luminescence (which still shows a distinct structure) and the emergence of a strong broad-band emission in the green spectral region at ~ 500 nm (~ 2.3 eV), shown in *figure 4.3*. The band edge (BE) luminescence centered on ~ 3.360 eV in the PLD samples are substantially broader at room temperature than at 20K. At 20K the FWHM of the BE feature in the PLD material is ~ 15 meV on average for the PLD samples (*table 4.2*). This value can be compared to a ZnO bulk crystal which has a BE value of ~ 1 meV at the same temperature and individual lines can be resolved in the BE region for the bulk crystal compared to the PLD material. The results are summarised in *table 4.2*.

Sample	Conditions	Peak shift (20-300K)	FWHM 20K	FWHM 300K
(i)	No Anneal	62.5meV	15meV	140meV
(ii)	400°C 10 mins	53.7meV	13meV	162meV
(iii)	500°C 15 mins	89meV	16meV	186meV

Table 4.2: Comparison of low temperature and room temperature results for the PL spectra of the PLD-grown samples.

The PL data for the three samples at room temperature are very similar with the green band becoming more prominent in the samples annealed in the oxygen atmosphere. It has been mentioned that absolute PL intensities cannot be reliably used for quantitative comparisons as variations may occur in the alignment of samples and other factors. However on average, the overall luminescence intensity for sample (i) unannealed, is lower than for the two annealed samples. This is more evident at low temperatures. At low temperatures the two annealed samples are very similar with a relative increase in the green band intensity compared to the band edge emission for the annealed samples. There is also some clear structured luminescence in lower energies below the BE emission in the two annealed samples, which is not strongly present in the unannealed samples. One must be always careful in making sample to sample comparison of PL intensities due to the variations that may occur in alignment etc., however as said above there is a definite increase in the annealed sample intensities compared to the unannealed sample. With increased annealing, there is a substantial and consistent

growth in the overall contribution of band edge luminescence and phonon replicas to the PL spectra, compared to unannealed samples. This increase in the band edge luminescence may be expected due to the reduction of the surface to volume ratio of the nanocrystals and the consequent reduction in the point and extended defect density as the grain size increases [1, 14]. In addition, the effects of electric fields due to charge trapping at grain boundaries will reduce as the grain size increases. All these effects will tend to increase the radiative efficiency of the annealed samples compared to the unannealed sample, in agreement with our data.

4.3.1: Low temperature PL spectra

In *figure 4.4*, the PL spectra of the PLD material at 20K is shown and is acquired at a higher resolution than the spectra presented in *figure 4.3*. For the unannealed sample, the higher energy peak (3.363eV) on the shoulder of the main PL peak (3.356eV) is likely to be due to a “surface” exciton, which is expected for samples with small grain size and consequently large “surface-like” character of the material [14,15]. There is a weak band at 3.327eV, which may be another defect-related band or a phonon replica of the B exciton. However in comparison to the annealed samples this band is very weak and not prominent. The main band at 3.356eV is assigned to a defect (most probably donor) bound excitons.

For the two annealed samples we see a substantial change in the band edge PL. We note the appearance of two broad lines below the main PL line at energies of 3.330 and 3.256 eV with a separation of ~ 74 meV for sample (ii) which corresponds closely to the Longitudinal Optical mode (LO) phonon energy of 72meV [16]. These two broad bands in sample (iii) are at 3.328eV and 3.253 eV, with a separation of ~ 75 meV. We attribute these PL features either to donor-acceptor pair (DAP) and DAP-LO emission, to excitons bound to structural defects, or to the LO phonon replicas of the B exciton. While the DAP assignment of lines in the 3.33eV region is common in the literature (and such lines show strong LO phonon replicas), we note that the assignment to LO replicas of the B exciton is supported by the presence of the B exciton at 3.391eV in reflectance studies (will be discussed in section 4.5) and also by an increase in the ratio of LO to 2-LO emission intensities with increasing temperature in these samples as expected for the ratio between the first and second phonon replicas of a free exciton complex [17]. The assignment of transitions due to excitons bound to structural defects

is also sensible considering the highly defective crystal structure [18]. We discuss this point further in later chapters.

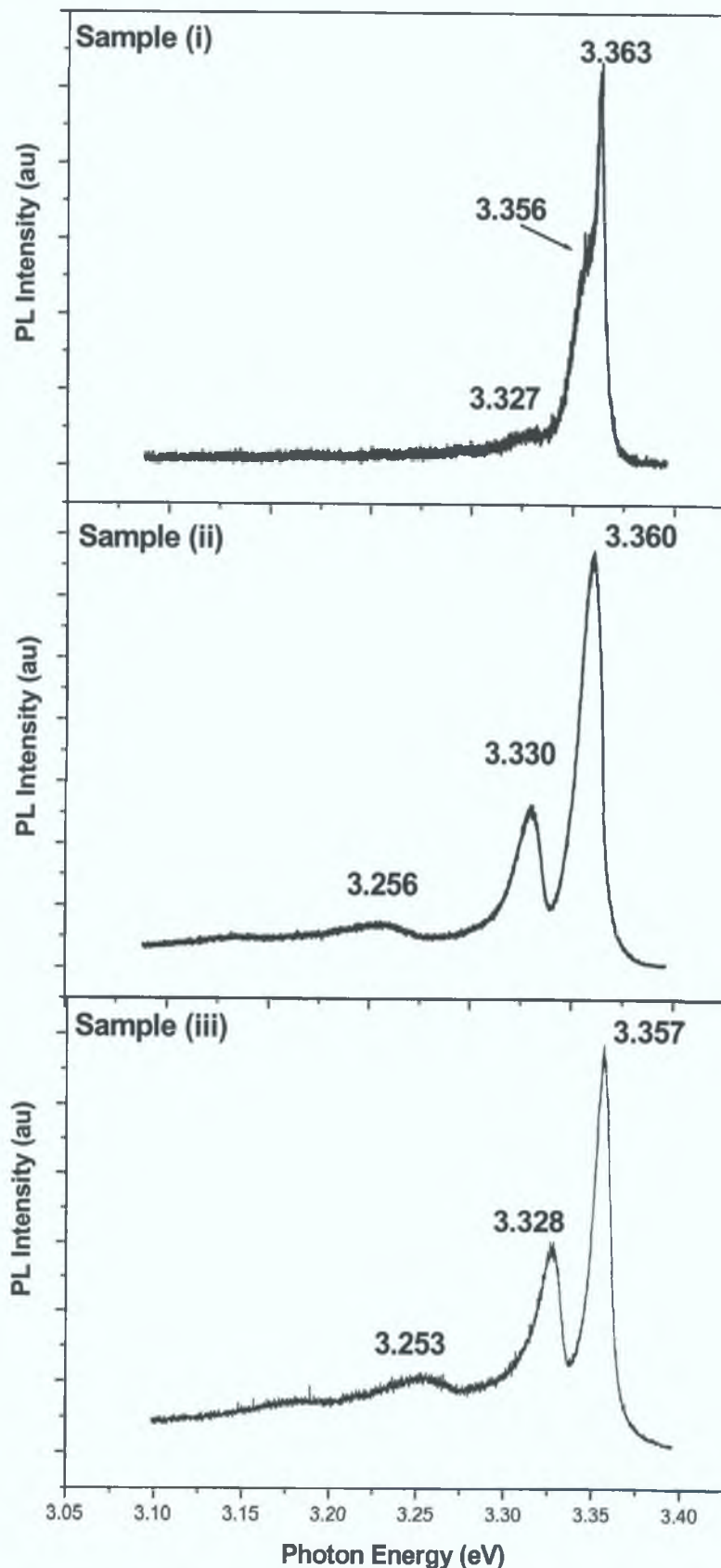


Figure 4.4: Low Temperature (20K) high-resolution PL spectra of the PLD ZnO samples. Increment 0.01nm, Integration 1.0s, slits 50 μ m.

A recent work by *Look et al* [13] has also described similar PL features, by assigning these features to an acceptor bound exciton.

4.3.2: Temperature dependence of PL emission from PLD samples

The temperature dependence of the PL features was investigated for the PLD-grown ZnO samples. The variation of PL intensity, spectral position and FWHM as a function of temperature can provide important information about the material quality and luminescence processes. In *figure 4.5* we show a comparison of the PL spectra at temperatures 15K, 20K, 25K, 30K, 55K, 77K, 100K for the unannealed sample (i).

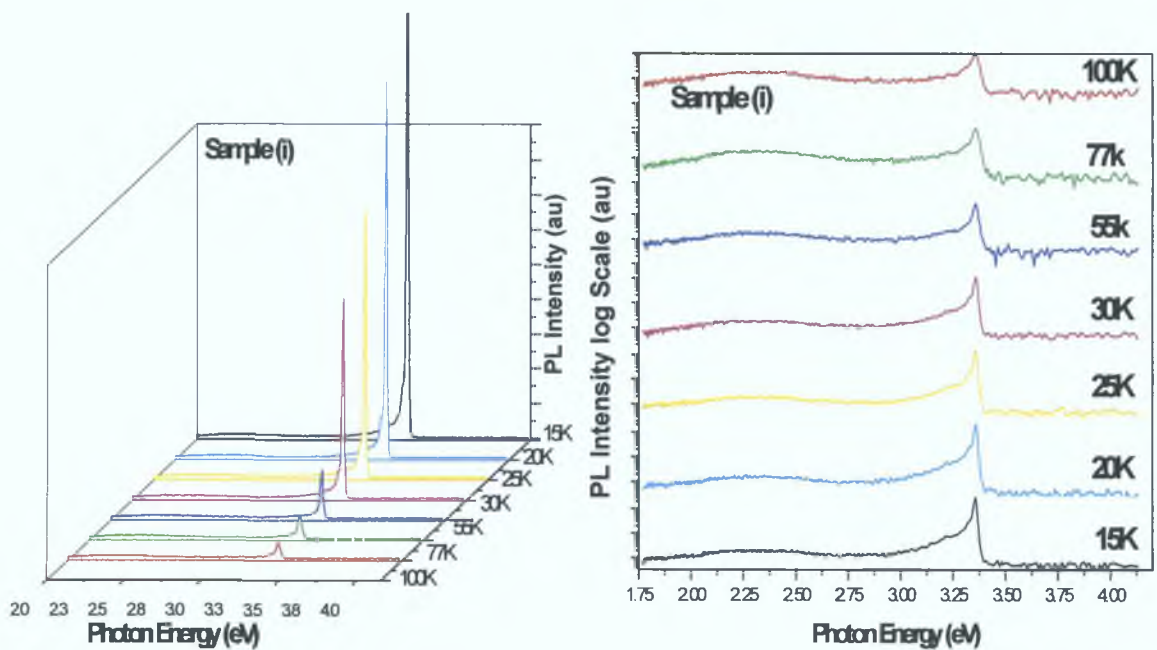


Figure 4.5: Temperature dependence sample (i), PLD-grown ZnO. Increment 1.0nm Integration 1.0s, Slits 50 μ m. The data is shown on a linear scale on the left hand side and on a log scale on the right.

Figures 4.6 and 4.7 show similar data for the samples annealed at 400°C and 500°C, respectively at temperatures of 15K, 20K, 25K, 30K, 55K, 77K, 100K and 150K.

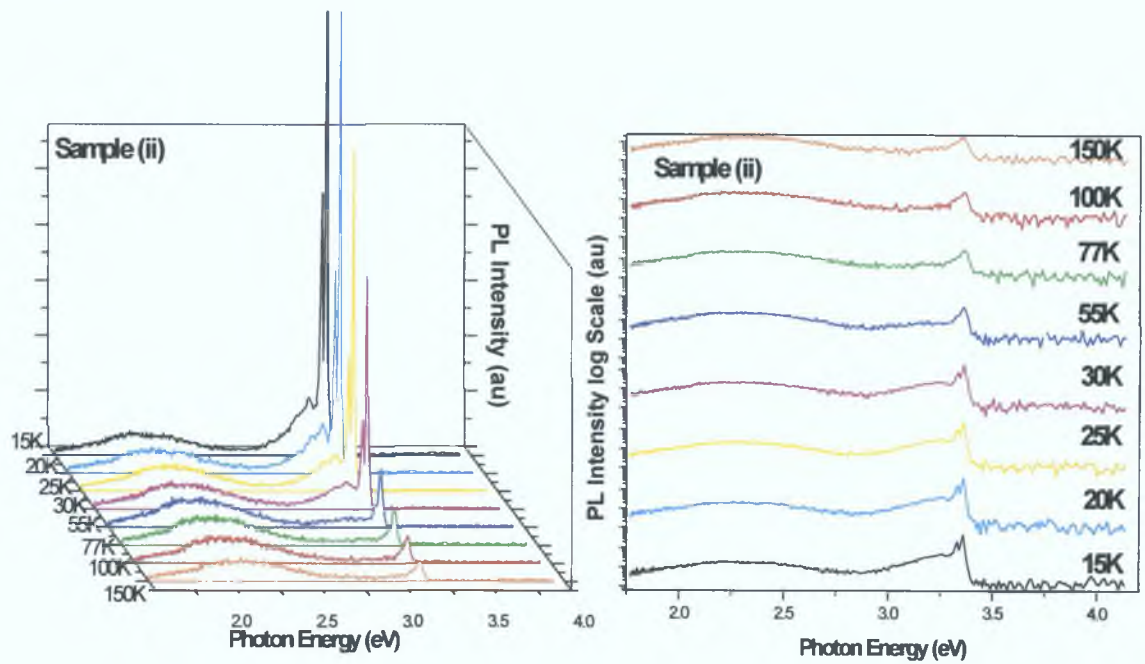


Figure 4.6: Temperature dependence sample (ii), PLD-grown ZnO. Increment 1.0nm Integration 1.0s, Slits 50 μ m. The data is shown on a linear scale on the left hand side and on a log scale on the right.

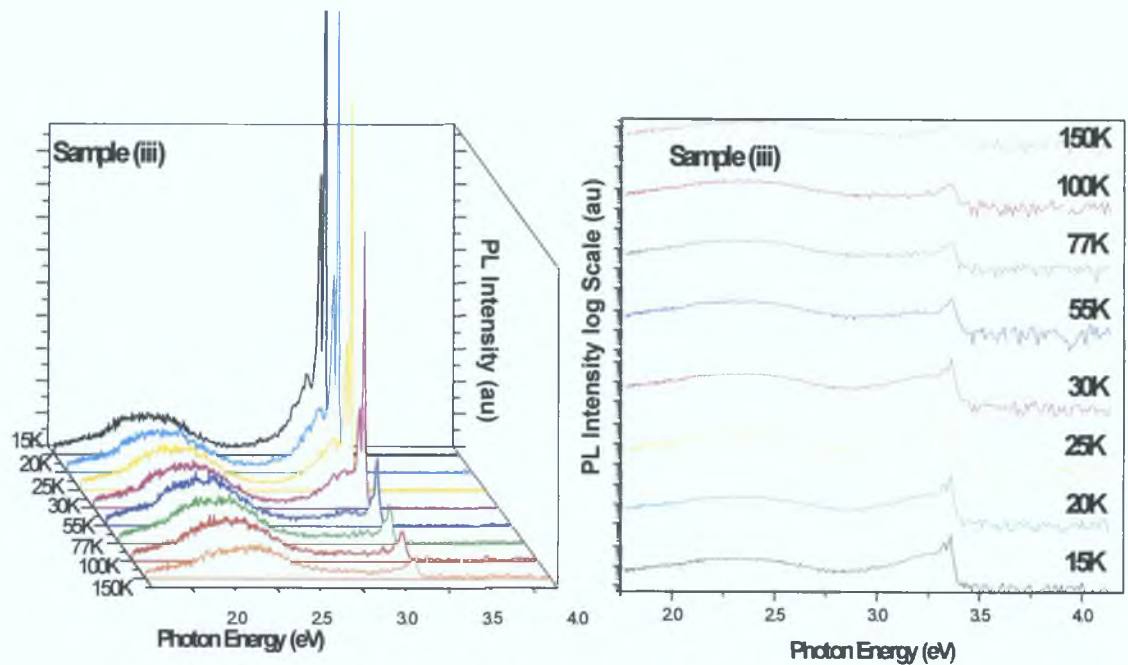


Figure 4.7: Temperature dependence sample (iii), PLD-grown ZnO. Increment 1.0nm Integration 1.0s, Slits 50 μ m. The data is shown on a linear scale on the left hand side and on a log scale on the right.

We note that the band edge region is dominant in all the samples at low temperatures and gradually decreases as the temperature increases. In very high quality, bulk ZnO, as

the temperature increases, the PL emission from the donor bound excitons gradually decays, as the bound excitons are thermally ionized to the free exciton band, and the free exciton emission grows. This is shown in *figure 4.8* (Eagle-Picher material, data courtesy of Mr. Alan Meaney).

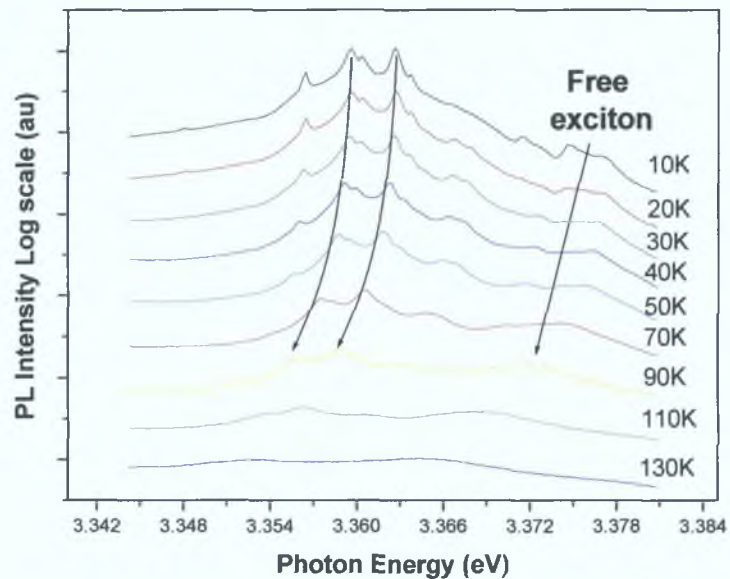


Figure 4.8: Temperature dependence of bulk Eagle-Picher material, showing growth of FE features due to thermal ionisation of bound excitons.

We do not see this free exciton growth distinctly in any of our samples, however the rather broad linewidths may preclude direct observation of the growth of a separate FE band. When we plot the PL FWHM of the band edge region as a function of temperature (shown in *figure 4.9*) we observe that the unannealed sample (i) has the broadest linewidth at low temperatures, as one would expect given the inferior material quality, presence of strong electric fields etc. However, as the temperature increases we see that above temperatures of $\sim 60\text{K}$ (equivalent to an energy of $\sim 8\text{ meV}$, via the relationship $3/2k_{\text{B}}T = \text{eV}$), corresponding closely to the temperature at which FE PL begins to dominate in the bulk sample, samples (ii) and (iii) now show broader linewidths, with a stronger temperature dependence than sample (i). At a temperature of 60K , the thermal energy of $\sim 8\text{ meV}$ becomes a significant fraction of the localization energy of the bound exciton ($\sim 15\text{ meV}$, using the position of the PL peak and the free exciton energy in section 4.5 below) and significant exciton delocalization is expected to begin.

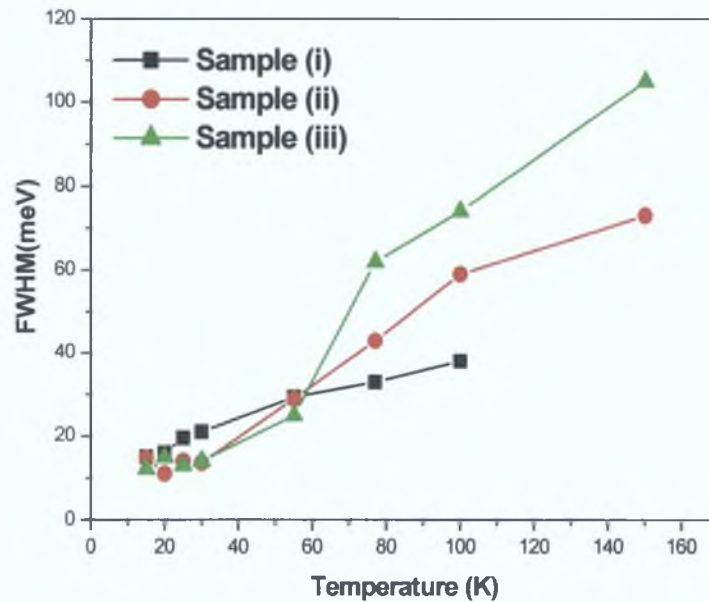


Figure 4.9: Temperature dependence of band edge FWHM for PL-grown samples (i), (ii) and (iii).

The explanation for this behaviour may originate in the varying grain size and grain boundary electric fields in the three samples. With increasing temperature, as the bound excitons delocalize from their binding donors, they may diffuse through the grain. In the unannealed sample with smaller grains there is a large surface to volume ratio and a larger percentage of the grain volume perturbed by the depletion regions at the grain boundaries. The free excitons will be strongly quenched by these surface effects, akin to a surface recombination velocity effect for charge carriers [19]. Consequently the FE emission is largely quenched in the unannealed sample and does not contribute as strongly to the emission and consequently the FWHM with increasing temperature. In the annealed samples, where such surface quenching effects are reduced due to the larger grain size we observe a larger contribution from the free exciton emission, and, although not resolved in the spectrum, it is evident in the FWHM data. We note that reflection data presented later show that the free exciton resonance in the unannealed sample is significantly weaker than in either of the two annealed samples, in agreement with our PL data. This interpretation also supports the identification of the PL peaks at 3.330 and 3.256eV with LO phonon replicas of the free exciton.

Figure 4.10 shows a plot of integrated intensity in the band edge region as a function of temperature for all the samples.

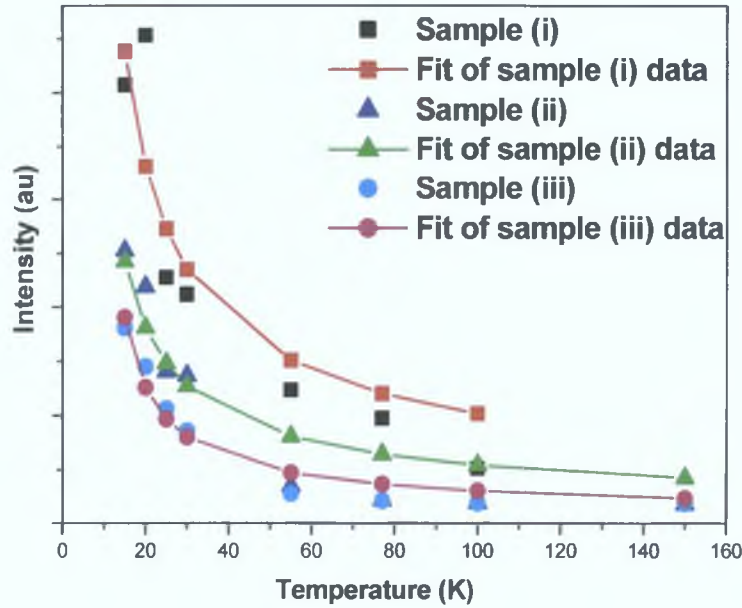


Figure 4.10: Plot of integrated intensity in the band edge region as a function of temperature for all the PLD-grown samples.

None of these intensity versus temperature graphs are well fitted by the conventional Boltzmann equation describing thermal carrier/exciton release into a band:

$$I = \frac{I_0}{1 - GT^{\frac{3}{2}} \exp\left(-\frac{\Delta E}{kT}\right)} \quad (4.2)$$

In this equation, G represents the effective band density of states and ΔE represents the localization of the bound exciton relative to the free exciton. In all cases attempts to fit the data to this equation have yielded unphysical values for the fit parameters, and in particular for the ionization energy ΔE where we get values far below the bound exciton localization energies. Thus the intensity is being quenched much more quickly as a function of temperature for all samples than one would expect based on the spectroscopic localization energies and provides further indication of a surface-related quenching mechanism influencing the PL data [14]. Due to the unphysical nature of the parameters found from the fitting routine it is difficult to judge the degree to which each sample's emission is affected, and to compare the unannealed with the annealed samples.

In *figure 4.11* we show the variation of the peak energy position as a function of temperature for the three samples, and fits of each data set to a Varshni equation.

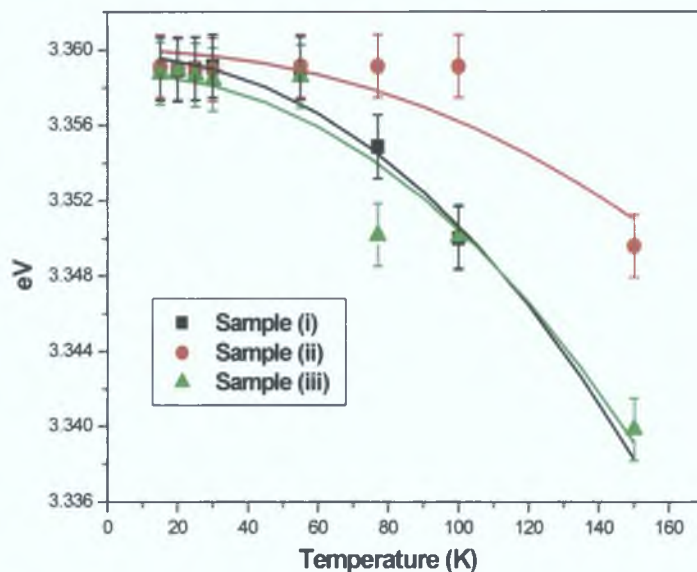


Figure 4.11: The variation of the peak energy as a function of temperature for the PLD-grown samples.

The Varshni parameters are shown in *table 4.3* below, and compared with the values given in reference [20]. The data are reasonably well described by the Varshni equation in all cases and the Varshni parameters obtained for our samples compare well with those found in [20]. Sample (ii) shows a slightly anomalous behaviour, with a weaker temperature dependence than the other two PLD-grown samples, whose origin is not clear (as reflected in the α parameter of sample (ii) in *table 4.3*).

Parameters	Ko	Sample (i)	Sample (ii)	Sample (iii)
α	-7.3×10^{-4}	-8.7×10^{-4}	-3.6×10^{-4}	-8.1×10^{-4}
β	-1077	-1060.70	-1051.0	-1073.46

Table 4.3: Comparison of Ko et al's [20] parameters for the Varshni fit with the parameters used in the data seen in figure 4.11 Error values in the range of .05%.

4.4: Green band

Figure 4.12 shows the three PLD-grown ZnO samples at 20K over a wider energy range. Clear evidence of the appearance of the unstructured green band is seen, which is strongest in the sample annealed at 500°C and weakest in the unannealed sample. The origins of the unstructured green band in ZnO have been discussed in section 3.3.4 of chapter three. The green band intensity increases relative to the BE with increased annealing. The relative strength of the green luminescence in comparison to the band

edge PL is often taken as a measure of the sample quality, with strong green luminescence indicating lower quality [21].

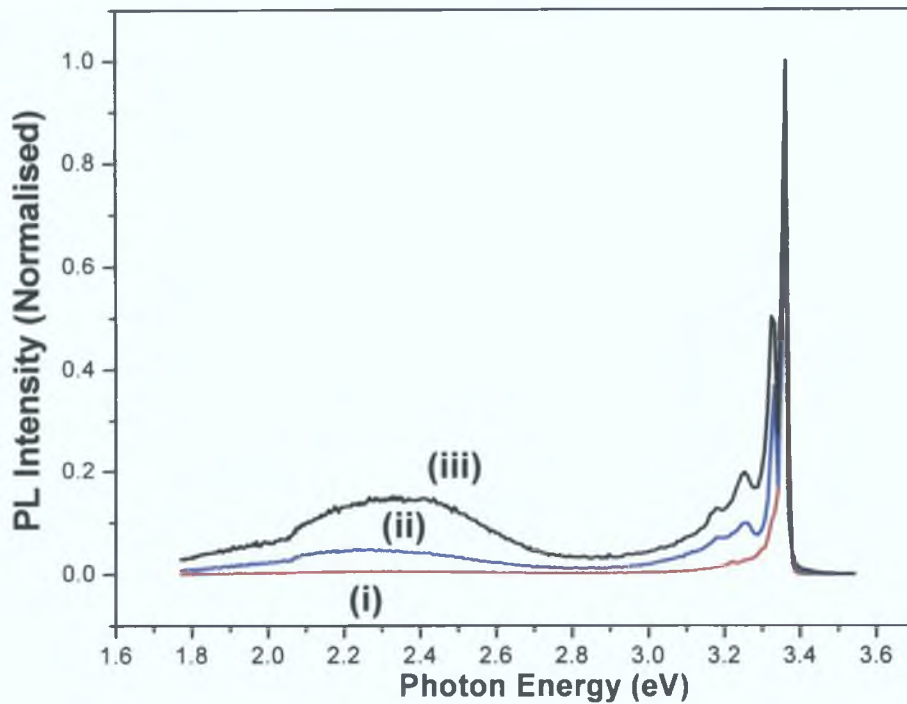


Figure 4.12: PL data for the three PLD samples at 20K. The samples are normalised so that the BE peak intensity is the same in all three graphs. Slits at $100\mu\text{m}$. Sample (i) not annealed, Sample (ii) annealed for 10 mins at 400°C and sample (iii) annealed at 500°C for 15 mins. Integration 1.0s, Increment 1.0s, Slits $100\mu\text{m}$.

This apparent contradiction with the results we observe for the annealed PLD-grown samples and the green band intensities measured in PL can be explained using the model proposed by *Vanhuesden et al.* [12]. In this model oxidation and reduction work treatments were performed on commercial ZnO powders, which allowed them to vary the intensity of the green emission. In this model, the green band is attributed to transitions at a singly charged oxygen vacancy (V_O^+). At grain boundaries, where band-bending effects are substantial due to trapped charges, these vacancies become doubly ionised (V_O^{2+}) (figure 4.13) and the green luminescence may be quenched due to the non-radiative character of the doubly ionised species.

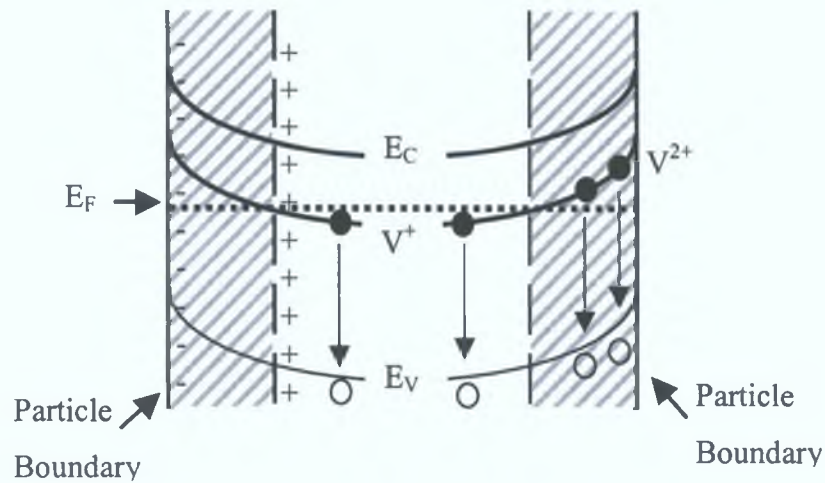


Figure 4.13: Schematic showing the energy band diagram of a ZnO grain cross section. The conduction band (E_C), valence band (E_V) and the Fermi level (E_F) are drawn. The hatched area is the grain boundary depletion region where oxygen vacancies become doubly ionised and therefore a non-radiative transition, hence quenching the green band emission (taken from reference [12]).

The data is consistent with this model as the increase in grain size with annealing causes a reduction in the grain boundary density and hence a reduction in the fraction of (V_O^{2+}) compared to (V_O^+). This results in an increase in the green band luminescence with increasing grain size. This work by *Vanhuesden et al* [12] highlights the problem of using the green band as an indicator of quality [22]. A small anomaly is visible in the green band at ~ 2.1 eV (~ 600 nm). This has been noted in measurements on a range of samples, and always occurs at the same spectral region and is due to the ‘‘Wood anomaly’’ [23].

4.5: Reflectance

In the discussion of the PL data from the PLD-grown samples given above, we have suggested that electric fields due to charge trapping at grain boundaries significantly affects both the band edge PL and green band signals, and that the reduction in these effects as a function of annealing gives rise to the results we see. We have conducted reflectance measurements on the bulk and PLD-grown material, which allows us to comment with more certainty on the influence of electric fields on the optical properties of the material. Reflectance data will typically show structure at the free exciton energies, and the magnitudes of the reflectance anomalies correlate with the degree of quenching or damping in the sample.

Reflectance measurements were performed using a Fourier transform (FT) spectrometer fitted with a photomultiplier tube. Samples were studied at temperatures between 20-300K using a closed cycle cryostat. A 150 W Xe-arc lamp was used to illuminate the samples after beam confinement through a variable aperture. No focusing was used and the incident light was unpolarised. Since the spectral region of interest is in the UV region and to avoid saturation of the detector, visible wavelengths were removed from the reflected beam with an appropriate glass filter. As a reference, a silicon sample onto which a thick layer of aluminium was deposited was used. Typical reflectivity for this reference sample is approximately 93% and is constant across the spectral range of interest.

In *figure 4.14* a comparison of PL data with reflectance (at 45° incidence angle) data is shown. The three PLD samples are measured at 20K and the bulk material is measured at 50K (temperature for the bulk sample was chosen to show the LO phonons replicas in PL more strongly) in the near band edge region of the spectrum. Comparing the PL and reflectance spectra for the bulk sample (*figure 4.14(d)*) leads to the identification of PL lines with LO replicas of both FE(A) (~3.373eV, transverse energy) and FE(B) (~3.381eV, transverse energy) recombination.

Although reflectance data on the PLD samples is substantially damped in comparison to the bulk material we see clear resonances in samples (i), (ii) and (iii), at ~3.374eV and 3.390eV. The energy difference between the 3.390eV reflectance resonance and the 3.330eV PL line in these two samples match the LO phonon energy of 72meV (with the difference explained by the difficulty in locating the lower energy “cut-on” for the LO phonon replica with such broad lineshapes), and this lends support to the previous assignment of the 3.330eV PL as being due to FE(B)-LO emission.

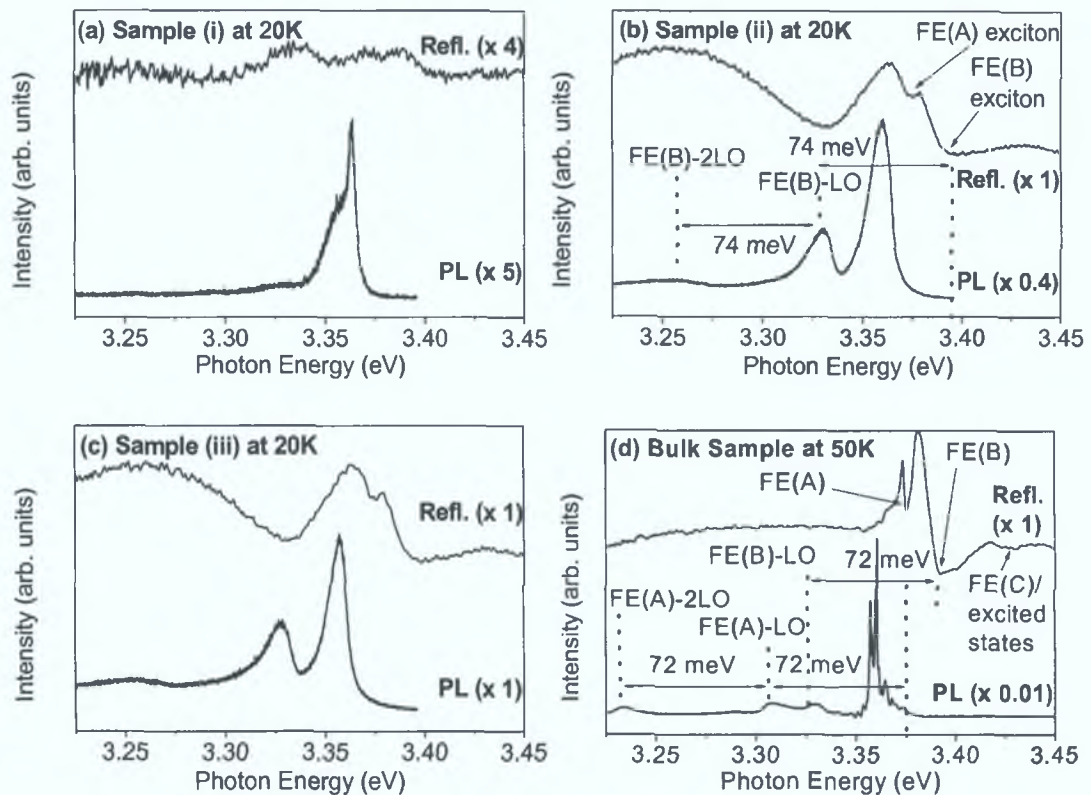


Figure 4.14: PL and reflectance (at 45° incident angle) data for the three PLD samples at 20K and the bulk material at 50K. Positions of FE and LO phonon replicas are indicated for sample (ii) and the bulk crystal, with similar assignments for samples (i) and (iii). All linewidths are sample limited.

Considering now the PLD samples in more detail, we note that the excitonic reflectance anomalies are substantially damped compared to the bulk crystal especially in the unannealed sample case. These features recover in the annealed samples. Figure 4.15 shows more detailed reflectance spectra of the three PLD-grown samples that are investigated in this work. In the top curve of figure 4.15 the excitonic features are very weak. The A and B excitons features (region II) are much clearer in the two annealed samples, the middle and lower curves of figure 4.15 and also show clear oscillations at both low and high energies (regions I and III).

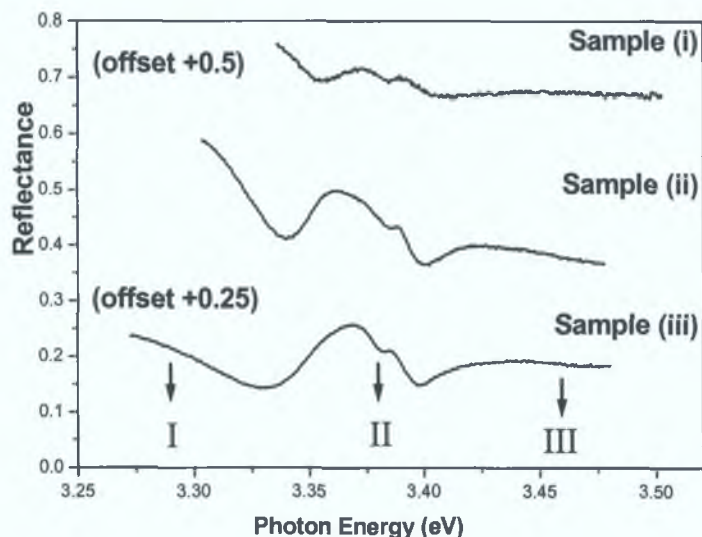


Figure 4.15: Experimental reflectance data for the PLD samples at 17K (normal incidence).

A significant strain exists in all the PLD-grown samples as seen in the XRD measurements mentioned earlier. We have plotted the variation of the A-, B- and C-transverse exciton energies with tensile biaxial strain using the deformation potential Hamiltonian and ZnO parameters in reference [24] and taking into account the strain in the PLD samples [7]. The A, B and C exciton positions of the bulk material as well as the A and B transverse energies of the PLD-grown samples are shown on the graph in figure 4.16.

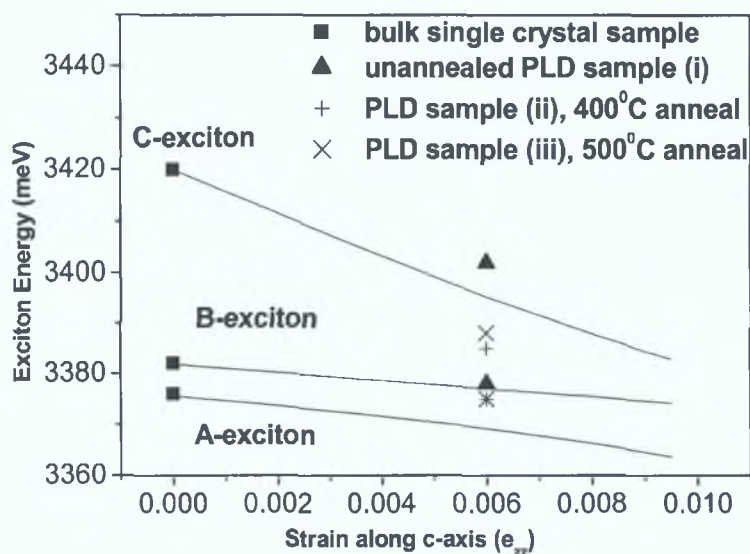


Figure 4.16: Plot of variation of exciton energy with strain. The continuous lines are the prediction based on the deformation potential model. The other points show the position of the A-exciton and B-excitons for the PLD samples and the bulk sample.

To determine the longitudinal exciton energies a commonly accepted empirical procedure was used. The position in energy of the (*figure 4.14*) reflectance minimum is taken as the longitudinal exciton energy [25] and the positions of the B- and C-excitons are corrected by the longitudinal-transverse splittings ($\sim 10\text{meV}$) [26] to give the transverse exciton position. The calculation of the transverse energies of the PLD excitons will have an error associated with them, $\sim \pm 2.5\text{meV}$ for the B-exciton and $\sim \pm 1\text{meV}$ for the A exciton. This error is due to the broad reflectance results compared to the bulk material.

One can immediately note that the bulk crystal exciton energies are well described by the model Hamiltonian and the fit parameters from Refs. [7,24,26]. The exciton energies for the PLD samples, however, are different to those predicted by the model. For the unannealed sample, the energy difference for the A-exciton is $+9\text{ meV}$, and $+25\text{ meV}$ for the B-exciton. This reduces in the annealed samples to $+6\text{ meV}$ and $+8\text{ meV}$, respectively, for the sample annealed at 400°C and to $+6\text{ meV}$ and $+11\text{ meV}$, respectively, for the sample annealed at 500°C . The energy differences for the two annealed samples are identical within the experimental error, but there is a very substantial reduction compared to the unannealed sample. The energy differences are positive in all cases, indicating that the actual energy positions are higher than those expected purely on the basis of strain effects. Additionally, the energy difference for the B-exciton is in all cases larger than that of the A-exciton. These energy shifts are too large to be the result of quantum confinement (QC) shifts because the expected largest QC shift to be seen in sample (i) is $\sim 1.3\text{meV}$ and reduces to $\sim 0.5\text{meV}$ for the annealed samples [27].

There must be some other perturbing effect on the excitons to account for the energy difference seen in the PLD materials. As we have mentioned earlier, Raman data [1] has shown evidence for electric fields due to depletion layers formed by charge trapping at grain boundaries, which decreased as the grain size increased because of the reduced grain boundary density. This idea was mentioned previously in discussing the variation of green band intensity in the annealed PLD-grown samples. We believe that these electric fields also account for the differences in free exciton energy observed for the PLD-grown samples. This would explain why the energy differences are smaller in *figure 4.14* for the two annealed samples as the electric field effects are reduced due to

the larger grain sizes after annealing. Thus the exciton energies will be perturbed less from the values predicted by the strain Hamiltonian.

The sample annealed at 500°C actually has the same A-exciton energy difference as the sample annealed at 400°C, and a slightly larger B-exciton energy difference. However, considering that the grain size in the two annealed samples is quite similar and given the rather large error associated with the transverse energy estimation (particularly for the B-exciton) as mentioned above, we feel that more detailed work on modelling the reflectance lineshapes using a polariton model will be needed to correctly assign transverse exciton energy differences between these two samples for a meaningful comparison.

Our interpretation of the origin of exciton energy shifts in the PLD samples is in good agreement with theoretical descriptions of the effect of electric fields on exciton energies [28,29]. In reference 28, a universal curve relating the change in exciton energy to the electric field in the sample is given (as a multiple of the ionisation field, corresponding to a potential drop of 1 Rydberg across the exciton Bohr radius, when substantial exciton ionisation begins). For electric fields equal to or greater than the ionisation field the exciton energy difference compared to the zero field case is always positive, in agreement with our data. For ZnO the exciton energy difference due to such an electric field will have values of the order of ~ 6 meV and greater, again in general agreement with the order of magnitudes in our data.

Visual inspection of the reflectance anomalies shows that there is certainly substantial exciton damping for both A- and B-excitons, which is known to occur for electric fields greater than or equal to the ionisation field [29]. However we can make an independent check of the rough magnitude of the electric field and the ZnO ionisation field as follows. The ionisation field of a wide variety of semiconductors scales linearly with the exciton binding energy [28]. If we extrapolate using the values in reference 25 and the 60 meV binding energy for the exciton in ZnO [1] we find that the ionisation field for ZnO is $\sim 300 \times 10^3$ V/cm. We may estimate the electric fields in the depletion regions at the grain boundaries using a simple model, similar to that used to determine depletion layer widths in p-n junctions [30]. The residual n-type carrier density in ZnO films grown by PLD on sapphire is generally in the range $\geq 5 \times 10^{17}$ cm⁻³ [10, 31] and the typical potential barriers between grains (of the order of magnitude observed here),

associated with these depletion regions, is ≥ 0.1 eV [32]. Using these carrier concentrations and the static dielectric constant of ZnO [33, 29], we can estimate that the average electric fields in the depletion layers in our PLD samples will be slightly greater than the ionisation field. Thus we are confident that the electric fields in our samples have values equal to or greater than the ionisation field for the excitons and that the consequent energy perturbations and damping predicted by theory are fully consistent with our data. We also note that the predicted width, $\Delta E(F)$, of absorption spectral lines as a function of electric field, based on WKB theory [34, 35], is given by the equation:

$$\Delta E(F) = (0.35 E_B) \exp\left(\frac{-0.32 F_{ion}}{F}\right) \quad (4.3)$$

where F is the electric field strength, F_{ion} is the ionisation field, and E_B is the exciton binding energy. Using the parameters given earlier for ZnO, and the estimated field strengths, we calculate a linewidth for our samples of ~ 15 meV, yielding a good order of magnitude agreement with the values of $\sim 12 - 16$ meV seen in the PL spectra at low temperature (mentioned earlier), given the nature of the approximations made.

4.6: Summary

PL and reflectance measurements show a consistent increase of PLD material quality with annealing in terms of PL band edge emission intensity, linewidth and excitonic reflectance features. We propose that this is due to a reduction in surface and electric field effects, which quench the luminescence for small grain size samples. Our results also show that all the samples are of significantly poorer quality than the ZnO bulk material with excitonic linewidths an order of magnitude larger. A consistent increase in the intensity of the green luminescence band with increased annealing was also observed. We show that the optical properties of the PLD-grown samples cannot be explained by strain effects alone, and we propose that electric field effects due to charge trapping at grain boundaries strongly influence all these properties. The reduction of electric field effects due to an increase in grain size with annealing and consequent reduction in grain boundary density leads to an increase in the optical quality of the material, and to predictable changes in the band edge and green PL signals and the reflectance data. We demonstrate that the electric fields in the material have a magnitude of the order of the ionisation field of the free excitons, and that theoretical predictions of the effects of such fields match our experimental data well.

Chapter Four References

- [1] C.Roy, S.Byrne, E.Mcglynn, J.P.Mosnier, E.dePosada, D.O'mahony, J.G.Lunney, M.O.Henry, B.Ryan, A.A.Cafolla, *Thin Solid Films*, 436, (2003), 273.
- [2] Eagle-Picher Technologies,L.L.C.,200 B.J. Tunnell Blvd, Miami, OK 74354,USA
<http://www.epcorp.com/>
- [3] T.Oshima, R.K Thareja, Y.Yamagata, T.Ikegami, K.Ebihara, J.Narayan, *Sci.Tech.Adv.Mater.*, 2, (2001), 517.
- [4] B.D.Cullity, *Elements of X-ray Diffraction*, 2nd, Addison-Wesley, (1978).
- [5] V.Gupta, A.Mansingh, *J.Appl.Phys*, 80, (1996), 1063.
- [6] T.Nakamura, Y.Yamada, T.Kusumari, H.Minoura, H.Muto, *Thin Solid Films*, 411 (2002), 411.
- [7] E. McGlynn, J.Fryar, G.Tobin, C. Roy, M. O. Henry, J. -P. Mosnier, E. de Posada, J.G. Lunney, *Thin Solid Films*, Vol. 458, Iss.1-2, (2004), 330.
- [8] M. K. Puchert, P.Y.Timbrell, R.N.Lamb, *J. Vac. Sci. Technol. A*, 14, (1996), 2220.
- [9] K.Thonke, Th.Gruber, N.Teofilov, R.Schonfelder, A.Waag, R.Sauer, *Physica B*, 308-310, (2001), 945.
- [10] B.J Jin, S.Im, S.Y.Le, *Thin Solid Films*, 366, (2000), 107.
- [11] M. E. Lin, Z. Ma, F. Y. Huang, Z. F. Fan, L. H. Allen, and H. Morkoç, *Appl. Phys. Lett.* 64, (1994), 1003.
- [12] K.Vanheusden, W.L.Warren, C.H.Seager, D.R.Tallant, J.A.Voigt, B.E.Gnade, J. *Appl. Phys.*, 79, (1996), 7983.
- [13] D.C.Look, D.C.Reynolds, C.W.Litton, R.L.Jones, D.B.Eason, G.Cantwell, *Appl.Phys.Lett.*81, (2002), 1830.
- [14] J. Grabowska et al., accepted for publication in *Phys. Rev. B* vo71, part 11,(page numbers not allocated yet), (2005).
- [15] S.Savikhin, A.Freiberg, *J.Lumin.*, 55, (1993), 1.
- [16] R.L.Weiherr, W.C.Tait, *Phys. Rev.*, 166, (1968), 791.
- [17] C.Klingshirn, *Phys.Rev.Lett.*, 15, (1965), 22.
- [18] B.K.Meyer, H.Alves, D.M.Hofmann, W.Kriegseis, D.Forster, F.Bertram, J.Christen, A.Hoffmann, M.Straburg, M.Dworzak, U.haboeck, A.V.Rodina, *Phys.Stat.Sol. (b)* No 2, (2004), 231.
- [19] S.M. Sze, *Semiconductor devices;Physics & Technology*,2nd edition, New York,Wiley, (2002).
- [20] H.J. Ko, Y.F.Chen, Z.Zhu, T.Yao, I.Kobayashi, H.Uchikil, *Appl. Phys. Lett.*, Vol.76, No. 14, (2000),1905.

- [21] S.Bethke, H.Pan, B.W. Wessels, *Appl. Phys.Lett.* 52, (1998),138.
- [22] G. Tobin, J. Fryar, E. McGlynn, J.P. Mosnier, M.O. Henry, E. dePosada, D. O'Mahony, J. Lunney, Study of the Excitonic Properties of Bulk and Polycrystalline ZnO Thin Films. Proceedings of the 26th ICPS (Edinburgh 2002), IOP, Bristol (2003) P22.
- [23] C.Palmer, *Diffraction Grating Handbbok*, Fifth Edition, Thermo RGL, (2002),102.
- [24] J.Wrzesinski, D.Frohlich, *Phys. Rev. B* 56, (1997), 13087.
- [25] J.J.Hopfield, D.G. Thomas, *Phys. Rev. Lett.* 15, (1965), 22.
- [26] B.Gil, A. Lusson, V. Sallet, S. Daid-Hassani, R.Triboulet, P.Bigenwald, *Jpn. J. Appl. Phys.* 40, (2001), L1089.
- [27] P.K. Basu, *Theory of Optical Processes in Semiconductors*; Oxford Science Publications: Oxford, 1997; pp 358-359.
- [28] D.F. Blossey, *Phys. Rev. B* 3, (1971), 1382.
- [29] Taken from data in Landolt-Bornstein, Numerical Data and Functional Relationships in Science and Technology; Rossler, U.; Ed.; New Series III; Springer: Berlin, (1999); Vol. 41B, on CD
- [30] E.S.Yang, *Fundamentals of semiconductors devices*; Mcgraw-Hill:New York.NY,(1978),pp85-89
- [31] A.Ohtomo, K.Tamura, K.Saikusa, K.Takahashi,T.Makino, Y.Segawa, H.Koinuma, M.Kawasaki, *Appl.Phys.Lett.* 75, (1999),2635.
- [32] V.Srikant, D.R.Clarke, *J.Appl.Phys.* 81, (1997), 6357.
- [33] J.Lagois, *Phys.Rev.B* 23, (1981),5511.
- [34] H.I.Ralph, *J.Phys.C.* 1, (1968), 378.
- [35] L.Schultheis, J.Lagois, *Phys.Rev.B*, 29, (1984), 6784.

Chapter Five

High excitation Effects and Random Lasing

The general material qualities and optical characteristics of bulk and PLD-grown ZnO samples have been discussed in chapters three and four. The extreme stability of excitons (indicated by the large exciton binding energy) in table 1.1 means that excitonic emission mechanisms are dominant at room temperature and above. These characteristics indicate the suitability of ZnO as a practical lasing material utilising exciton emission at room temperatures. A short review of lasers and the theory of lasing is given in section 5.2. The key concepts associated with non-linear optical processes (section 5.3) and lasers (section 5.4) are discussed and a study of the potential of ZnO PLD-grown thin films to display laser action under high level optical excitation is presented in section 5.5. Finally in section 5.6 a discussion of the various non-linear optical processes which may lead to stimulated emission and lasing effects in ZnO is presented.

5.1: Introduction

LASER is an acronym for “Light Amplification by the Stimulated Emission of Radiation” and was first reported experimentally in the 1960’s [1]. For lasing to occur in a material, electrons must be excited to levels above the ground state. This process is called “pumping”, where either intense optical pumping or an electrical discharge is used to excite the material. If a substantial percentage of electrons are excited into the upper levels, leaving the lower levels empty, this normally unstable situation is known as “population inversion”. An incident photon of light of suitable frequency can trigger an avalanche of these excited electrons (via stimulated emission), which then relax with the emission of photons, all of which are in phase (i.e. monochromatic and coherent). Thus an incident photon will be amplified, and the material will exhibit optical gain. Non-radiative and spontaneous emission recombination processes will lead to electron-hole recombination without emission into the lasing photon mode and thus will contribute to an energy dissipation. If energy continues to be pumped in to sustain the population inversion one may produce a coherent, monochromatic beam of photons.

To extract energy efficiently from a medium where population inversion is present and create an output laser beam, a resonant cavity is needed that builds up a large optical intensity by positive optical feedback, reflecting some fraction of the light back into the cavity. Placing the lasing medium between two mirrors forms a conventional laser cavity. Cavity modes are set up which correspond to light waves travelling back and forth through the medium and such a situation generates a continuous wave (CW)

output laser beam. The mirror at one end of the laser is partially transparent and transmits a small fraction of the cavity mode as the output beam. The first laser built was the ruby laser in the 1960's with a wavelength of 694nm [1]. The active medium was the Al_2O_3 crystal containing about 0.05% of Cr_2O_3 and shaped into a rod. The rods end faces were polished flat, parallel and normal to the axis, with silvered ends to form the cavity.

5.2: Theory of lasing

The last three letters in the acronym LASER are intended to imply how the device operates: i.e. by the “stimulated emission of radiation”. Therefore the relationship between spontaneous and stimulated emission are reviewed and the criteria for lasing in semiconductors is developed.

5.2.1: Interaction of light with matter:

Light interacts with matter generally via three processes (1) absorption (2) spontaneous emission and (3) stimulated emission. These processes will be illustrated in a simple, two level atomic system but the results are generally applicable to all systems. The effects of various types of light scattering will not be discussed in these three processes.

(1) Absorption of light

In the case of absorption, the atom which is initially in the ground state (E_1); absorbs a photon of energy $h\nu$ and moves to an excited state (E_2), where

$$E_2 - E_1 = h\nu \quad (5.1)$$

The process of light absorption is shown in *figure 5.1*.

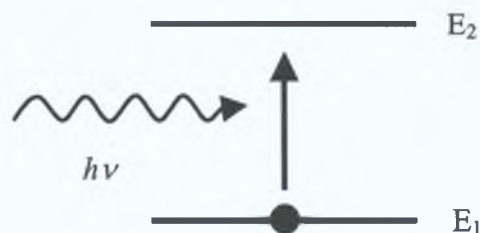


Figure 5.1: Schematic diagram of the absorption process in a two level atomic system.

(2) Spontaneous Emission:

Virtually all of the light we see in nature comes from spontaneous emission. As seen in *figure 5.2* the atom, in this case is initially in the excited state, E_2 , may make a transition to the ground state, E_1 , without any apparent external perturbation, releasing a photon $h\nu$ with arbitrary phase and direction. The photon energy can be expressed as

$$h\nu = E_2 - E_1 \quad (5.2)$$

Excited electrons have a characteristic spontaneous emission lifetime, which is the average time that they remain in the upper level before spontaneously emitting a photon and dropping to the lower level.

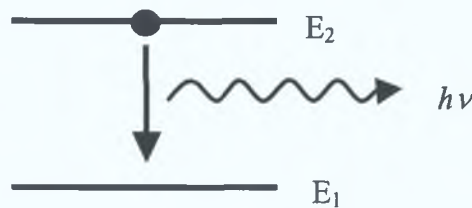


Figure 5.2: Schematic diagram of the spontaneous emission process in a two level atomic system

(3) Stimulated Emission:

In stimulated emission the atom initially in the excited state, is perturbed by the electromagnetic field of a photon of energy $h\nu$ equal to

$$h\nu = E_2 - E_1 \quad (5.3)$$

The atom makes a transition to the ground state emitting a second photon of the same energy as the incident photon as shown in *figure 5.3*. The emitted photons are coherent (i.e. in the same electromagnetic mode).

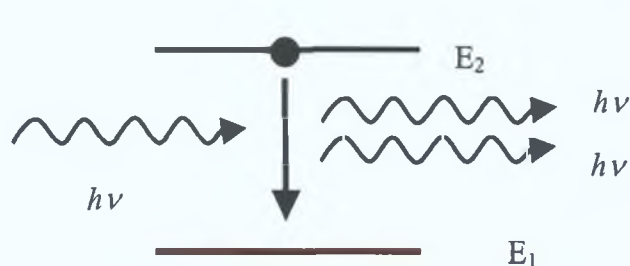


Figure 5.3: Schematic diagram of stimulated emission in a two level atomic system.

The diagrams of light interaction with matter shown in *figure 5.1, 5.2 and 5.3*, are for the isolated atom, which has two energy levels, E_1 and E_2 . Under normal conditions, most of the electrons are in the ground state E_1 and very few electrons are in the upper state E_2 . Assigning the population of E_1 and E_2 to be n_1 and n_2 respectively, the distribution of electrons between the two states can be expressed as a Boltzmann distribution at thermal equilibrium:

$$\frac{n_2}{n_1} \propto e^{-(E_2-E_1)/kT} = e^{-h\nu_{12}/kT} \quad (5.4)$$

If the electrons exist in a radiation field of photons with energy $h\nu_{12}$, such that the energy density of the field is $\rho(\nu_{12})$, then stimulated emission (*figure 5.3*) can occur along with absorption (*figure 5.1*) and spontaneous emission (*figure 5.2*). The stimulated emission is dependent on the number of electrons in the upper field n_2 and to the energy density of the stimulating field $\rho(\nu_{12})$. The rate of stimulated emission can be expressed as $B_{21}n_2\rho(\nu_{12})$, where B_{21} is a constant of proportionality. Similarly the absorption rate can be written as $B_{12}n_1\rho(\nu_{12})$, where B_{12} is a proportionally constant for absorption. In the case of spontaneous emission, the rate is only proportional to the population in the upper level, i.e. $A_{21}n_2$, where A_{21} is another coefficient of proportionality. For steady state thermal equilibrium at any temperature the two emission rates, stimulated and spontaneous must balance the rate of absorption to maintain constant populations in n_1 and n_2 [2] i.e.

$$B_{12}n_1\rho(\nu_{12}) = A_{21}n_2 + B_{21}n_2\rho(\nu_{12}) \quad (5.5)$$

Rate of = Spontaneous + Stimulated
absorption Emission Emission

This steady state relationship was first described by Einstein and the coefficients A_{21} , B_{21} , B_{12} , are known as the Einstein coefficients [2]. One may then relate these coefficients using the fact that in thermal equilibrium n_1 and n_2 are given by Boltzmann statistics as:

$$\frac{n_2}{n_1} = \frac{g_2}{g_1} \exp\left(-\frac{E_2 - E_1}{kT}\right) \quad (5.6)$$

(g_1 and g_2 are the degeneracies of the lower and upper levels, respectively). Using *equation 5.5 and 5.6* combined with Planck's distribution of the energy density in a black body radiation field the Einstein coefficients can be expressed by

$$B_{21} = B_{12} \frac{g_1}{g_2} \quad \text{and} \quad \frac{A_{21}}{B_{21}} = \frac{E_{21}^2}{\pi^2 \hbar^3 c^3} \quad (5.7)$$

The expressions in *equation 5.7* are known as the Einstein relations and have been obtained using the thermal equilibrium condition. Their validity however is completely general, and not limited to thermal equilibrium situations.

As *equation 5.5* indicates, the spontaneous emission term is independent of the photon density $\rho(\nu_{12})$. At thermal equilibrium the ratio of stimulated to spontaneous emission rates is very small and the contribution of stimulated emission is negligible in normal thermal sources such as e.g. a lightbulb. With a photon field present the ratio can be expressed as,

$$\frac{\text{Stimulated Emission Rate}}{\text{Spontaneous Emission Rate}} = \frac{B_{21}n_2\rho(\nu_{12})}{A_{21}n_2} = \frac{B_{21}}{A_{21}}\rho(\nu_{12}) \quad (5.8)$$

Equation 5.8 indicates that the stimulated emission rate is directly dependent on the photon fields energy density $\rho(\nu_{12})$. Providing an optical resonant cavity in which the photon density can build up to a large value through multiple internal reflections can dramatically improve this rate.

To obtain more stimulated emission than absorption it is necessary to have $n_2 > n_1$, i.e.

$$\frac{\text{Stimulated Emission Rate}}{\text{Absorption Rate}} = \frac{B_{21}n_2\rho(\nu_{12})}{B_{12}n_1\rho(\nu_{12})} = \frac{B_{21}n_2}{B_{12}n_1} \quad (5.9)$$

If stimulated emission, the process via which lasing takes place, is to dominate, there must be a way of maintaining more electrons in the upper level than in the lower level. This non-equilibrium condition $n_2 > n_1$ is known as population inversion. In practice this is done by artificially ‘‘pumping’’ the system to a non-thermal excited state because at thermal equilibrium, electrons and molecules will accumulate in the lower levels. The population of a level decreases as its separation from the ground state energy increases, according to the Boltzmann relation. Pumping may be done optically, electrically or by other means to obtain and maintain population inversion. The results reported in this present work are based on optical pumping of the PLD-grown ZnO. *Einstein's* [2] first relation in *equation 5.7* relates to the population inversion required for lasing. The second relation in *equation 5.7* accounts for the difficulty in achieving lasing action at high frequencies such as in the x-ray region ($\sim 10^{16}$ Hz). At high frequencies, spontaneous emission occurs very rapidly and stimulated emission is not as easily achieved as in the visible region.

Einstein [2] proposed that stimulated emission could occur but it was not until *Maiman* [1] in the 1960's addressed the problems of cavity creation and population inversion in the ruby laser, that stimulated emission and lasing become more than a matter of theoretical interest. The application of the laser has become extremely important in many branches of science due to its exceptional optical characteristics. The light that is created is monochromatic, coherent, highly directional and large power densities are routinely possible.

5.3: Non-linear optical processes

To investigate stimulated emission and the onset of lasing using optical excitation, a sample is probed with a laser of higher power than those used for photoluminescence experiments. This high-powered laser, when incident on ZnO, produces a range of “new” optical and emission properties, many of which exhibit non-linear behaviour as a function of pump intensity. We may characterise such excitation by an intermediate and high excitation regime.

5.3.1: Intermediate excitation regime

At low light intensity levels single electron hole pairs, either in the exciton state or in the continuum, determine the optical properties. However, as the pump intensity increases into an intermediate regime, the exciton density becomes sufficiently high to cause exciton interactions with other particles/excitations. Transitions involving exciton-exciton (ex-ex) emission may be observed which give rise to a large variety of optical nonlinearities as such processes will generally scale according to the exciton density squared (or higher powers).

In bulk, single crystal ZnO at low temperatures ($< 200\text{K}$) under intermediate level excitations, a number of new optical emission bands appear. We will describe these in rough order of appearance with increasing excitation density.

The first band, which appears, is called the M-band [3]. The origin of the M-band remains unclear, and in fact may be due to a combination of processes. In the following we list the main models used in the literature to explain the M-band luminescence:

- The decay of biexcitons into photon like polaritons and transverse mixed-mode or longitudinal excitons

- The stimulated emission of the acoustic wing of bound excitons arising from the radiative recombination of an exciton bound to an impurity under simultaneously emission of an acoustic phonon.
- Inelastic scattering processes between bound excitons and free carriers or excitons
- The recombination of electron hole pairs in a plasma droplet, which forms at an impurity level acting as a nucleation center.

These possible models are discussed in more detail in reference [4], with different processes responsible for its appearance in different samples. The fact that the M-band tends to appear only at lower temperatures according to many workers [5,6] lends support to arguments assigning it to processes involving bound excitons.

Another process that takes place in the lower intermediate intensity region of the regime is the inelastic scattering between an exciton and a free carrier, usually an electron (ex-el) in which the exciton recombines radiatively while the carrier is scattered to a higher state in its band [3]. This process is characterised by a red shift relative to the energy of the free exciton. The transition occurs at an energy (given by theory);

$$E_g(T) - E_{ex} - P_n = \gamma kT \quad (5.10)$$

where $E_g(T) - E_{ex}$ is the free exciton energy, P_n is the photon energy and γ is the coefficient describing the temperature dependence (for ZnO ~ 7.74) [3]. Equation 5.10 yields a value for the energy shift between the free exciton and the emitted photon of 200 meV. This band is related to the ex-el collision and will generally be observed as a broad band centred ~ 200 meV at 300K below the free exciton emission.

In the intermediate excitation region at RT processes such as exciton-exciton (ex-ex) collisions become prominent due to the higher exciton density. This exciton-exciton collision process results in the recombination of one exciton and the emission of a photon with the remaining exciton promoted to an excited state, in a process analogous to Auger emission [3]. The exciton-exciton collision process will scale in proportion to the exciton density squared. The emitted exciton may be promoted into one of a manifold of excited states and the emitted photon will have a range of energies given by a simple hydrogenic model [7] of the free exciton [3]:

$$P_n = E_{ex} - E_b^{ex} \left(1 - \frac{1}{n^2} \right) - \frac{3}{2} kT \quad (n = 2, 3, 4, \dots, \infty) \quad (5.11)$$

where P_n is the photon energy, E_{ex} is the free-exciton emission energy, E_b^{ex} is the binding energy of the exciton, n is the quantum number of the envelope function and kT is the thermal energy. Equation 5.11 yields values for the energy shift between the free exciton and the emitted photon of 83 meV for $n = 2$ and ~ 98 meV as $n \rightarrow \infty$. This band is known as the P-band, and the emission associated with such exciton-exciton collisions will generally be observed as a broad band centred ~ 90 meV below the free exciton emission. In PLD-grown ZnO samples with relatively broad excitonic features a P-band is expected in the range 80–100 meV below the free exciton band energy.

5.3.2: High excitation regime

When the pump intensity is increased further, exciton densities reach such levels that the excitons overlap and the exciton binding energy tends to zero, i.e. the exciton state becomes unstable. This high density regime is referred to as the Mott density [8]. This is the result of a combination of physical processes, including the decrease of the band gap energy as a function of increasing carrier density (band gap renormalization), which can destabilise the exciton state compared to the free carrier state. Other important factors, at and beyond this Mott density, include phase space filling (occupation of the states near the band extrema, which are necessary to build up the exciton wavefunction, tends to saturate the exciton states) and Coulomb interactions (due to screening of the Coulomb attraction between electrons and holes) will tend to saturate and quench the exciton optical signatures. The combined effects of such processes will destabilise the exciton state in favour of the free carrier state until eventually a new collective phase known as the “electron hole plasma” (EHP) results where an electron is no longer bound to a single hole to form an identifiable quasi-particle. These types of plasma phenomena are most easily observed in direct band gap materials with large Bohr radii [8], but may also be seen in materials with a large exciton binding energy under more extreme conditions.

Figure 5.4 outlines the common features observed in a material being pumped as a function of increasing pump intensity. However observations of the various nonlinear processes can be very different for different materials. For instance, in Ge the EHP can be seen under the illumination of an incandescent lamp due to the long life times of the carriers while the opposite is true for CuCl where an EHP is produced in the range \sim GW/cm² of pump intensity. II-VI semiconductors behave in an intermediate fashion, which allows observation of all the non-linear bands roughly simultaneously [8].

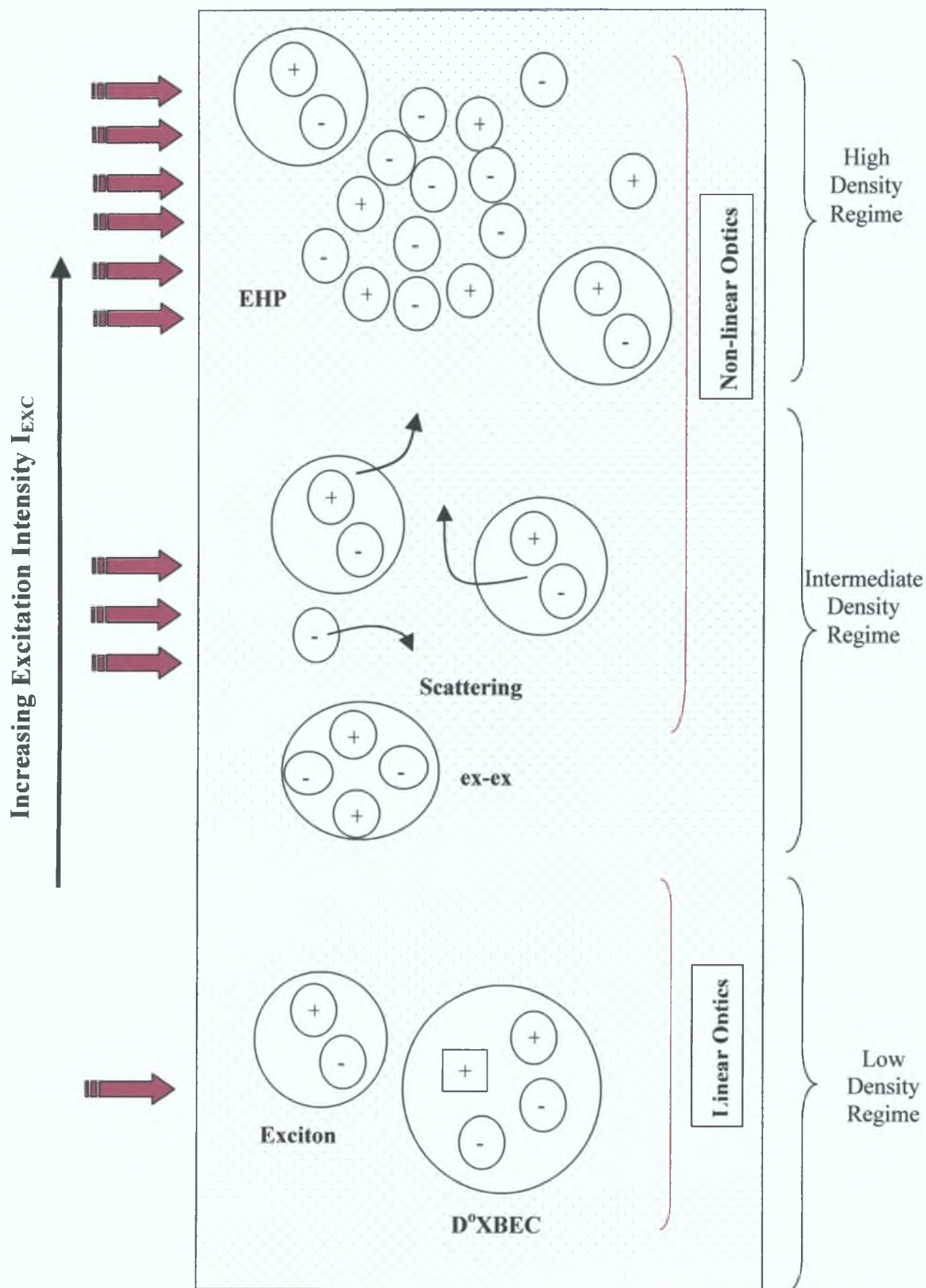


Figure 5.4: Diagram of the main regimes that are associated with high excitation effects [8].

5.4: Lasing conditions and cavity effects

In a material under sufficiently high levels of optical pumping, creation of population inversion, both stimulated and spontaneous emission can occur. As the pumping intensity and hence recombination rate increases the photon density builds up stimulating further recombination. As the system is pumped to higher and higher intensities, stimulated emission effects begin to dominate over spontaneous emission.

5.4.1: Conditions for lasing

In order to achieve lasing in any system two conditions must be met: (1) that the gain must be at least equal to the losses, and (2) positive feedback of the radiation must be present, which can be obtained by placing the source of radiation in a cavity, which will favour the growth of a limited number of modes with discrete frequencies. This selective amplification is produced as a result of positive feedback of the electromagnetic waves, which form a standing wave pattern in the simple cavity as shown in *figure 5.5*.

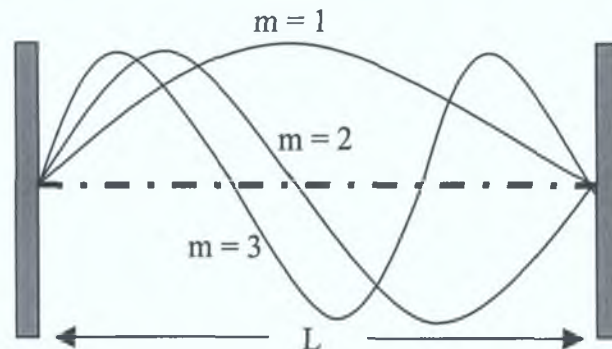


Figure 5.5: Resonant modes within a cavity laser, shown are orders $m = 1, 2, 3$.

Light of a particular frequency can be reflected back and forth within the resonant cavity if an integral number of half-wavelengths fit between the end mirrors. Therefore the length of the cavity for stimulated emission can be expressed as

$$L = \frac{m\lambda}{2} \quad (5.12)$$

where L is the length of the cavity and m is an integer value. Lasing occurs when the gain provided by the medium overcomes the losses in the cavity for a single roundtrip. The degree of coherence is determined by the quality of the cavity [9]. The “gain” is defined as the degree of amplification, i.e. the fractional increase in optical intensity per unit travel along the cavity.

5.4.2: Stimulated emission

The nature of the emission from a semiconductor laser depends on the excitation intensity. When the excitation is below a certain threshold (where the roundtrip gain is less than the various cavity losses via scattering etc.) the emission is mostly spontaneous in nature and with increased intensity, stimulated emission in the small number of cavity modes begins to dominate and the intensity of the output rises sharply. This threshold of lasing is marked with the dotted line in *figure 5.6*, and this pattern is referred to as the “knee-joint” effect. The presence of this sharp increase in emission intensity and coherence is one strong indication that stimulated emission has begun to dominate the emission from the material.

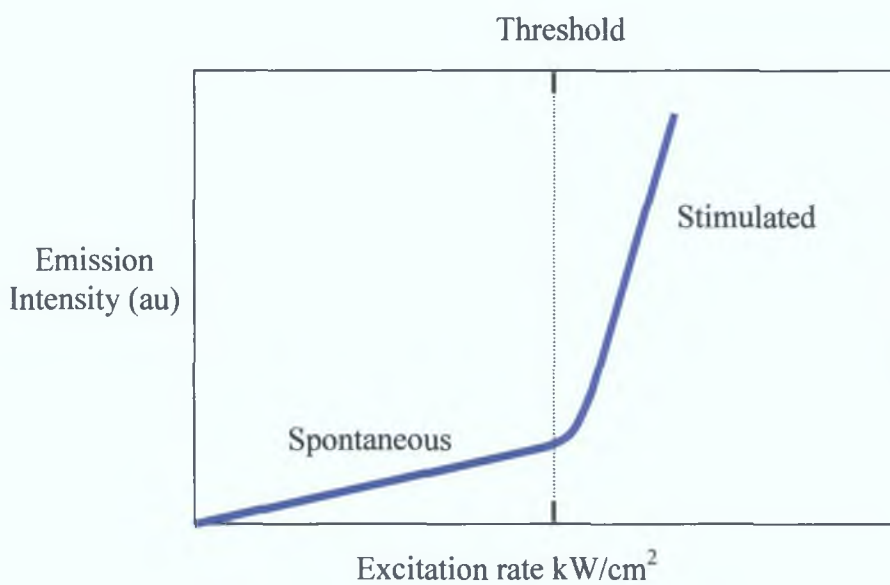


Figure 5.6: A plot of the excitation intensity versus emission intensity of a semiconductor material.

5.5: Random lasing effects with no defined cavity structure

There has been increasing interest in the development of microlasers, i.e. confining of light in a small volume over the past few years [10]. Many of these microlasers have shown stimulated emission effects as outlined in the previous section. In order to produce materials suitable as microlasers, state of the art growth techniques are required to create a physical cavity. However *Cao et al* [10] have shown lasing effects that are observed in a disordered material, in which the lasing cavities are “self formed” due to strong optical scattering and reflection at grain boundaries. These are not traditional lasers, in which cavities and mirrors are well formed. When the optical excitation source is incident on a sample, lasing cavities can be “self-formed” due to strong optical scattering in the layers and because the scattering is completely random it has been

referred to as random lasing. The theory of ultraviolet (UV) lasing/stimulated emission produced by random lasing effects (with particular focus on ZnO nanocrystalline films grown on sapphire substrates) will be discussed.

5.5.1: Theory of random lasing

Letokhov et al [11] suggested the possibility of generation of amplified light using a random scattering medium over 25 years ago [11]. In an amplifying medium the intensity of the light wave increases as the light travels through it but such a state can only be maintained over a finite region of space. This can be illustrated as shown in *figure 5.7*. Light enters a medium and can become “trapped” due to multiple scattering. This light will make a long random walk before it leaves the medium, and will be amplified throughout this walk, and losses will occur due to the various scattering processes. Lasing occurs when the gain becomes greater than the loss. The gain increases with the amount of time the light remains in the material while the loss depends on how quickly the light escapes.

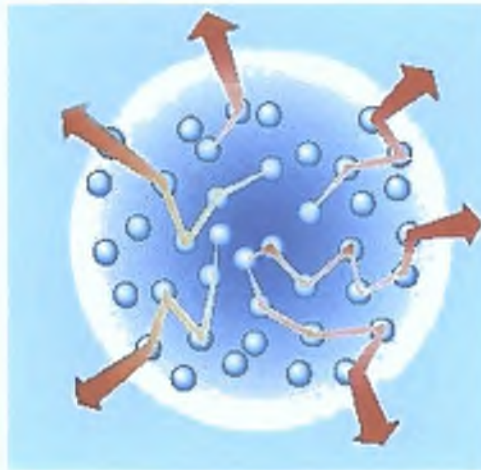


Figure 5.7: In a random laser the cavity is absent but multiple scattering between particles in the disordered material keeps the light “trapped” long enough for the amplification to become efficient, and for the laser light to emerge in random directions [10].

Due to local variation of the particle density and spatial distribution in systems such as ZnO films, regions of lower disorder and stronger scattering exist in the material. Light can be confined in these regions through multiple scattering [12]. If the number of scatterers continually increases, the coherent multiple scattering and interference between the counter propagating waves give rise to what is called light localization (closed loops) [10]. The interference is wavelength sensitive for a particular

configuration of scatterers and only light at certain wavelengths are confined [12]. In a different region of the sample, the configuration of the scatterers is different, and thus light at different wavelengths is confined. These closed loop feedback paths are essentially resonant cavities [13]. Along individual loop paths the probability of a photon being scattered back to its starting point is different and therefore the loss is specific to each loop. Due to the finite size of the random medium, some photons can escape through the surface of the cluster. It is well known that optical absorption destroys photon localisation because it suppresses the interference of scattered light. Optical gain on the other hand has the opposite effect and enhances photon localisation [12]. With an increase in the pump intensity, the material gain will increase. In cavities with sufficiently low losses laser oscillations will occur with the lasing frequencies determined by the cavity resonances. The laser emission from these resonators results in a small number of discrete narrow peaks in the emission spectrum associated with the material gain curve. In ZnO, the levels of optical pumping required for sufficient gain coincide with the appearance of nonlinear optical processes discussed above, and hence lasing effects are generally reported for these processes. A further increase in the pumping intensity results in more gain and less losses in the cavity and therefore more resonant cavities achieving the lasing threshold.

This localisation effect of closed loops occurs where light transport comes to a complete stop, in a phenomenon known as Anderson localisation of light [14]. This effect originates from the interference of photons that have undergone multiple scattering from defects in the solid. Anderson localisation of waves in disordered systems originates from wave interference due to multiple elastic scattering. In *figure 5.8* an excited atom emitting a photon labelled X is positioned in a disordered material. A random light path that results in the light source completing a close loop can be followed in two directions. These two waves, which propagate in opposite directions, will acquire the same phase and therefore interfere constructively at X. This leads to a higher probability of the wave coming back to X.

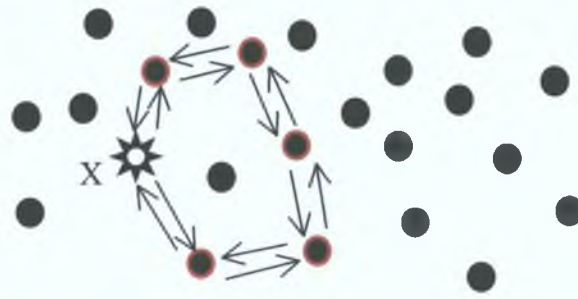


Figure 5.8: Schematic diagram of the closed loop path that takes place with multiple scattering. The red marked grains are involved in the scatter of the closed loop.

A greater number of scattering centres means that the probability of such closed loop paths forming is increased, leading to an increase in the localisation time of a photon in the gain material. A change in the density of the grains will affect the mean free path of the light and hence the time the light stays in the sample. The mean free path is the average length travelled by a photon between two successive collisions. A decrease in the mean free path increases the probability of a loop being created. However these parameters are difficult to control in the growth process and therefore it is problematical to achieve improvements in the lasing behaviour by changing these parameters. With an increase in the excitation area, a larger number of possibly suitable cavities are being pumped and hence this increases the chances of lasing cavities forming and consequently the threshold pumping intensity decreases. However when the excitation area is reduced to below a critical size, laser oscillations stop due to the excitation of an area with an insufficient number of scattering centres. This allows some control of the “random” lasing process using this principle [15].

The fact that the grains of the PLD-grown ZnO samples used in this work show a six-fold orientation can result in strong optical scattering effects. For instance *Mitra et al* [16] studied the properties of PLD-grown ZnO on a glass substrate. The quality of these samples may be inferior to ZnO grown on sapphire but this however may aid stimulated emission because the mismatch of glass and ZnO leads to a large polydispersity in grain sizes.

5.6: Identification of effects due to high excitation intensities

The effects of high excitation on semiconductor materials can lead firstly to the observation of non-linear optical processes in the emission spectra of the material. It is important to distinguish in principle between such non-linear processes and stimulated

emission / lasing effects although in practise the difference may be hard to define. For non-linear processes to be seen, high injection levels (using a pulsed pump laser) is required. With sufficiently high excitation levels it is then possible to get sufficiently high gains and photon densities via photon localisation (in our case through scattering at the grains of the PLD samples which enable random cavity formation) to enable stimulated emission and, under certain conditions, lasing to take place. The observation of non-linear processes and the identification of stimulated emission and random lasing effects and the distinction between these are very important characteristics of a system, dependent both on its innate material properties and its detailed microscopic morphology. Both aspects substantially influence the potential for the material for use as a practical laser material.

5.6.1: Non-Linear optical processes and their spectral identification

The most important bands associated with intermediate and high excitation levels in ZnO material (particularly PLD-grown material) at room temperatures are the P-band and the EHP. In this section we discuss these bands in slightly more detail for ZnO. Due to the inherently broad features in PLD samples, most identification is via the spectral position of the features relative to the FE position. The P band can be spectrally identified using *equation 5.11*, which gives the energy separation of the P band from the free exciton (FE). The FE emission energy can be identified from PL spectra at room temperature and the separation energy between a particular band appearing at high excitation intensity and the FE may be thus determined. If this value is of the order of the theoretical P-band separation it enables identification of this band with the P-band originating in a ex-ex collision, i.e. a non-linear optical process. Following the same procedure as the P-band can identify the ex-el band but in this case *equation 5.10* gives the expected energy separation for the ex-el band and the FE band. The EHP band can be recognised by its appearance at the highest pumping intensities. It appears at longer wavelengths than the P-band. With increased pumping intensities this band is expected to shift slightly to longer wavelengths. This shift of the EHP is due to the fact that the renormalization red shift is substantially larger than the band filling blue shift (P-band) [8]. Both these non-linear processes occur at room temperature. At low temperature the M band may also be observed at lower excitation values, and with increased pumping intensity the P-band becomes dominant in the spectra at longer wavelengths/ lower energy than the M-band.

We have discussed the non-linear optical processes in a sequential manner, mirroring the general pattern of their appearance as a function of pumping intensity. For such processes taking place in II-VI compounds, it is common that the various non-linear bands can be seen simultaneously in certain excitation ranges and the non-linear bands can gradually evolve from one band to another with changing excitation, rather than changing in a sharply defined manner. This evolution, in combination with the broad linewidths generally seen in emission from nanocrystalline materials such as those grown by PLD, complicates the individual identification of the various bands greatly. A largely qualitative method of distinguishing these bands is given by *Newbury et al* [17] where increases in the linewidth of the P-band (normally $\sim 20\text{meV}$) indicates the growth of the EHP emission. When the EHP emission is present the P-band is much broader, up to $\sim 100\text{meV}$ [17]. *Yu et al* [18] have suggested that if the ratio of integrated emission intensity of a non-linear band is measured versus the excitation intensity at RT, a four fold increase ought be observed for the P-band and a nine-fold increase in the EHP band [18] for a doubling of excitation intensity. Hence, if one plots the excitation intensity versus emission intensity of these bands, one obtains a graph, which has a noticeable “knee-joint effect” or threshold, even in the absence of stimulated emission effects [18]. This innate non-linear growth also complicates the identification of a distinct lasing threshold as this “knee-joint” effect is not due to stimulated emission and is wholly based on the non-linear bands characteristics [3,19]. Consequently, the presence of coherent emission, in the form of a distinct “speckle” pattern in the emission is needed to distinguish the lasing transition, as discussed below.

5.6.2: Stimulated emission and lasing effects

Emission from systems displaying random lasing displays an interference effect known as “speckle” [9]. When coherent light is incident on a disordered surface, the scattered light has a “grainy” intensity pattern with very bright and dark spots. At the bright spots the waves are interfering constructively and at the dark spots they interfere destructively. This effect is not seen for illumination of the surface with an incoherent light source or where the scattering particles are moving, e.g. in liquid suspension.

In general stimulated emission and subsequently lasing effects can be conclusively identified in the ZnO samples we have studied by the simultaneous observation of three effects: (1) a strongly superlinear increase of the optical luminescence output as a function of the pump intensity above a certain threshold, i.e. the “knee joint” effect and

(2) a spectral narrowing of the emission with the possible appearance of laser modes and (3) the observation of a distinct “speckle-pattern” emission from the sample.

In most cases, identification of laser modes (2) comes from visually inspecting the spectra. A small number of discrete narrow peaks or a distinct narrowing of the emission spectra are observed and as the pump excitation increases these peaks become more defined. The mode spacing ($\Delta\lambda$) of these peaks can give the length of the natural cavity that is formed using the equation [20]:

$$\Delta\lambda = \frac{\lambda_0^2}{2L(n - \lambda_0 \frac{dn}{d\lambda})} \quad (5.13)$$

where L is the cavity length and n is the index of refraction at λ_0 the wavelength of one of the modes. (The refractive index of ZnO is 2.46 at 400nm). The emission peak narrows due to the preferential amplification at frequencies close to the maximum of the gain spectra. For example, a cavity length of 5mm leads to a predicted mode separation of ~ 0.006 nm.

The expressions “stimulated emission” and “lasing” are often used synonymously in the literature [21,14]. The reason for this is that these processes are usually seen together. However there are slight technical differences. Stimulated emission is identified by a superlinear increase in the optical luminescence as a function of the excitation intensity, the “knee-joint” effect, and is occasionally distinguished by using the term “amplified spontaneous emission (ASE)”. Other indications of stimulated emission are the narrowing of the bands with increased excitation intensity from the pumping source and by the coherence of the output beam. However it is not true to say that lasing has taken place solely because of stimulated emission characteristics identified in the material. In our opinion genuine lasing is more properly identified through the evidence of longitudinal cavity mode formation.

Chapter Five References

- [1] T.H.Maiman, *Nature*, Vol.187, (1960), 493.
- [2] A.Einstein, *Phys. Zeit*, 18, (1917), 121.
- [3] C.Klingshirn, *Phys.Status Solidi B* 71, (1975), 547.
- [4] C.Klingshirn, H.Haug, *Physics Reports*, 70, No.5, (1981), 315.
- [5] H.Schrey, C.Klingshirn, *Phys.Stat.Sol. (b)* 90, (1978), 67.
- [6] H.J.Ko, Y.F.Chen, T.Yao, K.Miyajima, A.Yamamoto, T.Goto, *Appl. Phys.Lett.* 77, (2000), 537.
- [7] R.J. Elliott, *Phys. Rev.* Vol.108, No.6, (1957), 1384.
- [8] C.F.Klingshirn, *Semiconductor Optics*, Springer (1997)
- [9] J.I.Pankove, *Optical Processes in Semiconductors*, Dover Publications, New York, (1971)
- [10] H.Cao, J.Y. Xu, E.W. Seelig, R.P.H. Chang, *App. Phys. Lett.*, Vol. 76, No.21, (2000),2997.
- [11] V.S. Letokhov, *Sov. Phys. JETP* 26, (1968), 835.
- [12] D.S.Wiersma, P.Bartolini, A. Lagendijk, R.Righini, *Nature*, Vol. 390, (1997), 671.
- [13] N.M.Lawandy, R.M. Balachandran, A.S.L. Gomes, E.Sauvain, *Nature*, Vol.368, (1994), 436.
- [14] P.W.Anderson, *Phys. Rev.*, Vol.109, No.5, (1958), 1492.
- [15] R.K. Thareja, A.Mitra, *Appl. Phys B: Lasers Opt.* 71, (2000), 181.
- [16] A.Mitra, R.K.Thareja, *J.Appl. Phys.*, Vol.89, No.4, (2001),2025.
- [17] P.R.Newbury, K.Shahzad, D.A.Cammack, *Appl.Phys.Lett.* 58, (1991),1065
- [18] P.Yu, Z.K.Tang, G.K.L.Wong,M.Kawasaki, A.Ohtomo, H.Koinuma, Y.Segawa, 23rd International Conference on the Physics of semiconductors, edited by M.Scheffler and R.Zimmermann, (World Scientific, Singapore, 1996),1453.
- [19] C.Klingshirn, *Semicond.Sci.Technol.* Vol 5, (1990), 457.
- [20] Z.K.Tang, G.K.L.Wong, P.Yu, M.Kawasaki, A.Ohtomo, H.Koinuma, Y.Segawa, *Appl. Phys.Lett.*, Vol.72, No.25, (1998), 3270.
- [21] H.Cao, Y.G.Zhao.H.C.Ong, S.T.Ho, J.Y.Dai.J.Y.Wu, R.P.H.Chang, *ppl.Phys.Lett*, Vol.73, No.25, (1998), 3656.

Chapter Six

High excitation and Random Lasing Results I

Stimulated emission and lasing phenomena in ZnO under high excitation optical pumping has been reported at cryogenic temperatures for many years [1]. More recently, a number of groups have measured such phenomena at room temperature (RT) in ZnO, aided in part by the rather large exciton binding energy of ZnO, compared to the thermal energy at RT [2]. The results presented in this chapter show RT measurements of high excitation optical pumping, using a Nd:YAG laser, on bulk ZnO and PLD-grown ZnO samples. The identification of features associated with linear and non-linear optical processes, and the presence of stimulated emission and lasing effects is discussed in section 6.2. Sections 6.3 and 6.4 describe the results obtained when the optical pumping was performed using a spherical and cylindrical lens, respectively. The differences between these two methods and the effects on the spectra obtained are also discussed. The results of this study and a discussion of their relevance to the PLD-grown samples are presented in section 6.5.

6.1: Introduction

The experimental arrangement used for these measurements has been described previously in section 3.4. The initial arrangement used a spherical lens (fused silica, plano-convex lens, focal length of 125 mm) and the frequency-tripled output of a Nd:YAG laser (emitting at 355 nm, corresponding to a photon energy of 3.496 eV).

In order to investigate non-linear optical processes and the possible onset of stimulated emission it is necessary to have a variable range of pumping intensities. To achieve this, a neutral density filter was used to modulate the laser power. A laser power meter was used to measure the unattenuated power and the laser peak intensity at 355nm recorded by the spectrometer was assigned as 100% of this power. A neutral density filter placed in the laser path resulted in a decrease in the pump laser line peak intensity recorded by the spectrometer, depending on the filter setting (see *figure 6.1(a)*). The actual intensity of the pump laser hitting the sample at each setting can then be calculated by the percentage drop of the pump laser line in the spectra compared to the unattenuated signal. The results of a calibration measurement to verify this method are shown in *figure 6.1(b)*. The correlation between the intensity measured by the spectrometer at 355nm and the actual power hitting the sample is good, with a straight line fit with a slope of 1.03.

The excitation level is measured in units of kW/cm^2 , corresponding to the average power levels on the sample during the laser pulse. They are calculated by firstly dividing the power meter reading by the cross sectional area of the beam profile and then dividing by the total laser pulse duration in a one second real-time interval. The laser pulse width and repetition rate are ~ 5 ns and 10Hz, respectively, hence the total laser pulse duration in one second is 50 ns. The beam profiles in the case of both the spherical lens and the cylindrical lens were measured using both a knife-edge technique and also laser burn paper. In calculating the pumping intensity the effects of reflected or transmitted light were not taken into account, these parameters would only make a very small difference to the final values.

The spectra were all obtained with the spectrometer set to a slit width of $500 \mu\text{m}$, an increment of 0.1 nm and integration time of 1.0 s , unless stated otherwise. The rather wide slit setting is needed as the signal levels are quite low compared to photoluminescence measurements. The spectrometer resolution in this configuration is $\sim 0.5\text{nm}$.

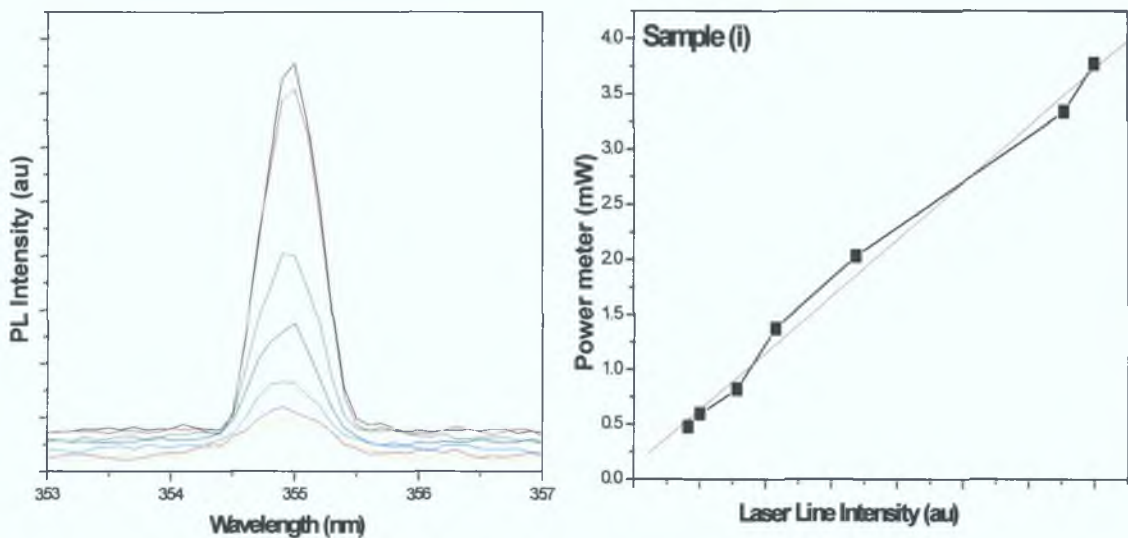


Figure 6.1: (a) The 355nm line of the Nd:YAG laser as a function of varying pumping intensity from 6188 to $680\text{kW}/\text{cm}^2$. Slits $500\mu\text{m}$, Integration 1.0s , Increment 0.1nm .

(b) Graph of laser power meter as a function of intensity of laser line. Slope of the line is 1.029 .

The neutral density filter was adjusted with a thumbscrew and therefore it was difficult to exactly reproduce a particular intensity setting from one sample to the next. However the pump intensity could be varied over a reasonable range (up to $\sim 6200 \text{ kW}/\text{cm}^2$) with

a reasonable level of reproducibility. An example of the evolution of the emission spectrum for a PLD-grown ZnO sample at RT as a function of pump laser intensity shown in *figure 6.2* (with the spectra normalised to the laser peak height).

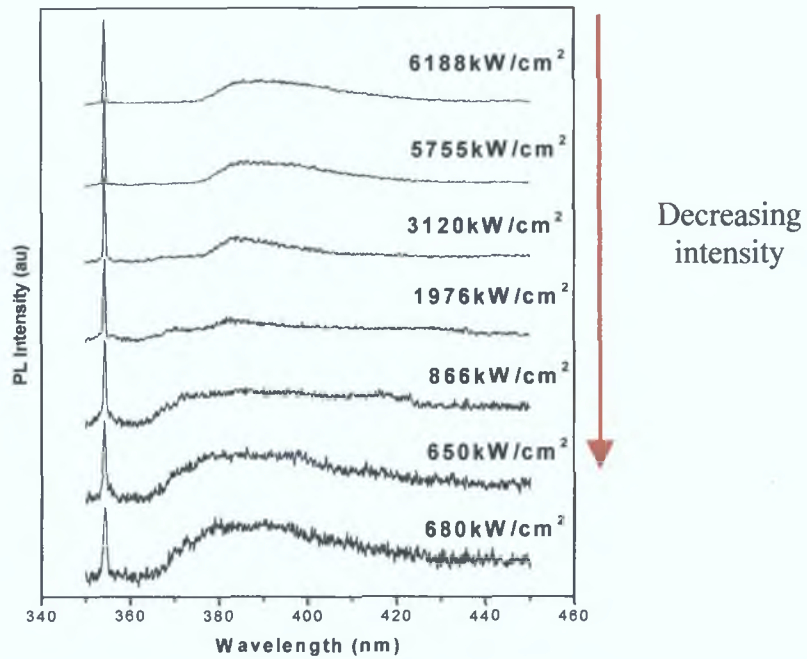


Figure 6.2: The spectral output as the pumping intensity is decreased from 6188-680kW/cm². Slits 500 μ m, Integration 1.0s, Increment 0.1nm.

6.2: Discussion of spectral features

As discussed in chapter five, three different regimes of varying excitation are normally identified, the low, intermediate and high-density regimes. The low-density regime corresponds to the spectra obtained using an unfocussed HeCd laser (e.g. results presented in chapter 4) where the spectra are dominated by bound exciton and deep level emission at low temperatures and by free exciton and deep level emission at higher temperatures.

In the intermediate excitation region at RT processes such as exciton-exciton (ex-ex) and exciton-electron collisions become prominent due to the higher exciton density. This exciton-exciton collision process results in the recombination of one exciton and the emission of a photon with the remaining exciton promoted to an excited state. This band is known as the P-band, and the emission associated with such exciton-exciton collisions will generally be observed as a broad band centred ~ 90 meV below the free exciton emission. In PLD-grown ZnO samples with relatively broad excitonic features a P-band is expected in the range 80–100 meV below the free exciton band energy. The

exciton-electron collision process involves predominantly similar effects, but with the excitation of a free electron to a higher energy level and the emission of a red-shifted photon. This feature is observed at room temperature at a spectral position of $\sim 200\text{meV}$ less than the free exciton. The P-band grows in proportion to the square of the excitation density, while the band associated with exciton-electron collisions grows linearly with excitation density [3].

At low temperatures, $< 200\text{K}$ a band called the M band appears first with increasing excitation level [3] followed by the P-band. The origin of the M-band remains unclear, and in fact may be due to a combination of processes, discussed in more detail in the previous chapter [4]. The fact that it tends to appear only at lower temperatures according to many workers [5,6] lends support to arguments assigning it to processes involving bound excitons.

Finally, the high excitation region can be distinguished by the presence of the electron hole plasma (EHP). The EHP recombination appears in the spectrum as a broad band at longer wavelengths than the P-band. It is characterised by a shift to longer wavelengths at higher intensities, due to the band gap shrinkage which gives rise to a change in the optical spectra [7] and tends to dominate the spectra as the pump laser intensity increases. This band also shows a highly non-linear dependence on excitation intensity [3].

These non-linear bands (i.e. the P-band and EHP) usually grow and diminish in sequence as the excitation level increases from medium to high pumping intensities at room temperature. While these bands may be seen individually and quite distinctly in some materials (such as CuCl [8]), in ZnO the excitation levels at which the bands are observed are found to be rather close in some samples (e.g. 800 kW/cm^2 for the EHP compared to 400 kW/cm^2 for the P-band [9]) and thus they are often seen simultaneously in a spectrum. In certain sets of data presented in this work both the EHP and P-bands are seen simultaneously. This may also be due to the lack of spatial and temporal resolution of the acquisition equipment. These two emissions may originate from different regions of the excitation area, or at different intervals during excitation [10]. Similar data, whereby both bands are seen in a single spectrum have been reported for II-VI semiconductors previously [11].

One of the main driving motivations of this thesis work is to examine the stimulated emission and lasing processes in nanocrystalline PLD-grown material, as discussed in chapter 5. Under optical pumping, stimulated emission and lasing has been reported by a number of workers in the intermediate to high excitation regime [9]. While the appearance of the P-band and/or EHP demonstrates that the sample is in the high excitation regime, the question of whether stimulated emission and/or lasing is occurring in a sample is a slightly more complicated matter and will be dependent on a range of effects, including cavity formation and feedback as discussed earlier. One of the most obvious characteristics of stimulated emission and lasing in a sample is a sharp increase in the emitted optical power as a function of the excitation intensity, which shows a sharp “knee-joint” effect at the threshold [11], as shown in *figure 5.6*. However, the fact that both the P-band and the EHP have a super-linear dependence of emission intensity on excitation density can tend to mask this effect. Other signatures of stimulated emission are necessary to provide a more unambiguous signature of a transition to stimulated emission and lasing. As mentioned earlier, the coherence of stimulated emission from a sample gives rise to a visible, speckled cloudy appearance on a sample surface when the excitation intensity is increased above a certain value. Another signature of lasing is the appearance of mode structure in the emission spectra associated with the formation of cavity modes in the random lasing process in such nanocrystalline materials.

Due to the rather low spectral resolution of the system mentioned above and the intrinsically broad bands associated with the PLD-grown material in particular, the bands we observe under high excitation intensity are rather broad and overlap to a significant degree. In order to calculate a consistent value for the emission intensity associated with various bands, a Gaussian lineshape is fitted to the particular band and the area under the peak is determined from this fit. The Gaussian fit appears to fit most of the bands reasonably well, particularly for purposes of comparison, although various other lineshapes are used in the literature (such as inverted Boltzmann etc. [12]). *Figure 6.10* shown later compares the values obtained using the fitting of the Gaussian compared to extracting the area using a manual procedure. These results show the validity of using a Gaussian fit to obtain the intensity of each of the bands.

The Gaussian distribution is defined by the equation:

$$y = y_0 + \frac{A}{w\sqrt{\frac{\pi}{2}}} e^{-\frac{2(x-x_c)^2}{w^2}} \quad (6.1)$$

where y_0 is the baseline, x_c is the center of the band, w is the width of the band and A is the amplitude. These parameters are adjusted to fit each individually band using a curve fitting routine in Microcal Origin 6.0. This allows the component peaks from various bands to be individually resolved as shown in *figure 6.3*.

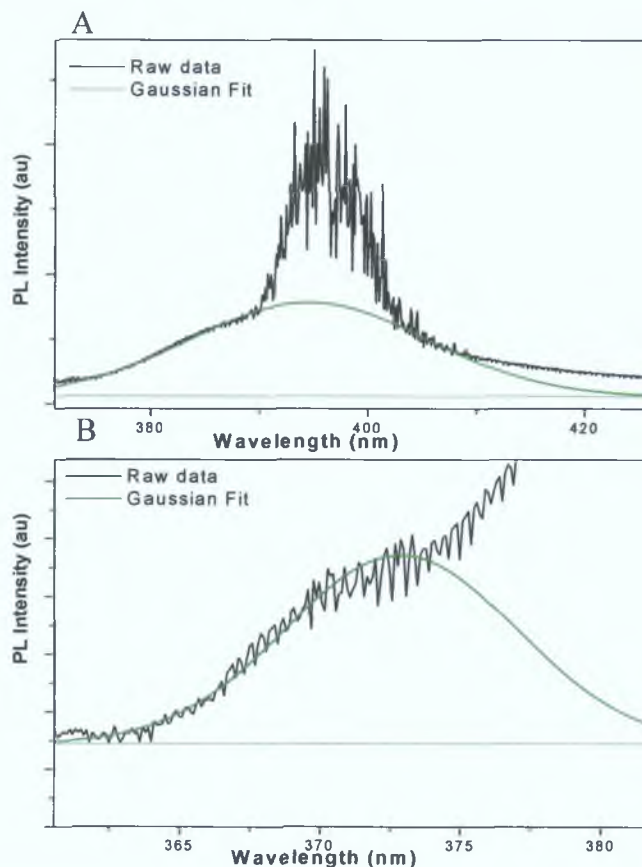


Figure 6.3: (A) The Gaussian fit of the P-band that appear under high excitation, (B) The Gaussian fit for the free exciton band. The Gaussian fit are the green lines, original data is the black line.

There have been very few reported studies of curve fitting of the bands associated with non-linear and lasing processes in ZnO. It is a computationally intensive procedure and the fits presented here constitute a “first-order” approximation, where the computed peak areas may be confidently used for comparison as the excitation intensity increases for a particular sample. However, a more thorough study would require fitting the bands with lineshapes based on a physical theory of the emission processes.

6.3: Investigation of high excitation effects using a spherical lens

The first investigation of high excitation effects was undertaken with a spherical lens which created a spot size of the pump laser beam on average of 1.2mm in diameter on the surface of the sample and excitation intensities typically in the range of 500-7000 kW/cm² were used. These parameters were chosen, as they represented the average settings for various groups who have investigated lasing under similar experimental setups [13]. The pumping laser was at normal incidence to the sample with the pump laser spot positioned as close as possible to the edge of the sample so that the maximum amount of emitted luminescence could be captured and directed onto the spectrometer. The investigation of lasing effects using the spherical lens for the bulk and PLD-grown ZnO samples is presented in the following sections.

6.3.1: Eagle Picher ZnO bulk material

Bulk ZnO material was used as a reference in the photoluminescence results and is also used as a starting point in the high excitation intensity measurements. *Figure 6.4* illustrates the variation of the luminescence spectra for the bulk ZnO crystal sample with varying pumping intensity. Two peaks emerge as the excitation intensity increases, one at ~ 3.26 eV and the other centred at ~ 3.08 eV.

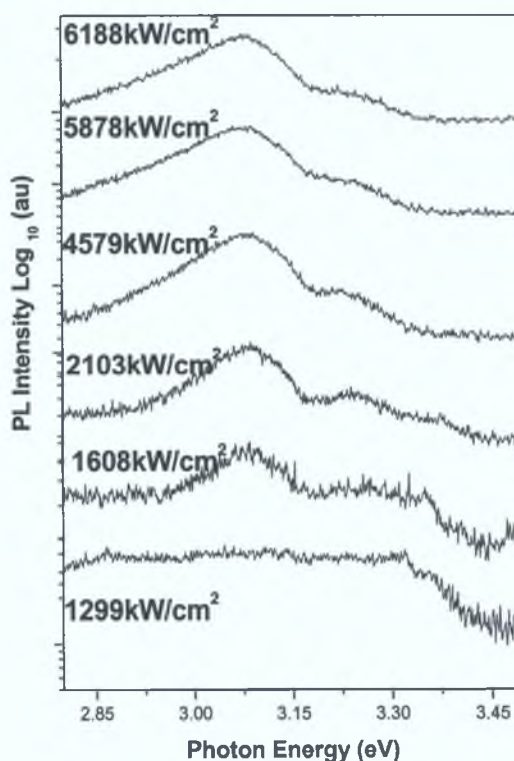


Figure 6.4: Spectra of the Eagle Picher bulk ZnO material with increasing pumping intensity, Slits 500 μ m, Integration 1.0s, Increment 0.1nm. The spectra are normalised to the intensity of the highest feature.

In figure 6.5 the spectrum for this sample under Nd:YAG excitation is compared with the spectrum under HeCd excitation (both at room temperature). The spectrum under HeCd excitation shows two peaks at $\sim 3.28\text{eV}$ and 3.18eV , which are associated with the FE and a deeper lying defect level, respectively [14]. The energy separation between the FE seen under HeCd excitation and the bands under Nd:YAG excitation can be used to try to identify the various features.

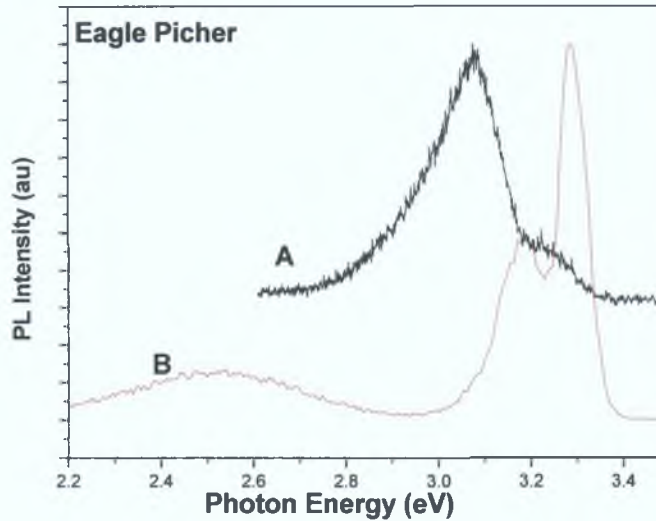


Figure 6.5: Comparison of spectra from the bulk ZnO sample at RT. Spectrum labelled A is obtained under the Nd:YAG excitation at an excitation intensity of $6188\text{kW}/\text{cm}^2$. Increment 0.1nm , Integration 1.0s , Slits $500\mu\text{m}$, Spectrum labelled B is obtained under the HeCd excitation. Increment 1.0nm , Integration 1.0s , Slits $10\mu\text{m}$.

Figure 6.6 shows a close-up of the spectra A in figure 6.5. We label the band at $\sim 3.26\text{eV}$ as “X” and the band centered at $\sim 3.08\text{eV}$ as “Y”. The energy separation between X and Y does not correspond to that expected for the P-band. Nor do the energy separations between either “X” or “Y” and the FE peak in the spectrum under HeCd excitation correspond to the expected P-band position. Based on the alignment in energy between spectra A and B in figure 6.5, we assign the X band to the free exciton emission with a slight red-shift due to sample heating under the intense laser pulse, as the spectral position is in good agreement with that observed under HeCd excitation. The Y band we attribute to emission from the exciton-electron collision process, as the peak of this band occurs in the correct spectral region (at $\sim 3.08\text{eV}$) where such emission is expected (Equation 5.10). The carrier concentration in the bulk material is expected to be $\sim 10^{17}\text{cm}^{-3}$ at room temperature, as mentioned previously in chapter 3. Thus there is a substantial background n-type concentration, which can lead to strong emission due to the exciton-electron collision process as the excitation density

increases. The total emission from this band may also involve some deep level emission from the lower energy band observed under HeCd excitation but this is obscured by the strong emission due to the exciton-electron collision process at higher excitation levels. There is no evidence to associate the Y band with the EHP or P-band, based on the excitation dependence measurements below.

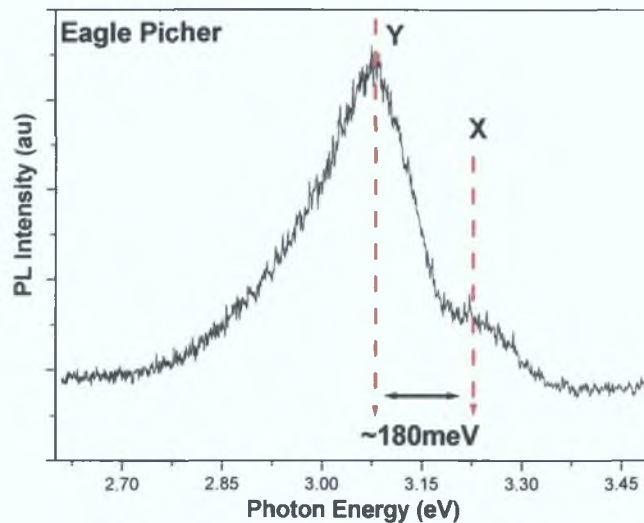


Figure 6.6: Two peaks labelled X and Y in the Eagle Picher bulk material recorded with the Nd:YAG at pump laser intensity of 6188 kW/cm^2 . Slits $500\mu\text{m}$, Integration 1.0s, Increment 0.1nm.

We have used Gaussian fits of the peaks X and Y in figure 6.6 to study the evolution of the band intensities of the X and Y bands as a function of excitation intensity. Figure 6.7 shows these results, indicating that the Y band shows much larger emission intensity compared to the X band for the same excitation intensities. There is no evidence of any super-linear increase in emitted intensity as a function of excitation intensity for either of the bands, which supports the assignment made above that they are associated with either free exciton or exciton-electron collision emission, rather than ex-ex or EHP processes. No evidence is seen of a speckle pattern on the sample surface for any excitation intensity and no evidence is seen for the development of mode structure in any of the spectra.

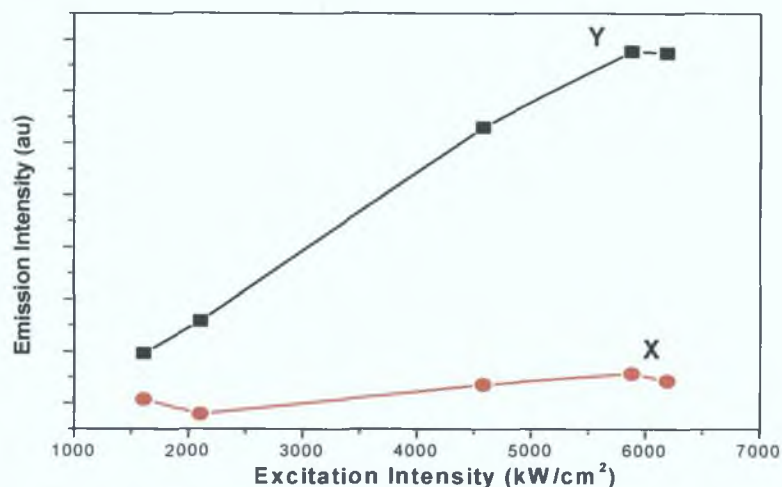


Figure 6.7: A plot of varying excitation intensity versus emission intensity for the two peaks X and Y, identified in figure 6.6

Figure 6.8 shows the variation in peak wavelength for the X and Y bands determined from the Gaussian fit. There are no dramatic shifts in the peak wavelength of the two bands as the pumping intensity is increased. This suggests that neither of the bands is the EHP band, which would be expected to show a shift to longer wavelengths with increasing pumping intensity.

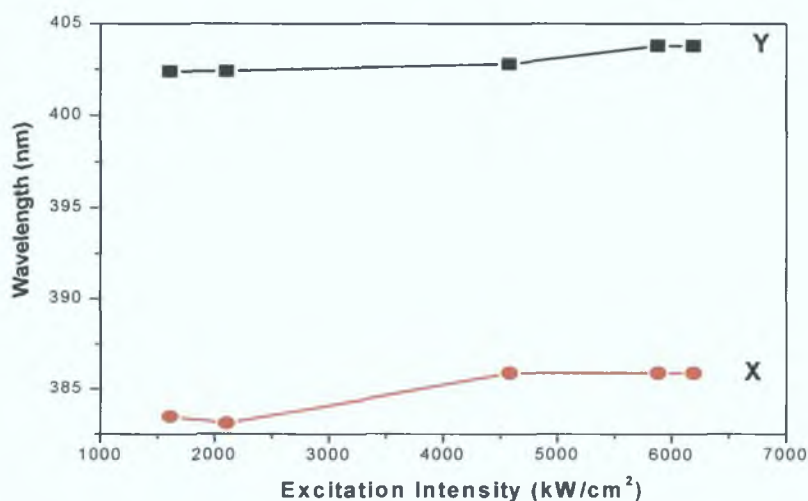


Figure 6.8: The peak wavelengths of the X and Y bands as a function of varying excitation intensity identified in figure 6.6.

In conclusion, we observe no evidence for the presence of any non-linear optical processes in this material at the excitation intensity range we have examined, nor do we observe any evidence of stimulated emission or lasing effects. The data are assigned to FE and exciton-electron collision-related emission. We see no evidence for higher level excitation effects such as P-band or EHP emission in this sample. We will discuss the

reasons why such high excitation effects are not seen in the bulk crystal sample at the end of the chapter (section 6.5), comparing the data here with data for the PLD-grown samples.

6.3.2: PLD ZnO sample (i)

A high excitation level investigation of the PLD-grown ZnO samples using the spherical lens was undertaken. *Figure 6.9* shows the variation of the luminescence spectra of sample (i) under increased pumping intensities. A broad band at low excitation intensities is seen centred at ~ 3.30 eV, close to where the expected free exciton energy is observed. At higher pumping excitations (~ 2000 kW/cm²), a band appears at the lower energy side of the free exciton. We identify this tentatively with the P-band at this stage. At the highest excitation levels a new band begins to grow at even longer wavelengths. This is actually observed as an increase in the asymmetry to longer wavelengths of the P-band and thus it is difficult to identify a spectral position with this emerging band. However we identify it with the EHP emission band, and discuss the reasons for these assignments further below.

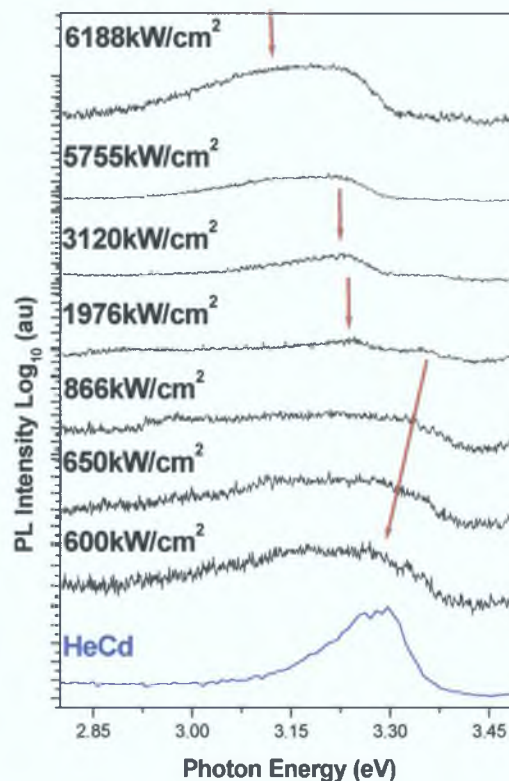


Figure 6.9: Plot of emission intensity versus wavelength for sample (i) for increasing excitation intensity. Slits 500 μ m, Integration 1.0s, Increment 0.1nm. HeCd excitation spectra acquired at room temperature, Increment 1.0nm, Integration 1.0s, Slits 150 μ m. (Graphs are normalised to the intensity of the highest feature)

In order to associate the band which appears at intermediate excitation levels with an inelastic collision between excitons (P-band), the spectral separation between it and the FE band was measured. This separation is expected to be in the range 80 – 100 meV, as discussed previously. *Figure 6.9* compares the resultant spectra under HeCd and Nd:YAG excitation at room temperature, where the separation (between the FE and this band) is estimated to be of the order of 110meV, which is a reasonable value for the P band separation considering that both the FE band and the P like band are rather broad and overlap considerably.

At higher excitations a new band grows at longer wavelength, which may suggest the presence of the EHP emission. This is seen as a broadening to longer wavelengths of the P-band, rather than as a clearly resolved new feature. *Newbury et al [15]* reported that a substantial broadening of the P-band feature by the EHP emission may be expected for certain excitation levels. The composite broad band we observe at the highest excitation levels is in the region expected for both of these features (P and EHP bands). However, there is no indication that these bands are more clearly resolved at higher pump laser excitations. *Figure 6.9* demonstrates that the centre wavelength of the broad band shifts to longer wavelengths with increased excitation intensity, which is an attribute of the EHP band.

In *figure 6.10* the integrated intensity as a function of the excitation intensity for sample (i) is plotted. A large increase in the emission at an excitation level of $\sim 2000 \text{ kW/cm}^2$ is observed. This excitation level coincides with appearance of the P-band in the spectra, and may be partially due to the non-linear growth of the ex-ex emission, as discussed previously, however the appearance of a distinct speckled appearance to the emission strongly indicates that stimulated emission is occurring in the sample. Above this threshold of $\sim 2000 \text{ kW/cm}^2$ a violet speckled appearance can be clearly observed on the sample surface, which is not seen at the lowest excitation intensities or under HeCd excitation.

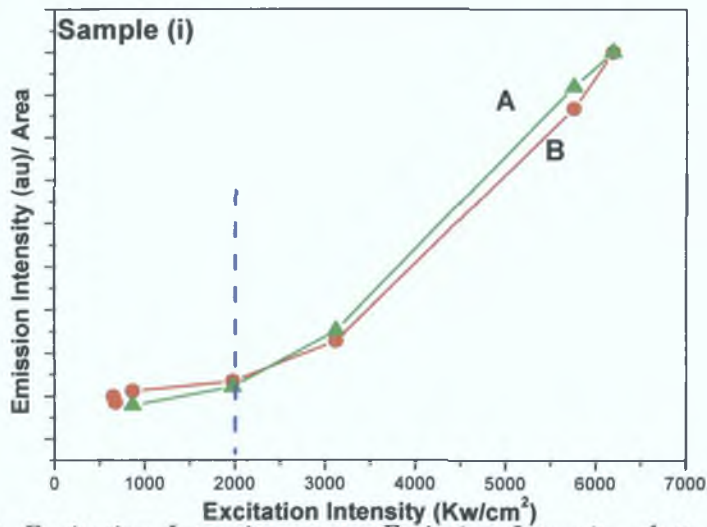


Figure 6.10: Excitation Intensity versus Emission Intensity plotted for ZnO sample (i) using the Nd:YAG laser. Data marked A is the emission intensity of the peak. The data labelled B is the area under the normalised peak.

Figure 6.10 also shows (A) the maximum emission intensity of the broad band, (B) the direct area of the band (taking into account baseline changes) plotted versus the pump laser intensity. A distinct threshold is seen in the data plotted in both manners. Based on the discussion earlier, this may be expected as non-linear optical processes such as ex-ex emission begin to dominate the spectra, however the appearance of a distinct speckle pattern show that substantial stimulated emission is taking place in the sample also (Appendix F and an example of the speckle cloud is seen in figure 6.12). No mode structure associated with intrinsic cavity formation is seen for this sample.

6.3.3: PLD ZnO sample (ii)

The PLD-grown ZnO material labelled sample (ii), which was annealed for 10 minutes and has a larger grain size than sample (i) was investigated in a similar manner to sample (i) in section 6.3.2 above and the resultant data is shown in figure 6.11. In most respects they are very similar to sample (i) with one broad band centered at $\sim 3.26\text{eV}$ for lower pumping intensities, which we associate with free exciton emission and the appearance of a band (3.17eV) at lower energies with increasing pumping excitation levels, associated with the P-band. As in sample (i) these bands are rather poorly resolved. There is also slight evidence of the appearance of the EHP band at the highest pumping intensities at a position of $\sim 3.10\text{eV}$. Once again a violet speckled pattern is observed visually on the sample surface at the highest pumping intensities.

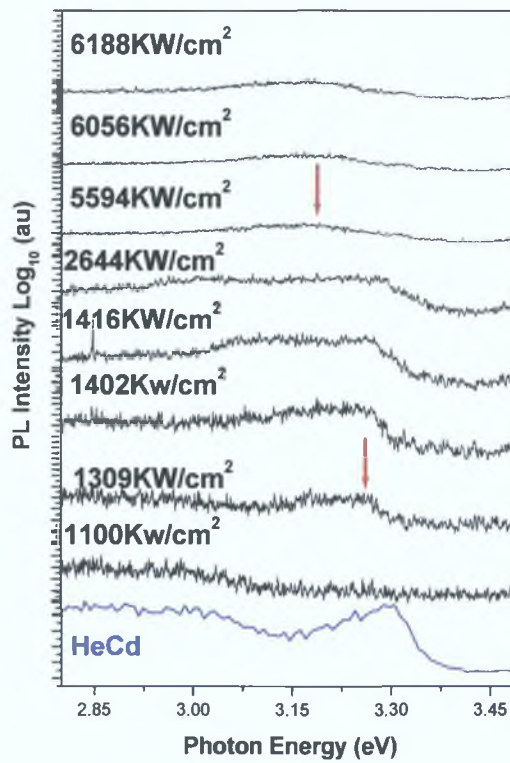


Figure 6.11: Graph of sample (ii) with the first band centred at $\sim 3.26\text{eV}$ and a second band at $\sim 3.17\text{eV}$. The excitation intensity range is from 6188 to 1100 kW/cm^2 . Slits $500\mu\text{m}$, Integration 1.0s, Increment 0.1nm. HeCd excitation spectra acquired at room temperature, Increment 1.0nm, Integration 1.0s, Slits $150\mu\text{m}$.

The separation between the FE peak and the band under high excitation centred at 3.17eV is $\sim 91\text{meV}$, similar to that determined for sample (i), in agreement with the assignment of this feature to the P-band.

A plot of the emission intensity as a function of excitation intensity (not shown) showed no evidence of a distinct threshold for emission, which may be due to the difficulties associated with correctly choosing background levels for integration. Nevertheless the observation of non-linear ex-ex and EHP emission and a distinctive speckled emission pattern indicates that in the high excitation regime some stimulated emission was seen for this sample also. Once again we have observed no evidence of mode structure in the emission.

6.3.4: PLD ZnO sample (iii)

Figure 6.13 shows the emission intensity versus energy for the PLD-grown ZnO sample labelled as sample (iii) with increasing excitation intensity. The band centered at $\sim 3.31\text{eV}$ dominates at lower pump laser intensities and may be associated with the free

exciton and as the pump laser intensity increases a second narrower band appears at $\sim 3.22\text{eV}$, which we associate with the P-band (separated by $\sim 100\text{ meV}$ from the free exciton position). We also note the presence of some modal-like structure at the low energy side of this second band observed at the highest pumping intensities, and the appearance of a speckled emission pattern at the highest pumping intensities (figure 6.12).

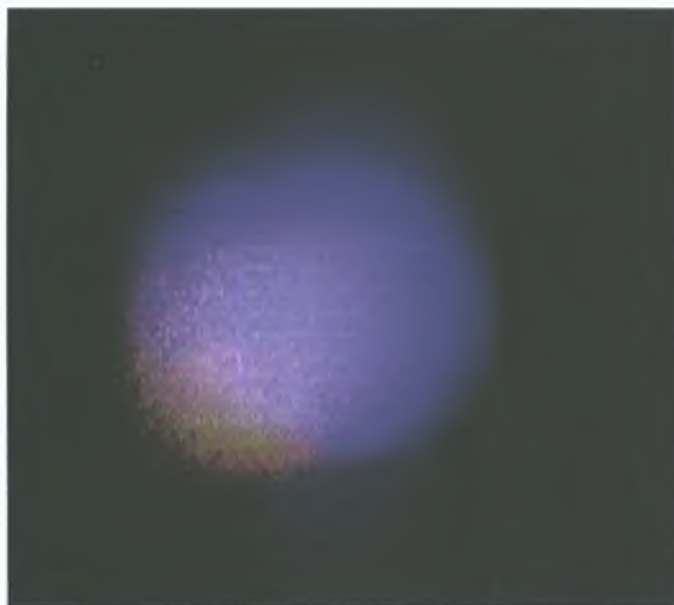


Figure 6.12: Image of the speckled emission cloud from sample (iii) that appears under excitation from the Nd:YAG laser taking with a digital camera in a darkened room.

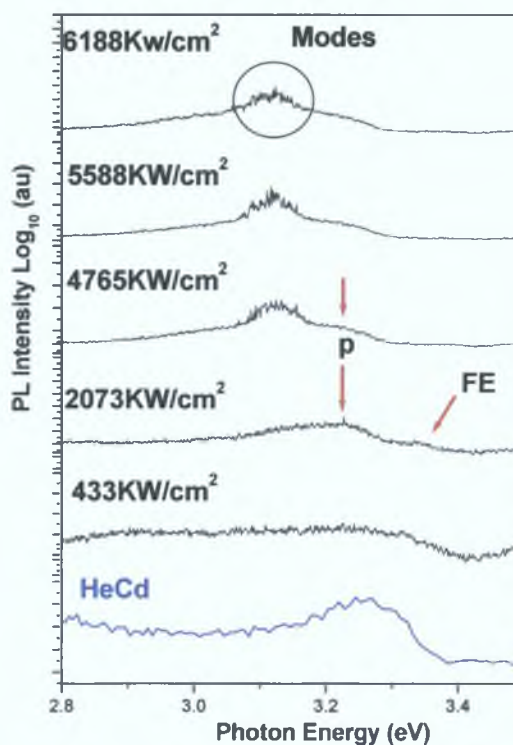


Figure 6.13: The emission intensity versus wavelength behaviour is plotted for sample (iii). Slits $500\mu\text{m}$, Integration 1.0s , Increment 0.1nm . HeCd excitation spectra acquired at room temperature, Increment 1.0nm , Integration 1.0s , Slits $150\mu\text{m}$.

There is substantial evidence of both non-linear, ex-ex emission and stimulated emission in this sample, in addition to the appearance of definite modal structure in the spectrum at the highest excitations.

Figure 6.14 illustrates the integrated luminescence intensity versus the excitation intensity, and displays a clear threshold at slightly greater than 2253 kW/cm^2 . Above the excitation intensity threshold of 2253 kW/cm^2 there is both an increase and narrowing of the peak, which is expected for the stimulated emission process.

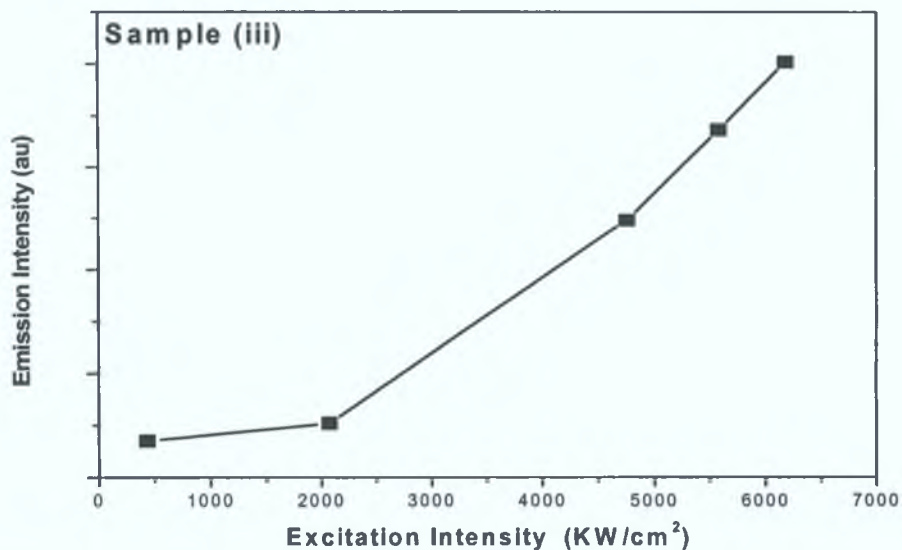


Figure 6.14: Excitation Intensity versus Emission Intensity of the EHP like band in sample (iii) with a “knee-joint” like effect.

The modal pattern varies from run to run, due to the inherently unrepeatability of the cavity formation mechanism in random lasing phenomena. However all spectra display a distinct “spiky” nature to the spectral emission from the P-band at high excitation levels, indicating that we are observing such modes being formed [16].

Sample (iii) shows the clearest evidence for strong stimulated emission and lasing phenomena of all the three samples, and also shows little or no evidence of EHP emission. These characteristics may be expected based on the discussion of the optical quality of the three samples deduced from PL and reflectance data in earlier chapters. Sample (iii) has consistently shown the strongest PL signals with the minimal evidence of signal quenching due to surface effects at grain boundaries, and, in particular, shows minimal evidence (of the three PLD samples) of perturbations due to depletion layer electric fields at grain boundaries. Thus the observation of the strongest stimulated

emission and lasing phenomena would naturally be expected from the sample with the lowest optical losses. The lack of observation of the EHP band at the excitation levels used indicates that the exciton state remains stable in this sample at such excitation levels, while it becomes unstable in samples (i) and (ii) due to the greater perturbing effects of the electric fields in these samples. Specifically we have noted previously that reflectance data from the three samples indicate that the exciton resonance is more strongly damped in samples (i) and (ii) indicating that the exciton state will be destabilised more easily with increasing excitation in these samples than in sample (iii), as we observe.

6.3.5: Discussion of spherical lens setup

The thresholds at which stimulated emission effects are seen appear relatively constant at $\sim 2000 \text{ kW/cm}^2$ in the various samples as noted earlier. Using the spherical lens, we produced an excitation area with a spot size of average diameter of 1.2mm. Once the excitation intensity increased above $\sim 6500 \text{ kW/cm}^2$ level, the samples started to become damaged through ablation as has been reported by other workers [9]. To reduce the effects of ablation of the samples, the dependence of threshold pump intensity on excitation area was investigated. Increasing the excitation area (at constant excitation density) should decrease the threshold pump intensity hence reducing the possibility of ablation. This was attempted but with no significant change observed. If the excitation area is changed to a significant extent then high excitation effects could stop [17].

Discernible modal structure was prominent for sample (iii). It was centered on the dominant P-band as shown in *figure 6.15*. Modal structure clearly indicates that the sample has reached the lasing threshold and the separation between the modes/spikes relates to the cavity structure. In conventional lasers where the cavity is defined clearly the modal structure is of a repeatable nature with a consistent separation between the modes.

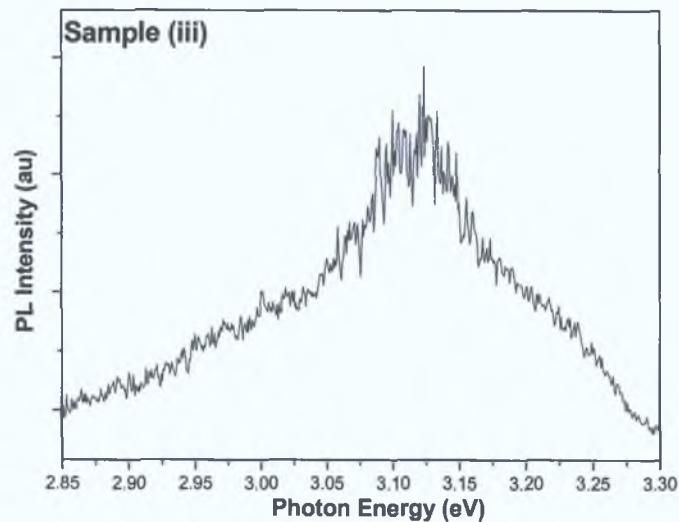


Figure 6.15: An example of the modal structure that appears from sample (iii). Slits $500\mu\text{m}$, Integration 1.0s, Increment 0.1nm.

Figure 6.15 shows an example of one such spectrum above the lasing threshold for sample (iii); most spectra in this work do not show such a consistently spaced set of modes. In fact, the mode pattern observed is not identically repeated from one spectrum to the next even under nominally identical conditions. This is perfectly reasonable given the experimental arrangement used. Each data point on the spectrum corresponds to a small number of laser shots, so consequently at each spectrometer reading one is sampling the spectrum at that wavelength for those particular laser shots. The details of the self-formed cavities are very sensitive to the local laser illumination. Slight changes in power, beam profile or position can cause changes in the nature of the self-formed cavities, which can cause the amplified modes to change. The work of *Bagnall et al.* [16] shows this sensitivity clearly when measurements are made with a PDA detector, capturing the full spectrum corresponding to a single laser shot. We also show this in the next chapter, where we use a PDA-based spectrometer to capture the full spectrum corresponding to individual laser shots. The data clearly shows the pulse to pulse variability of the lasing spectrum above threshold under nominally identical conditions. Our present data must be considered therefore as a crude “average” of the lasing spectra of a series of laser shots. Nevertheless, the self-formed cavity dimensions derived from these data do appear to correspond well to the data to that in the literature.

The implementation of a cylindrical lens in the high excitation arrangement was attempted and will be discussed immediately below, where a rectangular excitation stripe could be formed by imaging a certain stripe length onto the sample. The creation of an excitation stripe allows us to systematically study the variation of the effects we

see with stripe length and to attempt to measure the optical gain via the well-known variable strip length method, which is discussed in chapter seven.

6.4: Investigation of high excitation processes using a cylindrical lens

The cylindrical lens was made from fused silica with a focal length of 200mm and was mounted on a variable x-y stage for adjustment of the beam stripe position and focus. The excitation stripe was incident normal to the sample and positioned as close as possible to the edge of the sample so that the maximum amount of luminescence could be directed on to the entrance slits of the spectrometer. The stripe produced had dimensions of 5mm × 1mm when the sample was positioned at the focal length of the lens. Excitation intensities achievable were typically from 100-2200 kW/cm², using the neutral density filter and associated optics for control.

Reviewing the existing literature has shown that many groups have used the stripe profile of pump laser light for the investigation of stimulated emission from ZnO [9,17,18 for example]. This stripe profile of excitation could be considered as an “artificial” cavity in the traditional laser sense, and may be used to study the gain in the medium etc. The investigation of high excitation effects using the stripe length method is discussed for the bulk ZnO crystal and the PLD-grown ZnO materials.

6.4.1: Eagle Picher ZnO bulk material

Figure 6.16 shows the variation in the luminescence spectra as a function of increasing excitation intensity for the bulk ZnO material with a fixed area excitation stripe. The main band is at ~ 3.08eV and a second band appears at higher energies, at ~ 3.28eV, which is not present at low pumping intensities and only appears with the highest pumping intensities.

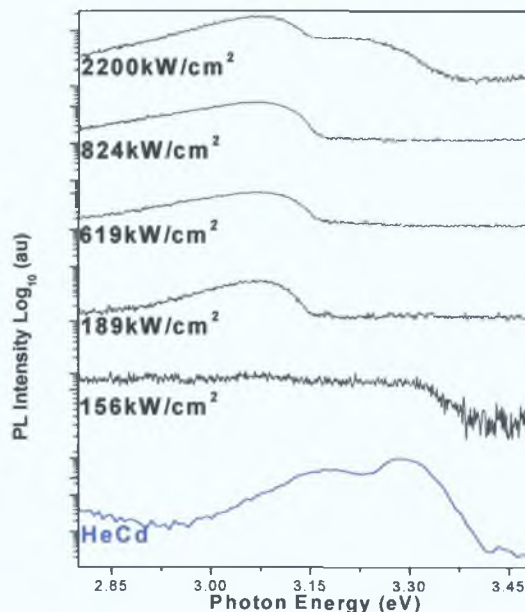


Figure 6.16: Graph of emission intensity versus wavelength for the bulk material at different excitation intensities using the cylindrical lens. Slits $500\mu\text{m}$, Integration 1.0s, Increment 0.1nm. HeCd excitation spectra acquired at room temperature, Increment 1.0nm, Integration 1.0s, Slits $150\mu\text{m}$.

Figure 6.16 also compares the spectra obtained under HeCd excitation and the stripe length excitation area with the Nd:YAG laser. The data is seen to be very similar to that observed using the spherical lens arrangement. The one main difference is the rather sudden growth of the higher energy peak (at ~ 3.28 eV), which is only seen at the highest pumping intensity, in contrast to the situation observed for the spherical lens excitation arrangement. Again we associate the peak in the region of ~ 3.28 eV with free exciton emission, while the emission centred at ~ 3.08 eV is due to the emission from the exciton-electron collision process. No evidence is seen for this excitation mode of a superlinear increase in the output intensity as a function of the excitation intensity, nor is any evidence seen of the appearance of stimulated emission from this sample. In nearly all respects the behaviour is identical to that observed earlier in section 6.3.1. The rather unusual sudden growth of the feature at 3.28 eV is attributed to some localised effects. When a similar measurement is made at a number of other regions on the sample surface, we obtain an apparently “normal” growth of both features. This is shown in figure 6.17 below. This behaviour may be due to the effects of sustained laser exposure at a particular area of the sample, resulting in a slight ablation and consequently perhaps a quenching of the shallower levels locally. Slight wandering of the excitation beam at higher powers may then account for the sudden appearance of the higher energy band in the spectrum.

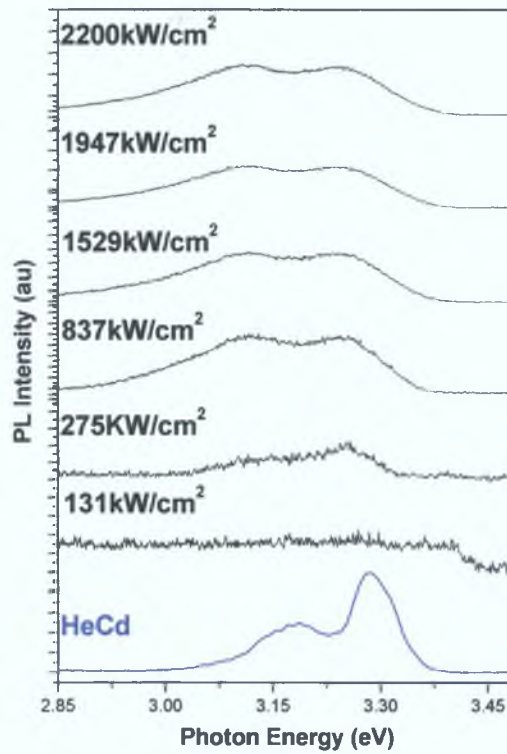


Figure 6.17: The ZnO bulk material at a different excitation position recorded with the cylindrical lens. Slits $500\mu\text{m}$, Integration 1.0s , Increment 0.1nm . HeCd excitation spectra acquired at room temperature, Increment 1.0nm , Integration 1.0s , Slits $150\mu\text{m}$.

6.4.2: PLD ZnO sample (i)

In figure 6.18 the emission spectra from sample (i) as a function of increasing excitation intensity with a fixed stripe excitation area is shown. Again the data is very similar to that shown in figure 6.9 under excitation using the spherical lens experimental arrangement. A threshold effect in the emission versus pumping intensity is seen at $\sim 1500\text{kW/cm}^2$.

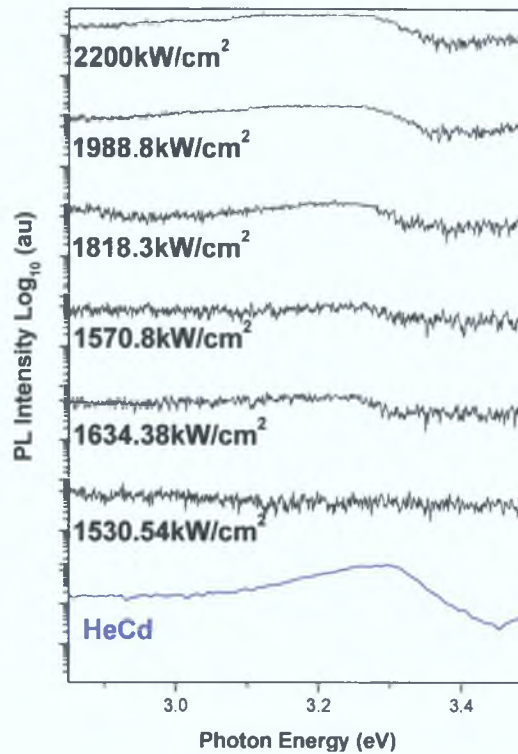


Figure 6.18: Graph of PLD-grown ZnO, sample (i) with the Nd: YAG and the cylindrical lens. Slits $500\mu\text{m}$, Integration 1.0s, Increment 0.1nm. The spectra are normalised to the intensity of the highest feature. HeCd excitation spectra acquired at room temperature, Increment 1.0nm, Integration 1.0s, Slits $150\mu\text{m}$.

6.4.3: PLD ZnO sample (ii)

The second of the PLD samples, sample (ii), which was annealed and has an average larger grain size than sample (i), was investigated with the cylindrical lens. Figure 6.19 illustrates the variation of the luminescence spectra for sample (ii) with varying pumping intensity. There is a broad band centered at $\sim 3.2\text{eV}$, labelled “X” which is consistently present with increased excitation intensity. At the highest pumping intensities a band appears at $\sim 3.12\text{eV}$, labelled “Y” on the lower energy side of the broad band. The pattern of growth of these bands is similar to that seen previously, firstly a P-band (X band) grows and at higher pumping intensities an EHP band appears at longer wavelengths than the P-band. There is evidence of cavity mode formation and lasing on the low energy side of the P-band (labelled Y) under excitation with the cylindrical lens, which was not seen in the case of the spherical lens

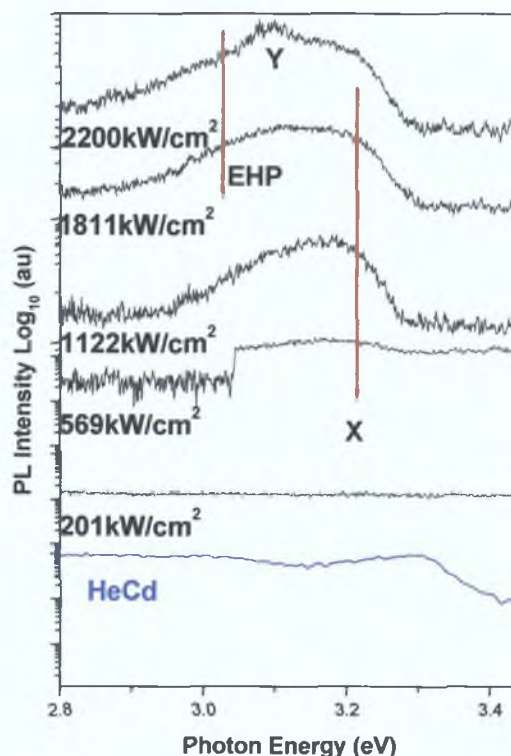


Figure 6.19: Sample (ii), cylindrical lens, with a band appearing at $\sim 3.12\text{eV}$ at the highest excitation intensity and a band consistent at $\sim 3.24\text{eV}$. The second lowest pumping excitation (569kW/cm^2) acquired spectra drops to 0 at approximately $\sim 3.06\text{eV}$; this is where the pump laser had been turned off. Slits $500\mu\text{m}$, Integration 1.0s , Increment 0.1nm . HeCd excitation spectra acquired at room temperature, Increment 1.0nm , Integration 1.0s , Slits $150\mu\text{m}$.

The separation between the FE band in the HeCd spectra and the band labelled X (3.24eV) of the Nd:YAG spectra is $\sim 90\text{meV}$, close to the P-band expected separation.

Figure 6.20 shows a plot of peak wavelength of the bands labelled X and Y against excitation intensity. There is no variation in the wavelength position of the P-band (X) with increasing excitation intensities, which is the expected behaviour. The Y band at 3.12eV tends with higher excitation intensities towards slightly longer wavelengths. Further increases in the pumping intensity caused the ablation of the sample.

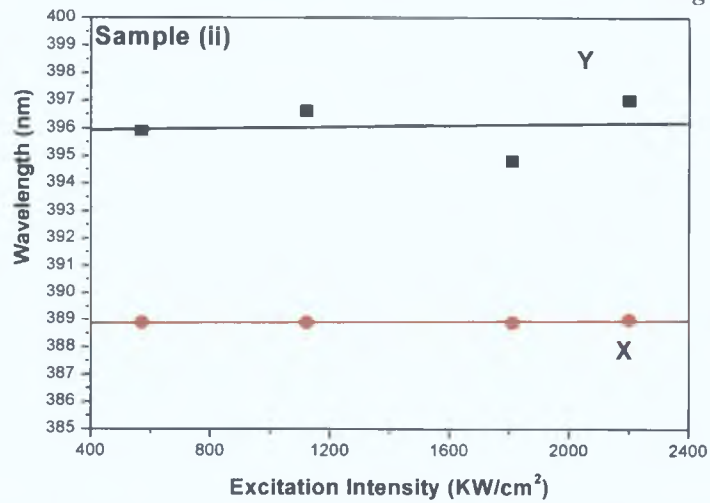


Figure 6.20: Comparison of the two bands (X and Y seen in figure 6.19) for wavelength peak position against excitation intensity.

The Gaussian fits of the bands X and Y were used to study the evolution of the emission intensity versus pumping intensity and are shown in figure 6.21. Both bands show evidence of a threshold at $\sim 1200 \text{ kW/cm}^2$. The presence of a speckled cloud at the sample surface was seen at the highest excitation intensities. The narrow linewidth and the superlinear increase of the Y band and the speckled appearance of the emission are all indicative of stimulated emission taking place in the sample. The presence of cavity modes under fixed stripe excitation, which was not seen under the spherical lens excitation, remains a puzzling feature of the data. It certainly indicates that the quality of this sample is just about good enough for lasing effects to be seen, and that the observation of such effects is sensitive to the details of the experimental arrangement. The longer path length for the stripe excitation may favour the appearance of modes due to the effects described in section 7.3

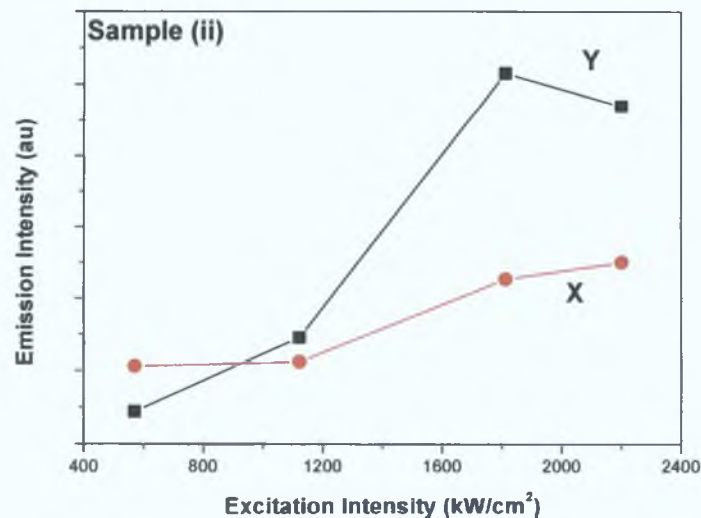


Figure 6.21: Emission intensity versus excitation intensity for the two bands in sample (ii). Graph is of the Gaussian area fit for the P like band (X) and the EHP like band (Y) with varying excitation intensity.

6.4.4: PLD ZnO sample (iii)

As seen previously, sample (iii) shows the strongest signatures of high excitation effects in its optical spectrum under excitation with the spherical lens. *Figure 6.22* shows the response of this sample as a function of increasing pump intensity under a fixed stripe excitation area. The data is once again very similar to that shown in *figure 6.9* under excitation using the spherical lens experimental arrangement, with a threshold in the emission intensity versus excitation intensity at $\sim 1000\text{kW/cm}^2$.

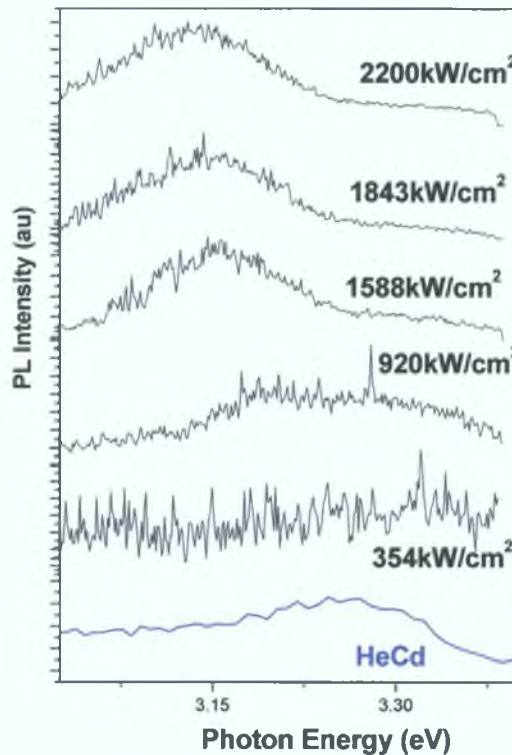


Figure 6.22: Sample (iii) spectra acquired with the cylindrical lens. The range of intensities goes from a max of 2200 to 560 kW/cm^2 . Slits $500\mu\text{m}$, Integration 1.0s, Increment 0.1nm. HeCd excitation spectra acquired at room temperature, Increment 1.0nm, Integration 1.0s, Slits $150\mu\text{m}$.

6.5: Discussion of cylindrical lens setup and comparison with data obtained using spherical lens experimental arrangement

The investigation of the Eagle Picher ZnO bulk material showed no substantial differences in the data obtained using the cylindrical and spherical lens experimental arrangements. The absence of any distinct threshold in the emission intensity indicates that the bands observed are associated either with the free exciton or exciton-electron collision-related emission and that ex-ex and EHP emission associated with higher excitation levels are not observed. No evidence of coherent emission or speckle-like appearance of the emission was seen for this material.

In contrast, all the PLD-grown samples showed evidence for threshold effects in the emission spectra and also for stimulated emission and even random lasing effects, in samples (ii) and (iii) where some evidence of mode structure on the non-linear bands was seen.

The origin of this distinct difference in behaviour of the bulk and PLD-grown samples for excitation in the same intensity range is not fully clear. A number of authors have noted that poly- or nanocrystalline thin films or nanostructures appear to show unusually low thresholds for the appearance of non-linear emission bands and optically pumped stimulated emission [19]. Various explanations have been given for this dramatic difference. The concept of giant oscillator strength for the exciton in low dimensional nanocrystalline structures has been suggested by a number of authors based on theoretical studies of the oscillator strengths in the transition from strong to weak coupling of the electron-hole pair [20]. However, the theoretical underpinnings of such an explanation are not appropriate for grain sizes of the order of 70 nm and greater (as in our samples) for a semiconductor such as ZnO [21]. In order to observe such giant oscillator strength effects the grain size would have to be a small multiple (< 4) of the exciton Bohr radius (~ 2 nm in ZnO). In any case, reflectance data on our samples have shown a reduction in the oscillator strengths compared to bulk material, rather than an increase [22]. Furthermore, even in the studies which show such effects, the EHP emission also appears at rather low thresholds [2]. There is no suggestion that the EHP emission threshold is strongly affected by the small grain sizes in such sample, and hence the appearance of the EHP band at low thresholds (~ 250 kW/cm²) remains a puzzling feature of such reports. Additionally, people have suggested that the waveguiding properties of the thin films have a substantial effect on the stimulated emission properties. The large gains observed have been attributed to the modification of the spontaneous emission properties by the waveguiding nature of the air/ZnO/sapphire slab ($n_{\text{air}}=1$, $n_{\text{ZnO}}=2.45$, $n_{\text{sapphire}}=1.8$) [23]. The critical film thicknesses identified for this effect are less than ~ 50 nm, which is substantially thinner than any of our films, and hence we do not believe that this waveguiding nature in the material is appropriate in our situation either.

6.5.1: Effects of exciton diffusion on non-linear processes

A simpler explanation, which has not been suggested before to the best of our knowledge, is that the exciton density in nanocrystalline materials may be substantially different to that in bulk material due to the absence of significant diffusion in the nanocrystalline samples due to grain boundaries. Given that the exciton-exciton collision-related P-band, and the EHP bands in which stimulated emission and lasing are normally seen grow in proportion to the second (or higher) power of the excitation intensity (and hence exciton density), even small changes in the exciton density may cause large changes in the emission from such bands. In nanocrystalline samples the exciton population created by optical absorption in the $\sim 65\text{nm}$ skin depth is rather strongly confined in this volume by the effects of finite film thickness and small grain sizes. In contrast the free exciton diffusion lengths in bulk material may be of the order of ~ 0.2 micron at 77K [24] and larger at room temperature [25], and thus the initially created exciton population will tend to diffuse and lower its density substantially in consequence.

We may make a rough estimate of the magnitudes of these effects. Many of the physical parameters associated with these effects are actually rather poorly known, or known only in a limited temperature range. Consequently the analysis will be approximate, but nevertheless it does support the main physical idea proposed.

For the PLD samples, the generation rate of the pump laser (355nm, assuming unit quantum efficiency in the absorption process) as it impinges on the PLD samples is

$$\frac{I}{hf} = G \quad (6.2)$$

where G is the total number of excitons generated per second, per unit area, I is the intensity of the laser per unit area, h is Planck's constant and f is the frequency.

In the PLD samples these excitons are confined within the generation volume of $\sim 65\text{nm}$, which is represented by the variable T below.

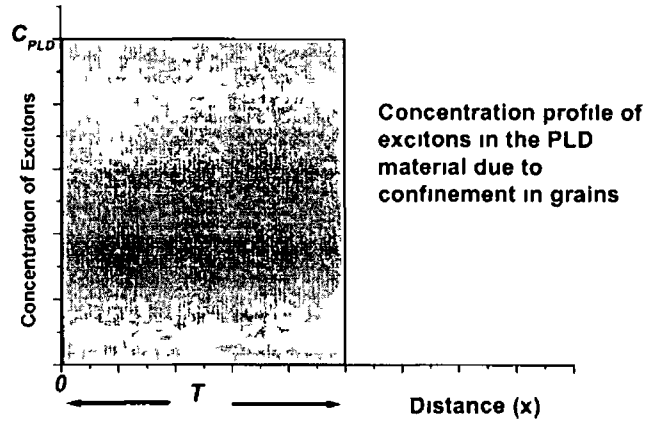


Figure 6.23 Concentration profile of excitons that is present in a polycrystalline sample

The total number of excitons recombining per unit time per unit area is

$$\frac{(C_{PLD}T)}{\tau} \quad (6.3)$$

C_{PLD} is the concentration at $x = 0$, T the thickness of the skin depth and τ the lifetime of the excitons. Letting the generation rate equal the total number of excitons in dynamic equilibrium we have

$$\frac{(C_{PLD}T)}{\tau} = \left(\frac{I}{hf} \right) \quad (6.4)$$

Therefore the concentration of excitons created in the polycrystalline material is given by

$$C_{PLD} = \frac{\tau}{T} \left(\frac{I}{hf} \right) \quad (6.5)$$

For the bulk material the generation rate of excitons is the same in the bulk material as the PLD materials within the same skin depth

$$G = \frac{I}{hf} \quad (6.6)$$

We will assume that within the skin depth the concentration is a constant value C_{BULK} , and that beyond this region it decays according to a normal diffusion profile [26], as shown below, where L is the diffusion length of excitons in bulk ZnO

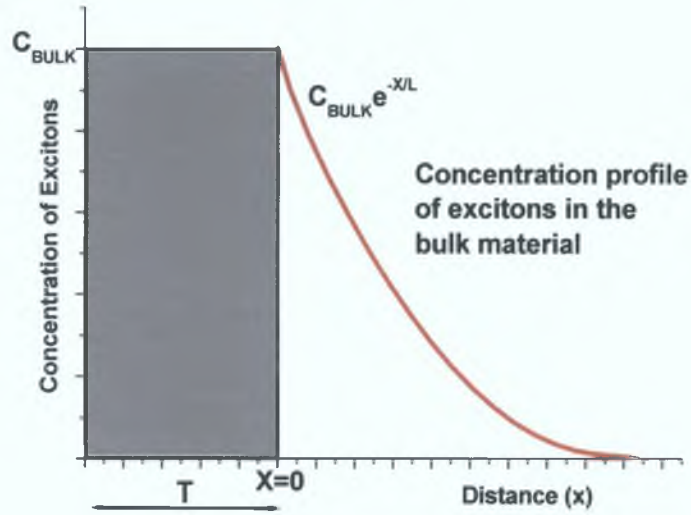


Figure 6.24: The concentration profile of excitons that is present in a bulk sample.

The total rate of loss of excitons per unit area from the skin depth region may be expressed as the sum of the recombination and diffusion current terms (in a manner similar to diffusion current losses in a laser diode structure [27]).

$$\left[\frac{C_0 T}{\tau} \right] + J_D = G \quad (6.7)$$

The first term represents the recombination of the uniformly distributed excitons in the skin depth of thickness T , which is the same as the PLD material term and the second term is the diffusion current density, J_D , from Fick's Law [28]:

$$J_D = D \left. \frac{\partial c}{\partial x} \right|_{x=0} \quad (6.8)$$

where D is the diffusion coefficient. At $x = 0$ the diffusion current has the form:

$$J_D = \frac{DC_{BULK}}{L} \quad (6.9)$$

Therefore the rate of loss of excitons from the skin depth region in the bulk material is equal to

$$\frac{C_{BULK} T}{\tau} + \frac{DC_{BULK}}{L} \quad (6.10)$$

Letting this equation equal the generation rate in the skin depth region in dynamic equilibrium, the concentration of excitons in the bulk can be calculated as:

$$C_{BULK} \left[\frac{T}{\tau} + \frac{D}{L} \right] = \frac{I}{hf} \quad (6.11)$$

We now have two equations to describe the concentrations of excitons in the bulk and polycrystalline material in terms of the generation rate (6.5, 6.11).

It is then possible to calculate the difference in exciton population levels for the bulk and the PLD material.

$$C_{BULK} \left[\frac{T}{\tau} + \frac{D}{L} \right] = \frac{I}{hf} = \frac{C_{PLD} T}{\tau} \quad (6.12)$$

$$\frac{C_{BULK}}{C_{PLD}} = \frac{T/\tau}{T/\tau + D/L} = \frac{1}{1 + \frac{D\tau}{TL}} \quad (6.13)$$

The diffusion length for excitons in ZnO has not been measured at all temperatures, but a value has been reported for low temperature (77 K) of $\sim 0.2\mu\text{m}$ [24] and we will use this value in the subsequent analysis. We have found no direct measurements of the exciton diffusion coefficient D , but we will use the relationship $L = \sqrt{D\tau}$ and a value of $\tau = 400\text{ps}$ [29], therefore the diffusion coefficient D is $0.0001\text{m}^2/\text{s}$. When we substitute these values into *equation 6.13* we find that the ratio of the concentrations in bulk to PLD material is given by

$$\frac{C_{BULK}}{C_{PLD}} = \frac{1}{4.0} \quad (6.14)$$

This result indicates that the concentration of excitons in the bulk material may be substantially different to that seen in the PLD-grown material.

Given that the non-linear optical emission bands grow proportional to the second or higher power of the exciton density, this indicates that such bands ought be at least one order of magnitude stronger in the nanocrystalline PLD-grown material based purely on this diffusion argument and is in agreement with our experimental results where non-linear bands were seen only in the PLD material. It must also be acknowledged that the exciton diffusion length value used here is taken from a single measurement at low temperature, and in principle may be substantially different for room temperature. It may be seen however that *equation 6.13* may be rewritten as:

$$\frac{C_{BULK}}{C_{PLD}} = \frac{T/\tau}{T/\tau + D/L} = \frac{1}{1 + \frac{L}{T}} \quad (6.15)$$

In systems where the diffusion length of carriers has been measured over a broad temperature range, the diffusion length L increases as a function of temperature [25] and

indeed often displays an exponential-type activation behaviour. Since broadly similar LO phonon scattering mechanisms govern the exciton scattering as a function of temperature [25,30] we propose that the diffusion length of the excitons increases with temperature in the bulk ZnO material, implying that the ratio of bulk exciton concentration to that in the PLD samples will reduce with increasing temperature substantially beyond that indicated in the calculations above, and that the non-linear emission bands will be very weak in bulk material at room temperature compared to low temperatures, as has been reported before[3].

In order to verify the expressions for carrier density we have used above we apply them to calculate the exciton densities generated under the normal threshold excitation intensities used in our experiments and compare them to the theoretical exciton Mott density in ZnO at (or below) which such threshold effects are expected. The Mott density is the density at which a transition from an insulating gas of excitons at lower densities to the metallic state of an EHP at higher densities occurs. In polycrystalline material, using the model above for nanocrystalline material with no diffusion allowed, the predicted carrier densities are given by the formula (assuming unit quantum efficiency in the absorption process):

$$C_{PLD} = \frac{I}{hf} \left[\frac{\tau}{T} \right] \quad (6.16)$$

At a pumping intensity of 900 kW/cm² (which is the threshold excitation level for PLD-grown sample (iii) using the cylindrical lens arrangement) it is estimated that the carrier density is $\sim 9.8 \times 10^{25} \text{ m}^{-3}$, based on an exciton lifetime of $\sim 400 \text{ ps}$, a skin depth of 65 nm and an excitation wavelength of 355 nm. This density is comparable to the Mott transition density given by [31]:

$$C_{MOTT} = \frac{k_B T}{2a_B^3 E_B^{ex}} \quad (6.17)$$

of $\sim 4 \times 10^{25} \text{ m}^{-3}$ expected in ZnO at room temperature; where $a_B = 18 \text{ \AA}$ is the exciton Bohr radius and $E_B^{ex} = 60 \text{ meV}$ is the exciton binding energy of ZnO. Thus the formulae we have used appear to adequately describe the exciton densities in the material. Assuming the low temperature diffusion length value of $\sim 0.2 \mu\text{m}$, the exciton density in bulk material under equivalent excitation intensity would be $\sim 3 \times 10^{25} \text{ m}^{-3}$, and even

less taking into account the substantially larger diffusion lengths expected at room temperature.

While this model of exciton diffusion lowering the exciton density in bulk material does provide a new perspective on the processes which may effect optical emission under high intensity pumping in ZnO, there remain a number of problems which cannot be explained fully by simple diffusion considerations.

We refer specifically to the ultra-low thresholds seen in certain single crystal ZnO nanowires at room temperature ($\sim 40 \text{ kW/cm}^2$) [32], which have lengths greater than the exciton diffusion length ($\sim 10 \mu\text{m}$) and hence ought to behave very similarly to bulk material, in sharp contrast to observed behaviour. There are some clues to the possible origin of this behaviour however. These ultra-low lasing thresholds only appear to be seen in nanorods grown by a gold- or self-catalysed process which leaves a metallic tip on the nanowire [33]. The effects of the attractive exciton interaction (due to image charge effects [34]) with the gold nanotip may lead to exciton localisation close to the metallic tip. Similar repulsive image charge effects which lead to “dead-layer” phenomena are known to exclude the exciton from a region $\sim 3\text{nm}$ from the sample surface. If the attractive image charge effect was to confine the exciton population in a region of similar dimension close to the nanowire tip (overcoming the exciton diffusion) one could account for such ultra-low thresholds. Obviously this is a rather speculative proposal. A range of lasing thresholds is seen in nanowire/nanorod systems, but, as mentioned previously, all reports of lasing are for samples grown by a metal-catalysed route. The nature of the nanowire tip (i.e. whether a metallic nanoparticle remains after growth) would appear crucial to the operation of this mechanism. Support for this theory is found in near-field scanning optical microscopy (NSOM) of the emission from single nanowires under high excitation [32], which shows the light emission strongly confined at one end of the nanowire, suggesting a confinement of the exciton population also.

The second area where difficulties arise is in the interpretation of e-beam excited high excitation effects in ZnO reported by *Hvam* [1]. While no evidence for lasing is seen in bulk material at room temperature, in agreement with our data, the lasing thresholds up to $\sim 240\text{K}$ are of the order of 4 A/cm^2 at a beam energy of 40 keV . Given that the penetration depth of the e-beam is $\sim 10\mu\text{m}$ at such beam energies, [35] and that one may

expect at most $\sim 10,000$ excitons generated per electron (by energy considerations), this is equivalent to a threshold of 100 kW/cm^2 of 355nm optical power. With the exciton population distributed over a depth of $\sim 10\mu\text{m}$, one may see that the exciton densities may be between 2 and 3 orders of magnitude lower than those in thin films excited optically, and the exciton-exciton collision processes would be expected to be $\sim 4\text{-}6$ orders of magnitude less intense. While the material quality in the interior of the sample ($10\mu\text{m}$ penetration depth compared to 100nm for thin nanocrystalline films) may be significantly better than that close to the surface, one cannot imagine that it can account for such high excitation effects and lasing being observed at such apparently low exciton densities.

6.5.2: Effect of differences in excitation geometry

Some slight differences in results between excitation using a spherical and cylindrical lens were observed, particularly for sample (ii). As mentioned previously, sample (ii) and sample (iii) show rather similar properties in terms of their PL, reflectance and other results. Consequently, the rather poor emission intensities and lack of strong modal structure under excitation with the spherical lens for sample (ii) compared to sample (iii) is rather puzzling. The data obtained using the cylindrical lens is more consistent with the broad range of experimental data for the two samples. We have noted however that the samples can be damaged over extended periods of exposure to the laser and that the emission may be quite dependent on the local sample and surface details, as seen in *figures 6.17*.

However, the data obtained for sample (ii) under excitation with the spherical lens was repeatable with different positions of the laser on the surface. The differences may be due to the longer path lengths for amplification in the fixed stripe length method. In section 7.3 we present evidence of light leakage from one random cavity mode to another and amplification along the stripe. Given that the thresholds for appearance of cavity modes is less for both samples (ii) and (iii) under excitation with the cylindrical lens arrangement (*table 6.1*), we propose that this leakage from one random cavity to another and amplification along the illuminated stripe is the reason for the lower threshold for the appearance of cavity modes in both samples (ii) and (iii).

Lens	Sample (ii)	Sample (iii)
<i>Spherical</i>	Not Seen	$\sim 4500\text{Kw/cm}^2$
<i>Cylindrical</i>	$\sim 2200\text{kW/cm}^2$	$\sim 1600\text{kW/cm}^2$

Table 6.1: Excitation intensity thresholds for the appearance of cavity modes in samples (ii) and (iii) for different excitation profiles.

Sample (ii) under excitation with the spherical lens is just below the critical pump power, while the increased path lengths under fixed stripe excitation allow cavity modes to be observed in the available pump power range.

Chapter Six References

- [1] J.M.Hvam, *Solid State Commun.* 12, (1973), 95.
- [2] Z.K.Tang, P.Yu, G.K.L.Wong, M.Kawasaki, A.Ohtomo, H.Koinuma, Y.Segawa, *Solid State Commun.* 103, (1997), 459.
- [3] C.Klingshirn, *Phys.Status Solidi B* 71, (1975), 547.
- [4] C.Klingshirn, H.Haug, *Physics Reports*, 70, No.5, (1981), 315.
- [5] H.Schrey, C.Klingshirn, *Phys.Stat.Sol. (b)* 90, (1978), 67.
- [6] H.J.Ko, Y.F.Chen, T.Yao, K.Miajima, A.Yamamoto, T.Goto, *Appl. Phys. Lett.* Vol.77, No. 4, (2000),537.
- [7] H.Haug, S.Schmitt-Rink, *J.Opt.Soc.Am.B*, Vol 2, No 7, (1985).
- [8] C.Klingshirn, *Semiconductor Optics*, Springer, (1997).
- [9] Y.Chen, D.Bagnall, T.Yao. *Mat. Sci. Eng.*, B75, (2000),190.
- [10] D.M.Bagnall, Y.F.Chen, Z.Zhu, T.Yao, M.Y.Shen, T.Goto, *App. Phys. Lett.*, Vol 73, No 8, (1998),1038.
- [11] J.I.Pankove, *Optical Processes in Semiconductors*, Dover Publications, New York, (1971).
- [12] A.Yamamoto, K.Miyajima, T.Goto, H.J.Ko, T.Yao, *J. Appl. Phys.*, Vol 90, No 10, (2001),4973.
- [13] A.Mitra, R.K.Thareja, *J.Appl.Phys.*, Vol 89, No 4,(2001),2025.
- [14] E. McGlynn, J. Fryar, G. Tobin, C. Roy, M. O. Henry, J. -P. Mosnier, E. de Posada, J. G. Lunney, *Thin Solid Films*, Vol 458,Iss.1-2, (2004), 330.
- [15] P.R.Newbury, K.Shahzad, D.A.Cammack, *Appl.Phys.Lett.* 58, (1991), 10.
- [16] D.M.Bagnall, A.Ralston, K.P.O'Donnell, P.C.Smith, P.Wright, B.Cockayne, *Appl. Phys. Lett.*, 66, (1995), 12.
- [17] H.Cao, Y.G.Zhao, S.T.Ho, E.W.Seelig, Q.H.Wang, .P.H.Chang, *Phys. Rev.Lett.*, Vol 82, No 11, (1999),2278.
- [18] P.Yu, Z.K.Tang, G.K.L.Wong,M.Kawasaki, A.Ohtomo, H.Koinuma, Y.Segawa, 23rd International Conference on the Physics of semiconductors, edited by M.Scheffler and R.Zimmermann, (World Scientific, Singapore, 1996),1453.
- [19] M.Kawasaki, A.Ohtomo, I.Onkubo, H.Koinuma, Z.K.Tang, P.Yu, G.K.L.Wong, B.P.Zhang, Y.Segawa, *Mat.Sci.Eng*, B56, (1998), 239.
- [20] A. Ohtomo, M. Kawasaki, Y. Sakurai, Y. Yoshida, H. Koinuma , P. Yu, Z.K. Tang, G.K.L. Wong, and Y. Segawa, *Mater. Sci. and Eng. B* 54, (1998), 24.
- [21] Y.Kayamura, *Phys.Rev.* B38, (1988), 9797.

- [22] E McGlynn, J Fryar, M O Henry, J P Mosnier, J G Lunney, D O'Mahony, E de Posada *Physica B* 340–342, (2003), 230
- [23] P Yu, Z K Tang, G K L Wong, M Kawasaki, A Ohtomo, H Koinuma, Y Segawa, *J Crys Growth* 184-185, (1998), 601
- [24] R L Weiher, W C Tait, *Phys Rev B*, Vol 5, No 2, (1972), 623
- [25] T L Tansley, *J Phys D*, Vol 5, (1972), 1146
- [26] B G Streetman, *Solid State Electronic Devices*, Prentice Hall, (1995), 120
- [27] H C Casey Jr, *J Appl Phys* Vol 49, part 7 (1978), 3684
- [28] S M Sze, *Physics of semiconductor devices*, 2nd edition, New York, Wiley, (1981)
- [29] J Wilkinson, G Xiong, K B Ucer, R T William, *Nonlinear Optics*, Vol 29, (2002), 529
- [30] L Chernyak, A Osinsky, H Temkin, J W Yang, Q Chen, M Khan et al, *Appl Phys Lett*, Vol 69, part 17 (1996), 2531
- [31] Y Chen, N T Tuan, Y Segawa, H J Ko, S K Hong, and T Yao, *Appl Phys Lett* 78, (2001), 1469
- [32] P Yang, *Advanced Functional Materials*, Vol 12, No 5, (2002), 323
- [33] M H Huang, S Mao, H Feick, H Yan, Y Wu, H Kind, E Weber, R Russo, P Yang, *Science*, 292, (2001), 1897
- [34] J D Jackson, *Classical Electrodynamics*, 2nd edition, New York, Wiley, 1975
- [35] B G Yacobi, D B Ho, New York, London, Plenum, (1990)

Chapter Seven

High excitation and Random lasing results II

The variable stripe length (VSL) technique is used to measure the stimulated emission and gain of semiconductor materials. In the VSL method the excitation stripe length is adjusted while the excitation intensity remains constant, and the resultant emission is monitored. In section 7.1 the results obtained applying the VSL method at room temperature is presented and a similar investigation at low temperatures is discussed in section 7.2. The gain results from the VSL method are outlined in section 7.3. In order to obtain better spectral resolution of these high excitation effects, the spectrometer and PM tube arrangement are replaced by a charge-coupled device (PDA) and these results are discussed in Section 7.4.

7.1: Variable stripe length data for samples at room temperature

The experimental arrangement for the variable stripe length (VSL) [1] method has been discussed in section 2.3.4. In this experimental arrangement the excitation stripe length was initially set to 0.2mm and the stripe length was increased to an average maximum length of 2.0mm, with a step size of 0.2mm. This adjustment of the excitation stripe length was carried out using the teeth of a vernier calliper, which has an instrumental accuracy of $\pm 0.05\text{mm}$. A neutral density filter placed in the laser path resulted in a decrease in the pump laser line peak intensity recorded by the spectrometer, dependent on the filter setting. The acquisition of VSL results included a set without the neutral density filter i.e. at the highest excitation intensity, and two sets at lower intensities i.e. neutral density filter at different filter levels in the path of the pump laser beam. The input pump laser intensity was kept constant and the stripe length was varied in each of the three measurements. Therefore for each sample there were three sets of VSL results at high, medium and low pump laser intensity enabling the study of high excitation effects in the Eagle Picher material and the PLD-grown ZnO samples as a function of varying stripe length.

7.1.1: Eagle Picher bulk ZnO

*Figure 7.1 shows the spectrum obtained at a 1.8mm stripe length from the Eagle Picher bulk material at an excitation density of $\sim 6100\text{kW/cm}^2$. One dominant band at $\sim 3.10\text{eV}$ and two smaller bands at higher energies are observed. Comparing the spectra obtained with a Nd:YAG excitation in *figure 7.1* with a HeCd excited spectrum (not shown) allows identification of the bands as in previous chapters. The lines marked “X” and “Y” correspond to those observed in chapter 6 for this sample, and are associated with free exciton and exciton-electron collision-related emission respectively. A small*

feature at higher energy, labelled "X*" is also seen, and is marked by an arrow in the figure. This may be due to emission from the B-exciton or emission from the upper polariton branch of the exciton-polariton [2,2a]

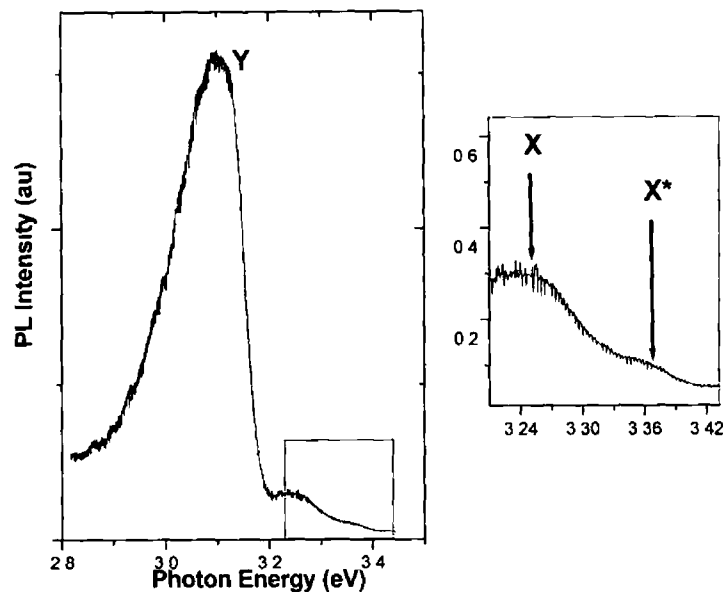


Figure 7.1 Spectra shown for the Nd:YAG laser with an excitation stripe of 1.8 mm. The main peak (Y) is at ~ 3.10 eV with two smaller peaks at (X*) ~ 3.35 eV and (X) ~ 3.24 eV. Inset shows close up of peaks X* and X. Slits $500\mu\text{m}$, Integration 1.0 s, Increment 0.1 nm. The data has been normalised according to the procedure outlined in chapter 2, section 2.3.4.

The results obtained at lower excitation intensities (21% and 50% of the maximum intensity) yield little extra information (figure 7.2). The X* band disappears at both lower pump laser intensities while the X band becomes less prominent. The two higher energy bands do not appear until the stripe length is increased or the excitation intensity increased above a certain point. However, these bands do not show any evidence of non-linearity in the emission versus excitation intensity data, and, given the variability of the X band as a function of laser position on the sample surface noted previously, the data here continues to support the previous assignment of these bands to free exciton and exciton-electron collision-related emission respectively.

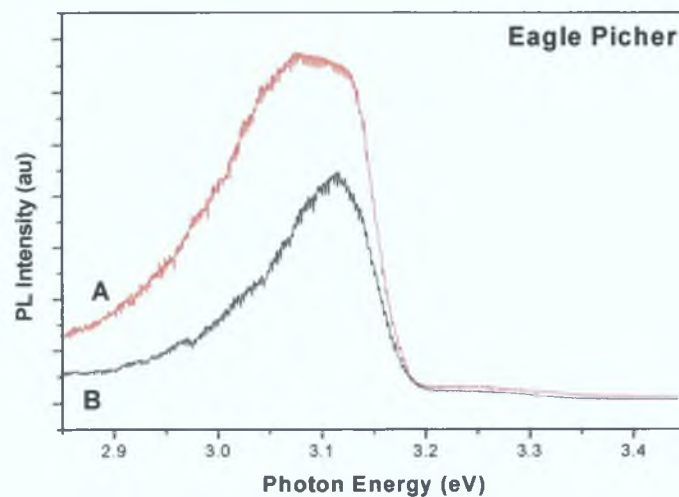


Figure 7.2: Comparison of the spectra at lower energies with both having the same stripe length of 2.00 mm. A is at pump laser intensity of 50% of the total intensity. B is of the lower pump laser intensity, 21% of the total intensity. Slits 500 μ m, Integration 1.0s, Increment 0.1nm.

Plotting a graph of the peak wavelength of band Y versus cavity length reveals that the peak shifts ~ 2 nm as the stripe length is increased as shown in figure 7.3. The other two bands remain at a constant peak wavelength even with varying input pump laser intensities and stripe lengths (not shown).

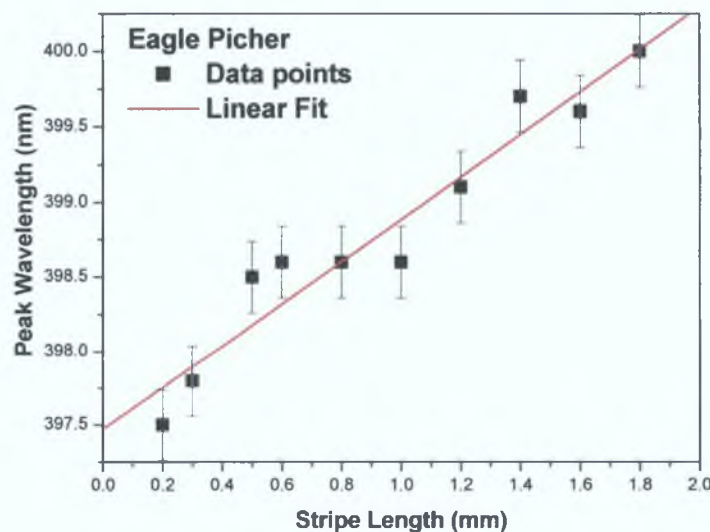


Figure 7.3: A graph of the main band "Y" as it shifts to longer wavelengths with increased cavity length.

Hence we conclude that the bulk material shows little or no evidence of non-linear emission bands, and we conclude that the bands present are associated with the free exciton and exciton-electron collision-related emission.

7.1.2: PLD ZnO sample (i)

Previous high excitation studies of the PLD-grown sample (i) (section 6.3.2 and 6.4.2) showed some indications of the occurrence of high excitation effects. Data taken using the VSL technique show very similar spectra to those observed in chapter 6, e.g. *figure 6.9*, with the appearance of a free exciton feature and features associated with the P-band and the EHP emission band, as shown in *figure 7.4* below.

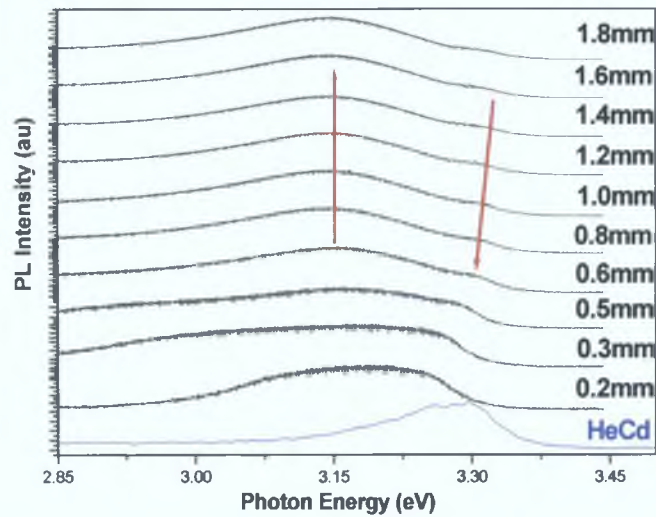


Figure 7.4: Spectra of sample (i) under medium pump laser intensity ($\sim 3000\text{kW}/\text{cm}^2$) with excitation stripe length increasing from 0.2mm to 1.8mm. Slits $500\mu\text{m}$, Integration 1.0s, Increment 0.1nm. HeCd excitation spectra acquired at room temperature, Increment 1.0nm, Integration 1.0s, Slits $150\mu\text{m}$. Data normalised.

The data from sample (i) shown in *figure 7.5* below, shows slight evidence of exponential signal growth, but only over a very restricted range much less than an order of magnitude. This is in agreement with the data in chapter 6, where indications of stimulated emission were observed. Values of the gain over the region of exponential growth for this sample and the other PLD-grown samples will be given in section 7.4.

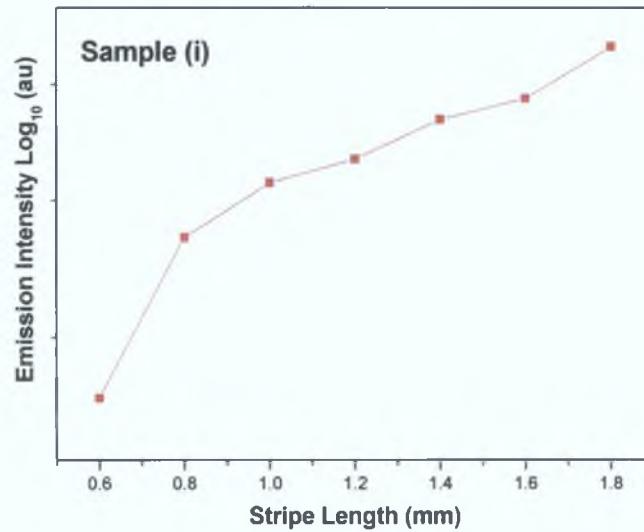


Figure 7.5: The emission intensity of $\sim 3.15\text{eV}$ band in sample (i) at the highest excitation intensity ($\sim 6000\text{kW/cm}^2$) versus stripe length.

Results of a rather similar nature have been reported by *Zhang et al* [3] for emission output versus laser output as shown in *figure 7.5*, in which it was considered that this pattern presented evidence of stimulated emission taking place in the ZnO samples. However the threshold effect observed in *figure 6.10* is not very abrupt and no evidence is seen of cavity modes in the emission. *Zhang et al's* work shows no signs of these definite threshold effects or cavity mode formation and yet they reported these effects as the result of stimulated emission in the material [4]. Significant differences are apparent in the literature concerning what effects actually constitute “evidence” of stimulated emission and lasing, and great care is needed when judging the results presented.

It may be noted from *figure 7.4* that the lowest pump laser intensity/lowest stripe length spectra showed only one broad band centred on $\sim 3.29\text{eV}$. When the pump laser intensity or stripe length increased this band narrowed considerably to one dominant band centered at $\sim 3.15\text{eV}$. This pattern was repeated for the same stripe length with different pump laser intensities.

7.1.3: PLD ZnO sample (ii)

When the emission from sample (ii) was studied as a function of excitation intensity (sections 6.3.3 and 6.4.3), high excitation effects and stimulated emission were observed from the sample. Under excitation using a spherical lens evidence of stimulated emission was found, and evidence for cavity mode formation and lasing was seen under excitation with the cylindrical lens. The quality of this sample was seen to be

intermediate between that of sample (i) and sample (iii), and in some sense is “on the edge”, with changes in excitation geometry leading to a loss of lasing behaviour.

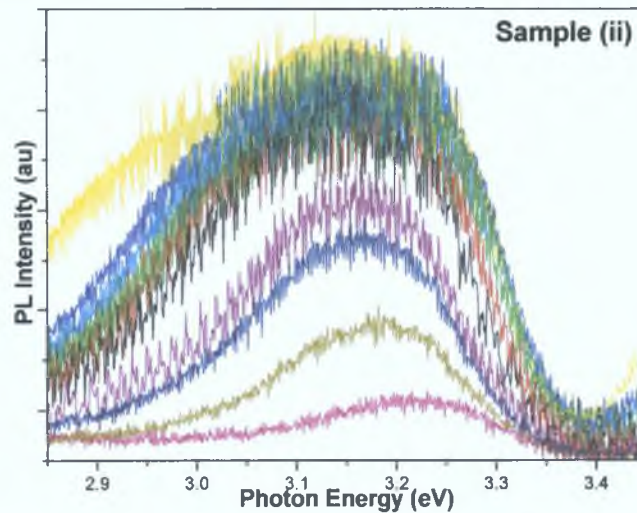


Figure 7.6: Sample (ii) spectra acquired with the Nd:YAG laser for different stripe lengths (2.00mm to 0.2mm). Slits $500\mu\text{m}$, Integration 1.0s, Increment 0.1nm. Data normalised.

Using the Gaussian fit of this broad band the plot of the emission intensity (on a log scale) as a function of cavity length as shown in figure 7.7. Again, there is some evidence of exponential signal growth as a function of cavity length, by approximately an order of magnitude, greater than that observed for sample (i).

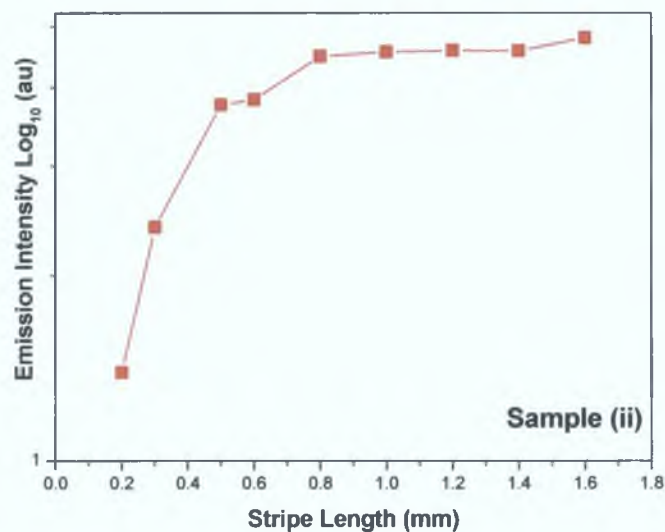


Figure 7.7: Plot of stripe length versus emission intensity for sample (iii).

The sensitivity of this sample to excitation geometry is shown in figure 7.8 below, where spectra acquired in different experimental runs using similar excitation intensities are shown. In one case (using a fixed stripe length of 5mm) evidence of cavity formation and lasing is clearly seen, as discussed in section 6.4.3, while in the other

case (using the VSL set-up, with a stripe length of 2mm) no such behaviour is observed. This supports the proposal in section 6.5.2.

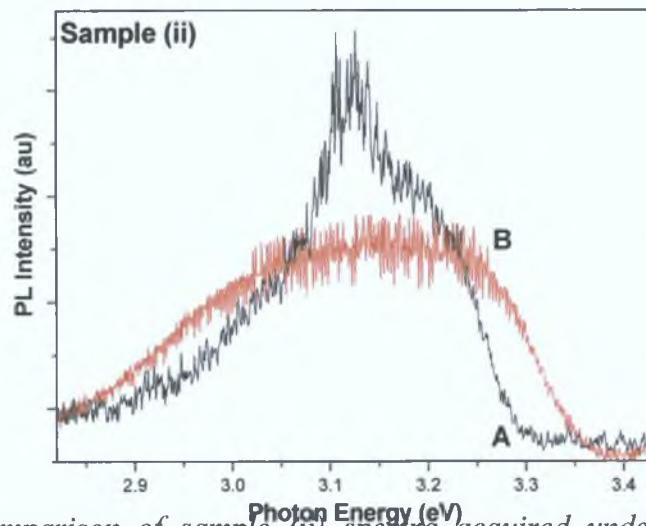


Figure 7.8: Comparison of sample (ii) spectra acquired under fixed stripe length arrangement (A) and the VSL method (2.00mm) (B).

7.1.4: Sample (iii)

Sample (iii) has consistently demonstrated high excitation effects, stimulated emission and lasing (sections 6.3.4 and 6.4.4). In figure 7.9 at low stripe lengths (0.2mm) there is one broad band due mainly to free exciton recombination and as the stripe length increases the P-band becomes visible in the spectra. At the largest stripe lengths modal structure is observed on this band, which is very prominent at the longest stripe length (2.00mm).

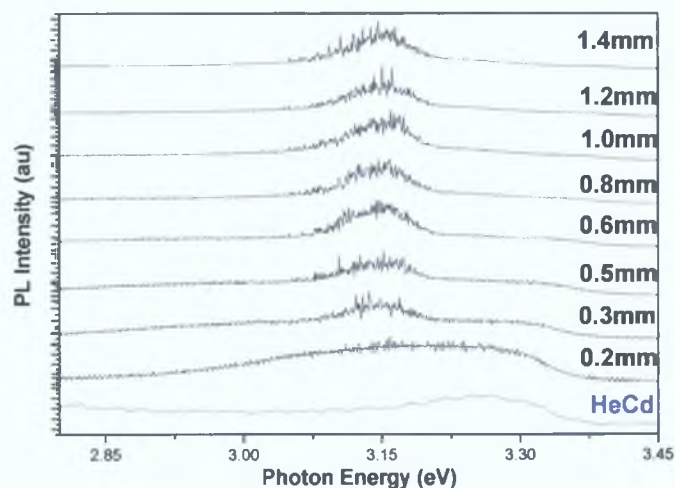


Figure 7.9: Sample (iii) under investigation with the VSL method, pump laser intensity is the same throughout with the stripe length varying. Slits $500\mu\text{m}$, Integration 1.0s, Increment 0.1nm. HeCd excitation spectra acquired at room temperature, Increment 1.0nm, Integration 1.0s, Slits $150\mu\text{m}$. Data normalised.

The spectrum acquired at an intermediate stripe length of 1.4mm is shown in *figure 7.10* and is compared to a HeCd induced spectra of the same samples. The bands are labelled X*, ~ 3.31eV (376nm), X, 3.19eV (388nm) and Y, 3.13eV (396nm) respectively. The X* and X bands are aligned with the FE of the HeCd spectra (A) and the high energy side of the P-band. The band labelled Y appears only at higher pumping intensities or cavity lengths and is associated with the formation of cavity modes and lasing in this spectral region of the P-band gain curve.

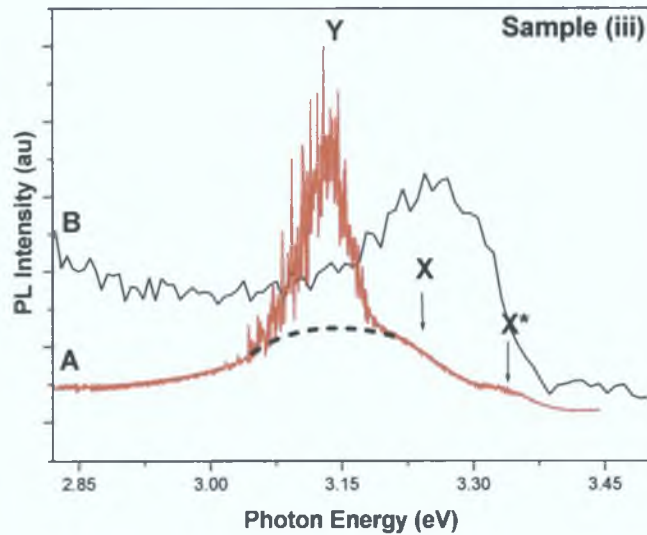


Figure 7.10: Sample (iii), for the highest pump laser intensity at a stripe length of 1.4mm. Indicated are the three bands (X,X ,Y) that appear at longer stripe lengths under the excitation of the Nd:YAG laser (A). Slits 500 μ m, Integration 1.0s, Increment 0.1nm. Also seen is the HeCd spectra (B) obtained at room temperature. Slits 50 μ m, Integration 1.0s, Increment 1.0 nm*

The separation between the FE and the underlying P-band, shown with a dotted lineshape, is of the order of ~ 100meV, When the data was acquired without the neutral density filter, i.e. highest average pumping intensity (~6000kW/cm²), there was no measurable wavelength shift in the any of the bands with increased cavity length.

The three bands X*, X and Y are fitted with a Gaussian curve and the area under the gaussian fits plotted against the excitation length and shown in *figure 7.11* on a log scale. Inspection of the graph shows that both peaks X and Y grows exponentially over a range of approximately an order of magnitude with increasing cavity length, confirming their role in gain processes in the material. The X* band shows very little change in intensity with an increase in the cavity length, as one would expect for the FE emission.

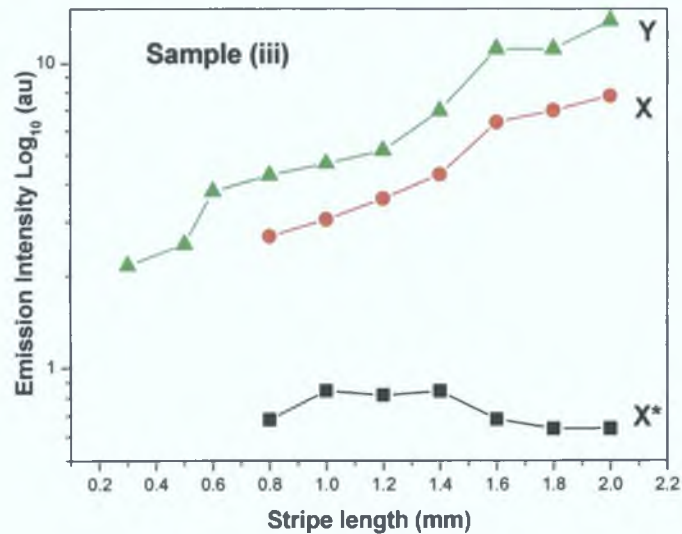


Figure 7.11: Comparison of the three bands (Gaussian area) versus the cavity length. This is from the spectrum that appears in figure 7.11.

In figure 7.10, band Y shows modal structure, as discussed previously in section 5.6.2. This behaviour, and the exponential growth of this band in the VSL mechanism, presents something of a puzzle. The excitation stripe length (1.4mm) does not agree with the separation between the peaks as predicted by equation 6.2. The combined effects of excitation pulse variation, the lack of temporal and spatial resolution in acquisition equipment as well as theoretical small mode spacing would suggest that modes will not be resolved in this sample if the stripe lengths used in the VSL technique (1.4mm) define the cavity. Furthermore, the cavity defined by such a gain-guiding mechanism would be rather weakly guiding and lossy. It should also be noted there is no indication that these modal features change separation as the stripe length increased (figure 7.9). This would be expected if the excitation stripe length were defining the cavity. Instead, our data indicate that internal, random cavities are produced at different stripe lengths, and this process is reflected in the random modal structure. However, it appears that amplified emission can “leak” from one random, self-formed cavity to the next along the excitation stripe defined by the pump laser, being amplified continuously, giving rise to the exponential growth in the Y-band and its appearance only at longer cavity lengths which we observe. A more detailed discussion this modal structure and behaviour will take place in section 7.3.

At very small stripe lengths the modal structure disappears (see figure 7.12 below). This also indicates that the modal structure observed at longer stripe lengths is due to light propagation, gain and lasing in more than a single self-formed cavity, and that the

typical gain during propagation in a single cavity is insufficient to enable lasing (as proposed earlier in section 6.5.2). At very short stripe lengths such effects may be especially important. An additional possibility is that at very small stripe lengths, laser diffraction through the 0.2mm calliper jaws may reduce the local intensity below the threshold.

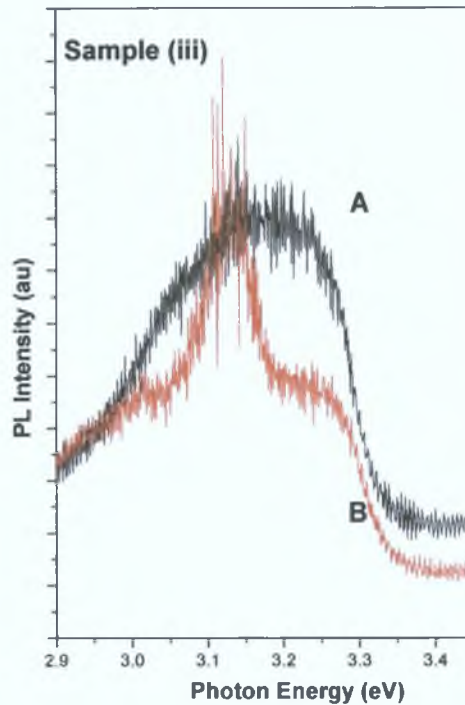


Figure 7.12: Comparison of sample (iii) for two different stripe lengths. A spectrum is at 0.2mm and B at 0.3mm. Slits 500 μ m, Integration 1.0s, Increment 0.1nm.

Figure 7.13 shows the data obtained when the stripe length remained constant at 2.00mm and the pumping intensity varied using the neutral density filter for PLD sample (iii). Spectrum (A), corresponding to the lowest pump laser intensity, shows no indication of the third band Y. With the medium pump laser intensity (B) the band Y begins to appear. At the highest pump laser intensity (C) the Y band becomes dominant. This data indicates that at a fixed cavity length, only above a certain material gain does the random lasing process occur, in an exactly similar manner to that shown in section 6.4.4, but in this case the cavity length is 2mm, rather than 5mm. This reinforces that interpretation that the modal structure is due to random cavity formation within the illuminated region, rather than the illuminated stripe defining the cavity, as is normally the case in VSL studies of single crystal materials. Similar results are obtained for a 1mm stripe length.

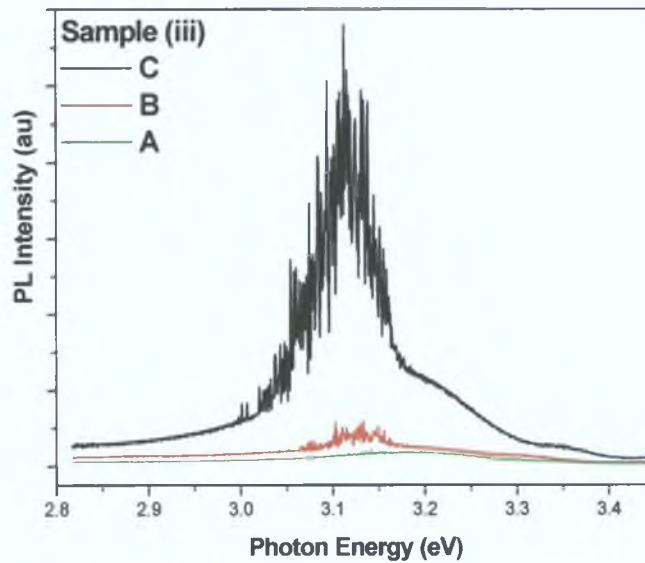


Figure 7.13: Comparison of sample (iii) under three different excitation pump laser intensities but with the same stripe length of 2.0mm. C is for the highest intensity ($\sim 6000\text{kW}/\text{cm}^2$). B is for the medium intensity ($\sim 3000\text{kW}/\text{cm}^2$). A is for the low intensity ($\sim 1200\text{kW}/\text{cm}^2$). Slits $500\mu\text{m}$, Integration 1.0s, Increment 0.1nm.

7.1.5: Discussion of the VSL technique at room temperature

The application of the VSL technique at room temperature to the bulk and PLD-grown samples has largely confirmed the data and interpretations discussed in chapter six.

One of the most unusual features of the data from PLD-grown samples (ii) and (iii) is the evidence for the involvement of multiple self-formed cavities in the laser emission from such samples as the light leaks from one cavity to suitable (in terms of resonant wavelengths) adjacent cavities, being amplified at each stage, but with the modal frequencies being determined by the local self-formed cavities rather than the pump laser stripe length.

7.2: Low Temperature VSL studies

Bulk ZnO pumped by an electron beam has produced stimulated emission and lasing effects at cryogenic temperatures [5, 6]. The variable stripe length method has resulted in some of the clearest evidence of high excitation effects in bulk material at these temperatures. In fact, as mentioned in chapter 6, no evidence for lasing has been found in bulk ZnO above $\sim 240\text{K}$ [6]. Therefore, the VSL method is used here at low temperatures to investigate high excitation effects in both bulk and single crystal material. It was broadly expected that at lower temperatures thermal effects are substantially reduced, including exciton diffusion, leading to increases in the exciton

density for a particular pump intensity in bulk material, and also, more generally, improved optical emission and smaller linewidths, as is seen for most materials systems [7] and consequently that it would be substantially easier to see the onset of high excitation effects, stimulated emission and lasing at such temperatures. The ZnO samples were all investigated at low temperatures ($\sim 9\text{K}$) with the same experimental arrangement used for the RT VSL measurements but with the samples placed inside a cryostat. Low temperature spectra of the non-linear bands should be shifted to higher energies (shorter wavelengths) and the width of the bands should also be reduced.

The motivation to perform these experiments at low temperatures centred on the desire for improved signal to noise ratio and reduced linewidths. We expected that the spectra would be broadly similar to those seen at room temperature, and in particular that the P-band would play a dominant role in the emission processes under high excitation in the PLD-grown samples. In chapter 6 we proposed that the exciton diffusion length may play a substantial factor in explaining the absence of high excitation effects at room temperature. We wished to examine whether the expected reduction in diffusion length at low temperatures would lead to the appearance of non-linear emission bands in the bulk material at low temperatures. However, other workers have identified that the threshold for lasing processes in bulk material at low temperatures is actually higher than at $\sim 70\text{K}$, due to localisation of free excitons on binding complexes at such low temperatures. We see evidence for this in bulk material, and also in some of the PLD material, and discuss the effect further below.

7.2.1 Eagle Picher bulk ZnO material

The graph of intensity versus energy for the VSL measurements recorded at 9K is shown in *figure 7.14* with 6 main bands/lines. The excitation stripe length is increased from 0.4mm to 2.8mm in the data shown in this figure.

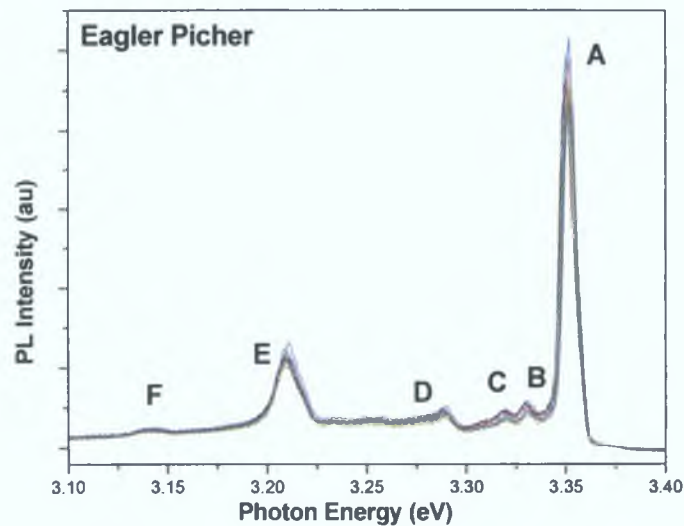


Figure 7.14: Eagle Picher bulk ZnO sample material at low temperature (9K) under excitation from the Nd:YAG laser with the stripe length decreased from 2.8mm to 0.4mm, Slits 500 μ m, Integration 1.0s, Increment 0.1nm. Data normalised.

The six bands in figure 7.14 are identified in table 7.1 with their corresponding energy and wavelength position.

Peak name	Wavelength (nm)	Energy (eV)
A	370.0	3.35
B	372.1	3.34
C	373.4	3.33
D	376.9	3.29
E	386.3	3.22
F	395.2	3.14

Table 7.1: Corresponding values of peaks identified in the bulk material at 9K in figure 7.14.

These six bands (A –F) are compared to PL spectra obtained with a HeCd, which shows normal photoluminescence bands at 25K as shown in figure 7.15. It indicates that there are no significant new bands produced under excitation from the Nd:YAG laser, and the origins of the various bands seen are discussed in chapter 3. The shift in the peaks of the bands is due to the pulsed nature of the Nd:YAG laser which causes a substantial local heating to temperatures above 25K (actually \sim 65K based on a Varshni model of the energy versus temperature behaviour, as discussed before) and hence we see a redshift

in the emission bands. This is especially pronounced at low temperature due to the smaller heat capacity at such temperatures [8].

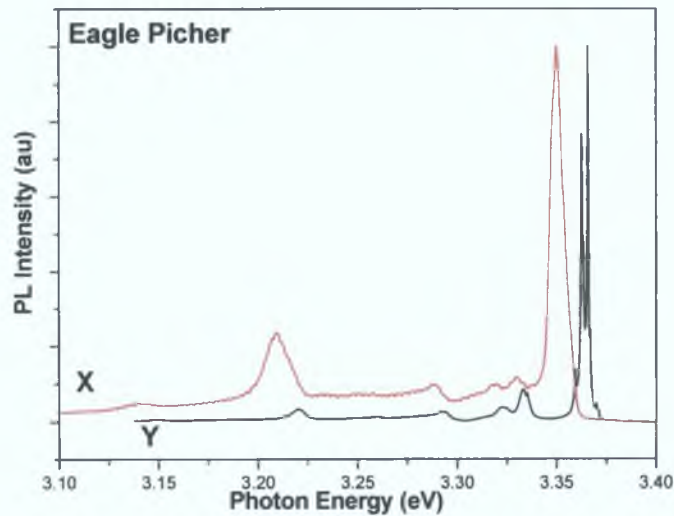


Figure 7.15: Comparison of the Nd:YAG (X) (Slits $500\mu\text{m}$, Integration 1.0s , Increment 0.1nm) acquired spectra at 9K and the HeCd spectra (Y) at 25K . Increment 0.01nm , Integration, 3.0s , Slits $10\mu\text{m}$.

The first reported study of low temperature stimulated emission on bulk ZnO was carried out by *Hvam* [6] in 1973. The bulk material used was of a similar purity level and structural quality as the bulk Eagle Picher ZnO sample used here.

We note that we see no evidence of the growth of any nonlinear bands, either exciton-electron, P- or EHP bands, up to the largest stripe lengths, at the highest excitation levels ($\sim 6000 \text{ kW/cm}^2$). We believe that the reasons for this are based on the fact firstly that the cryostat windows (quartz) are slightly absorbing at the 355nm wavelength and tend to reduce the incident intensity on the sample (we see evidence of damage to the windows at such intensity levels over periods of minutes to hours), hence reducing the achievable exciton generation rate. Secondly and more importantly, at such low temperatures the free excitons will tend to be localised on binding centres (such as those responsible for the I-line series) and consequently the free exciton population which is responsible at higher temperatures for the exciton-electron and P-bands, and which would ultimately condense to form the EHP band, is actually bound onto defect centres and the exciton-exciton interaction is largely eliminated. Only when the exciton generation rate is sufficiently high to fully saturate all the binding defects will a significant free exciton population form. The combination of this factor with the reduced excitation intensity on the sample in the cryostat means that we are unable to

access the high excitation regime in the bulk material at low temperatures. This conclusion is supported by the work in reference [6], where a substantial increase in the lasing threshold was seen between 10K and 60K, and associated with quenching of the free exciton population due to exciton binding onto defect centres.

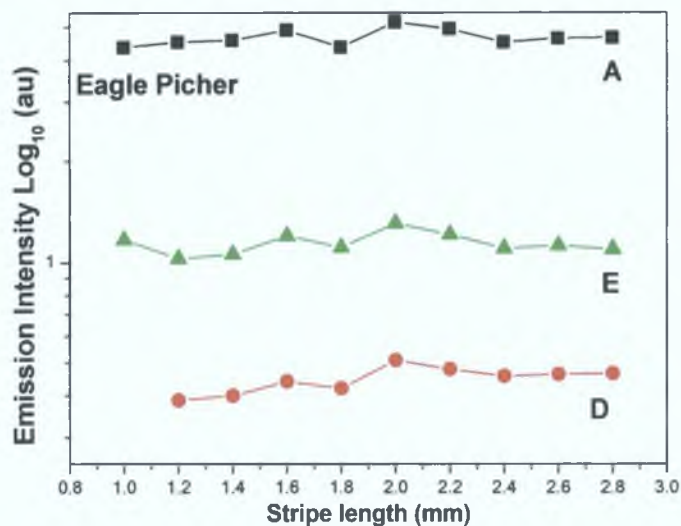


Figure 7.16: Characteristics of the bands as the stripe length increases at 9K. A is the bound Exciton Region. E is the second phonon replica. D is the first phonon replica.

In the VSL room temperature experiment no evidence of gain was observed. Figure 7.16 confirms a similar result for the VSL measurement on the bulk material at low temperatures. No evidence whatsoever of gain effects were seen, as might be expected from the spectral appearance, characteristic of the low excitation density regime.

7.2.2:PLD ZnO Sample (i)

The next sample investigated at 9K was the first of the PLD-grown ZnO samples, sample (i), which was not annealed post growth. All of our studies on this sample have indicated that it is the sample with the poorest optical quality and while it shows some evidence of non-linear and stimulated emission it shows no evidence of lasing and cavity formation. Consequently we investigated the effects of low temperatures, and in particular if the expected improvement in emission intensity at low temperatures reported in chapter 4 would be reflected in the high excitation behaviour. The spectra in figure 7.17 shows three peaks; band A at an energy of $\sim 3.36\text{eV}$ (368.8nm); band B is at $\sim 3.32\text{eV}$ (373.6nm) and finally band C is at $\sim 3.16\text{eV}$ (392.6nm). Figure 7.18 shows a comparison with the spectrum obtained with HeCd excitation, which looks very similar. These bands show no sign of any optical gain as deduced from measurements of excitation intensity as a function of increasing stripe length. Measurements at different

excitation densities at low temperature also show no evidence for non-linear growth of any of the features, and it appears that the spectra once again look very similar to the low excitation density regime.

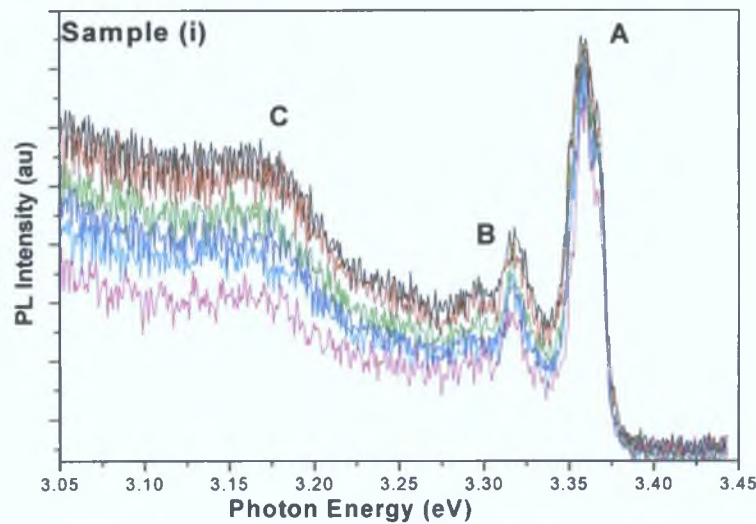


Figure 7.17: Sample (i) at 9K under excitation from the Nd:YAG laser. Stripe length varied from 2.0mm to 1.0mm. Slits 500 μ m, Integration 1.0s, Increment 0.1nm. Data normalised.

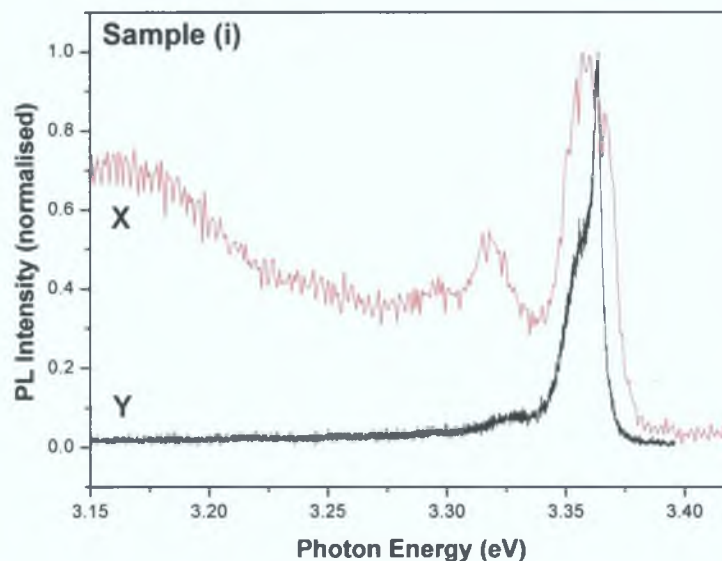


Figure 7.18: Comparison of the Nd:YAG spectrum (X) at 9K. Increment 0.1nm, Integration 1.0s, Slits 500 μ m and a HeCd acquired spectrum (Y) at 20K, (Increment 0.01nm, Integration 3.0s, Slits 10 μ m)

We believe the absence of any non-linear emission bands and any gain effects is due to the same factors that affect the bulk material. Both in bulk material and in sample (i) we see no evidence in PL spectra under HeCd illumination for any FE, or FE-LO emission (as reported in chapter 4), and the spectra are dominated by BE emission in both cases. Thus we believe, as in section 7.2.1 above, that the combination of reduced excitation density due to laser losses in the cryostat windows and localisation of excitons on

binding centres and resultant reduction in the free exciton population mean that we are not effectively accessing the high excitation density regime where exciton-exciton interactions are dominant.

7.2.3:PLD ZnO sample (ii)

Previous measurements in chapter 6 and the earlier section of this chapter indicate that the optical quality of PLD-grown sample (ii) is significantly better than that of sample (i) and that high excitation effects and lasing are observed in this sample as discussed in section 6.4.3.

Figure 7.19 shows the data for VSL measurements on this sample at 9K, and provides the first indications of non-linear optical process taking place at low temperature in our samples. The data from the lowest stripe length measurement shows only one band centered at $\sim 3.36\text{eV}$ (372.3nm) which is associated with FE and BE emission (figure 7.20). As the stripe length increases, we observe the clear emergence of a band centred on $\sim 3.225\text{eV}$, whose separation from the FE is $\sim 85\text{meV}$, corresponding well to the expected P-band separation at low temperatures. It is significantly more difficult to observe and especially to record any evidence of speckle patterns in the emission when the sample is in the cryostat, however at the longest stripe lengths we observe narrowing of the band emission and emergence of distinct modal structure on the P-band emission, indicating that the sample is lasing, and that a similar “leaking” type of gain process is occurring at low temperature as was observed clearly for sample (iii) at room temperature.

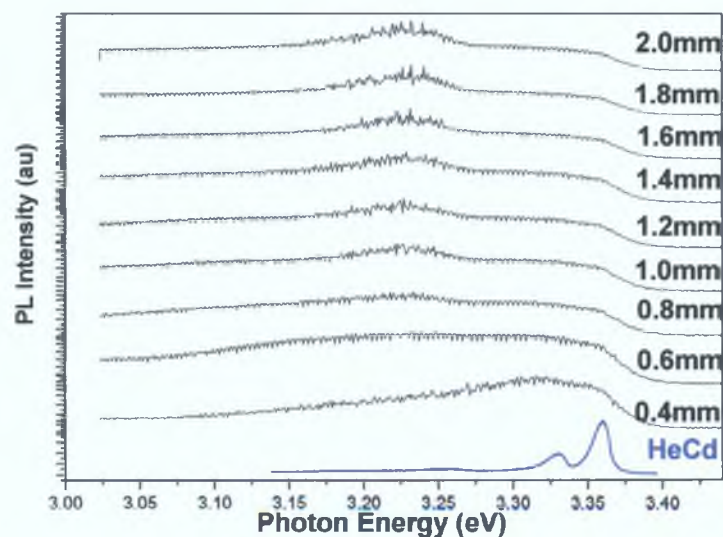


Figure 7.19: Nd:YAG spectra of sample (ii) at 9K. Slits $500\mu\text{m}$, Integration 1.0s, Increment 0.1nm. Data normalised.

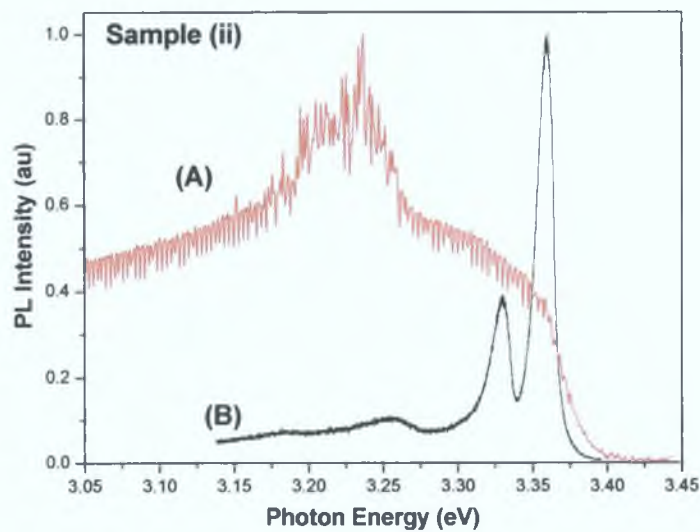


Figure 7.20: Comparison of the Nd:YAG (A) at 9K for a stripe length of 2.0 mm, increment 0.1nm, Integration 1.0s, Slits 500 μ m and HeCd spectrum (B) at 20K Increment 0.01nm, Integration, 3.0s, Slits 10 μ m.

In figure 7.21, the stripe length was kept constant at 2.4mm and the spectra for three different intensities were compared. As the pump laser intensity was increased the band at ~ 3.275 eV began to appear and shows a distinct threshold for spectral narrowing and the appearance of modal structure between the excitation intensities of ~ 3000 kW/cm² and 6000kW/cm², similar to the threshold intensity observed at room temperature for samples (ii) and (iii).

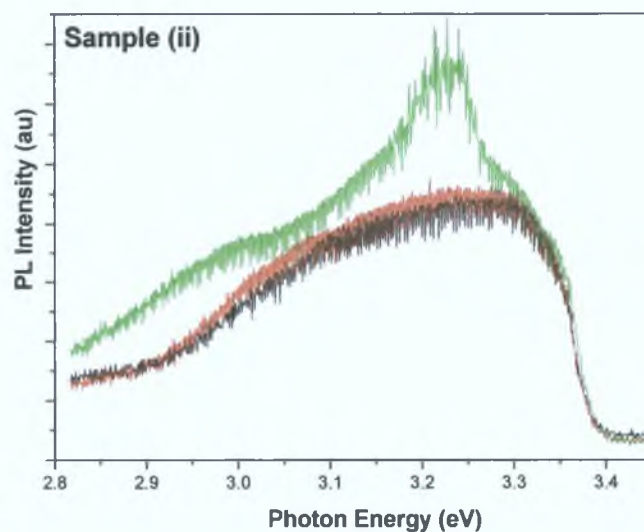


Figure 7.21: Comparison of three different intensities with the same stripe length of 2.4mm at 9K for sample (ii). Green spectrum is at the highest intensity. Red spectrum is at the intermediate intensity and black spectrum is at the lowest intensity. Slits 500 μ m, Integration 1.0s, Increment 0.1nm.

Studies of the excitation intensity as a function of cavity length are shown in *figure 7.22*. The intensities of the P-band shows an exponential growth over approximately one order of magnitude confirming that stimulated emission is taking place and that the gain mechanism is similar to that outlined earlier where gain occurs in randomly formed cavities with light leaking from cavity to cavity and being amplified as it propagates down the illuminated stripe.

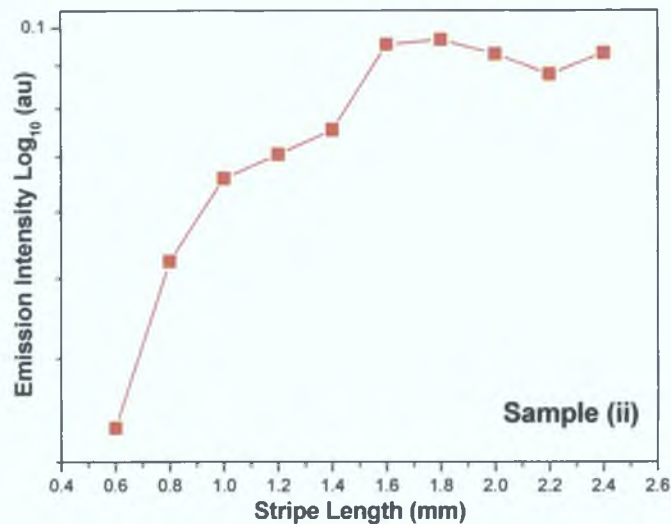


Figure 7.22: The emission intensity versus the cavity length of the band that appears at $\sim 3.275\text{eV}$.

Sample (ii) demonstrates clear evidence for high excitation and stimulated emission effects at low temperatures, unlike either the bulk sample or PLD-grown sample (i). PL data on this sample have previously indicated that its optical quality is far superior to that of sample (i) and is similar to sample (iii), as discussed in section 4.3.1. Specifically this sample appears to have a substantially reduced density of traps. These PL measurements at low temperature also showed evidence for FE emission (specifically FE-LO emission) as well as BE emission (see *figure 4.4* and discussion). While the evidence from PL alone did not allow us to assign the PL peak at 3.33 eV definitively to FE-LO emission (as DAP emission and emission due to structural defects has also been reported in this spectral region), the evidence presented above for high excitation effects and specifically for exciton-exciton collision effects manifested by the P-band provide strong evidence that a substantial FE population exists in the material at low temperatures under both HeCd and Nd:YAG excitation. Specifically we now propose that the emission at 3.33eV under HeCd excitation is due to FE-LO emission and that the FE population present in this sample at low temperatures explains the presence of

high excitation effects in this sample which were not seen in the poorer quality sample (i).

7.2.4: PLD ZnO sample (iii)

We have seen earlier in section 7.1.4 that sample (iii) has shown emission from non-linear bands and stimulated emission most clearly of the three PLD samples. There are two main bands identified in the VSL spectra at 9K in *figure 7.23*, one centered at 3.35eV and the second dominant band, which shows a shift from 3.24eV to 3.22eV with increased stripe length at the highest excitation intensities. These are associated with the free exciton and exciton-exciton P-band emission, respectively. Clear evidence is seen once again for cavity mode formation on the P-band emission.

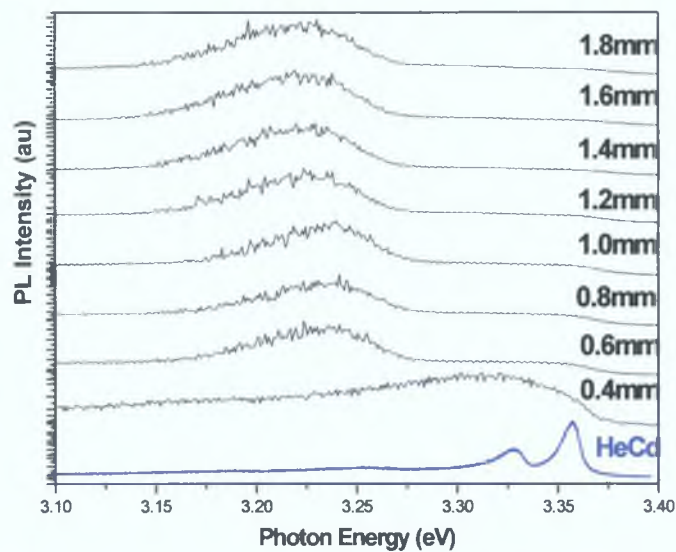


Figure 7.23: Sample (iii) at a low temperature of 9K. Slits 500 μ m, Integration 1.0s, Increment 0.1nm. Data normalised.

In *figure 7.24*, the spectra excited by the Nd:YAG laser at short (0.4mm) (A) and long excitation stripe lengths (2.00mm) (B) at 9K and excited by the HeCd laser at 20K (C) are shown. This shows clearly the growth of the P-band with increasing stripe length compared to the FE emission.

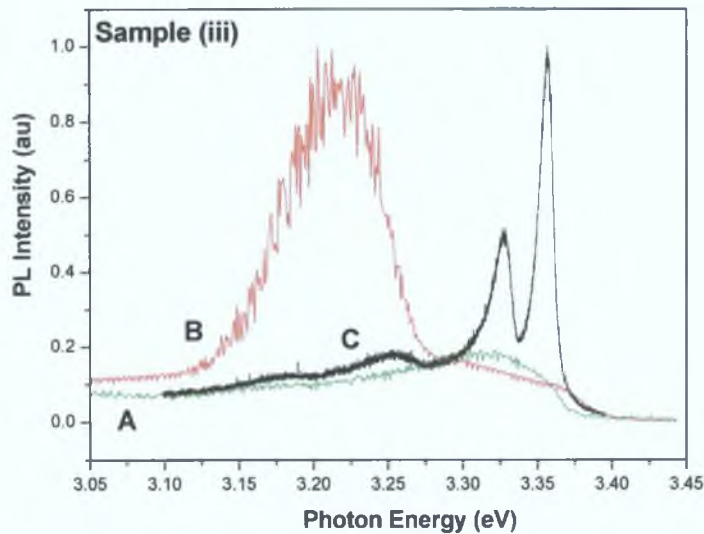


Figure 7.24: Comparison of HeCd and Nd:YAG laser on sample (iii). The C spectrum is of the HeCd at 20K. Increment 0.01nm, integration, 3.0s, slits 10 μ m. The B spectrum is of the Nd:YAG at 9K with a stripe length of 2.00mm, The A spectrum is the Nd:YAG spectra at 9K with an excitation length of 0.4mm. HeCd spectrum, increment 0.01nm, integration, 3.0s, slits 10 μ m.

A comparison of results obtained at the same excitation length but with different pump laser intensities is shown in figure 7.25 and illustrates the growth of the P-band with increased pump intensity.

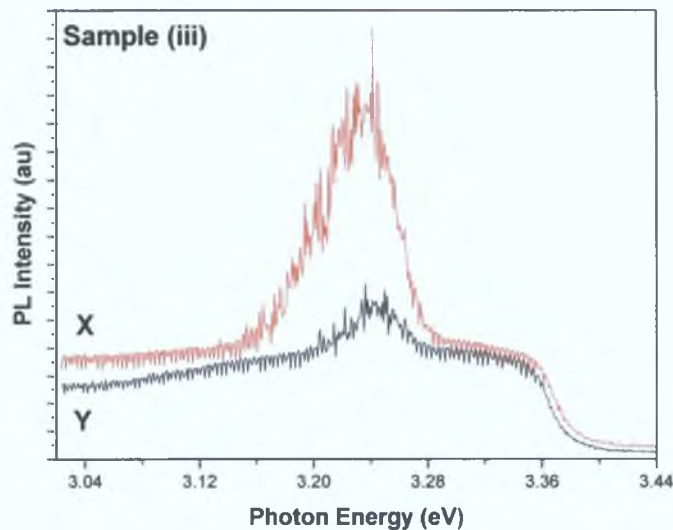


Figure 7.25: Comparison of different pump laser intensities (100% and 50%) with the same stripe length of 0.8mm at 9K. Slits 500 μ m, Integration 1.0s, Increment 0.1nm.

Figure 7.26 showing the growth of the P-band in sample (iii) as a function of stripe length, illustrates that stimulated emission is occurring on the P-band, with an exponential growth shown over approximately one order of magnitude.

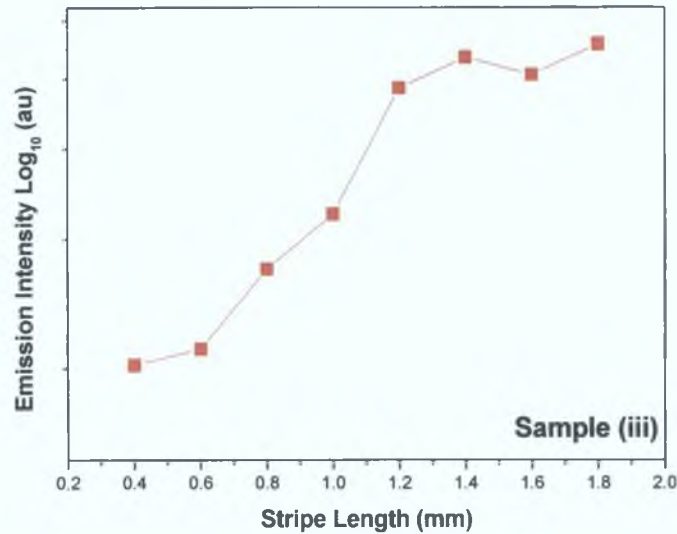


Figure 7.26: The resultant emission intensity of the P like band as a function of increased stripe length.

Thus, at low temperature, sample (iii) shows clear evidence of emission from the non-linear P-band and demonstrates the onset of stimulated emission and lasing effects through random modal structures, just as it did at room temperature.

7.2.5: Discussion of the low temperature VSL

The low temperature measurements for the PLD-grown samples followed more or less the trends of the equivalent room temperature measurements, with sample (iii) clearly showing the highest optical quality of the three samples. The bulk material shows no evidence for any high excitation effects or gain, nor does the PLD sample (i). We have interpreted this behaviour to be due to two factors (1) that the cryostat windows (quartz) are slightly absorbing at the 355nm wavelength and tend to reduce the incident intensity on the sample hence reducing the achievable exciton generation rate and (2) at such low temperatures the free excitons will tend to be localised on binding centres (such as those responsible for the I-line series) and consequently the free exciton population which is responsible at higher temperatures for the exciton-electron and P-bands, and which would ultimately condense to form the EHP band, is actually bound onto defect centres and the exciton-exciton interaction is largely eliminated. This is consistent with other experimental work on bulk material, where higher thresholds for nonlinear emission and lasing are seen at temperatures of the order of 10K compared to higher temperature (~70K), due to exciton localisation. In both the bulk material and PLD-grown sample (i) we see no evidence of FE (or FE-LO) emission in normal PL data at low temperature, indicating a high concentration of bound excitons. In contrast, both PLD-grown samples

(ii) and (in) show evidence for FE-LO emission in normal PL spectra at low temperature, indicating a reasonable population of free excitons and correspondingly show evidence for exciton-exciton interaction, as evidenced by P-band emission and lasing, under high excitation

It should be noted that the low temperature results were obtained using a cryostat. Therefore alignment of the excitation area was problematic, with the presence of multiple cryostat windows and occasional problems such as condensation in the chamber and on the windows. In addition, the inner windows, being unavoidably closer to the laser focus tend to become marked rather easily and great care must be taken in performing the measurements.

7.3 Gain measurements from RT and low temperature VSL data

Calculation of the gain can be measured using the variable strip length (VSL) method, as outlined in the experimental section 2.3.4. In the normal VSL method, part of the spontaneous emission rate per unit volume J_{spont} , propagates along the stripe axis, and is amplified in the excited region by stimulated emission [1]. The light intensity at the output J_{stim} is dependent on the stripe length l by the relationship

$$J_{stim} = \frac{J_{spont} A}{g} [\exp(gl) - 1] \quad (7.1)$$

where A is the cross-sectional area of the excited volume and g is the net optical gain (gain due to stimulated emission minus optical losses) [9]. A graph of the variation of output intensity with increasing length can be used to study the gain of the system. A region of linear variation on this logarithmic plot corresponds to values of l large enough for the exponential factor in the equation 5.13 to dominate. In such a region the gain can be determined from the slope. At large values of stripe length saturation of the emission intensity can occur due to exhaustion of the excited radiative centres, which leads to only linear variation of the light output with stripe length. Lasing occurs when the gain overcomes the losses in a medium. The gain depends on how much time the light spends inside the material and the loss depends on how easily the light can escape. *Shaklee et al* [1] were the first to implement this calculation into their own experimental results on CdS crystals at low temperatures and the resultant data of *Shaklee et al* experiment can be seen in *figure 7.27*

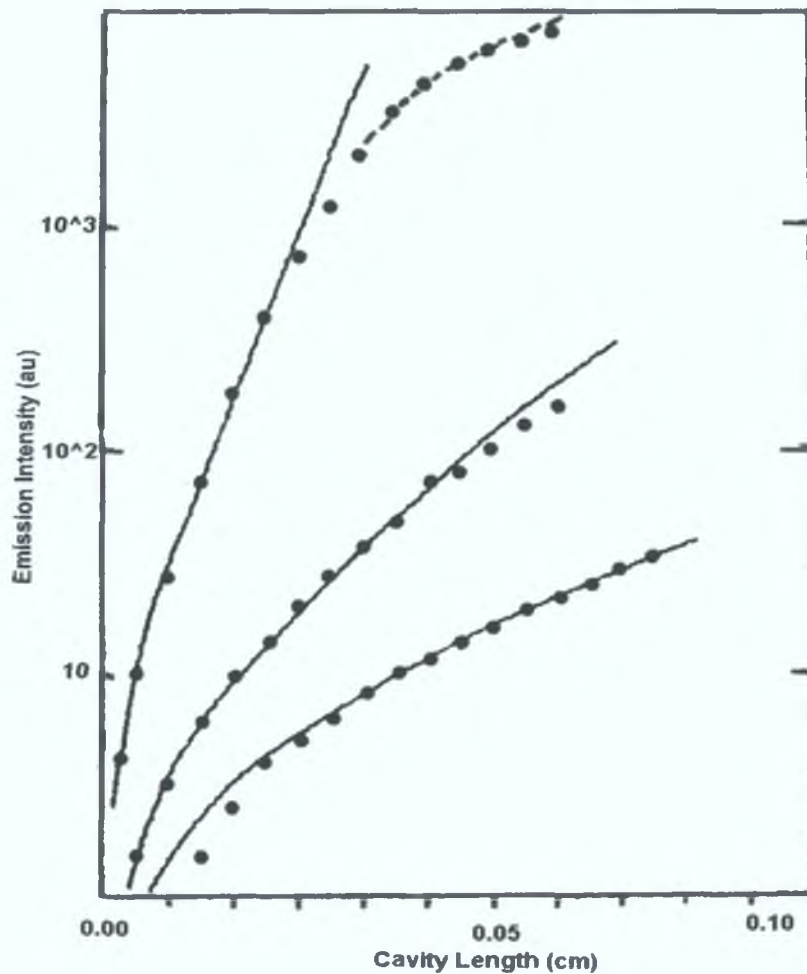


Figure 7.27: Variation of light output with length of excited region for three different pumping intensities from Shaklee et al [1].

It appears from the data and discussions presented in section 7.1.4 and 7.1.6, that although the lasing mechanism is dominated by self-formed, random cavities, unlike the well defined gain guided cavity envisaged with by Shaklee and co-workers, and other publication [10], because of the light leakage from one self-formed cavity to the next along the stripe length, one does see an amplification of spontaneous emission. This can be used to calculate an “effective” gain, although this may not be the actual gain of the sample due to the complicated light propagation in the self-formed cavities. The general picture envisaged for the VSL measurements on the PLD-grown samples is discussed below and shown in figure 7.28. Multiple scattering of spontaneously emitted light at grain boundaries creates self-formed, random cavities, as seen in figure 7.28, which initiates stimulated emission and gain. When stimulated emission is amplified at the modal frequencies of these natural formed cavities, it may leak to a nearby cavity with suitable modal frequency or travel out through the surface. For gain measurements we captured only emission from the end/edge of the sample, which will have propagated

along the length of the optically pumped stripe, leaking from cavity to cavity and being amplified at each step. This captured emission arises from cavities only at the edge of the sample; however, it may have propagated along the entire length of the stripe. However, due to the potential for surface losses from each self-formed cavity along the stripe length, the potential losses are rather high. The competing effect is that the light may propagate around multiple loops in a single cavity, hence increasing the potential path length over which gain may occur, compared to the simple geometric dimension of the cavity. However, it is beyond the scope of the present work to determine the quantitative degree of these two effects. As shown below, the measured data show effective gains which are rather low by comparison with “normal” VSL measurements on single crystal data, and which may indicate that surface losses dominate the process. This low effective gain is reflected in the rather small range over which exponentially increasing emission intensities are measured.

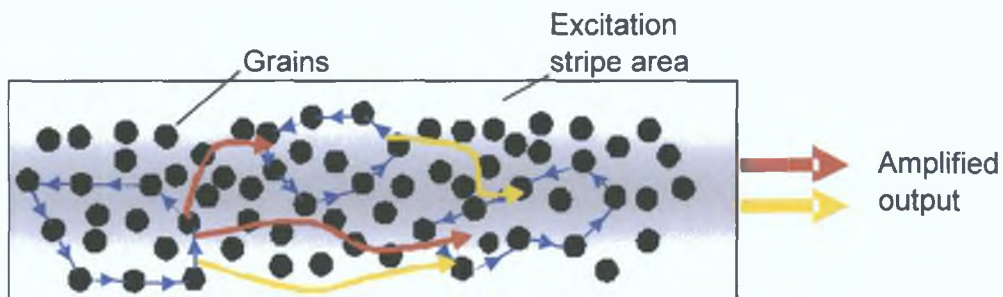


Figure 7.28: A schematic drawing showing the formation of a closed loops path through recurrent scattering in the samples. The blue lines show the closed loop paths, while the red and yellow lines indicate light (of different modal wavelengths) leakage from one cavity to another.

The large losses through the surface from each cavity give rise to the distinctive speckled cloud that appears at the higher excitation intensities. The main difficulty in calculating the gain in the data acquired in this work is the lack of emission intensity values showing exponential growth over a wide range. As seen in *figure 7.27*, the data from Shaklee et al covers a range of values over three orders of magnitude, while the results acquired in this work are only over one order of magnitude at most. An example of this is shown in *figure 7.29*, and other examples can be seen in *figure 7.5* and *figure 7.7*.

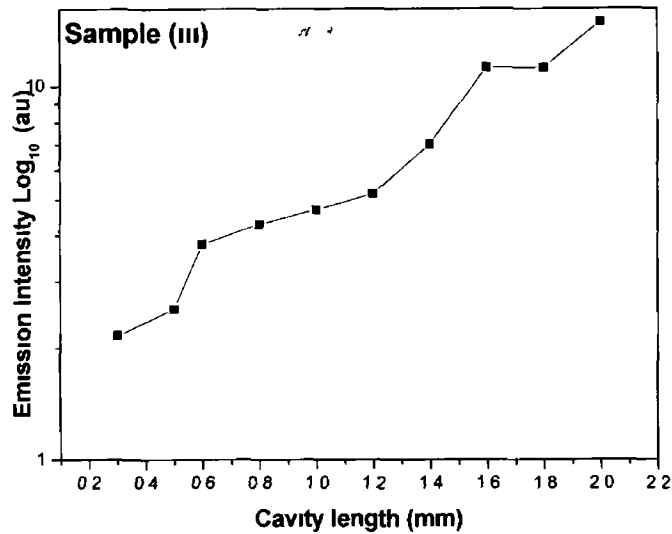


Figure 7.29 Sample (iii) shows variation of output emission intensity as a function of stripe length

Nevertheless a fit of the results to calculate the gain was carried out for each of the samples investigated and the results are shown in table 7.2 below

Material	Gain VSL RT	Gain VSL 9K
Sample (i)	14.21 cm ⁻¹	No value
Sample (ii)	20.15 cm ⁻¹	3.31 cm ⁻¹
Sample (iii)	74.59 cm ⁻¹	29.2 cm ⁻¹

Table 7.2 The results of the curve fit to calculate the gain of the samples

The gain values increase with grain sizes in the PLD samples, as we would expect from previous data indicating substantial increases in optical quality in samples (ii) and (iii) compared to sample (i). The gain values are consistently higher at room temperature than at low temperature, and this initially implausible result demonstrates again that at low temperatures the free excitons population tends to be localised on binding centres and consequently the free exciton population responsible for the non-linear emission and gain is actually bound onto defect centres and the non-linear processes responsible for gain are consistently reduced at lower temperatures in all the samples studied. Another reason why the gain values are lower than expected may be due to the way that they are measured. They are not measured at individual wavelengths but over a band of wavelengths, some of which may not show gain.

7.4 PDA experiment at room temperature

In order to study the pulse to pulse variations in the emission spectra, and the details of the modal structure, we performed measurements by replacing the photomultiplier and boxcar integrator by a charge coupled device (PDA) camera and integrated spectrometer set-up. The experimental arrangement for PDA experiment has been discussed in section 2.3.5.

As shown previously in this chapter and in chapter 6, the variable stripe length (VSL) method using a cylindrical lens set-up has produced good data, clearly demonstrating the non-linear emission processes. Hence this method was incorporated with the PDA camera. The excitation density used for all samples was $\sim 6000 \text{ kW/cm}^2$, which was above the threshold for lasing for both samples (II) and (III).

Long integration times were necessary in accumulation mode, due to the rather weak emission signals, particularly at small stripe lengths. In consequence the laser signal on the PDA generally saturated the detector over the course of the accumulation, which meant that it was not possible to properly normalise the emission to keep the laser peak signal at 355nm constant, as was done for the boxcar setup and discussed in chapter 2.3.4. This means that the data in accumulation mode are not normalised and can only be used to broadly confirm the data from the boxcar set-up. The kinetic series spectra were obtained for only stripe lengths that showed evidence of modal structure in the accumulated graphs, and due to the short integration times associated with a single pulse per spectrum, the signal to noise ratio was generally rather poor.

Due to the speed of the PDA camera acquisition it is possible to capture a larger number of spectra for different stripe lengths in reasonable timescales. This is shown in *figure 7.30*. Stripe lengths from 0.4 to 3.00mm with an increment of 0.2mm were generally acquired with the PDA set-up. We have examined the same series of samples used in the boxcar setup, beginning with the bulk material, and progressing to the PLD-grown material.

7.4.1: Eagle Picher Bulk ZnO material

The data from the Eagle Picher material is shown in *figure 7.30* with increasing stripe length. We see identical emission as a function of stripe length variation to that seen using the boxcar set-up, with both FE and exciton-electron collision-related emission observed. The variation in intensity we observe is simply due to the capture of luminescence from the larger excited area by the collection optics with increasing stripe length. Correct normalisation, as done in the boxcar set-up, would show that no gain effects are seen for this sample.

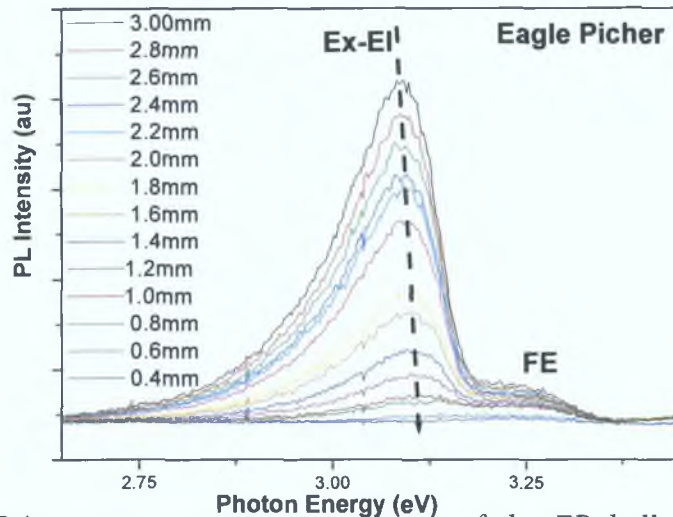


Figure 7.30: PDA spectra at room temperature of the EP bulk material with 100 accumulations and an exposure time of 0.04s. Stripe excitation length was from 0.4 to 3.0mm with an increment of 0.2mm.

The kinetic series mode was used to investigate the pulse to pulse variability of the spectral output of this sample; 20 spectra were taken and are displayed in *figure 7.31*. As evident in the *figure 7.31* there is no evidence of lasing modes in the sample emission. The pump laser emission line seen at 355nm remains relatively constant during the entire kinetic series acquisition. The pulse to pulse variation in the laser output is at most 20% and on average is less than 15% variation. This level of variation is seen in all the kinetic series data obtained. In fact, the actual pulse to pulse power variation may be less than this value (10% from measurements detailed in chapter two), as slight wandering of the laser beam may lead to changes in the collection efficiency of the spectrometer and associated optics. However, these kinetic series data provide a definite upper limit on the pulse to pulse variation of laser intensity.

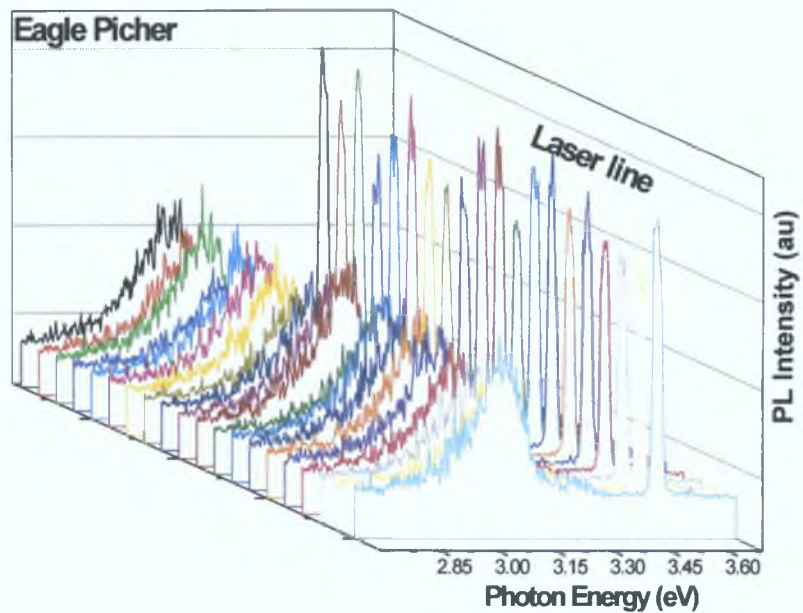


Figure 7.31: Kinetic Series graph of Eagle Picher material, 20 plots successively at a stripe length of 2.00mm.

7.4.2: PLD ZnO sample (i)

This sample has consistently shown the poorest optical quality of the three PLD-grown samples. Figure 7.32 shows the PDA software screenshot image of the emission accumulating over 100 laser pulses. The figure shows only the 355nm Nd:YAG laser line. There is no evidence of any other bands in the spectrum. The brighter colours correspond to an increased count at a particular wavelength. At the bottom of figure 7.32 the spectrum is displayed in a more familiar format and again shows only the 355nm line.

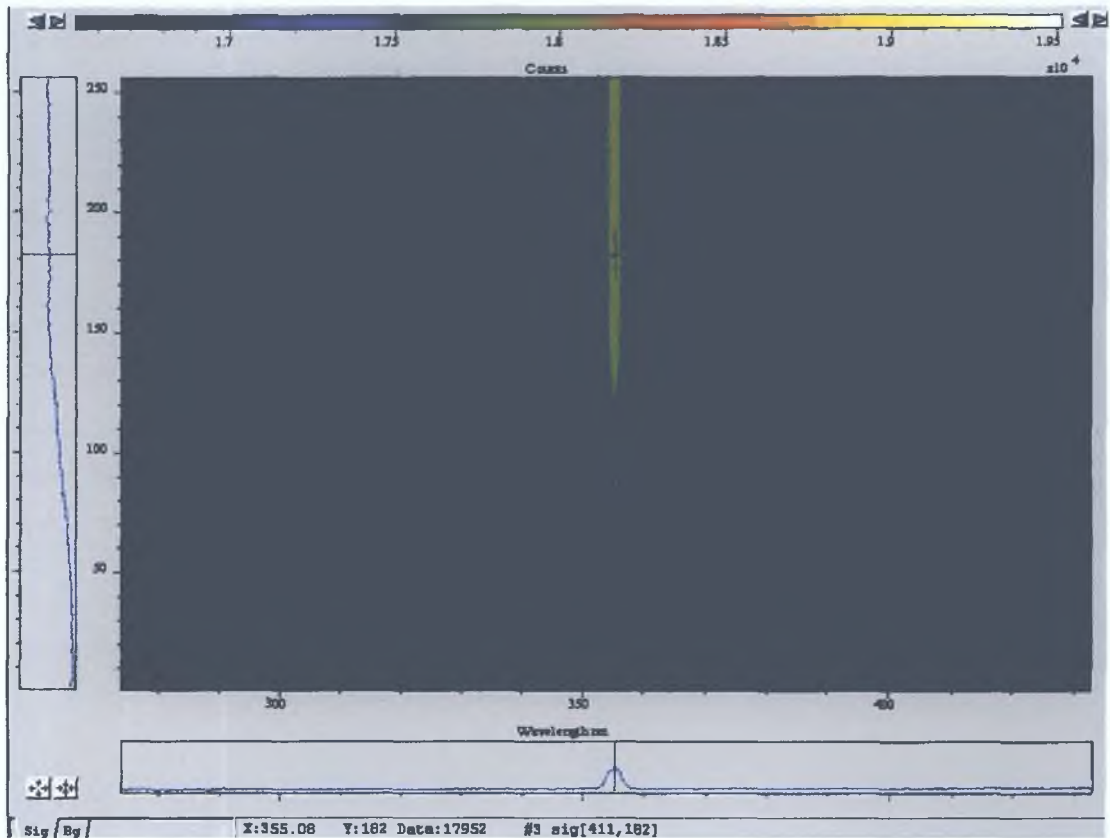


Figure 7.32: The screenshot image from sample (i) shows only a 355nm line with no other visible structure. The line spectrum is shown in lower part of the figure.

These data show that the sensitivity of the PDA set-up is considerably less than that of the boxcar integrator arrangement, which could capture the PL emission from this sample at room temperature.

7.4.3: PLD ZnO sample (ii)

Sample (ii) has shown evidence of high excitation and lasing at high laser pump intensity, and its optical quality is significantly better than that of sample (i). In figure 7.33 the spectra acquired with the PDA detector as a function of increasing stripe length are shown. The spectra are similar to those reported previously, with the P-band emission dominating at higher excitation density. Once again, the spectra are not correctly normalised.

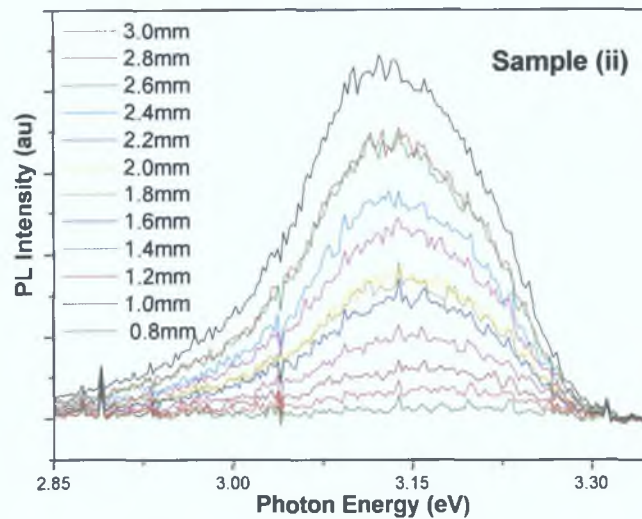


Figure 7.33: PDA acquired spectra at room temperature for sample (ii). Stripe length is from 0.8mm to 2.8mm with an increment of 0.2mm. Accumulation of 100 scans.

Previously this sample has shown random modal structure appearing on the dominant peak using the VSL set-up with a cylindrical lens. As shown in 7.33 there is some modal structure appearing in the kinetic series spectra with the appearance of sharp lines (indicated by the arrow in figure 7.34), whose position and intensity alters from laser shot to shot, indicative of random lasing. The accumulated spectra are therefore a multi-shot average of such behaviour and produce the data in figure 7.33.

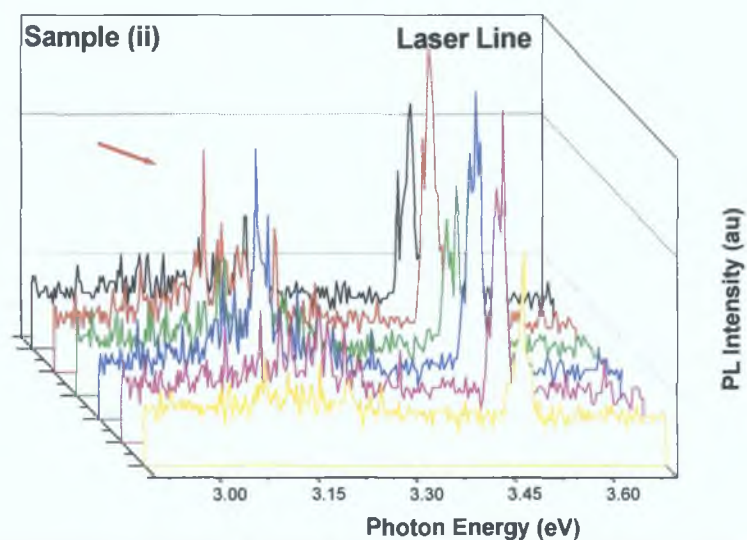


Figure 7.34: Kinetic series spectra of sample (ii) for the investigation of laser modes in the band at $\sim 3.14\text{eV}$. The stripe length is 3.00mm.

When spectra from two of the kinetic series are examined in detail one may see a number of very sharp lines, which change from pulse to pulse, characteristic of lasing modes from randomly formed cavities, as shown in figure 7.35. The linewidths of the

individual modes is $\sim .4$ nm, and appears to be limited by the spectrometer resolution of ~ 0.2 nm.

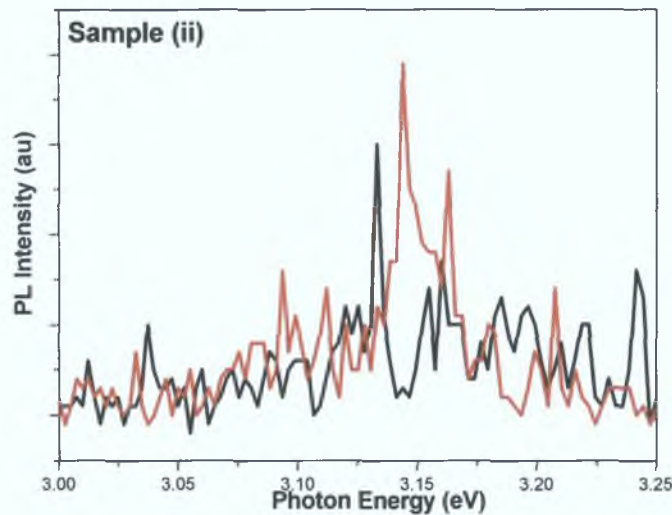


Figure 7.35: Close up view of two individual kinetic series in figure 7.34.

7.4.4: PLD ZnO sample (iii)

Sample (iii) has consistently shown the highest optical quality of the three PLD-grown samples, and has shown strong evidence for the presence of non-linear emission bands under high excitation conditions and also for lasing in random self-formed cavities. Figure 7.36 shows the accumulated spectra on the PDA spectrometer as a function of stripe length (again not normalised to the laser peak height). We see the FE and P-band emission clearly (marked with arrows in the figure). We do not see individual cavity modes clearly in the accumulated spectra on the PDA spectrometer.

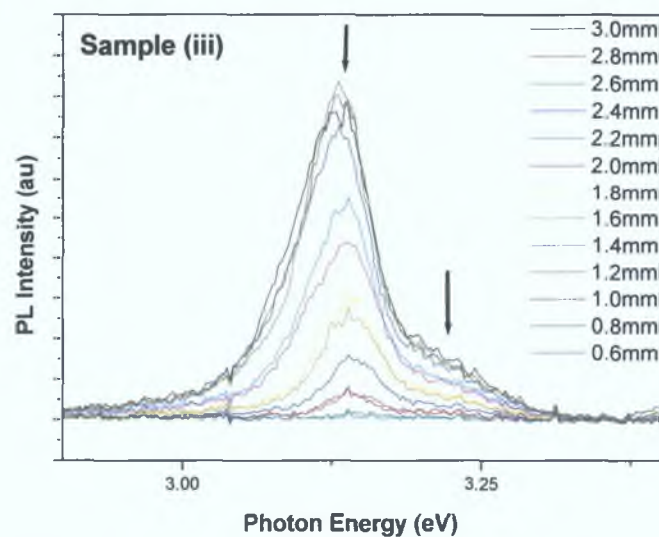


Figure 7.36: Sample (iii) at room temperature at stripe length of 3.00 to 0.6mm with an increment of 0.2mm.

Figure 7.37 shows a comparison of the data acquired with the boxcar set-up with that acquired with the PDA spectrometer for a stripe length of 2.0mm. The spectra are seen to be very similar, although the PDA spectrometer sensitivity decreases at higher photon energies, and the FE emission is less prominent in the PDA spectrum. The lower spectral resolution of the PDA spectrometer ($\sim 3\text{nm}$ (at $200\mu\text{m}$ slits) compared to $> 2\text{nm}$ for the boxcar set-up) and the large number of accumulations tend to wash out the individual cavity modes seen for the boxcar arrangement.

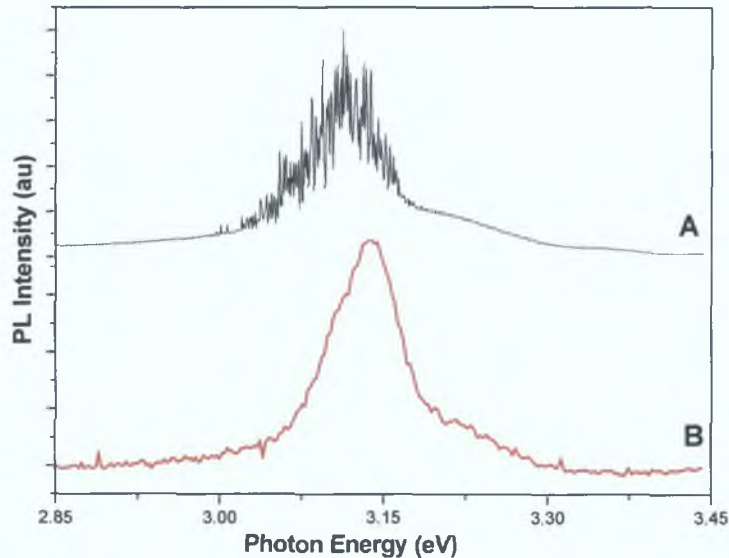


Figure 7.37: The comparison of the spectra acquired using the PM tube (A) and the PDA camera (B). The excitation stripe length for both was 2.00mm.

A kinetic series was taken for sample (iii), as shown in figure 7.38, where 20 spectra are acquired, each from a single pulse of the pump laser. The emission intensity and spectral detail in the P-band region vary dramatically from shot to shot. The pump laser emission line is reasonably constant throughout the experiment data and therefore the variation is not due to any pulse-to-pulse variation of the pump laser itself. It can be shown how an accumulation of many such peaks can produce the broad band spectrum, seen in the accumulation graph in figure 7.36.

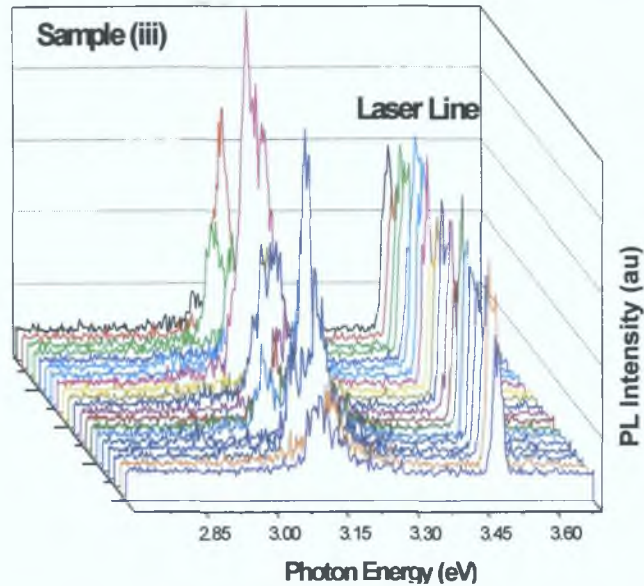


Figure 7.38: Kinetic series of sample (iii) with the pump laser output. Excitation stripe length is 2.2mm.

Again, a series of sharp lines, whose position and intensity vary from laser shot to shot is observed, indicative of random lasing in self-formed cavities. The addition of the 20 single shot spectra shown in figure 7.38 is shown in figure 7.39.

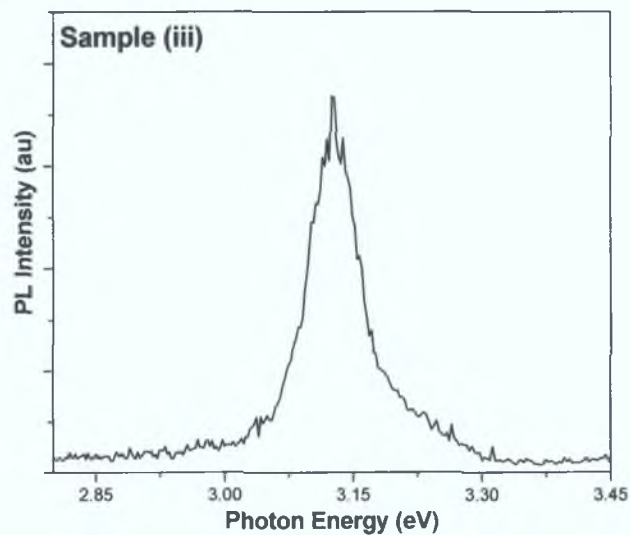


Figure 7.39: The average of the 20 scans in the kinetic series of sample (iii) as seen in figure 7.38.

This sample was also investigated at a lower power level ($\sim 3000 \text{ kW/cm}^2$) using the neutral density filter and similar results were seen. One interesting feature was seen at this power level at a stripe length of 2.8mm, which showed up in the accumulation mode. This is the sharp line feature shown in figure 7.40. This is significant, as it was seen in a number of accumulated spectra at the same spectral position and was not

smoothed into a broad Gaussian-like band, which would be expected after accumulation of 100 spectra.

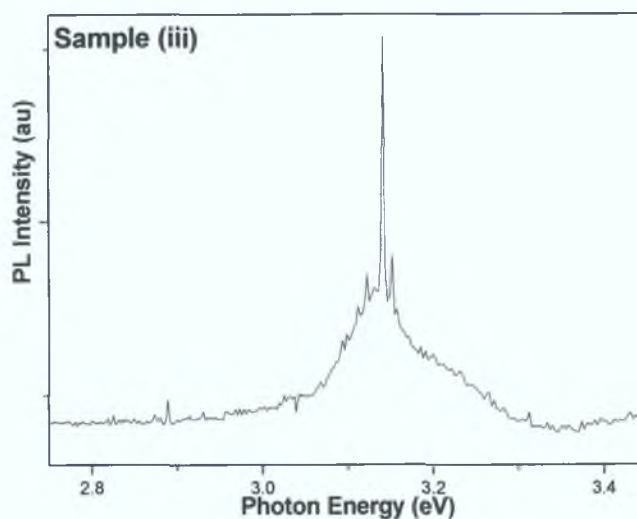


Figure 7.40: Sample (iii) at a stripe length of 2.8mm.

A kinetic series was taken at this power density and stripe length to see if the feature showed a laser pulse to pulse variation, and this is shown in figure 7.41 below.

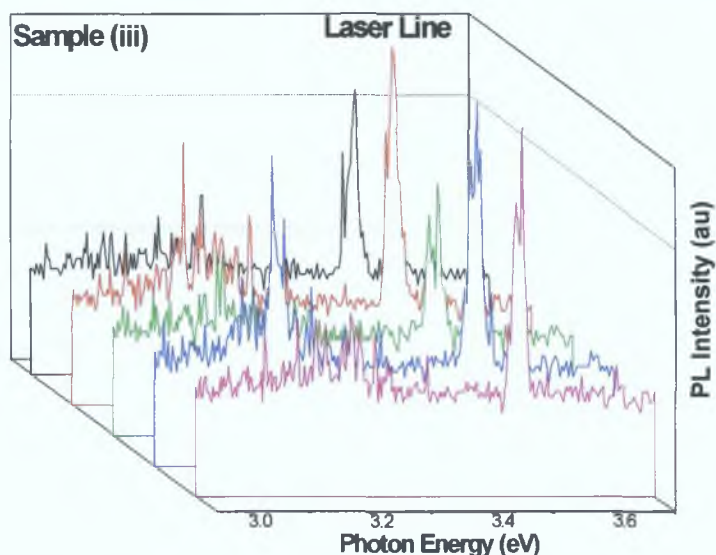


Figure 7.41: Kinetic Series of sample (iii) with a stripe length of 2.8mm.

No evidence is seen for this feature in the kinetic series. Its origin remains unknown, and may be due to some problems with the accumulation software, or perhaps due to problems with specific pixels in the PDA array.

7.4.5: Low Temperature PDA Measurements

The measurements using the PDA system all indicate that the sensitivity of this experimental arrangement is significantly poorer than that of the boxcar and PMT experimental arrangement. We have also made PDA measurements at low temperatures in an attempt to produce higher signal levels.

As with other low temperature measurements, the windows of the cryostat caused difficulty in aligning the excitation stripe on the ZnO samples, and reduced the excitation levels considerably. This problem, in addition to the reduction in free exciton population discussed previously meant that the data at low temperature were extremely poor, compared to the room temperature data, and only sample (iii) showed an observable signal. This was a bit surprising as we initially expected that measurements at low temperature with a PDA camera to be the best opportunity to observe the details of lasing modes. In all the measurements with the PDA arrangement the weaker bands at higher energies were not seen with the PDA camera compared with the PM tube (due to the spectral response of the PDA/spectrometer system, shown in *appendix D*).

7.4.6: PLD ZnO sample (iii)

Figure 7.42 shows data for PLD-grown sample (iii) at low temperature as a function of increasing stripe length at a nominal power density of $\sim 6000\text{kW/cm}^2$. We see the FE and P-band emission clearly. These spectra again reveal the lack of sensitivity of the PDA-based system, and we observe very little emission at lower stripe lengths (below 1.00mm) at low temperature. In *figure 7.9*, the equivalent spectra acquired with the boxcar and PMT set-up, data is obtained down to excitation lengths of 0.2mm. Alignment of the smaller stripe lengths on the samples inside the cryostat is particularly difficult which may account partly for this lower limit.

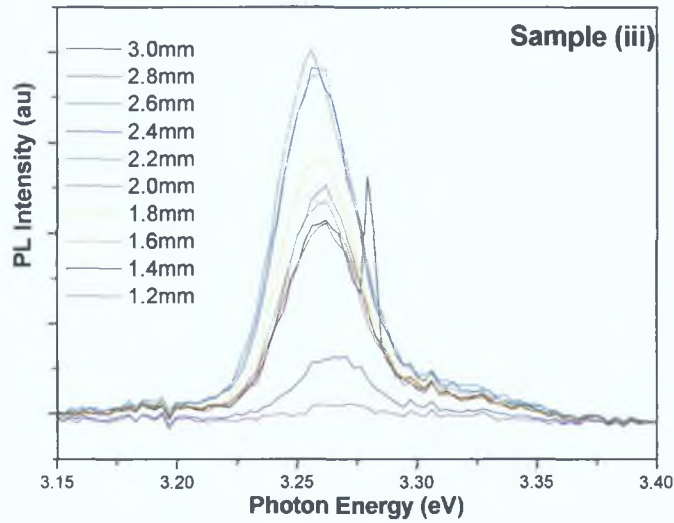


Figure 7.42: Sample (iii) at 9K with the varying stripe length investigated. Stripe length from 3.00 to 1.2mm, Increment 0.2mm.

In figure 7.42 at the longest stripe length (3.00mm), we see a narrow peak at $\sim 3.28\text{eV}$, which is present even in the accumulation-acquired data. This peak was not seen in the kinetic series data shown below, and may be due to problems with the accumulation software or problems with specific pixels in the PDA array, mentioned previously.

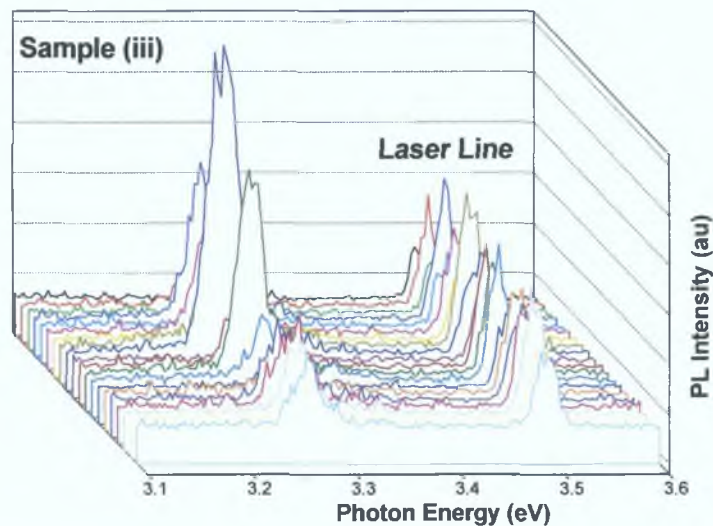


Figure 7.43: Kinetic Series of sample (iii) at 9K with a stripe length of 3.0mm. There are twenty spectra in the series with a cycle of one second.

The kinetic series data does not show conclusive evidence of cavity mode emission but there are significant changes in the pulse to pulse emission intensity and the emission observed does show evidence of spectral narrowing, and changes in the spectrum from pulse to pulse, consistent with previous measurements on this sample at 9K.

7.5: Summary

For all the measurements discussed in this chapter a similar pattern is observed, consistent with the data from chapters 5 and 6. In the bulk material at both room and low temperature we see no evidence of high excitation effects in the optical spectra. At room temperature we observe emission corresponding to the free exciton and electron-exciton collision-related mechanisms, both of which scale linearly with excitation density, and show no evidence of stimulated emission. This is consistent with the data from chapter 6, and may be explained in a similar manner, in terms of the reduction in the exciton population in the bulk material compared to PLD-grown material due to the effects of exciton diffusion. At the excitation densities used we are barely accessing the intermediate range of exciton densities in this sample at room temperature. At low temperatures the localisation of the free excitons onto binding centres means that we see only luminescence from bound excitons up to the highest pumping intensities.

For the PLD-grown samples, we see a definite progression, already noted in chapters 5 and 6, with sample (i) displaying the poorest optical properties, and sample (iii) the best. These have already been discussed in terms of the grain structure and associated defects and electric fields in the samples. At low temperatures only samples (ii) and (iii) show evidence for high excitation effects. This is consistent with their low temperature PL emission which shows evidence for a free exciton population in both samples. Gain measurements reveal that the gain in the three PLD-grown samples follows this progression in terms of optical quality, with sample (iii) showing the highest gain at both room and low temperatures, followed by sample (ii) and (i) (whose gain could only be measured at room temperature). The gains at room temperature were consistently higher than those at low temperature and the origins of this initially confusing result may be found in the reduction of the free exciton population at low temperatures via localisation on defect binding centres.

Studies of the spectra at high excitation in samples (ii) and (iii) using both a boxcar experimental arrangement and a PDA-based system reveal that the mode structure observed is due to random lasing in self-formed cavities due to multiple scattering effects between grains, and we observe that light leakage from one cavity to another plays a significant role in the emission and is necessary to understand our VSL gain measurements.

References Chapter Seven

- [1] K L Shaklee, R F Leneny, Appl Phys Lett , Vol 18, No 11,(1971)
- [2] R L Weherr, W C Tait, Phys Rev B, Vol 5, No 2 (1972), 623
- [2a] D D Sell, S E Stokowski, R Dingle, J V DiLorenzo, Phys Rev B Vol 7, (1973), 4568
- [3] P Yu, Z K Tang, G K L Wong, M Kawasaki, A Ohtomo, H Koinuma, Y Segawa, 23rd International Conference on the Physics of semiconductors, edited by M Scheffler and R Zimmermann, (World Scientific, Singapore, 1996),1453
- [4] X Q Zhang, Z K Tang, M Kawasaki, A Ohtomo, H Koinuma, J Crys Growth, Vol 259, (2003), 286
- [5] F H Nicoll, Appl Phys Lett 9, (1966), 13
- [6] J M Hvam, Solid State Commun 12, (1973), 95
- [7] R A Stradling, P C Klipstein, Growth and Characterisation of semiconductors, Adam Hilger press, (1990)
- [8] C Kittel, Introduction to Solid State Physics, 8th Edition, Wiley, (2005)
- [9] Z Q Zhang, Phys Rev B 52, (1995), 7960
- [10] R Thomasunas, I Pelant, B honerlage, R Levy, T Cloitre, R L Aulombard, Phys Rev B, Vol 57, No 20, (1998),13077

Chapter Eight

Conclusion and Further work

8.1: Conclusions

The work presented in this thesis describes the results of a photoluminescence and high level optical excitation study of nanocrystalline ZnO grown by PLD. The PLD-grown material was referenced against a commercially grown bulk ZnO material of high quality. We have discussed the identification of the sharp bound exciton features seen in the PL spectra from bulk material under HeCd excitation and highlighted the variations encountered in the literature concerning the identification and origin of these lines. PL data from the PLD-grown material showed a distinct increase in optical quality with the post growth annealing treatment. However the quality of the PLD material falls well short of the commercial bulk ZnO material in all cases. A consistent increase in the intensity of the green luminescence band with increased annealing was also observed. It was proposed that electric field effects due to charge trapping at grain boundaries strongly influence all these properties. The reduction of electric field effects due to an increase in grain size with annealing and consequent reduction in grain boundary density leads to an increase in the optical quality of the material, and to predictable changes in the band edge and green PL signals and the reflectance data. These experimental observations are in agreement with theoretical models of the effects of electric fields on excitons in ZnO and models of the origin of the green band emission in this material.

In this study the bulk material has shown no characteristics of non-linear or stimulated emission taking place at high level optical pumping. The FE and ex-el bands were identified which scale linearly with pump intensity and are associated with low level excitation effects. It was proposed in chapter six that exciton diffusion (unhindered by grain boundaries) leads to a decrease in the population density of excitons and consequent quenching of non-linear optical processes high excitation intensities. At low temperatures the localisation of the free excitons onto binding centres means that we see only luminescence from bound excitons up to the highest pumping intensities used in this work.

Optical emission bands due to nonlinear processes involving bi-exciton collisions and the electron-hole plasma state were observed in the PLD-grown material under high pumping intensities. Samples with larger grain sizes showed distinct evidence for random lasing, with the presence of a mode structure on the non-linear bands clearly observed at both room and cryogenic temperatures. Based on data acquired with both a

PM tube-based arrangement and a PDA-based arrangement we believe that the modal structure observed was due to lasing in the material in naturally formed random cavities created by scattering events due to the granular structure of the material but that light amplification also occurs due to cavity to cavity leakage.

The work presented here makes a number of contributions to this field of research, and three aspects in particular are worthy of note:

- The effects of electric fields due to charge trapping at grain boundaries on the photoluminescence, both band edge and green band emission, has been shown to be a significant factor in both shifting the position of the shallow donor bound exciton emission and broadening the spectral emission. It has been demonstrated that the experimental data are in good general agreement with theoretical predictions concerning exciton behaviour in electric fields. In addition, the behaviour of the unstructured green band emission in samples with different size grains gives strong evidence in support of the oxygen vacancy model of this band proposed by *Vanheusden et al* [1].
- A systematic study of the conditions and sample types in which lasing is observed leads to the conclusion that the conventionally accepted reasons for observation of random lasing in nanocrystalline samples at room temperature, but not in high quality bulk material at room temperature (in terms of giant oscillator strength or waveguiding effects) are quite probably incorrect. We propose a simpler model based on diffusion inhibition, which qualitatively explains the trends seen by many authors (including this author) for optically pumped stimulated emission. Simple numerical estimates of the effects proposed show that it is a model worthy of broader consideration. While diffusion effects have been considered in passing in the study of excitation density effects in single crystal materials, they have not been considered as a major factor enabling room temperature lasing in such nanocrystalline films.
- We observe strong evidence that, in addition to lasing and stimulated emission in randomly formed cavities, light leakage between random cavities plays a role in the lasing mechanism in such nanocrystalline films, and that gain

measurements using the VSL technique show this effect clearly. This is one of the first reports of this effect to our knowledge.

8.2: Future work

The origin of the modal structure observed for the annealed PLD-grown ZnO samples requires a more detailed analysis at higher spectral, temporal and spatial resolutions to confirm definitively that the modal structure is associated with self-formed cavities due to scattering at grain boundaries. The possible effect of the pumped region in forming a “gain-guided” type of cavity could not be absolutely ruled out by our work, and the ability to measure mode separations and temporal variations in these modes, in addition to spatially mapping the emission from the sample surface would enable such discrimination.

A more detailed investigation of the effect of varying grain sizes on the optical and lasing process could also be attempted. We have seen a definite progression in the PLD samples with reference to optical quality, stimulated emission, lasing events etc i.e. with increased grain sizes, however a more detailed analysis with a larger distribution of grain sizes for samples would help to clarify the origins of such stimulated emission and lasing differences with regard to grain sizes.

Investigations of high excitation effects at a range of temperature between 10K and 300K, particularly for the bulk sample, may enable verification or refutation of the role of exciton diffusion in altering the exciton density and its lasing behaviour. In particular measurements at ~ 77 K where excitons are delocalised from traps and the diffusion length remains small may be the key to understanding such effects.

One of the recurrent problems associated with the investigation of stimulated emission and random lasing phenomena was the precise control of the pump laser intensity. The laser excitation intensity was calculated from the intensity of the laser line feature subsequent to acquiring the spectrum, and hence setting the intensity before each scan was a matter of some experience and skill. In particular, if a band or modal structure appeared at a certain laser intensity it only could be investigated in more detail after the spectra was analysed. However such reproduction of experimental conditions was rather difficult as the area of excitation could “wander” slightly due to variations in the laser

output and the surface can suffer significant damage quite quickly at higher power densities making reproduction impossible. The variable neutral density filter gave intensity values across a range however it was impossible to reproduce exactly the excitation intensities for each experimental run at a particular excitation area. This problem is highlighted in chapter six and in particular for the studies on the bulk material, where two quite different spectra were attained for measurements on slightly different areas of the sample. Better control and reproduction of pumping intensity levels will allow a more structured exploration of these high excitation phenomena.

Chapter Eight References

- [1] K.Vanheusden, W.L.Warren, C.H.Seger, D.R.Tallant, J.A.Voigt, B.E.Gnade,
J.Appl.Phys.Lett. 64, (1994), 7983.

Appendix A

Photomultiplier Tube Specifications

HAMAMATSU

PHOTOMULTIPLIER TUBES R3310-02, R4330-02

InGaAs (Cs) Photocathode, Wide Spectral Response, 51mm (2") Dia., Head-on Type
For Photon Counting : Low Dark Counts, Excellent P.H.D.

■ APPLICATIONS

- Raman Spectroscopy
- Fluorescent Spectroscopy
- Astrophysical Measurement
- Laser Detection

■ FEATURES

Wide Spectral Response

R3310-02 300 to 1040nm

R4330-02 160 to 1040nm

High Quantum Efficiency in IR 0.25% at 1 μ m

Fast Rise Time 3.0ns at 1500V

Excellent Single Photoelectron

Pulse Height Distribution

..... Peak to Valley Ratio 2.3 (at -20°C)

Low Dark Counts 30cps Typ. (at -20°C)



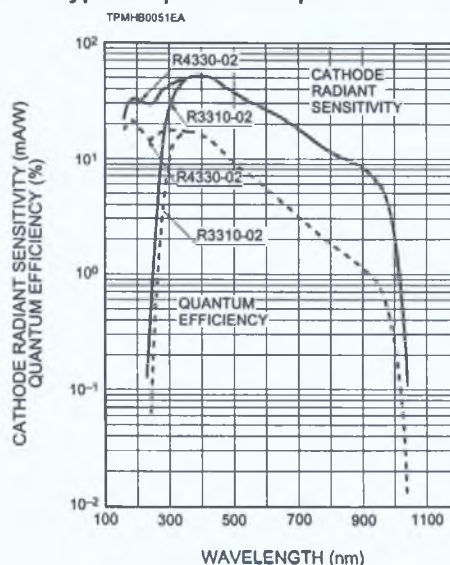
Hamamatsu R3310-02 and R4330-02 are 51mm (2") diameter head-on type photomultiplier tubes having InGaAs (Cs) photocathodes, and linear focused CuBeO dynodes. The InGaAs (Cs) photocathode allows high sensitivity over a wide spectral range up to 1040nm.

The R3310-02 and the R4330-02 are selected for photon counting, and they feature low dark counts and excellent pulse height distribution (PHD) of single photoelectrons.

■ GENERAL

Parameter	Description/Value	Unit
Spectral Response		
R3310-02	300 to 1040	nm
R4330-02	160 to 1040	nm
Wavelength of Maximum Response	400	nm
Photocathode		
Material	InGaAs(Cs)	—
Minimum Effective Area	10 X 10	mm
Mode	Opaque	—
Window Material		
R3310-02	Borosilicate glass (K-free)	—
R4330-02	Synthetic silica glass	—
Dynode		
Secondary Emitting Surface	Cu-BeO	—
Structure	Linear Focused	—
Number of Stages	10	—
Direct Interelectrode Capacitances		
Anode to Last Dynode	Approx. 2	pF
Anode to All Other Electrodes	Approx. 3	pF
Base	21-pin Base	—
Suitable Socket	E678-21C (Supplied) E678-21D (Option)	—
Weight		
R3310-02	110	g
R4330-02	93	g

Figure 1: Typical Spectral Response



Subject to local technical requirements and regulations, availability of products included in this promotional material may vary. Please consult with our sales office.

Information furnished by HAMAMATSU is believed to be reliable. However, no responsibility is assumed for possible inaccuracies or omissions. Specifications are subject to change without notice. No patent right are granted to any of the circuits described herein. © 1997 Hamamatsu Photonics K.K.

PHOTOMULTIPLIER TUBES R3310-02, R4330-02

MAXIMUM RATINGS (Absolute Maximum Values)

Parameter	Value	Unit
Supply Voltage		
Between Anode and Cathode	2200	Vdc
Between Anode and Last Dynode	250	Vdc
Average Anode Current [Ⓐ]	1	μA
Average Pulse Count Rate [Ⓑ]	6 × 10 ⁶	cps
Average Cathode Current [Ⓒ]	10	pA
Ambient Temperature [Ⓓ]	-80 to +50	°C

CHARACTERISTICS (at 25°C)

Parameter	Min.	Typ.	Max.	Unit
Cathode Sensitivity [Ⓔ]				
Quantum Efficiency				
at 253.7nm (Hg-Line) R4330 Series	—	15	—	%
at 1000nm	0.13	0.25	—	%
Luminous [Ⓕ]	80	150	—	μA/lm
Radiant at 253.7nm (Hg-Line) R4330 Series	—	30	—	mA/W
at 852.1nm (Cs-Line)	—	9.4	—	mA/W
at 900nm	—	8.1	—	mA/W
at 1000nm	1.1	2	—	mA/W
Red/White Ratio [Ⓖ]	—	0.4	—	—
Anode Sensitivity [Ⓖ]				
Luminous [Ⓕ]	15	50	—	A/lm
Radiant at 253.7nm (Hg-Line) R4330 Series	—	1.0 × 10 ⁴	—	A/W
at 852.1nm (Cs-Line)	—	3.1 × 10 ³	—	A/W
at 900nm	—	2.7 × 10 ³	—	A/W
at 1000nm	—	6.6 × 10 ²	—	A/W
Gain [Ⓖ]	—	3.3 × 10 ⁵	—	—
Equivalent Anode Dark Current [Ⓙ]	—	5	20	nA
Anode Dark Current [Ⓚ]	—	30	150	cps
Single Photoelectron PHD (Peak to Valley Ratio)	—	2.3	—	—
Time Response [Ⓛ]				
Anode Pulse Rise Time [Ⓜ]	—	3.0	—	ns
Electron Transit Time [Ⓨ]	—	23	—	ns

NOTES

- Ⓐ Averaged over any interval of 30 seconds maximum.
- Ⓑ Measured at single photoelectron level. The discriminator level is set at valley point.
- Ⓒ In practical operation, the cathode current should be lower than 2pA to prevent shortening the life of the photocathode.
- Ⓓ For cooling operation, another ceramic socket, type number E678-21D is recommended, because the teflon socket type number E678-21C supplied with the tube is not suitable for cooling operation due to its high thermal expansion coefficient. Alternatively, it is recommended to solder a resistor, capacitor, etc. directly on stem pins using a socket contact (100-2520S) supplied by Winchester.
- Ⓔ Supply voltage is 150 volts between the cathode and all other electrodes.
- Ⓕ The light source is a tungsten filament lamp operated at a distribution temperature of 2856K.
- Ⓖ The quotient of the cathode sensitivity measured with the light source is the same as Note Ⓔ passing through a red filter (Toshiba R-68) divided by the cathode luminous sensitivity without the red filter.
- Ⓛ Measured with supply voltage and voltage distribution ratio in Table 1.
- Ⓜ Measured with supply voltage to provide the anode luminous sensitivity of 40 (A/lm) and the voltage distribution ratio in Table 1 after 30 minutes storage in the darkness.
- Ⓨ Measured with supply voltage that gives 2 × 10⁶ gain and with the voltage distribution ratio shown in Table 1 after one hour storage in the cooler set at -20°C.

Ⓨ The electron transit time is the interval between the arrival of a delta function light pulse at the entrance window of the tube and the time when the output pulse reaches the peak amplitude. In measurement the entire photocathode is illuminated.

- Ⓛ The rise time is the time it takes the output pulse to rise from 10% to 90% of the peak amplitude when the entire photocathode is illuminated by a delta function light pulse.

- Ⓨ The electron transit time is the interval between the arrival of a delta function light pulse at the entrance window of the tube and the time when the output pulse reaches the peak amplitude. In measurement the entire photocathode is illuminated.

Warning—Personal Safety Hazards
Electrical Shock — Operating voltages
 applied to this device present a shock hazard.

Table 1: Voltage Distribution Ratio

Electrodes	K	Dy1	Dy2	Dy3	Dy4	Dy5	Dy6	Dy7	Dy8	Dy9	Dy10	P
Distribution Ratio	3	1.5	1	1	1	1	1	1	1	1	1	1

Supply Voltage : 1500Vdc, K : Cathode, Dy : Dynode, P : Anode

Figure 2: Typical Single Photoelectron Pulse Height Distribution

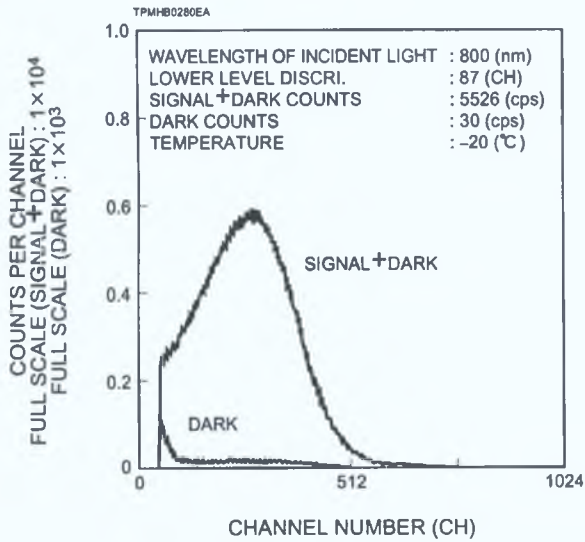


Figure 3: Typical Gain

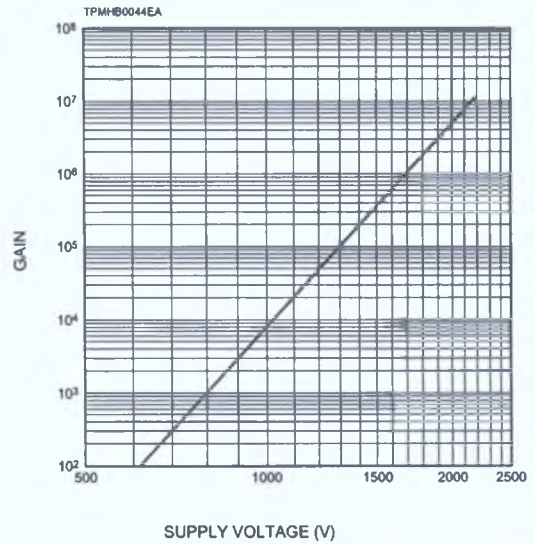


Figure 4: Typical Time Response

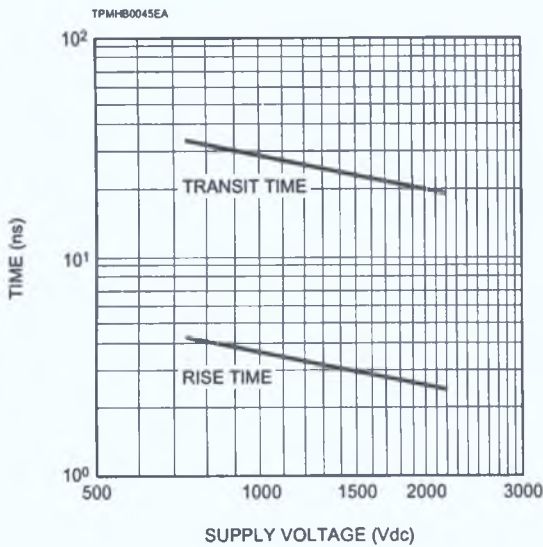


Figure 5: Typical Temperature Coefficient of Quantum Efficiency

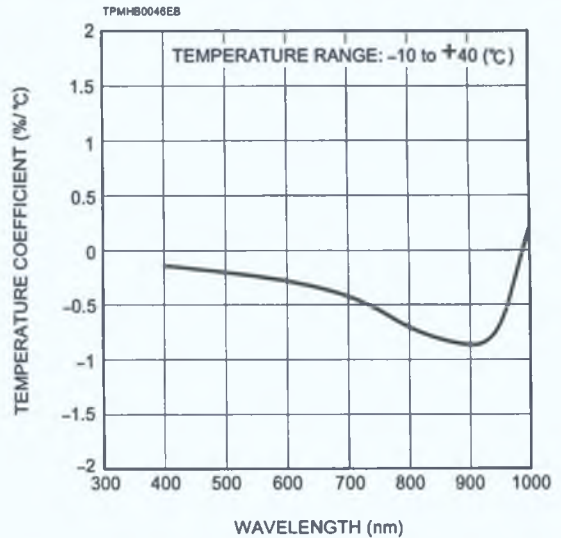
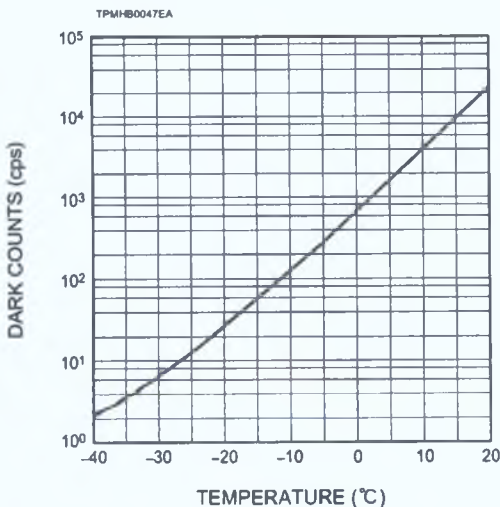


Figure 6: Typical Dark Counts vs. Temperature

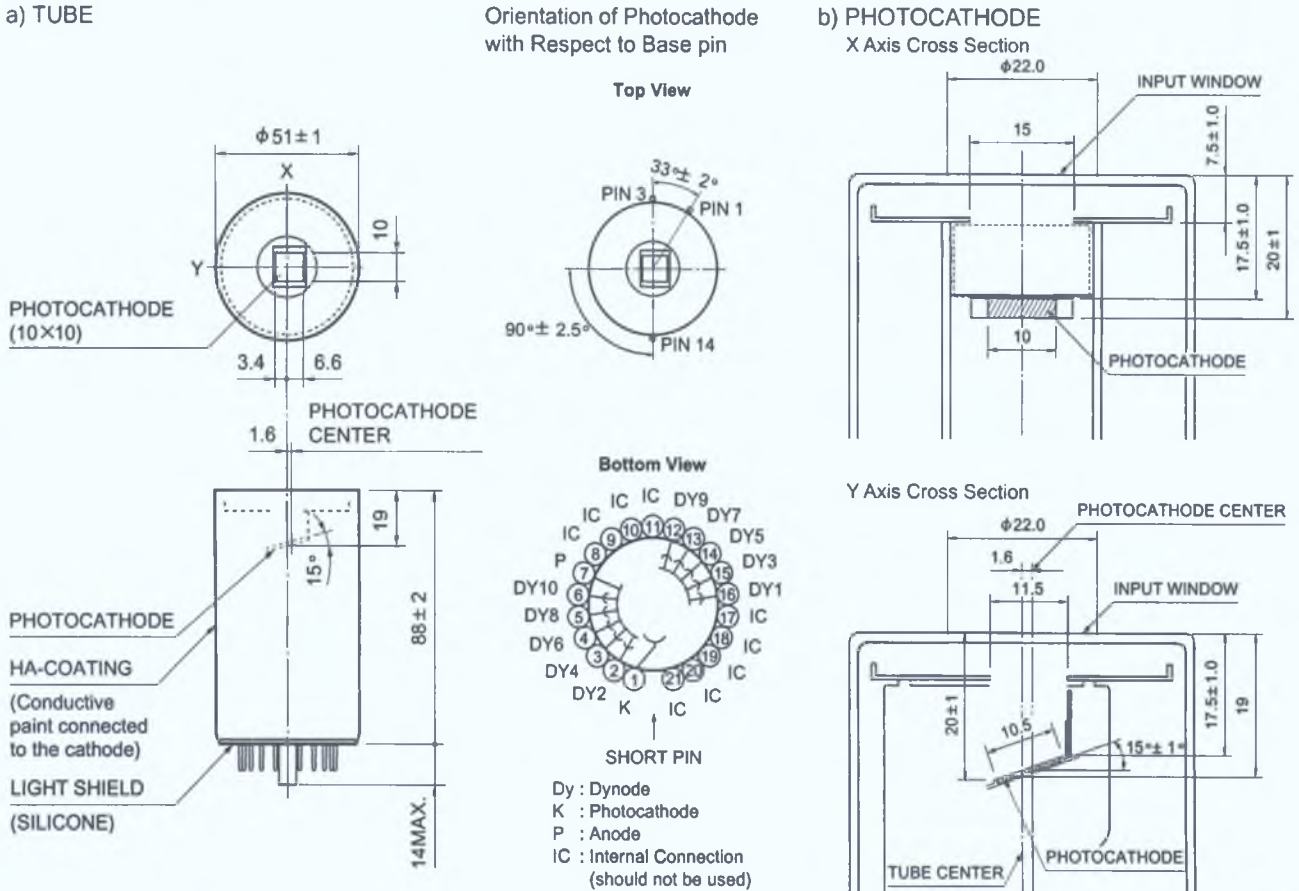


COOLING

As Figure 6 shows, the dark counts of the R3310-02 and R4330-02 decreases by cooling the tube. Therefore, when performing photon counting, it is recommended that the tube be cooled down to about -20°C . The cooler C2761 which features temperature control from -30°C to 0°C is available from HAMAMATSU.

PHOTOMULTIPLIER TUBES R3310-02, R4330-02

Figure 7: Dimensional Outline and Basing Diagram (Unit : mm)



<p>REMARKS</p> <ul style="list-style-type: none"> ● HA coating <p>The R3310-02 and R4330-02 are coated with the conductive paint connected to the cathode, which is covered with an insulating material (HA coating). This method decreases noise. Care should be taken not to damage the insulating cover wrapping around the bulb.</p>	<p>CAUTIONS</p> <ul style="list-style-type: none"> ● Use the HAMAMATSU SOCKET E678-21C or E678-21D. ● When soldering the voltage dividers to the socket, the PMT should be inserted in the socket.
--	---

HAMAMATSU

HAMAMATSU PHOTONICS K.K., Electron Tube Center
 314-5, Shimokanzo, Toyooka-village, Iwata-gun, Shizuoka-ken, 436-0193, Japan, Telephone: (81)539/62-5248, Fax: (81)539/62-2205

U.S.A.: Hamamatsu Corporation, 380 Foothill Road, Bridgewater, N.J. 08807-0910, U.S.A., Telephone: (1)908-231-0960, Fax: (1)908-231-1216

Germany: Hamamatsu Photonics Deutschland GmbH, Arzbergstr. 10, D-82211 Herrsching am Ammersee, Germany, Telephone: (49)8152-375-0, Fax: (49)8152-2658

France: Hamamatsu Photonics France S.A.R.L.: 8, Rue du Saule Trapu, Parc du Moulin de Massy, 91882 Massy Cedex, France, Telephone: (33)1 89 53 71 00, Fax: (33)1 89 53 71 10

United Kingdom: Hamamatsu Photonics UK Limited: Lough Point, 2 Gladbeck Way, Windmill Hill, Enfield, Middlesex EN2 7JA, United Kingdom, Telephone: (44)181-367-3560, Fax: (44)181-367-6384

North Europe: Hamamatsu Photonics Norden AB: Färögatan 7, S-164-40 Kista Sweden, Telephone: (46)8-703-29-50, Fax: (46)8-750-58-95

Italy: Hamamatsu Photonics Italia: S.R.L.: Via Della Moia, 1/E, 20020 Arese, (Milano), Italy, Telephone: (39)2-935 81 733, Fax: (39)2-935 81 741

TPMH1021E04
SEP. 1997

Appendix B

Equipment Specifications

Specification of the spectrometer (model 1704 by Jobin Yvon):

Performance characteristics are in terms of 1200 gr/mm grating in the first order

Specification	Model 1704
Focal length	1.0 m
Aperture	f/9
Gratings: Standard size	110 × 128 mm
Grooves/mm	30 – 3600
Type	Ruled or Holographic
Spectral Coverage,	175 – 1500 nm
Dispersion, nm/mm	0.8
Resolution, (at 313.1nm)	0.008 nm
Accuracy, (over 600nm)	±0.1 nm
Repeatability	±0.03 nm
Drive step size	0.00025 nm
Dimensions (HWL)	42×47×114 cm
Weight	78 Kg

Table B.1: Specifications for the spectrometer.

Specifications for the HeCd Laser Model (IK5652R-G by Kimmon):

Item	Specification
WAVELENGTH	325.0 nm / 441.6 nm
SPECIFIED POWER	40mW / 120mW
TRANSVERSE MODE	TEM multimode
MODE SPACING (C/2L)	113 MHz
SPECTRAL BANDWIDTH	3 GHz
COHERENCE LENGTH	10 cm
POLARIZATION	Linear, Vertical
POLARIZATION RATIO	> 500:1
NOISE (peak-to-peak)	15% 30kHz - 2MHz
NOISE (r.m.s.)	4% 30kHz - 10MHz
BEAM DIAMETER (1/e ²)	1.8 mm
BEAM DIVERGENCE	1.0 mrad
BEAM POINTING STABILITY (25°C constant temperature)	±25 μrad
POWER STABILITY (25°C constant temperature).	±2%/4hr
POWER STABILITY (10°~40°C)	20%
ENVIRONMENTAL CONDITION (operation)	TEMP. 10°~40°C
VIBRATION (operation)	0.25 G
DIMENSIONS and WEIGHT	1420 x 146 x 197 mm and 23.5 kg

Table B.2: Specifications for the 325nm laser.

Specification for the Nd YAG laser Model (Surelite II® by Continuum Lasers)

Item	Specification
Repetition Rate	10 Hz
Energy	160 mJ
Pulsewidth (FWHM)	4-6 nsecs
Linewidth	0.2-1.0 cm^{-1}
Divergence	0.6 mrad
Rod Diameter	7mm
Beam pointing Stability	100 μrad
Jitter	0.5 $\pm\text{ns}$
Energy Stability	4.0 $\pm\%$
Power Drift	6.00 $\pm\%$
Beam Spatial Profile	
Near Field (<1m)	0.70
Far Field (∞)	0.95

Table B 3 Specifications for the 355nm laser

TCSPC system by Edinburgh Instruments

Item	Specification
<i>Flash Lamp Head nF900</i>	
Focus Adjustment	250mm to infinity
Lens Aperture	40mm
Lens material	Spectrosil B
Rear Reflector	MgF ₂ coated
Electrode Material	Tungsten/Thorium (90/10)
Pressure range	< 0.01 bar to 2 bar
<i>Power supply for flash lamp head</i>	
Trigger Pulse	+200V, 2 μ s
Trigger Frequency	1 – 100KHz, computer controlled
<i>Specifications for Hydrogen filler gas</i>	
Pulse width	1.0 - 1.6ns
Pulse Tail	<10 ⁻⁴
Photons/Pulse	10 ¹⁰
Pulse Repetition Rate	\leq 50 kHz
Spectral Range	Ca 220-800nm

Table B 4 Specifications for the flashlamp head used in the TCSPC system

Computer Module For TCSPC by Edinburgh Instruments

Item	Specifications
<i>Signal input</i>	
Principle	Constant Fraction Discrimination
Impedance	50 Ω
Input Pulse Amplitude Range	-10mV to -1V
Electrical Time Jitter (FWHM)	5ps
<i>Time to Amplitude Converter</i>	
Principle	Ramp generator
TAC Ramp Range	10ns to 50 μ s
TAC offset	0 to 50% of TAC range
<i>Analogue to Digital Converter</i>	
Principle	Flash ADC with error correction
Resolution	4096 channels (12 bits)
<i>Data Acquisition</i>	
Dead time	112.5ns
Max. number of detectors channels	Up to 4096

Table B.5: Specifications for the computer modules used in the TCSPC system

Appendix C

Time Resolved Analysis

Instrument Response Function

The response function of the lamp was taken for each solution. This was achieved by acquiring a time resolved measurement of the flashlamp as it shined onto the spectrometer. The observed pulse FWHM is ~ 2 ns.

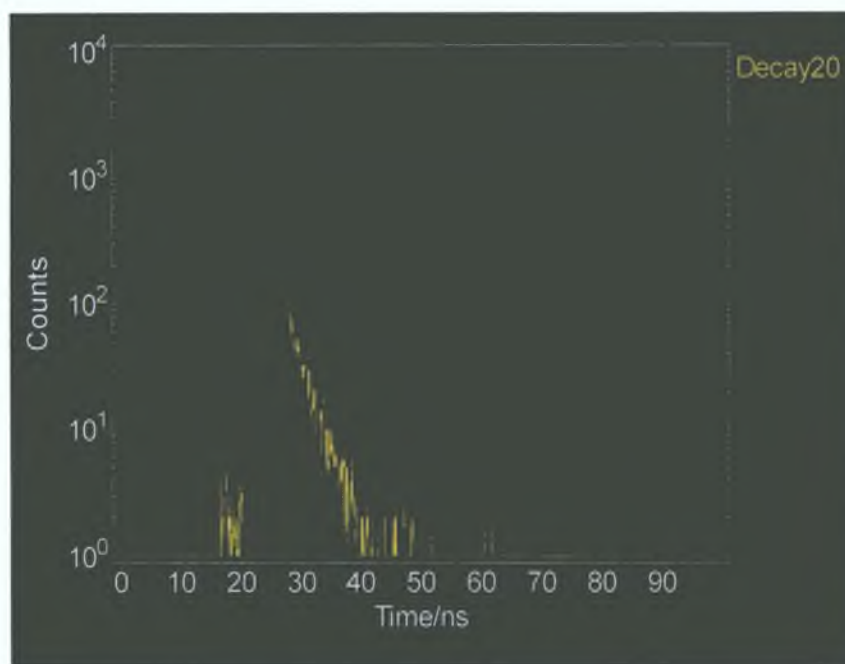


Figure C.1: Instrument Response Function for a flash lamp head.

Time Resolved Analysis

Using the raw histogram data and software supplied by Edinburgh Instruments the life times could be calculated. Raw lifetime data generally require a numerical analysis procedure for recovering the intrinsic lifetime parameters, either growth or decay parameters. In practice, many lifetime measurements do not decay starting right after a prompt, infinitely short, signal rise, but they have a finite edge often caused by the exciting light pulse. This initial part of the raw data contains valuable information. For example, short lifetimes can often be precisely recovered if the initial part of the fluorescence decay is included in the analysis. In this case the sample response function cannot be described with a simple decay model $R(t)$. In the initial part, the formation part and the initial decay part the sample response is determined primarily by the instrument response function (which includes the optical pulse widths as well as possible electrical effects). The mathematical relationship between sample response function $X(t)$, the instrumental response function ($E(t)$) and the sample decay model ($R(t)$) is the convolution integral:

$$X(t) = \int_0^t E(t^i) R(t - t^i) dt^i$$

Apart from the noise, $X(t)$ fully describes the measured data i.e. the rise of the signal, the initial part of the decay, and the tail of the decay. In order to calculate $X(t)$ one needs to know both the theoretical model for the decay ($R(t)$) and the (separately measured) instrument function ($E(t)$). Only in the case of an infinitely short sample excitation is the sample response function identical to the model function.

There are two fitting routines offered by the software. In the “tail fit” routine $X(t)$ is identical to $R(t)$. This routine is only applicable for data, which are fitted in a region with no further sample signal generation. The “reconvolution fit” routine is more universal. It fits the sample response $X(t)$ to the data. This procedure allows one to fit over the rising edge of the data. The tail fit procedure eliminates the statistical noise from the raw data, but can not handle the region in which sample excitation takes place. The reconvolution fit procedure eliminates both the noise and the effects of the exciting light pulse.

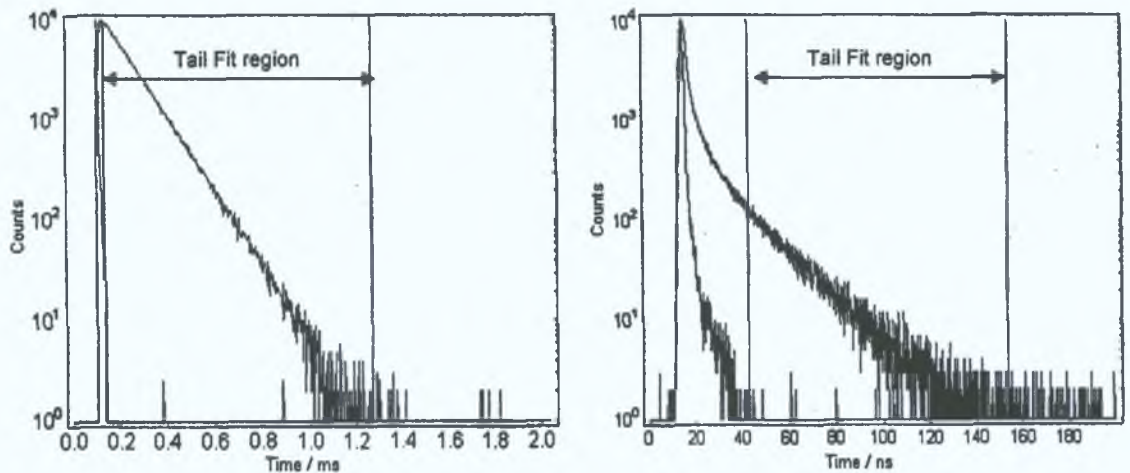


Figure C.2: Regions that can be identified with the tail fit

Tail fit:

The two pictures in *figure C.2* show typical measurement examples. Also indicated are the data regions, which can be analysed with tail fits. As stated previously, tail fits can only be performed in regions with no further sample excitation. Consequently the tail fit routine will be used to analyse those samples with long decay times. The picture not

only shows the decay data but also the instrumental response function. This is used to demonstrate the fitting range of the program. For a tail fit the instrumental response function is not required. A tail fit applied to the measurement in the left picture will yield all lifetime information intrinsic in the decay measurement, while a tail fit applied to the measurement in the right picture will obviously only result in lifetime parameters which have a dominating effect in the longer time region. The lifetime parameters in the shorter region cannot be recovered by using the tail fit routine. For this data it is far more appropriate to use the reconvolution fit routine described in the next paragraph.

Reconvolution:

If the raw data are not only superimposed by noise but are also affected by the effects of sample excitation and signal generation the numerical procedure requires the use of the convolution integral $X(t)$ to extract the lifetime parameters. The fit range expands over the convolution region and the tail region. With reconvolution fits, the fitting range should generally expand over the entire measurement, starting from about zero, ranging over the rising edge, the decay and back down to zero. An Instrument response function used in this data fit can be seen in *figure C.1*.

Appendix D

Spectrograph and PDA Specifications



LineSpec™ CCD Detector on output of MS125™ Spectrograph

- Versatile instrument - interchangeable slits and gratings
- Compact and low cost - the OEM choice
- Low stray light - no re-entrant spectra
- Impressive resolution 0.22 nm (with 1200 l/mm grating and 2048 element array)

Since its introduction several years ago, the MS125™ has quickly become our most popular spectrograph for non-imaging applications. Its superior performance, compact size, low cost and versatility make it attractive to researchers and Original Equipment Manufacturers.

ABOUT THE MS125™

The features of the MS125™ speak for themselves:

- Flat focal field for 1 inch diode arrays and CCDs
- Low F/number - F/3.7
- Short focal length - 120 mm
- 0.22 nm resolution with 1200 l/mm grating and 2048 element array
- Minimal coma
- Calibrated micrometer drive
- Compact and easily mounted in various configurations

EFFICIENT OPTICAL CONFIGURATION

Fig. 1 shows the MS125™'s unusual crossed optical arrangement. A 100° angle separates the input and exit faces. Notice the special ribs which are cast in position to baffle unwanted light paths and capture stray light reflections. The focal field is flat over the 1 inch (25.4 mm) length of common detector arrays.

CALIBRATED MICROMETER DRIVE

The MS125™ uses a calibrated micrometer drive for wavelength tuning. The micrometer is calibrated to read 1 nm per graduation for a 1200 l/mm grating. For other density gratings, multiply the micrometer reading by the "Micrometer Conversion Multiplier," in Table 1 on the following page.

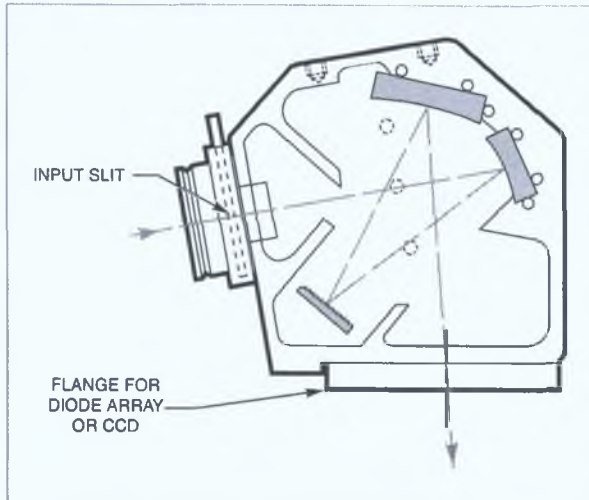


Fig. 1 Optical configuration of MS125™ Spectrograph.

TECH NOTE

A WORD ABOUT RESOLUTION

The resolution of a monochromator is determined by the dispersion and the slit width. The same is true for spectrographs, with an additional factor being the width of the diode array element since this is effectively an exit slit. The spectral resolution for a spectrograph is typically accepted as being limited to the bandpass over two array elements. The exceptional flat field and minimal optical aberrations of the MS125™ mean that the resolution is very nearly constant across the entire focal plane. With a 25 μm entrance slit and 1024 element array, the spectral resolution is about 50 μm across the entire field, i.e. about 0.4 nm with a 1200 l/mm grating.

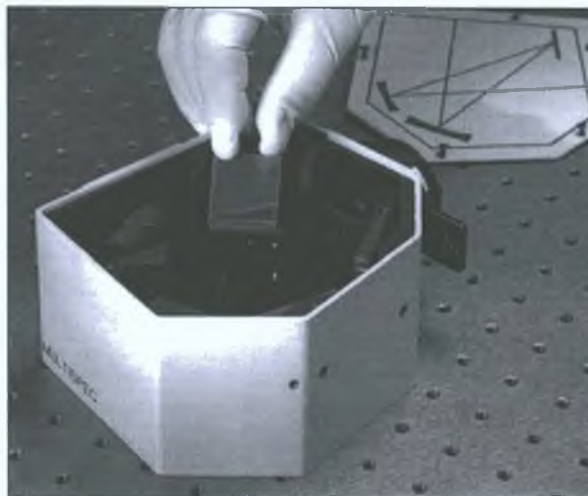
NEGLIGIBLE STRAY LIGHT

We know the problems that stray light causes to critical measurements, therefore we've spent a lot of time on the design and test of the MS125™. The result: an instrument with very low stray light. We use baffles (shown in Fig.1) to prevent light scatter inside the instrument, and low stray light gratings.

INTERCHANGEABLE GRATINGS

We offer a large selection of interchangeable gratings for the MS125™. Choose the one that covers the spectral range of interest and satisfies your resolution requirements.

You can easily interchange gratings without realigning the instrument.



Gratings are easily interchanged in the MS125™.

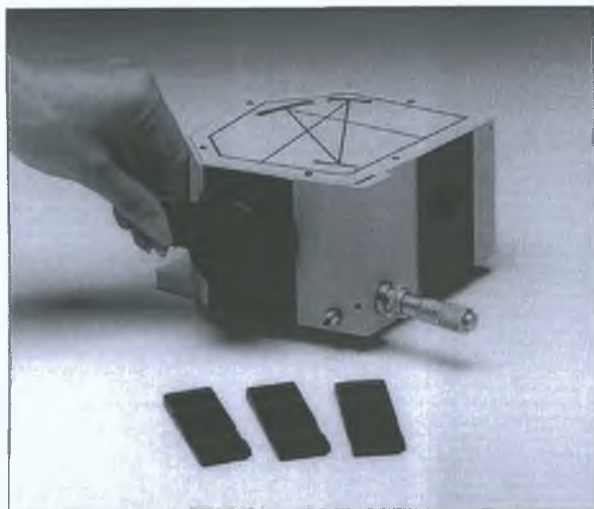
Table 1 Grating Specifications for MS125™ 1/8 m Spectrograph

Line Density (l/mm)	Blaze wavelength (nm)	Type	Peak Efficiency (%)	Spectral Resolution* (nm)	Multichannel Array Bandpass** (nm)	Primary Wavelength Region*** (nm)	Instrument's Upper Wavelength Mechanical Limit (For specified grating)	Model No.
2400	250	Holographic	65	0.11	84	200 - 500	500 nm	77419
2400	400	Holographic	65	0.11	81	230 - 500	500 nm	77420
1800	500	Holographic	80	0.14	109	300 - 670	670 nm	77421
1200	250	Holographic	80	0.22	168	180 - 650	1000 nm	77410
1200	350	Ruled	80	0.22	170	200 - 1000	1000 nm	77411
1200	750	Ruled	80	0.22	163	450 - 1000	1000 nm	77412
600	200	Ruled	70	0.43	338	180 - 500	2000 nm	77413
600	400	Ruled	85	0.43	338	250 - 1300	2000 nm	77414
600	750	Ruled	75	0.43	338	450 - 2000	2000 nm	77415
600	1250	Ruled	85	0.43	333	750 - 2000	2000 nm	77455
600	1600	Ruled	90	0.43	325	900 - 2000	2000 nm	77456
400	350	Ruled	65	0.65	503	200 - 800	3000 nm	77416
400	500	Ruled	80	0.65	505	300 - 1200	3000 nm	77417
400	1600	Ruled	85	0.65	505	900 - 2900	3000 nm	77457
300	300	Ruled	75	0.86	668	200 - 750	4000 nm	77422
300	1000	Ruled	85	0.86	675	575 - 2500	4000 nm	77458
246.16	226	Ruled	60	1.08	810	190 - 450	4800 nm	77459

* Measured with 10 μ m x 2 mm slit and 14 x 200 μ m pixel array (2048 pixels).

** Spectral bandpass depends slightly on the position of the grating. Here we give spectral bandpass values at the blaze wavelength setting of the grating.

*** The primary wavelength region is where the grating efficiency is $\geq 20\%$. System efficiency will also be affected by the reflectivity of the mirrors and the grating angle, at any wavelength.



MS125™ Spectrograph with various input slits.

INPUT SLITS

The MS125™ Spectrograph comes with an input slit holder; choose a slit from one of the four choices listed below.

Table 2 Input Slits for MS125™

Slit Width (μm)	Slit Height (mm)	Resolution at 546 nm (nm)	Model No.
10	2	0.22*	77222
25	3	0.4**	77220
50	3	0.6**	77221
100	3	0.9**	77728
200	3	1.4**	77730

* This value is for a 1200 l/mm grating and 14 x 200 μm size pixels (2048 element array); it is not achievable on 1024 arrays which have larger pixels.

** For 1200 l/mm grating and 1024 array. For 2048 arrays, the resolution is 1/2 this value.

FOR IMAGING SPECTROGRAPHS...

The MS125™ is not an imaging spectrograph; see the following pages for instruments designed for imaging applications.

Table 3 Imaging Spectrographs

Instrument	Features	Detail Page
MS260™ 1/4 m	Automated, triple grating; excellent resolution and imaging qualities; low cost alternative to MS257™.	4-88
MS127™ 1/8 m	Versatile (interchangeable gratings and slits); built-in shutter; suitable for most imaging applications.	4-83
FICST™ Family	Economical 23.3 to 25.6 mm focal length models; fixed grating; best suited for dedicated applications or OEM.	4-74
MS257™ 1/4 m Imaging Spectrograph/Monochromator	Fully automated; multiple (4) grating; dual input and output ports; ideal for UV-IR continuous scanning and advanced Multi-track Spectroscopy.	4-32

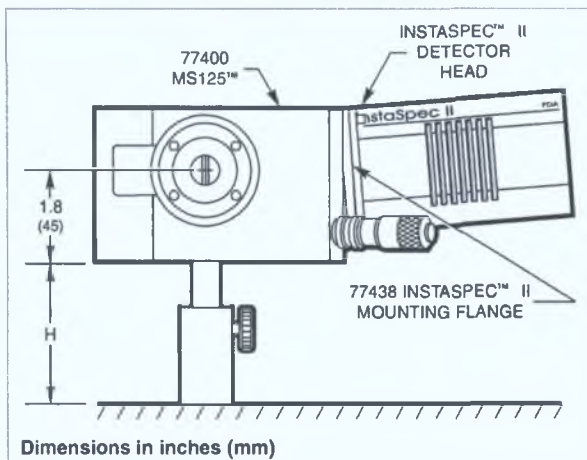


Fig. 2 MS125™ rod mounted to an optical table with InstaSpec™ Photodiode Array Detector on the output port.

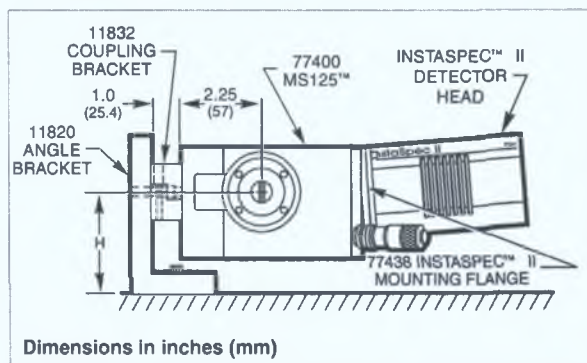


Fig. 3 MS125™ mounted to an angle bracket using the 11832 Coupling Blocks. InstaSpec™ is mounted to the output port.

MOUNTING

Because of the light weight and compact size of the MS125™, it can be mounted in a variety of configurations.

Rod Mounting

Rod mounting is the most popular mounting option because it affords height variability and 360° rotation. MS125™ has three 1/4-20 tapped holes spaced 1 inch (25.4 mm) apart, on the bottom of the instrument.

Table, Bench or Rail Mounting

The 11832 Set of Coupling Blocks lets you mount the MS125™ to optical tables or carriers for bench or rail mounting. We detail the 11832 Blocks on page 17-6.

Flange Mounting

The MS125™'s input slit holder has a 1.5 Inch Series male flange to accept any female flanged component such as fiber optic holders (page 18-37), filter holders (18-17), or focusing lens assemblies.

Spectra-Physics **MS125™ 1/8 m SPECTROGRAPH**

SPECIFICATIONS

Focal length: 120 mm
 F/number: F/3.7 (Input)
 Usable wavelength range: 180 m to 24 μm
 with interchangeable gratings
 Wavelength accuracy*: 1 nm over full range
 Wavelength reproducibility*: 1 nm
 Weight: 3.3 lbs (1.5 kg)

* With 1200 l/mm grating; for other density gratings, multiply this value by the "Micrometer Conversion Multiplier" from Table 1 on page 4-80.

ORDERING INFORMATION

77400 MS125™ Spectrograph
 Order grating and slit separately
 11832 Set of Coupling Blocks

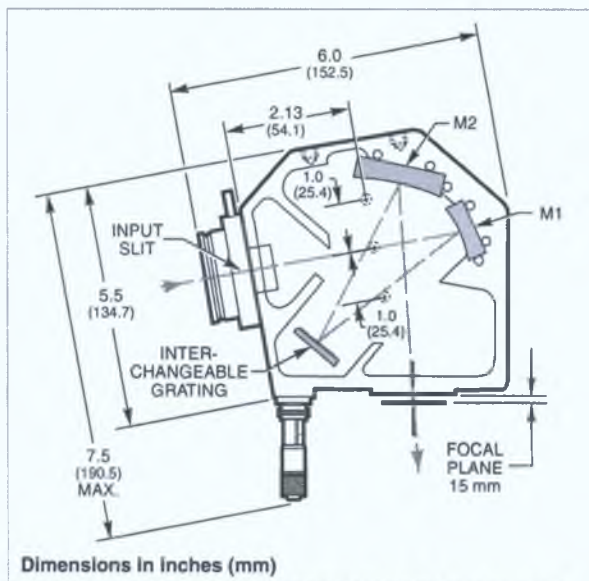


Fig. 4 Dimensional diagram of 77400 MS125™ Spectrograph.

Gratings

Line Density (l/mm)	Blaze Wavelength (nm)	Type	Primary Wavelength Region (nm)	Instruments Upper Wavelength Mechanical Limit (For specified grating)	Model No	Price
2400	250	Holographic	200 - 500	500 nm	77419	
2400	400	Holographic	230 - 500	500 nm	77420	
1800	500	Holographic	230 - 670	670 nm	77421	
1200	250	Holographic	180 - 650	1000 nm	77410	
1200	350	Ruled	200 - 1000	1000 nm	77411	
1200	750	Ruled	450 - 1000	1000 nm	77412	
600	200	Ruled	180 - 500	2000 nm	77413	
600	400	Ruled	250 - 1300	2000 nm	77414	
600	750	Ruled	450 - 2000	2000 nm	77415	
600	1250	Ruled	750 - 2000	2000 nm	77455	
600	1600	Ruled	900 - 2000	2000 nm	77456	
400	350	Ruled	200 - 800	3000 nm	77416	
400	500	Ruled	300 - 1200	3000 nm	77417	
400	1600	Ruled	900 - 2900	3000 nm	77457	
300	300	Ruled	200 - 750	4000 nm	77422	
300	1000	Ruled	575 - 2500	4000 nm	77458	
246.16	226	Ruled	190 - 450	4800 nm	77459	

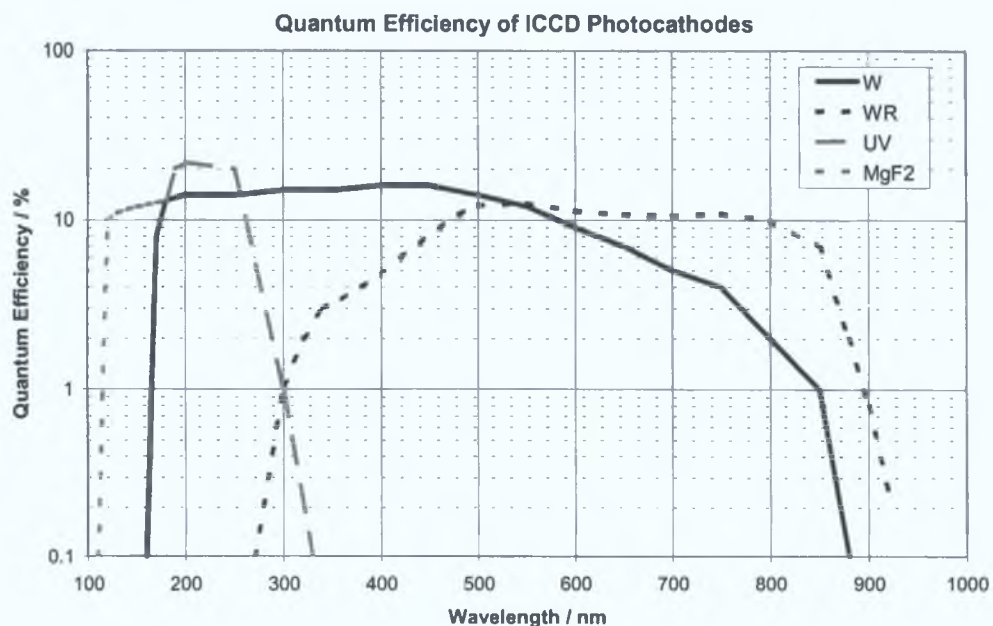
Slits

Slit Width (μm)	Slit Height (mm)	Model No	Price
10	2	77222	
25	3	77220	
50	3	77221	
100	3	77728	
200	3	77730	

The DH520 intensified CCD camera is designed for low-light spectroscopy applications that require fast gating. The 1024 x 256 array matches the 4:1 aspect ratio of the spectrograph's focal plane exit, providing maximum use of the CCD's sensitive region. A wide selection of photocathode options provides a range of solutions, whether a broad spectral response or optimization in a particular region is required.

● Sensor	Active Pixels	∅18 mm	690 x 256
		Effective Pixel Size (µm)	∅18 mm
		∅25 mm	960 x 256
		∅18 mm	26
		∅25 mm	26
Active Area (mm)		∅18 mm	18 x 6.7
		∅25 mm	25 x 6.7
Linearity (% , maximum) *1		1	

● Quantum Efficiency *2



Peak Quantum Efficiency at room temperature (%)

Intensifier Model Number	Minimum	Typical
18F-03 (W/HR/P43) @ 440 nm	13.5	15
18H-03 (W/HR/P43) @ 440 nm	17	18
18F-04 (W/HR/P46) @ 440 nm	13.5	15
18F-13 (WR/HR/P43) @ 520 nm	11	12
18F-23 (UV/HR/P43) @ 230 nm	10	20
25F-03 (W/HR/P43) @ 440 nm	13.5	15

● image Intensifier Details	Model Number [DH520-]	Intensifier Type					
		18F-03	18F-04	18F-13	18F-23	25F-03	
	Diameter (mm)	18	18	18	18	25	
	Minimum Optical Gate Width (ns) *3	U	2	2	5	N/A	3
		F	5	5	10	10	7
		H	50	N/A	N/A	N/A	N/A
	Photocathode*4	W	W	WR	UV	W	
	Input Window	Quartz*	Quartz*	Glass*	Quartz*	Quartz*	
	Spectral Range (nm)	180-850	180-850	250-920	180-320	180-850	
	Phosphor	P43	P46	P43	P43	P43	
	Phosphor Decay Time (to 10%)	2 ms	200 ns	2 ms	2 ms	2 ms	
	Max Gate rep rate (kHz)	25	25	25	25	25	
	Max Gain (typical; cts / photoe)*5	1250	500	850	500	850	
	Intensifier Tube Resolution Limit (µm)*6	25	30	25	25	35	
	EBI (photoe / pix-s)*7	0.02	0.02	0.1	0.01	0.02	

*Also available: glass input windows; MgF₂ input windows for operation to below 120 nm; fibre optic windows for easy optical coupling.

● Features & Benefits	TE cooling to -40°C	Negligible dark current, without the aggravation or safety concerns associated with LN ₂
	High resolution 18 and 25mm intensifier	Highest available intensifier tube resolution
	Close-Coupled Gating™	Gating as short as 1.2ns gating - the ultimate temporal resolution for both imaging and spectroscopy applications
	Single photon sensitivity	Pre-requisite for ultra-low light applications
	25kHz sustained gating rate	Compatible with high speed lasers
	Software gain control	Ease of use

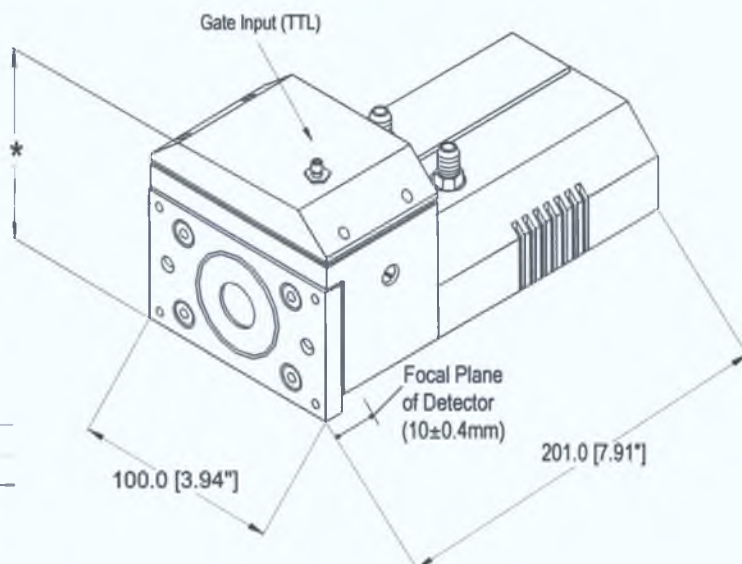
● Noise	System Readout Noise *8	Typical	Maximum:
	31kHz pixel readout rate	8	12
	1MHz pixel readout rate	24	35

● Temperature & Dark Current *9		Computer Power Supply		External PSU PS150	
		18mm	25mm	18mm	25mm
	Air-cooled Temp [Dark Current (typ; e-/pix/s)] (ambient air @ 20°C)	-10 [6.1]	-5 [10.5]	-20 [1.9]	-15 [3.5]
	Water-cooled Temp [Dark Current (typ; e-/pix/s)] (@ 10°C, 0.75 l/min)	-30 [0.6]	-25 [1.1]	-40 [0.15]	-35 [0.3]

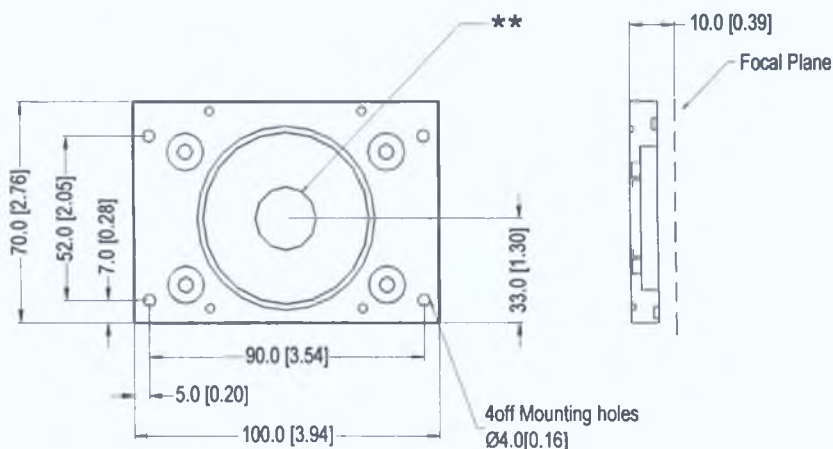
● Operating & Storage Conditions	Operating temperature	0 to 30°C ambient
	Relative humidity	< 70% (non-condensing)
	Storage temperature	-25 to +55°C

● Computer Requirements	Minimum:	Also:
	Windows 95/98: 100MHz Pentium + 64Mbytes RAM	• PCI-compatible computer
	Windows NT/2000: 100MHz Pentium + 128Mbytes RAM	• PCI slot must have bus master capability
		• 32 Mbytes free hard disc
	Recommended:	
	300MHz Pentium (or better) + 256 Mbytes RAM	

Dimension	18mm	25mm
*	90 [3.54]	106 [4.17]
**	20 [0.79]	27 [1.06]
Weight	2 kg [4lb 8oz]	2.1 kg [4lb 10oz]



Note – There are three mounting holes (1/4-20UNC) located on the base of the ICCD head. One is positioned centrally at a distance of 47mm from the front. The other two are positioned an inch on either side of the central one. Dimensions in mm [inches]



● For complete system use with...

The DH520 requires one of the following controller card options

CCI-001 PCI Controller card with 16-bit 62KHz & 31KHz pixel readout rate options

CCI-010 PCI Controller card with 16-bit 1MHz, 500KHz, 62KHz & 31KHz pixel readout rate options

The DH520 also requires one of the following software options.

Andor-MCD software – a ready-to-run Windows 95, 98, 2000, ME or NT -based package with rich functionality for data acquisition and manipulation

Andor-SDK-ICCD – a DLL driver and software development kit that let you create your own applications for the Andor camera

The DH520 may be used with the following accessories

PS150 Power Supply Module for achieving the lowest temperatures

IO160 Breakout box for interface signals

LM-NIKON-F Nikon F-mount lens adaptor

LMS-NIKON-F Nikon F-mount lens adaptor with shutter

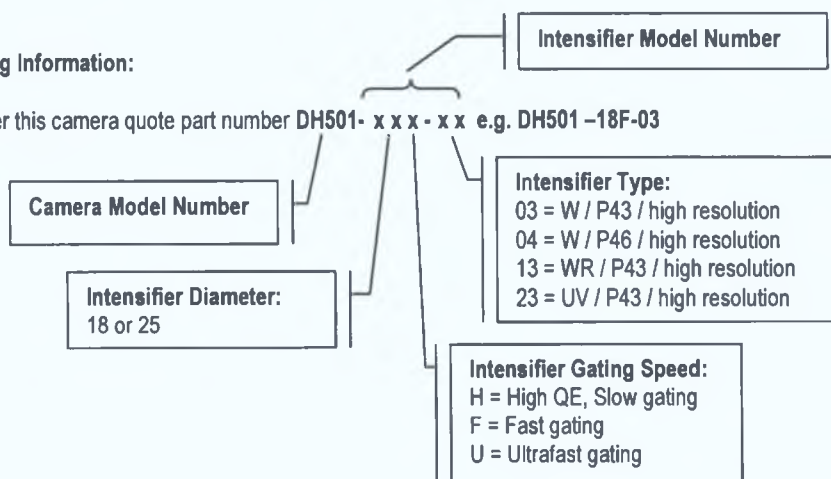
Contact Andor for details of spectrographs and adapters that can be used with the DH520.

● Notes

- ◆1 Linearity is measured from a plot of Counts vs. Signal over the upper 99% of the intensity range. Linearity is expressed as a %age deviation from a straight line fit for gain settings 0, 1 & 2. This quantity is not measured on individual systems.
- ◆2 This refers to the typical quantum efficiency of the photocathode and is measured by the tube manufacturer. As the QE of photocathodes is inherently linked to the gating speed of the tube, the W curve represents the QE of fast gating tubes. The QE of slower tubes tends to be around 20% higher.
The standard quartz input window cut-off occurs at around 160nm. If operation to below 120nm is required then this can be achieved by the use of a MgF₂ input window. Above 180nm, the MgF₂ curve follows the standard W tube response.
Detailed quantum efficiency specifications of other photocathodes are available.
- ◆3 The Minimum Optical Gate Width options refer to the measured optical full width half maximum (fwhm), not the electrical fwhm. Irising is less than a third of the optical fwhm.
- ◆4 The typical spectral response of the various photocathode options is shown in the QE graph on page 1.
- ◆5 The Maximum Gain is measured in A/D counts per photoelectron at the photocathode recorded at 16µs readout speed. Typical figures quoted. The ICCD gain is selectable from ~1ct/photoelectron to the maximum using the software gain control.
- ◆6 The resolution limit is the typical resolution of the image intensifier tube. This is not the overall resolution of the ICCD system. As a rough guide, the smallest resolvable FWHM feature on a CCD will be approximately 1.5 to 2 times the pixel size.
In a Lens-coupled Intensifier (LCI) system the resolution may be reduced as a result of the optical configuration.
- ◆7 Equivalent Background Illuminance (EBI) is measured in photoelectrons per pixel per second at the photocathode.
- ◆8 System Readout noise is for the entire system. It is a combination of CCD readout noise and A/D noise. Measurement is for single pixel readout with the ICCD at a temperature of -20°C and minimum exposure time under dark conditions.
- ◆9 Systems are specified in terms of minimum dark current achievable rather than absolute temperature.
- ◆10 Specifications are subject to change

Ordering Information:

To order this camera quote part number **DH501- x x x - x x** e.g. **DH501 -18F-03**



Ihr Kontakt:
 Olaf Koschützke
 Tel.: +49 6151 - 88 06 43
 Fax: +49 6151 - 88 06 89
 E-mail: olaf.koschuetzke@andor.com

Appendix E

Hall Measurements of PLD-grown samples

	Sheet resistivity ohm/sq	Hall Coefficient m ² /C	Mobility cm ² /V-s	Sheet Concentration /cm ²	Hall Voltage
Sample (i)					
0.1 μ amp	1.53E+04	-2.62	1.71	-2.38E+14	-1.36E-07
1.0 μ amp	1.53E+04	-1.54	1	-4.05E+14	
10 μ amp	1.53E+04	-0.639	0.417	-9.77E+14	-3.32E-06
10 μ amp	1.52E+04	0.225	0.148	2.77E+15	-1.17E-05
1 n amp	2.38E+04	105	44.1	5.93E+12	-2.53
Sample (ii)					
0.1 μ amp	5.61E+04	-4.43	0.79	-1.41E+14	-2.30E-07
1.0 μ amp	5.68E+04	-2.48	0.437	-2.52E+14	-1.29E-06
10 μ amp	5.71E+04	-2.55	0.448	-2.44E+14	-1.33E-05
100 μ amp	5.71E+04	-2.44	0.428	-2.56E+14	-1.27E-05
1n amp	6.42E+04	154	23.9	4.07E+12	7.98E-08
Sample (iii)					
0.1 μ amp	1.06E+05	32.7	3.07	1.91E+13	1.70E-06
1.0 μ amp	1.08E+05	71.7	6.63	8.70E+12	3.73E-05
10 μ amp	1.08E+05	19.5	1.81	3.20E+13	1.02E-04
Saturation after this point					

Table E.1: Hall measurements for the three PLD-grown samples.

Appendix F

Sample Images

Sample Images

This speckled cloud only appeared when the excitation intensity was increased above a certain threshold with the use of the neutral density filter. Emission was seen in all directions.



Figure F.1: Close up image of the speckled cloud in a darkened room. The excitation area is a stripe.

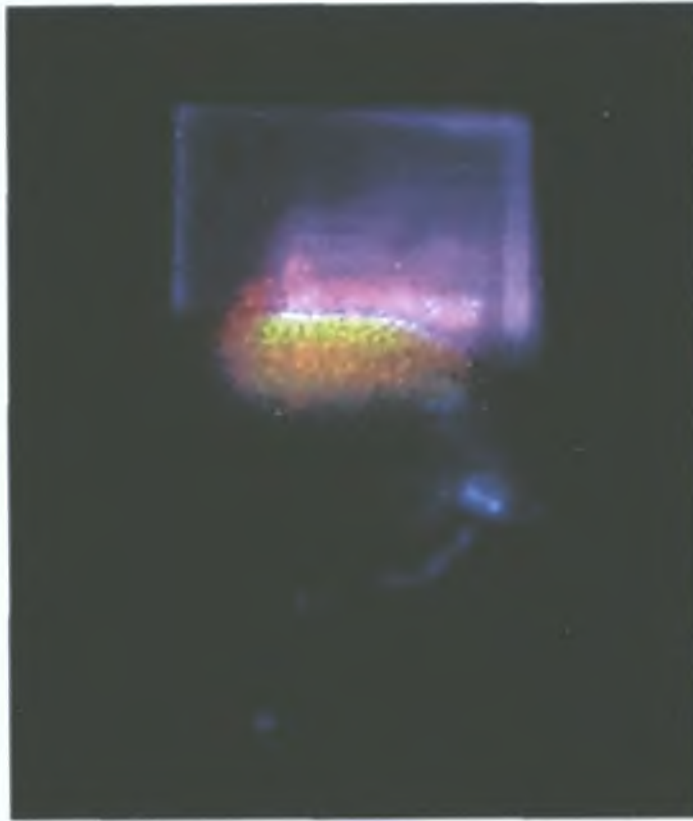


Figure F.2: Image of the excitation stripe on a PLD grown sample.



Figure F.3: Image of the PLD sample with a stripe excitation area in room light. Also shown is the sample holder.